STUDIES ON THE PROPERTIES OF PRISTINE AND DOPED NICKEL OXIDE NANOPARTICLES

Thesis submitted to

Mahatma Gandhi University, Kottayam

in partial fulfilment of the requirements for the award of the degree of

DOCTOR OF PHILOSOPHY IN PHYSICS

Under the Faculty of Science

by

SHEENA P. A.

Under the supervision of

Dr. THOMAS VARGHESE

LEAD KINDLY LIGHT

DEPARTMENT OF PHYSICS

Newman College, Thodupuzha

August 2019

MAHATMA GANDHI UNIVERSITY

CERTIFICATE ON PLAGIARISM CHECK

1.	Name of the Research Scholar	**SHEENA P. A**
2.	Title of the Thesis/Dissertation	Studies on the Properties of Pristine and Doped Nickel Oxide Nanoparticles
3.	Name of the Supervisor	Dr. THOMAS VARGHESE
4.	Department/Institution/ Research Centre	Department of Physics, Newman College, Thodupuzha
5.	Similar Content (%) identified	**2% (Two)**
6.	Acceptable Maximum Limit	25%
7.	Software Used	Urkund
8.	Date of Verification	07-08-2019

**Report on plagiarism check, items with % of similarity is attached*

Checked by (with Name, Designation & Signature) :

7/8/19

Anu George
07-08-2019
ANNU GEORGE
Deputy Librarian in-charge
University Library
Mahatma Gandhi University
Kottayam - 686 560

Name & Signature of the Researcher : SHEENA P. A

Name & Signature of the Supervisors : Dr. THOMAS VARGHESE

Name & Signature of the HoD/HoI(Chairperson of the Doctoral Committee)

Dr. THOMSON JOSEPH
PRINCIPAL
NEWMAN COLLEGE
THODUPUZHA

NEWMAN COLLEGE THODUPUZHA KERALA-685 585

URKUND

Urkund Analysis Result

Analysed Document:	SHEENA P. A - Studies on the Properties of Pristine and Doped Nickel Oxide Nanoparticles .pdf (D54726330)
Submitted:	8/7/2019 6:53:00 AM
Submitted By:	library@mgu.ac.in
Significance:	2 %

Sources included in the report:

http://www.jocpr.com/articles/optical-and-dielectric-behavior-of-nio-zn-quantum-dots.pdf
https://archive.org/stream/Httpwww.ijmer.com_20141021/IJMER-46046266_djvu.txt
https://scinapse.io/authors/1798554558
http://www.irjaes.com/pdf/IRJAES-V1N2Y16/IRJAES-V1N2P22Y16.pdf
https://www.science.gov/topicpages/d/doped+sno2+nanoparticles.html
https://worldwidescience.org/topicpages/l/li+doped+nio.html
http://www.ijmer.com/papers/Vol4_Issue6/Version-4/IJMER-46046266.pdf
https://link.springer.com/article/10.1007/s10854-015-3767-8
https://www.annauniv.edu/IQAC/AU%20NAAC_2019%20ALL%20PROOFS%2020190730%20OVERALL%20(SSR+DVV)/000.%20NAAC%20AU%20SSR%20%20ALL%20PROOFS/NAAC_2019_AU_3.4.5/PHYS_3.4.5_139_Structural,%20optical%20and%20high%20pressure%20electrical%20resistivity.pdf
ac48d3fb-2bd3-4fac-9a00-a91aa8e6601b
4467e1bc-f21a-44e6-8ab3-3889a48a7ca4

Instances where selected sources appear:

38

Annu George
07-08-2019

ANNU GEORGE
Deputy Librarian in-charge
University Library
Mahatma Gandhi University
Kottayam - 686 560

Department of Physics
Nirmala College, Muvattupuzha
(Affiliated to M.G. University, Kottayam & accredited by NAAC)
Ernakulam Dist., Kerala, India. PIN:686661
Tel: 914852836300, 2837290 Email: nanoncm@gmail.com

NSRC
NANOSCIENCE
RESEARCH CENTRE

Certificate

This is to certify that the thesis entitled **STUDIES ON THE PROPERTIES OF PRISTINE AND DOPED NICKEL OXIDE NANOPARTICLES** is an authentic record of the original research work carried out by **Ms. Sheena P. A**, in the Research Department of Physics, Newman College, Thodupuzha, under my guidance in partial fulfilment of the requirements for the award of the degree of Doctor of Philosophy, under the faculty of Science of Mahatma Gandhi University, Kottayam. The work presented in this thesis has not been submitted for any other degree or diploma earlier. It is also certified that **Ms. Sheena P. A.** has fulfilled the course requirements for the Ph.D degree of the university.

Muvattupuzha
August 2019

Dr. Thomas Varghese
(Supervising Teacher)

Declaration

I hereby declare that this thesis entitled **STUDIES ON THE PROPERTIES OF PRISTINE AND DOPED NICKEL OXIDE NANOPARTICLES** *is a record of the original research work carried out by me under the supervision of Dr. Thomas Varghese, in the Department of Physics, Newman College, Thodupuzha, Kerala. The work is original and has not been submitted earlier as a whole or in part for a degree/diploma at this or any other institution or university.*

Thodupuzha
August 2019

Sheena P. A.

Acknowledgement

I would like to convey my heartfelt gratitude to the people who extended their whole-hearted support and help during the period of my research work. First and foremost, I thank God Almighty for the blessings bestowed upon me.

I wish to express my deep gratitude to Dr. Thomas Varghese, my Research Guide, for his efficient guidance and invaluable support, without which this mission would not have been completed.

I am deeply indebted to the Principal and faculty members of the Department of Physics, Newman College Thodupuzha, with a special mention to Dr. Joe Jacob, Research Coordinator and Ms. Rajeena Joseph, former head of the Department of Physics for all the help rendered. I would like to thank the Principal and faculty members of the Department of Physics, Nirmala College, Muvattupuzha for all the facilities provided to carry out my research work.

I express my heartfelt gratitude to Dr. Ajims P. Mohammed, Principal, M E S Asmabi College, Dr. K. Shaji, former Principal and the Management for all the support and encouragement. I extend my sincere thanks to my colleagues in the Department of Physics and others at M E S Asmabi College and M E S College, Marampally for all the support provided.

I acknowledge SAIF, Kochi, U. C. College Aluva, Department of Physics, M. G. University and Cochin University of Science and Technology, Maharaja's College and S. B. College, Changanacherry for various experimental measurements. My special thanks to Dr. Shibu

Eapen of SAIF, Kochi, Dr. E. M. Mohammed and Ms. Viji of Maharaja's College and Ms. Divya of S B College for their timely help.

I would like to thank my fellow research scholars Dr. Aloysius Sabu, Dr. Priyanka K. P, Dr. Babitha K. K, Dr. Sreedevi A, Seenamol Stephen, Anjali Jose, Hitha H, Soumya Kuriakose, Francis Xavier and Mathew for their helpful feedbacks, cooperation and friendship. My special thanks to Dr. Radhu S, Dr. Rajeshkumar B and Dr. Jyothish Kuthanapillil of Nirmala College and Ms. Femina of Maharaja's College for their valuable suggestions. I acknowledge with sincere gratitude the help rendered by Mohammed and Bobby, former students of Nirmala College.

I thank the University Grants Commission for sanctioning the Teacher Fellowship under Faculty Development Programme.

The endless support and encouragement from my husband Kasim and children, Samir and Amina, helped a lot in completing my work successfully. Finally, I would like to acknowledge with gratitude the support and love my parents, brother, sister and all other family members showered me with, during this most crucial phase of my life.

Sheena P A

CONTENTS

Page No.

Preface

In the world of nanomaterials, metal oxide nanoparticles constitute a diverse and fascinating class of materials, which can exhibit metallic, semiconductor or insulator character. Among them, transition metal oxide nanoparticles have been extensively explored, because of their unique physico-chemical properties.

Nickel oxide (NiO) is a prominent example of transition metal oxide well known for its chemical stability. It is one of the few p-type semiconductors with a stable wide bandgap (3.6–4.0 eV). Bulk NiO is antiferromagnetic, but in a nanocrystalline form it exhibits superparamagnetic nature. NiO nanoparticles have prospects for wide applications in various fields like catalysis, gas sensing, lithium ion batteries, electrochromic films and supercapacitors.

Doping is the primary technique used to control the properties of nanostructured semiconductors and to obtain new materials of technological importance. The doping of transition metal elements like cobalt and zinc at the nickel site can strongly modify the optical properties of NiO. Doping of a rare-earth metal like cerium into metal oxide semiconductor is well known to display a high surface activity, fast oxygen ion mobility and interesting catalytic properties.

Nanocomposites are materials of considerable interest because of their unique design and excellent properties. Metal phthalocyanines are a class of organic semiconductors with good thermal and chemical stability. Their unique optical and electrical properties make them eligible candidates in electrochemical sensors, photovoltaic devices and photodetectors.

Several studies have been reported on the synthesis and characterization of NiO nanoparticles. However, reports on the influence of cobalt and cerium doping on the structural, optical, electrical and magnetic properties of NiO nanoparticles are sparse. Also, no studies have been reported on the structural, optical, electrical and magnetic properties of NiO/CoPc and NiO/SnPc nanocomposites. Hence, we have pursued a detailed investigation on the structural, optical, electrical and magnetic properties of pristine NiO, cobalt and cerium doped NiO, and NiO/CoPc and NiO/SnPc nanocomposites.

The subject matter of the thesis has been organized into seven chapters.

Chapter 1 contains a brief description of the structure and properties of NiO, along with a comprehensive review of the earlier studies on pristine and doped NiO. The objectives and relevance of the present study are also summarized in this chapter.

In Chapter 2, the materials and methods used for the synthesis and characterization are presented. The details of the equipment, experimental setup and procedures adopted for the various studies are also described in this chapter.

Chapter 3 presents the studies on the structural, optical, electrical and magnetic properties of NiO nanoparticles synthesized by chemical precipitation method. As calcination has a profound effect on different aspects of nanomaterials, the effect of calcination on the properties of NiO is also analyzed in this chapter.

Chapter 4 deals with the synthesis of cobalt doped NiO nanoparticles by chemical precipitation method. The modification in the

structural, optical, electrical and magnetic properties of nickel oxide nanoparticles due to cobalt (Co) doping are also dealt with in this chapter.

The synthesis of NiO nanoparticles doped with cerium (Ce) is described in chapter 5. A detailed study on the effect of cerium doping on the structural, optical, electrical and magnetic properties of NiO is also presented here.

The synthesis of NiO/M-Pc (M = Co, Sn) by solvent evaporation method is presented in chapter 6. The structural, optical, electrical and magnetic properties of the synthesized nanocomposites are investigated and given in detail.

Summary and conclusion of the present study along with the work to be carried out in future are presented in chapter 7.

Publications

1. Microstructural characterization and modified spectral response of cobalt doped NiO nanoparticles**, P.A. Sheena**, H. Hitha, A. Sreedevi, Thomas Varghese, ***Materials Chemistry and Physics****,* Elsevier, 229 (2019) 412-420

2. Nickel oxide/cobalt phthalocyanine nanocomposite for potential electronics applications*,* **P A Sheena**, A Sreedevi, C Viji, Thomas Varghese, ***European Physical Journal B****,* Springer, 92(2019) 13.

3. Characterization of NiO/CoPc nanocomposite material synthesized by solvent evaporation route, **P. A. Sheena**, K. P. Priyanka, A. Sreedevi, Thomas Varghese, ***Journal of Nanostructure in Chemistry****,* Springer, 8 (2018) 207 – 215.

4. Effect of electron beam irradiation on the structure and optical properties of nickel oxide nanocubes, **P. A. Sheena**, K. P. Priyanka, N. Aloysius Sabu, S. Gannesh, Thomas Varghese, ***Bulletin of Materials Science***, Springer, 38 (2015) 825 – 830.

5. Effect of calcination temperature on the structural and optical properties of nickel oxide nanoparticles**, P. A. Sheena**, K. P. Priyanka, N. Aloysius Sabu, B. Sabu, Thomas Varghese*,* ***Nanosystems: Physics, Chemistry and Mathematics***, St. Petersburg National Research University of Information Technologies, Mechanics and Optics Pub., 5(3) (2014) 441 – 449.

Presentations

1. "Influence of Co doping on the properties of NiO nanocrystals", **Sheena P. A** and Thomas Varghese, International Conference on "Recent Advances in Material Science and Biophysics", *Mangalore University, Mangalaore, Karnataka, 23-25 January 2018.*

2. "Synthesis and structural characterization of NiO/CoPc nanocomposite", **Sheena P. A** and Thomas Varghese, U G C sponsored National Seminar on "Recent Trends in Nano and other Materials for Energy Efficient Devices", *St. Aloysius College, Edathua, 20 – 22 July 2017.*

3. "Effect of Annealing on the Structural and Optical Properties of NiO Nanoparticles", **Sheena P. A** and Thomas Varghese, National conference on "Nanotechnology's invisible threat: Small science, big consequences", *Mahatma Gandhi National Institute of Research and Social Action (MGNIRSA), Hyderabad, India, 26-27 September, 2013*

List of Tables

Page No.

List of Figures

Page No.

Chapter 1

INTRODUCTION AND LITERATURE REVIEW

The structure and fundamental properties of nickel oxide (NiO) are discussed in this chapter. Following this, a detailed review of the studies done so far on pristine and doped NiO is presented. The objectives and relevance of the present investigation are also summarized.

1.1 Introduction

Nanotechnology is the art and science of manipulating matter at the nanoscale to create new and unique materials with enormous potential. With the advent of nanotechnology, the miniaturization of current and new instruments that can transform greatly the world we live in has become possible. The potential of nanotechnology can contribute more advancement in various fields including electronics, material science, medicine, biotechnology and information technology.

In the emerging field of nanotechnology, nanostructured materials have attracted much attention because of their exceptional physical and chemical properties compared to their bulk counterparts. Their limited size and high density of surface sites make them unique. The structural characteristics of the materials are greatly affected by the reduction in particle size. The nanostructure also produces a quantum confinement effect which makes it attractive in electronics [1, 2]. Moreover, the surfaces and interface induce an anomalous behaviour in the magnetic properties of nanostructures.

Among the variety of nanomaterials, metal oxide nanoparticles have been extensively explored for the development of new functional materials. They can acquire different structural geometries with an electronic structure that can exhibit metallic, semiconductor or insulator character. The conductivity and chemical reactivity of the oxide nanoparticles are significantly modified by the reduction in particle size [1].

This work reports the study of structural, optical, electrical and magnetic properties of nanocrystalline nickel oxide (NiO) synthesized by chemical precipitation method. The effect of cobalt and cerium doping on the properties of pristine NiO are studied. The synthesis of nanocomposite structures of nickel oxide and metal phthalocyanines, and their significant physical and chemical properties are also dealt with.

1.2 NiO Nanoparticles

The transition metal oxides form an interesting class of solids exhibiting wide variations in structure and properties [3]. Nanoparticles of transition metal oxides have been investigated by several workers in the last few years. Out of these, nickel oxide nanoparticles draw much attention due to its unique electrical, optical and magnetic properties. These novel properties make them suitable for wide range of applications in different fields.

Nickel oxide has the rock salt form of sodium chloride, with octahedral Ni(II) and O^{2-}sites.The Ni^{2+} ion has the configuration $3s^2 3p^6 3d^8$. Each Ni^{2+} ion has six O^{2-} surrounding ions forming an elementary octahedron with O_h symmetry [4]. As a binary metal oxide, NiO mostly deviates from stoichiometry which can be identified by the colour variation. NiO that is closely stoichiometric appears green, while the material with an excess of oxygen will have a black appearance [5, 6]. NiO has face centred cubic structure referred to as bunsenite with a lattice constant of 4.1769 Å at room temperature [7]. Crystal structure of

nickel oxide is presented in Figure1.1. Some important crystallographic properties of nickel oxide are presented in Table 1.1.

The physical properties of NiO nanoparticles are easily affected by crystal defects due to the deviation from the stoichiometry. The optical, electrical and magnetic properties are determined mostly by the electrons in the localized *d* band and defect levels associated with the anion/cation vacancies.

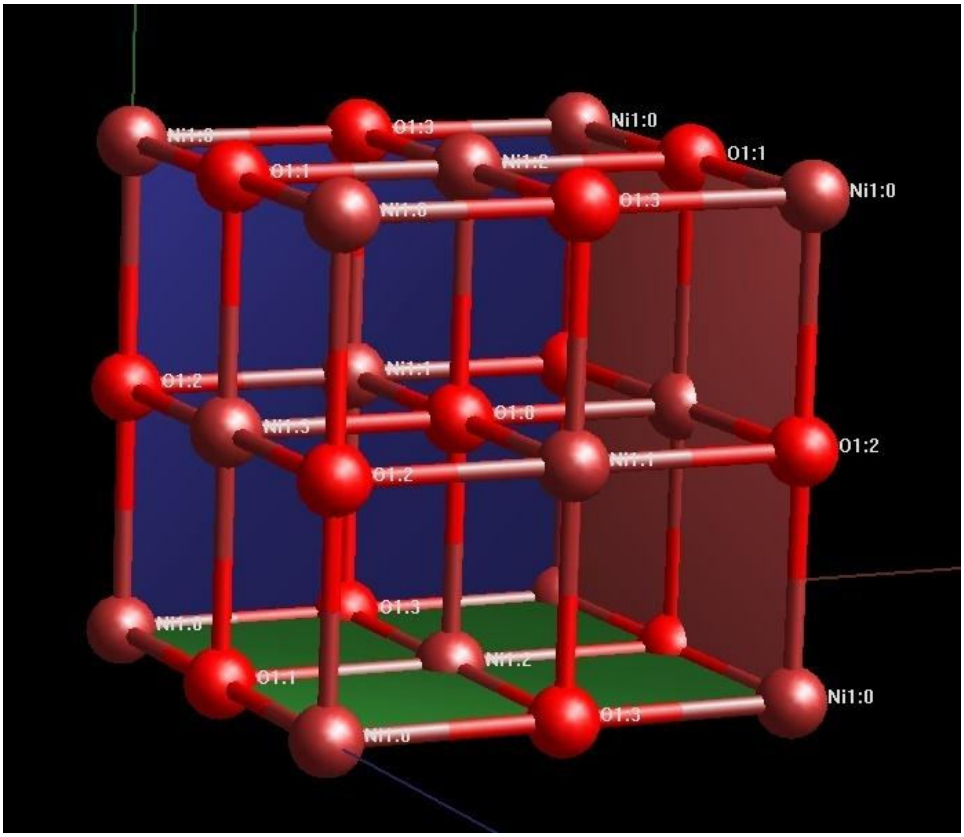

Figure 1.1: Crystal structure of NiO

NiO is one of the very few p-type semiconductors with a stable wide bandgap of the order of 3.6 – 4 eV [8]. NiO exhibits strong UV absorption which is attributed to its bandgap absorption. The photoluminescent emission of NiO is broadly divided into two sections, the near band edge ultraviolet emission and the defect related deep level emission in the visible region. The defects and the surface structures may create in-gap states which act as luminescence centres [9].

Table 1.1 : Fundamental parameters of nickel oxide [7, 10 – 12]

Property	**Value**
Crystal system\	Cubic (Bunsenite)
Appearance	Green
Space group	Fm3m
Lattice constant	4.1767 Å
Density	6.67 g/cm^3
Molecular weight	74.71 g/mol
Melting point	1955^{o}C
Optical bandgap	3.7 eV
Dielectric constant	11.9 at 25^{o}C
Neel temperature	523 K

Single crystalline NiO is classified as a Mott – Hubbard insulator having very low electrical conductivity at room temperature [13]. But the conductivity of nanocrystalline NiO is drastically increased due to the surface modification caused by microstructural defects such as nickel vacancies and interstitial oxygen in the lattice [8]. The grain boundaries and triple junctions decide the transport properties of NiO nanoparticles with size less than 10 nm [14]. Also, the high dielectric constant of NiO enhances its resistive switching property, which is utilized for improving the performance of resistive random access memory [15].

The magnetic properties of NiO nanoparticles are very sensitive to size, crystal structure, and morphology. Surface and finite size effects induce an anomalous magnetic behaviour which differs markedly from the corresponding bulk material. Bulk NiO is an antiferromagnetic material with a Neel temperature of 523 K, but in the nanocrystalline form, it exhibits superparamagnetism [16]. The superparamagnetic nature proposes NiO nanoparticles as a promising material for imaging and drug delivery [17].

The exceptional properties exhibited by NiO nanoparticles have resulted in diverse applications such as electrochemical supercapacitors [18], anodes for lithium- ion batteries [19], γ ray detector [20], electrode material for fuel cells [21], functional sensor layer for chemical sensing [22], dye-sensitized photocathodes [23, 24], gas sensor [25], a material for memory devices [26], an antioxidant material [27], transparent p-type semiconducting layer [28] solar thermal absorber [29], adsorbent of

heavy metal ions [30] and as an antiferromagnetic layer in exchange biased read head devices [31].

The anodic electrochromism exhibited by NiO finds application in smart windows with variable light transmission characteristics [32, 33]. NiO thin films with improved resistive switching properties are suitable for memory devices [34]. Mixed oxides of NiO and Ni_2O_3 can be used as an optical recording medium which is more stable in the air compared to conventional recording layers [35]. NiO nanosheets are very active for low temperature methanol decomposition and show their potential for applications in alternative energy technologies and catalytic combustion reactions [36]. NiO nanoparticles have been employed as photocatalyst in the degradation of organic dyes [37]. In the biomedical field, NiO is used as a contrasting agent for magnetic resonance imaging [38]. NiO plays a crucial role as a mediator in the electrocatalytic oxidation of glucose [39]. NiO nanoparticles are effective against a wide range of bacteria also [40, 41].

1.3 Doped NiO and NiO/Metal Phthalocyanine Nanocomposite Structures

Doping is the primary technique used to control the properties of nanostructured semiconductors and to obtain new materials of technological importance. The intentional introduction of atomic impurities into the system will strongly affect the electronic properties of the material. The doping of transition metal elements like cobalt at the nickel site introduces defect states in the NiO bandgap, thereby tuning its

bandgap energy [42]. As cobalt is a good luminescence activator, it can also modify the emission properties of NiO [43]. Doping of a rare-earth metal into metal oxide semiconductor will display a high surface activity, fast oxygen ion mobility and interesting catalytic properties. Among different rare earth metals, cerium has gained much interest as it could easily form oxygen vacancies with relatively high mobility of bulk oxygen species [44]. The oxygen vacancies produced on cerium doping in NiO leads to the improved electrocatalytic behaviour and antibacterial property of NiO nanoparticles [45]. The combination of organic/inorganic nanocomposites has attracted much attention because of the blending of their distinct physical and chemical properties. Metal phthalocyanines are a class of organic materials with good thermal and chemical stability, photoconductivity and semiconducting nature [46]. The unique properties possessed by metal phthalocyanines and NiO offer a potential combination of organic-inorganic nanocomposite material.

1.4 Literature Review

A brief review of the studies on the synthesis and properties of pristine and doped nickel oxide, and its phthalocyanine composites are presented here.

In recent years, significant progress has been achieved in developing novel methods for the synthesis of nanomaterials. Several methods have been reported for the synthesis of pristine and doped NiO nanoparticles based on both top-down and bottom-up methods such as chemical precipitation [47-50], sol-gel [51-53], solvothermal [54],

hydrothermal [55], solid state decomposition [56-58], microwave assisted [59], microemulsion [60], pulsed laser ablation [61], combustion [62, 63], sonochemical [64, 65] and thermal decomposition [66]. Among these methods, the precipitation technique is employed here, because it is comparatively simple and low cost, as the starting materials are few and inexpensive. The precipitation process can precisely control the morphology, stoichiometry and surface chemistry of the products [67].

Literature reports the use of different salts like nickel nitrate ($Ni(NO_3)_2$), nickel chloride ($NiCl_2$), nickel sulphate ($NiSO_4$) as the precursors for the synthesis of NiO nanoparticles [47, 50, 68]. The synthesis method, concentration of precursors, reaction temperature, pH and the amount of precipitating agent are the main factors influencing the particle size and morphology of NiO nanoparticles [51, 59]. Behnajady and Bimeghdar synthesized mesoporous NiO nanoparticles of size about 11 nm by chemical precipitation method using nickel nitrate and sodium hydroxide [48]. The size control of NiO nanoparticles synthesized by chemical precipitation method was done by using different surfactants, as reported by Mahaleh *et al.* [69]. Dharmaraj *et al.* reported the production of well dispersed cubic NiO nanoparticles from nickel acetate/polyvinyl acetate precursor by heat treatment at 723 K [70]. Anandan and Rajendran synthesized NiO nanoparticles of different morphologies by the solvent assisted facile solvothermal method [54]. Kaviyarasu *et al.* reported the synthesis of NiO nanorods by sol gel method using nickel nitrate and sodium hydroxide [51]. The synthesis of NiO nanowires by thermal decomposition of the precursor formed by the

reaction between $NiSO_4.6H_2O$ and urea was reported by Wu *et al.* [71]. Ni *et al.* synthesized NiO strips consisting of self-assembled nanosized particles through the thermal decomposition of nickel dimethylglyoximate precursors [72]. NiO nanotubes were synthesized through a precursor method using dimethylglyoxime and nickel acetate ($Ni(OAc)_2$) by Pang *et al.* [41].

Several reports are available on the study of the effects of calcination time and temperature on the crystallite size of NiO synthesized by different techniques. The formation of NiO nanoparticles and its structural features are strongly dependent on the calcination temperature [73]. The growth of NiO crystallites with an increase in calcination temperature was reported in many literatures [47, 69, 74 - 77]. Aggregation of nanoparticles due to sintering at a temperature of 700^oC was reported by Li *et al.* [74]. Wu *et al.* reported the breakdown of nanowires into nanoparticles at a calcination temperature of 600^oC [71]. A low calcination temperature is desirable to obtain a high specific surface area of NiO nanoparticles as reported by Teoh and Li [73]. Deterioration in the electrochemical behaviour of NiO with the increase in calcination temperature was reported in a study carried out by Channu *et al.* [78].

The XPS spectra of NiO nanoparticles showed two main peaks of $Ni2p_{3/2}$ and $Ni2p_{1/2}$ at 856.1 and 874.1 eV, as reported by Salavati-Niasari *et al.* [79]. They observed a shift of about 2 eV in the binding energy of Ni $2p_{3/2}$ peak to higher values compared to that of pure NiO (854.4 eV)

due to the oxygen vacancy existing on the surface. Madhu *et al*. observed in the O1s spectrum an intense peak at a binding energy of 530.32 eV indicating the presence of Ni^{2+} and a less intense peak at a binding energy of 531.56 eV indicating the presence of Ni^{3+} in the nickel oxide sample [38].

The optical properties of NiO depend on the method of synthesis and the precursor used. Strong UV absorption which is attributed to the bandgap absorption of NiO was reported by many researchers [57, 59, 67, 70]. The photoluminescent emission of NiO consists of a prominent UV peak attributed to band-edge luminescence and several defects – related shoulder peaks in the visible region [4, 80 - 82]. Chakrabarty and Chatterjee synthesized NiO nanoparticles which were almost transparent in the visible region, with a sharp absorbance peak around 3.75 eV [83]. A broad absorption peak in the range of 260–360 nm, due to interband $\pi - \pi^*$ electronic transition was reported by Usha *et al.* [80]. They observed a photoluminescence (PL) spectrum with a sharp peak at 3.4 eV in the UV region and several well-resolved peaks extending in the visible spectral region. The visible emissions centred at 492.0, 509.2 and 534.2 nm are attributed to the oxygen vacancies and Ni interstitials in the sample, as reported by Thema *et al.* [82]. Han *et al.* reported the phenomenon of blue shift in the absorption spectrum of NiO nanoparticles with the increase in the ratio of water to surfactant, which is an evidence of quantum confinement effect [77]. Compared to bulk NiO, an enhancement in UV absorption was observed for nanoparticles by Musevi *et al.* [64]. They also observed a blue shift in the PL spectrum

with a reduction in particle size. Al-Sehemi *et al.* reported a red shift in the bandgap of NiO nanoparticles from that of bulk due to the chemical defects and vacancies present in the crystal structure [59]. No quantum confinement effect upon size reduction in NiO nanowires was observed by Wu *et al.* [71]. NiO nanoparticles synthesized at room temperature and 60^{o}C have a bandgap of 3.65 and 3.8 eV respectively as reported by Umaralikhan and Jaffar [81]. Several well resolved peaks in the wavelength range 400 – 600 nm were observed in the emission spectra of both samples [81]. Two major peaks in the UV-blue band at 363 and 396 nm were observed for NiO nanoparticles synthesized by Kisan *et al.* [84]. They also reported a blue shift for the 363 peak with increase in crystallite size. Madhu and Biju reported a decrease in the PL emission intensity on annealing, due to the decrease in the number of O^{2-} vacancies [4]. They also reported the influence of the relative concentrations of Ni^{2+} and O^{2-} vacancies on the optical absorption. Blue emission in PL spectrum with a strong band centred at 434 nm and two shoulder peaks in the green region at 496 and 540 nm were observed by Meybodi *et al.* [85]. Ramasami *et al.* reported an indirect bandgap of 2.98 and 2.3 eV for the NiO nanoparticles synthesized using nickel nitrate and cassava starch taken in two weight ratios 1:0.5 and 1:1, respectively [63].

The dielectric behaviour of NiO strongly depends on temperature and frequency of the applied signal. The dielectric constant and the dielectric loss of nanocrystalline NiO was found to decrease with increase in frequency [86 - 88]. Gokul *et al*. explained the dielectric

relaxation using the Debye relaxation theory [86]. They observed loss tangent peaks in the high frequency region which are associated with the thermally activated relaxation processes. Two semicircular arcs in the Nyquist plot represent the grain and grain boundary contribution to the impedance. A high value of activation energy was observed for the samples due to the grain boundary effect [86].

Biju and Khadar observed a profound increase in the DC conductivity (σ_{DC}) of nanocrystalline NiO over that of its single crystalline counterpart due to the high density of uncompensated Ni^{2+} vacancies present on the grain boundaries [89]. They reported the effect of triple junction on the transport properties of nanoparticles with a size less than 10 nm. The most prominent conductivity mechanism over the temperature range 313 – 423 K is the large polaron conduction associated with holes in the 2p band of O^{2-} [90]. Makhlouf *et al.* reported a decrease in DC and AC conductivities for particles with size less than 10 nm due to the effect of triple junctions [14]. The increase in dielectric constant with temperature indicates thermally activated polarization mechanism in the sample [14]. Annealing leads to an enhancement in σ_{DC} due to the filling up of O^{2-} vacancies, as reported by Madhu and Biju [4]. The variation of AC conductivity with frequency and temperature was explained by Biju and Khadar based on the Correlated Barrier Hopping (CBH) model [90]. With increase in frequency the hopping mechanism changes from inter well to intra well mode [90]. The frequency independent conductivity at low frequencies indicates the regime of pure DC conduction, while for higher frequencies the dominance of AC conductance is verified [91].

The magnetic properties of NiO nanoparticles are very sensitive to size, crystal structure, and morphology. Néel suggested that nanoparticles with antiferromagnetic ordering of spin will exhibit magnetic properties such as superparamagnetism and weak ferromagnetism [16]. Mishra *et al*. reported unusually large magnetic moment for NiO nanoparticles which is attributed to both the uncompensated surface spins and re-orientation of magnetic sub-lattices due to finite-size effects [92]. The importance of inter particle interaction in analysing the magnetic properties of NiO particles was reported by Bodker *et al.* [93]. Khadar *et al*. reported a change from superparamagnetic to superantiferromagnetic state with the increase in crystallite size of nanocrystalline NiO [94]. A small hysteresis loop in the range of -1000 to 1000 Oe, indicating a weak ferromagnetic behaviour was observed in NiO nanorods by Pang *et al.* [41]. They reported the coercive force and saturation magnetization values of 130.50 Oe and 0.133 emu/g at 1.8 K and 61.58 Oe and 0.097 emu/g at 300 K, respectively. A decrease in the magnetization value and a gradual disappearance of hysteresis loop with increase in calcination temperature was observed by Thota and Kumar [52]. Bi *et al.* reported ferromagnetic-like behaviour for the ultrafine NiO nanocrystallites with an average size of 5 nm [95]. The observed large coercivity of 327.14 kA/m along with a large exchange bias field of 148.48 kA/m at 4.2 K are attributed to the combined effects of missing bonds and the lattice distortion. Proenca *et al.* observed a bifurcation in the ZFC and FC curves for NiO nanoparticles with size 13 and 18 nm, corresponding to the superparamagnetic behaviour [96]. But particles of larger average

diameter exhibited a paramagnetic property due to the incomplete compensation of the antiferromagnetic (AFM) sub-lattices at the surface. The observed non-saturation behaviour of the magnetization curve at room temperature for the samples with smallest particle size is associated with the AFM core of the nanoparticles[96]. Very large coercivity ~ 4000 Oe, with an increasing magnetization even at 70 kOe was observed for the 53 Å diameter NiO nanoparticles prepared by Makhlouf *et al*. [97].

Diverse applications of NiO make it a promising material among the transition metal oxides. Du *et al.* observed a very good response of NiO sensors synthesized by microemulsion method towards hydrogen sulphide [25]. By tuning the morphology of nanoparticles, the performance of NiO based sensors can be controlled, as reported by Aslani *et al*. [65]. They observed a better response towards nitrogen dioxide than carbon monoxide at very low operating temperatures. The surface states and deep level defects in the crystal lattice of NiO catalysts showed strong influence towards the photocatalytic degradation of methylene blue as reported by Wan *et al.* [37]. Nearly 100% degradation of the organic dye Rhodamin – B under visible light irradiation was achieved by Dey *et al.* for the NiO nanoflowers synthesized by thermo – decomposition technique [98]. The NiO nanosheets exhibited much favourable adsorptive properties than NiO powder for the removal of three typical textile dyes, reactive brilliant red X-3B, congo red and fuchsin red from waste water [99]. Mahmoud *et al*. reported the better performance of NiO nanoparticles prepared by organic solvent method

than that by precipitation method for removal of lead ions from aqueous solutions [30]. Santhoshkumar *et al*. studied the antibacterial property of NiO nanoplates which exhibited good zone of inhibition against *Bacillus subtilis, Staphylococcus aureus, Escherichia coli* and *Proteus vulgaris* [40]. Similar results were reported for the NiO nanotubes synthesized by Pang *et al.* [41]. The maximum specific capacitance of 167 F/g in 2M potassium hydroxide electrolyte was obtained for NiO thin films prepared by Patil *et al.*, which makes it a promising candidate for supercapacitor applications [100].

Doping is the best method for tuning the properties of pristine NiO. Ponnusamy *et al.* synthesized NiO nanoparticles doped with 5, 10 and 15 wt% of cobalt and observed a reduction in crystallite size and blue shift in the absorption spectra [101]. They found a shift from superparamagnetic to ferromagnetic behaviour upon cobalt doping, due to the spin coupling effect of smaller particles. An increase in particle size and an enhancement in lattice strain with cobalt doping were reported by Agarwal *et al*. for cobalt doped NiO nanoparticles of the composition $Co_xNi_{1-x}O$ (x = 0,0.03, 0.07, 0.1, 0.13, 0.15) [102]. A red shift in the absorption spectra and a decrease in bandgap energy from 3.05 to 2.19 eV were observed, due to the formation of additional energy levels in the bandgap. The emission spectra suffer a reduction in intensity and shift towards higher wavelength with increase in doping concentration [102]. Thi *et al.* reported improved p-type conductivity and hence an enhanced electrochemical performance for the cobalt doped NiO electrodes which makes it a promising anode material for

rechargeable lithium ion batteries [103]. Taşköprü *et al*. reported a decrease in optical bandgap from 3.7 to 3.31 eV with increase in cobalt doping concentration for the NiO thin films [104]. An increase in the density of acceptor states around the valence band edge and the lowering of Fermi energy level of NiO nanoparticles upon cobalt doping was reported by Natu *et al*. [105]. They observed an increase in the photovoltage of p-type dye-sensitized solar cells constructed using doped NiO with increase in cobalt content.

Anandhababu *et al*. performed a systematic study of NiO nanoparticles doped with 1, 3, 5 and 10 mol % cerium (Ce) and observed a decrease in crystallite size from 17.1 to 8.1 nm [106]. They observed a significant change in morphology with cerium doping. The presence of Ce^{3+} ions caused a blue shift in the emission spectra of the doped samples. A decrease in magnetization with increase in doping level was observed due to the uncompensated spins on the sample surface [106]. The substitution of Ni^{2+} with larger Ce^{3+} ions caused strain in the NiO lattice, as reported by Anjali *et al*. [107]. The improved electrochemical performance and cycling stability achieved by Ce doping proposes its potential for energy storage applications. The improved electrocatalytic behaviour of Ce doped NiO sample, due to the excess oxygen vacancies created on doping was reported by Muthukumaran *et al.* [108]. The absence of Ce peaks in the XRD pattern up to 9 wt% doping indicates uniform substitution of the dopant in the host lattice. The excellent antimicrobial activity of Ce doped NiO nanoparticles against a range of bacteria hold a great promise for biomedical applications [108]. Gawali

et al. observed an additional phase of CeO_2 in the XRD pattern for 5 wt% of Ce doping [109]. An increase in the local strain on Ce doping caused an expansion in the NiO lattice. The porous nature of 0.5% Ce doped sample makes it an efficient nitrogen dioxide gas sensor [109].

Several reports are available on the studies of NiO/organic nanocomposites, but not on NiO/M-Pc nanocomposites. Salama and Karim prepared NiO – metal-free phthalocyanine nanocomposites with crystallite size ranging from 51.1 to 82.1 nm by urea fusion technique [110]. They studied the frequency and temperature dependence of dielectric constant. A peak in the dielectric loss curve was observed, suggesting the presence of relaxing dipoles in the nanocomposite [110]. The performance of NiO in lithium ion batteries can be modified by the support of graphene in the form of nanocomposites, as reported by Mai *et al*. [111]. Singu *et al*. synthesized NiO nanosheets of less than 10 nm decorated by polyaniline nanofibers with uniform diameter of 30–40 nm via *in situ* aqueous oxidative polymerization, which exhibited superior electrochemical properties [112]. Diva *et al*. prepared NiO/carbon nanotube by co-precipitation method and achieved a change in morphology of NiO from cluster-like to filamentous structure [113]. The synthesized sample was very effective in the elimination of lead ions from aqueous solutions.

1.5 Relevance of the Present Study

Several studies have been reported on the synthesis and characterization of NiO nanoparticles. The large bandgap of NiO has

restricted its applications only into the harmful and expensive ultraviolet region. Therefore, tailoring of the bandgap is essential for modifying the properties of NiO for optoelectronic device applications. The bandgap of NiO can be tuned by doping it with a relatively small amount of cobalt. Among different rare earth metals, cerium can easily form oxygen vacancies in the NiO lattice leading to the improved electrocatalytic behaviour and antibacterial property. However, reports on the influence of cobalt and cerium doping on the structural, optical, electrical and magnetic properties of NiO nanoparticles are sparse. The physico–chemical properties of NiO can be strongly modified by forming NiO/M-Pc nanocomposites. But, no studies have been reported on the structural, optical, electrical and magnetic properties of NiO/CoPc and NiO/SnPc nanocomposites. Hence, more extensive and systematic studies of pristine and doped NiO nanoparticles are needed. The present study is mainly focussed on the synthesis and characterization of nanocrystalline NiO, cobalt doped NiO, cerium doped NiO, and NiO/CoPc and NiO/SnPc nanocomposites.

1.6 Objectives of the Study

- Synthesis of pure and crystalline NiO nanoparticles by simple chemical precipitation method.
-
- Investigation on the structural, optical, electrical and magnetic properties of the synthesized nanocrystalline NiO.
- Study the effect of calcination on the structural, optical, electrical and magnetic properties of NiO nanoparticles.

- Study the effect of cobalt doping on the properties of NiO nanoparticles.

- Study the effect of cerium doping on the properties of NiO nanoparticle.

- Synthesis of NiO/CoPc and NiO/SnPc nanocomposites by solvent evaporation method, and their characterization

References

1) M. Fernandez-Garcia, A. Martinez-Arias, J.C. Hanson, J.A. Rodriguez, Chem. Rev., 104 (2004) 4063 - 4104

2) P. Ayyub, V.R. Palkar, S. Chattopadhyay, M. Multani, Phys. Rev. B.,51(1995) 6135 - 6138

3) C.N.R. Rao, G.V. Subbarao, Phys. Status Solidi A, 1(1970) 597 - 652

4) G. Madhu, V.Biju, Physica E, 60 (2014) 200 - 205

5) K.O. Ukoba, A.C. Eloka-Eboka, F.L. Inambao, Renewable and Sustainable Energy Reviews 82 (2018) 2900 - 2915

6) A. B. Kunz, J. Phys C : Solid State Phys., 14 (1981) L455 - L460

7) F. Fievet, P. Germi, F. De Bergevin, M. Figlarz, J. Appl. Cryst., 12 (1979) 387-394

8) D. Adler, J. Feinleib, Phys.Rev.B, 2 (1970) 3112 –3134

9) V. I. Sokolov, V. A. Pustovarov, V. N. Churmanov, V. Yu. Ivanov, N. B. Gruzdev, P. S. Sokolov, A. N. Baranov, A. S. Moskvin, Phy. Rev. B, 86 (2012) 115128 (1 – 10)

10) https://pubchem.ncbi.nlm.nih.gov/compound/14805

11) W. Reichardt, V. Wagner, W. Kress, J. Phys. C: Solid State Phys., 8 (1975) 3955 - 3962

12) K. V. Rao, A. Smakula, J. Appl. Phys., 36 (1965) 2031 - 2038

13) F. J. Morin, Phys. Rev. B., 93(6) (1954) 1199 - 1204

14) S. A. Makhlouf, M. A. Kassem, M. A. Abdel-Rahim, J. Mater. Sci., 44 (2009) 3438 - 3444

15) P. Mario Lanza, Materials, 7 (2014) 2155 - 2182

16) L. Néel, in Low Temp. Phys., edited by C. Dewitt et al. (Gordon and Beach, New York, 1962), 413

17) A. G. Kolhatkar, A. C. Jamison, D. Litvinov, R. C. Willson, T. Randall Lee, Int. J. Mol. Sci. 2013, 14, 15977-16009

18) V. Srinivasan, J. Weidner, J. Electrochem. Soc., 144 (1997) L210 - L213

19) Yan-Na Nuli, Sheng-Li Zhao, Qi-Zong Qin, J. Power Sources 114 (2003) 113 - 120

20) K. Arshak, O. Korostynska, F. Fahim, Sensors, 3 (2003) 176 - 186

21) S. de Souza, S. J. Visco , L. C. De Jonghe, Solid State Ionics 98 (1997) 57 - 61

22) H. Kumagai, M. Matsumoto, K. Toyoda, M. Obara, J. Mater. Sci. Lett. 15 (1996) 1081 - 1083

23) A. Nattestad, M. Ferguson, R. Kerr, Y.B. Cheng, U. Bach, Nanotechnology, 19 (2008) 295304 (1 – 9)

24) J. He, H. Lindström, A. Hagfeldt, S.E. Lindquist, J. Phys. Chem. B, 103 (1999) 8940 –8943

25) Y. Du, W. Wang, X. Li, J. Zhao, J. Ma, Y. Liu, G. Lu,Mater. Lett., 68 (2012) 168 –170

26) V. Bisht, K.P. Rajeev, J. Phys. Condens. Matter, 22 (2010) 016003 (1 – 5)

27) J.P. Saikia, S Paul, B.K. Konwar, S.K. Samdarshi, Colloids Surf., B 78 (2010) 146– 148

28) H. Sato, T. Minami, S. Takata, T. Yamada, Thin Solid Films 236 (1993) 27– 31

29) G. Katumba, L. Olumekor, A. Forbes, G. Makiwa, B. Mwakikunga, J. Lu, E. Wackelgard, Sol. Energy Mater. Sol. Cells 92 (2008) 1285 - 1292

30) A. M. Mahmoud, F. A. Ibrahim, S. A. Shaban, N. A. Youssef, Egyptian Journal of Petroleum 24 (2015) 27 –35

31) A. J. Devasahayam, M. H. Kryder, IEEE Trans Magn. 35 (1999) 649 - 654

32) C.G. Granqvist (Ed.), Handbook of Inorganic Electrochromic Materials, Elsevier, Amsterdam, 1995, 325 - 334

33) J. Karlsson, A. Roos, Solar Energy 68 (2000) 493 - 497

34) J.W. Lee, I.H. Park, C.W. Chung, Integr. Ferroelectr., 74 (2005) 71 - 77

35) Hung-Lu Chang, Tzuzn-Ren Jeng, Jung-Po Chen, Wen-Hsin Yen, P. Yen, D. Huang, Jau-Jiu Ju, Jpn. J. Appl. Phys., 44 (2005) 6109 - 6112

36) J. Hu, K. Zhu, L. Chen, H. Yang, Z. Li, A. Suchopar, R. Richards, Adv. Mater.,20 (2008) 267 - 271

37) X. Wan, M. Yuan, S. Tie, S. Lan, Appl. Surf. Sci., 277 (2013) 40 - 46

38) G. Madhu, Vipin C. Bose, A.S. Aiswaryaraj, K. Maniammal, V. Biju, Colloids and Surfaces A: Physicochem. Eng. Aspects 429 (2013) 44 - 50

39) A. S. Danial, M.M. Saleh, S.A. Salih, M.I. Awad, J. Power Sources 293 (2015) 101 - 108

40) A. Santhoshkumar, H.P. Kavitha, R. Suresh, J. Adv. Chem. Sci., 2(2) (2016) 230 - 232

41) H. Pang, Q. Lu, Y. Li, F. Gao, Chem. Commun., 48 (2009) 7542 - 7544

42) B. Sahin, F. Bayansal, M. Yüksel, H.A. Çetinkara, Mater. Sci. Semicond. Process,18(2014) 135 - 140

43) M. J. Chithra, K. Pushpanathan, M. Loganathan, Mater. Manuf. Processes, 29 (2014) 771 - 779

44) M. Yousefi, M. Amiri, R. Azimirad, A.Z. Moshfegh, J. Electroanal. Chem., 661 (2011) 106 - 112

45) P. Muthukumaran, C.V Raju, C.S. Sumathi, G. Ravi, D. Solairaj, P. Rameshthangam, Wilson J, S Alwarappan, S. Rajendran, New J. Chem.,40 (2016) 2741 - 2748

46) P. S. Saravanan, C.J. Mathai, M.R. Anantharaman, S. Venkatachalam, P.V. Prabhakaran, J. Appl. Polym. Sci. 9 (2004) 2529 - 2535

47) K. Karthik, G. KalaiSelvan, M. Kanagaraj, S. Arumugam, N. Victor Jaya, J. Alloys Compd., 509 (2011) 181 - 184

48) M. A. Behnajady , S. Bimeghdar, Chem. Eng. J., 239 (2014) 105 - 113

49) Y. Ichiyanagi, N. Wakabayashi, J. Yamazaki, S. Yamada, Y. Kimishima, E. Komatsu, H. Tajima, Physica B 329–333 (2003) 862 - 863

50) M. El-Kemary , N. Nagy, I. El-Mehasseb, Mater. Sci. Semicond. Process., 16 (2013) 1747 - 1752

51) K. Kaviyarasu, E. Manikandan, J. Kennedy, M. Jayachandran , R. Ladchumananandasiivam, U.U. De Gomes, M. Maaza, Ceram. Int., 42 (2016) 8385 - 8394

52) S. Thota, J. Kumar, J. Phys. Chem. Solids 68 (2007) 1951 - 1964

53) A. C. Gandhi ,S. Y. Wu, Nanomaterials 7 (2017) 231

54) K. Anandan, V. Rajendran, Mater. Sci. Semicond. Process.,14 (2011) 43 - 47

55) S. Takami, R. Hayakawa, Y. Wakayama, T. Chikyow, Nanotechnology 21 (2010)134009

56) N.M. Hosny, Polyhedron, 30 (2011) 470 - 476

57) F. Davar , Z. Fereshteh, M. Salavati-Niasari, J. Alloys Compd., 476 (2009) 797 - 801

58) W. J. Duan, S. H. Lu,Z. L. Wu, Y. S. Wang, J. Phys. Chem. C, 116 (2012) 26043 - 26051

59) A. G. Al-Sehemi, A. S. Al-Shihri, A. Kalam , G. Du, T. Ahmad, J. Mol. Struct., 1058 (2014) 56 - 61

60) Y. Du, W. Wang, X. Li, J. Zhao, J. Ma, Y. Liu, G. Lu, Mater. Lett., 68 (2012) 168 - 170

61) M.A. Gondal, T. A. Saleh, Q.A. Drmosh, Appl. Surf. Sci., 258 (2012) 6982 - 6986

62) A. J. Christy, M. Umadevi, Mater. Res. Bull. 48 (2013) 4248 - 4254

63) A. K.Ramasami, M.V.Reddy, G. R. Balakrishna, Mater. Sci. Semicond. Process., 40 (2015)194 - 202

64) S. J. Musevi, A. Aslani, H. Motahari, H. Salimi, Journal of Saudi Chemical Society, 22 (2012)DOI: 10.1016/j.jscs.2012.06.009

65) A. Aslani, V. Oroojpour, M. Fallahi, Appl. Surf. Sci., 257 (2011) 4056 - 4061

66) Z. Fereshteh, M. Salavati-Niasari, K. Saberyan, S.M. Hosseinpur-Mashkani, F. Thavakoli, J. Clust. Sci.,23 (2012) 577 - 583

67) K. Anandan, V. Rajendran, Mater. Sci. Eng., B 199 (2015) 48 - 56

68) Mao-Sung Wu, Hung-Ho Hsieh, Electrochim. Acta., 53 (2008) 3427 - 3435

69) Y. B. M. Mahaleh, S. K. Sadrnezhaad, D. Hosseini, J. Nanomaterials, 470595 (2008) doi:10.1155/2008/470595

70) N. Dharmaraj, P. Prabu, S. Nagarajan, C.H. Kim, J.H. Park, H.Y. Kim, Mater. Sci. Eng., B 128 (2006) 111 - 114

71) L. Wu, Y. Wu, H. Wei, Y. Shi, C. Hu, Mater. Lett., 58 (2004) 2700 - 2703

72) X. Ni, Q. Zhao, F. Zhou, H. Zheng, J. Cheng, B. Li, J. Cryst. Growth, 289 (2006) 299 - 302

73) L. G. Teoh, Kun-Dar Li, Mater. Trans., 53 (2012) 2135 - 2140

74) X. Li, X. Zhang, Z. Li, Y. Qian, Solid State Commun., 137 (2006) 581 - 584

75) T. Nathan, A. Aziz, A. F. Noor, S. R. S. Prabaharan, J Solid State Electrochem., 12 (2008)1003 - 1009

76) K. Maniammal, G. Madhu, V. Biju, Physica E, 85 (2017) 214 - 222

77) D.Y. Han, H.Y. Yang, C.B. Shen, X. Zhou, F.H. Wang, Powder Technol., 147 (2004) 113 - 116

78) V.S.R. Channu, R. Holze, B. Rambabu, Colloids Surf., A: Physicochem. Eng. Aspects 414 (2012) 204 - 208

79) M. Salavati-Niasari, N. Mir, F. Davar, J. Alloys Compd., 493 (2010) 163 - 168

80) V. Usha, R. Vettumperumal, S. Kalyanaraman, R. Thangavel, International Journal of Nanoscience,17 (2018) 1850003

81) L. Umaralikhan, M. J. M. Jaffar, Iran J. Sci. Technol.Trans. Sci., (2017), doi.org/10.1007/s40995-017-0368-9

82) F.T. Thema, E. Manikandan, A. Gurib-Fakim, M. Maaza, J. Alloys Compd., 657 (2016) 655 – 661

83) S. Chakrabarty, K. Chatterjee, J. Phys. Sci., 13 (2009) 245 –250

84) B. Kisan, P. C. Shyni, S. Layek, H. C. Verma, D. Hesp, V. Dhanak, S. Krishnamurthy, A. Perumal, IEEE Trans. Magn., 50 (2014) 1 - 4

85) S. M. Meybodi, S.A. Hosseini, M. Rezaee, S.K. Sadrnezhaad, D. Mohammadyani, Ultrason. Sonochem. 19 (2012) 841 –845

86) B. Gokul, P. Matheswaran, K.M. Abhirami, R. Sathyamoorthy, J. Non-Cryst. Solids, 363 (2013) 161 –166

87) V. Usha, S. Kalyanaraman, R. Vettumperumal, R. Thangavel, Physica B, 504 (2017) 63 - 68

88) Y. Lin, L. Jiang, R. Zhao, C. Nan, Phys. Rev. B, 72 (2005) 014103

89) V. Biju, M. A. Khadar, Mater. Res. Bull., 36 (2001) 21 – 23

90) V. Biju, M. A. Khadar, J. Mater. Sci., 36 (2001) 5779 - 5787

91) P. Lunkenheimer, A. Loidl, C. R. Ottermann, K. Bange, Phys. Rev. B, 44 (1991) 5927 - 5930

92) S. K. Mishra, V. Subrahmanyam, Int. J. Mod. Phys. B, 25(18) (2008)DOI: 10.1142/S0217979211100035

93) F. Bodker, M.F. Hansen, C. Bender Koch, S.Morup, J. Magn. Magn. Mater., 221 (2000) 32 – 36

94) M. A. Khadar, V. Biju, A. Inoue, Mater. Res. Bull., 38 (2003) 1341 - 1349

95) H. Bi, S. Li, Y. Zhang, Y. Du, J. Magn. Magn. Mater., 277 (2004) 363 - 367

96) M. P. Proenca, C. T. Sousa, A. M. Pereira, P. B. Tavares, J. Ventura, M. Vazquez, J. P. Araujo, Phys. Chem. Chem. Phys., 13 (2011) 9561 - 9567

97) S. A. Makhlouf, F. T. Parker, F. E. Spada, A. E. Berkowitz, J. Appl. Phys. 81 (1997) 5561 – 5563

98) D. Dey, S. Das, M. Patra, N. Kole, B. Biswas, Journal of Organic & Inorganic Chemistry, 1(2015) DOI: 10.21767/2472-1123.100002

99) Z. Song, L. Chen, J. Hu, R. Richards, Nanotechnology 20 (2009) 275707

100) U.M. Patil, R.R. Salunkhe, K.V. Gurav, C.D. Lokhande, Appl. Surf. Sci., 255 (2008) 2603 –2607

101) P.M. Ponnusamy, S. Agilan, N. Muthukumarasamy, M. Raja, D. Velauthapillai, J. Mater. Sci.-Mater. Electron. 27 (2016) 399 - 406

102) S. Agrawal, A. Parveen, A. Azam, J. Lumin., 184 (2017) 250 - 255

103) T. V. Thi, A. K.Rai, J. Gim, J. Kim, J. Power Sources, 292 (2015) 23 - 30

104) T.Taşköprü, F.Bayansal, B. Şahin, M. Zor, Philos.Mag., 95 (2014) 32 - 40

105) G. Natu, P. Hasin, Z. Huang, Z. Ji, M. He, Y. Wu, ACS Appl. Mater. Interfaces, 4 (2012) 5922 - 5929

106) G. Anandhababu, G. Ravi, T. Mahalingam, M. Navaneethan, M. Arivanandhan, Y. Hayakawa, J. Phys. Chem. C, 118 (2014) 23335 - 23348

107) P. Anjali, R. Vani, T. S. Sonia, A. S. Nair, S. Ramakrishna, R. Ranjusha, K. R. V. Subramanian, N. Sivakumar, C. G. Mohan, S. V. Nair, A. Balakrishnan, Sci. Adv. Mater. 6 (2014) 1 – 8

108) P. Muthukumaran, C.V Raju, C. S. Sumathi, G. Ravi, D. Solairaj, P. Rameshthangam, J. Wilson, S.Alwarappan, S. Rajendran,New J. Chem., 40 (2016) 2741 - 2748

109) S. R. Gawali, V. L. Patil, V. G. Deonikar, S. S. Patil, D. R. Patil, P. S. Patil, J. Pant, J. Phys. Chem. Solids, 114 (2018) 28 - 35

110) A. H. Salama, A. M. Abdel-Karim, Egypt. J. Chem. 61(2) (2018) 281 - 294

111) Y. J. Mai, S. J. Shi, D. Zhang, Y. Lu, C. D. Gu and J. P. Tu, J. Power Sources, 204 (2012) 155 - 161

112) B. S. Singu, S. Palaniappan, K. R. Yoon, J Appl. Electrochem.,46 (2016) 1039

113) T. N. Diva, K. Zare, F. Taleshi, M. Yousefi,J. Nanostruct. Chem., 7 (2017) 273 - 281

…..ꕥ❋ꕥ…..

Chapter 2

SYNTHESIS AND CHARACTERIZATION TECHNIQUES

This chapter mainly focuses on the theory behind the experimental techniques used for the synthesis of nanoparticles and the characterization techniques for investigating different properties of the prepared samples. Thermogravimetric Analysis (TGA) is employed to study the thermal stability of the sample. The structural characterization techniques include X-ray Diffraction (XRD), Field Emission Scanning Electron Microscopy (FESEM), Energy Dispersive X-ray Spectroscopy (EDX), High Resolution Transmission Electron Microscopy (HRTEM), Fourier Transform Infrared Spectroscopy (FTIR) and X-ray Photoelectron Spectroscopy (XPS). Optical properties of the samples are analyzed using UV-Visible and Photoluminescence (PL) Spectroscopic methods. Electrical studies are carried out using DC and AC conductivity, and dielectric measurements. Vibrating Sample Magnetometer (VSM) is used to investigate the magnetic properties of the samples.

2.1 Introduction

Synthesis methods have a great influence in developing nanomaterials with different chemical and physical properties and thereby utilizing them for diverse applications. The methods for the synthesis of nanophase materials are categorized into two - top down and bottom up. The first involves the division of bulk solid into smaller and smaller portions, successively ending in nanometer size. Solid state route and ball milling come under this category. The second method is a self-assembly process. It involves the condensation of atoms or molecular entities in a gas or solution phase to form the material in the nanometer range. Chemical precipitation, sol-gel, micro-emulsion and hydrothermal methods are usually employed for the synthesis of ultrafine particles using this technique. Bottom-up method is the ideal and mostly employed method for the synthesis of nanoparticles. It offers a better chance to obtain nanostructures with fewer defects and more homogeneous chemical composition. Conversely, top-down approach introduces internal stress and also surface defects and contaminations.

When material dimensions are reduced to the nanoscale, they exhibit unique features and properties which are different from those of their bulk counterparts. To analyze this behaviour, several characterization techniques are mandatory. Characterization refers to the study of material features such as its composition, morphology, structure, thermal stability and various properties like optical, electrical, magnetic and so on.

2.2 Synthesis Methods

Chemical methods are extensively used for the synthesis of nanomaterials as they are more effective and versatile than physical methods. They provide better control over the size, shape and functionalization of nanomaterials [1].

2.2.1 Chemical Precipitation Method

Among various methods for controlled synthesis, the chemical precipitation method, based on the solution process is employed for the synthesis of pristine and doped nickel oxide nanoparticles.

In this method, often two or more reactants are mixed together at a controlled rate in a controlled environment to achieve precipitation of either the desired nanostructured sample itself or a suitable precursor. In the case of oxides, the precipitate could be in the chemical form of hydroxide, carbonate, oxalate etc, so that after decomposition it converts to oxide [2]. In this process particle size of the as-precipitated material is strongly dependent on the pH of the precipitation medium and molarity of the starting precursors. Consequently, control over the particle size can be easily attained. The reaction and transport rates are affected by the concentration of reactants, calcination temperature, pH of the solutions and the order in which the reagents are added to the solution and mixing.

Solvent evaporation method is employed for the synthesis of nickel oxide/cobalt phthalocyanine nanocomposite. The detailed procedures for the synthesis of the samples are elucidated in the corresponding chapters.

2.3 Thermal Analysis

Thermogravimetric analysis (TGA) and differential thermal analysis (DTA) are the techniques generally employed to predict the thermal stability of samples from room temperature up to a certain high temperature. Usually, a sample loses weight as it is heated up due to decomposition, reduction or evaporation. A sample could also gain weight due to oxidation or absorption. TGA tracks the change in weight of a sample as a function of temperature or time in an environment heated at a controlled manner. Derivative thermogravimetry (DTG) is the technique which yields the first derivative of the TG curve with respect to either time or temperature. In the DTA technique, the difference between the temperature of the sample and that of a reference material is recorded as a function of time or of temperature, as both of them are heated up at a constant rate. As a result of endothermic or exothermic chemical reactions, enthalpic changes can occur in the sample. An upward or downward peak in the DTA curve represents such an enthalpic change [3].

The thermogravimetric method can effectively be employed to determine the optimum calcination temperature of the sample. In the case of nanoparticles, the calcination temperature determines the size of the particle and crystallinity. Crystallisation temperature is different for different materials. In the thermogravimetric analysis, the temperature region which does not contain any peaks represents the crystallization region. So this is an efficient tool for the determination of temperatures at which crystallization occurs [4].

In the present work, the thermal behaviour of the samples are analyzed from 30-700^{o}C using *Perkin Elmer, STA 6000* instrument at a heating rate of 20^{o}C/min and accuracy of < ±0.5^{o}C.

2.4 Structural Characterization

Different techniques used for understanding the structure and morphology of the prepared samples in this work are X-ray diffraction, Field emission scanning electron microscopy, Energy-dispersive X-ray spectroscopy, High resolution transmission electron microscopy, Fourier transform infrared spectroscopy and X-ray photoelectron spectroscopy.

2.4.1 X-ray Diffraction (XRD)

XRD is a powerful technique for exploring the crystalline structure of the material. It provides information on the crystalline nature of the material, its phase composition and preferred orientation. By analyzing the XRD peaks, one can obtain information regarding the unit cell and microstructural (grain size, micro strain, etc.) parameters of the material. This is a non-destructive technique appropriate for all forms of samples [5].

The regular array of atoms in a crystal can act as a three dimensional grating for producing a diffraction pattern. X-rays reflecting from a series of crystallographic planes will superpose to produce a diffraction pattern which is governed by Bragg's law [6],

$$2d_{(hkl)}sin\theta = n\lambda, \qquad (2.1)$$

where $d_{(hkl)}$ is the interplanar spacing for a given set of Miller indices *(hkl),* 2θ the angle of diffraction or Bragg angle, n the order of diffraction and λ the wavelength of incident monochromatic X-rays. The intensity of the diffracted X-rays are measured and plotted as a function of diffraction angle *2θ*. If the crystal has long range periodicity, the diffraction pattern will have sharp peaks at *2θ* positions corresponding to various crystallographic planes. The phase identification of all the samples is performed by matching the peak positions and intensities in XRD patterns to those patterns in the JCPDS (Joint Committee on Powder Diffraction Standards) database.

The lattice spacing (*d*) values are calculated from the *2θ* values of the peaks using the equation (2.1). The lattice parameter '*a*' is computed from the lattice spacing of the prominent peaks of XRD pattern. For cubic crystal structure,

$$\boldsymbol{d_{(hkl)} = a/\sqrt{(h^2 + k^2 + l^2)}} \qquad \textbf{(2.2)}$$

The randomly oriented crystallites in nanocrystalline materials, lattice strain and structural imperfections lead to broadening of peaks in the diffraction patterns [7]. The average crystallite size *D* is estimated from the full width at half maximum (FWHM) β of a diffraction peak using the Scherrer equation [8] given by

$$\boldsymbol{D = \frac{k\lambda}{\beta cos\theta}}, \qquad \textbf{(2.3)}$$

where k (≈0.89) is a numerical factor frequently referred to as the crystallite-shape factor.

Scherrer equation gives only a rough estimate of crystallite size, it neglects the importance of microstrain ε, and its effects in the powder diffraction pattern [9]. A simple method to separate the contributions of particle size and microstrain to the line broadening in the XRD patterns is the Williamson–Hall (W-H) plotting [10, 11]. The contribution of microstrain ε to the line broadening of the diffraction peak is

$$\boldsymbol{\beta_{\varepsilon} = 4\varepsilon tan\theta}. \qquad \textbf{(2.4)}$$

Assuming that the particle size and strain contributions to line broadening are independent of each other, the observed line width for Lorentzian peak shape is simply the sum of the two,

$$\boldsymbol{\beta_{hkl} = k\,\lambda/Dcos\theta + 4\varepsilon tan\theta}. \qquad \textbf{(2.5)}$$

By rearranging this equation we get

$$\boldsymbol{\beta_{hkl}cos\theta = k\,\lambda/D + 4\varepsilon sin\theta}, \qquad \textbf{(2.6)}$$

which is the Williamson - Hall equation. $\beta_{hkl}cos\theta$ and $4sin\theta$ are plotted for all prominent peaks. From the linear fit to the data, the crystallite size is estimated from the y-intercept and the strain ε, from the slope of the fit.

In the present work, XRD measurements are carried out using *Bruker AXS D8 Advance X-ray diffractometer* (step size = 0.020°, step time = 31.2 s) with CuKα (λ = 1.5406Å) radiation at room temperature operating at a voltage of 40 kV and filament current of 35 mA.

2.4.2 Scanning Electron Microscopy (SEM)

SEM is one of the most versatile instruments available for the investigation of the topography and the composition near the surface region of the sample. SEM images have a characteristic three dimensional appearance and are helpful in judging the surface structure of the sample. A beam of high-energy electrons is focused on the surface of solid specimens to generate a variety of signals. The signals obtained from electron – sample interactions disclose information about the microstructural characteristics of the sample [12].

In SEM, an electron beam from a thermionic cathode accelerated by a relatively low voltage of 1-20 kV is rastered over the specimen surface. As a result of electron–sample interaction, secondary electrons, backscattered electrons, and Auger electrons are produced. The most common imaging mode in SEM is the monitoring of low energy (<50 eV) secondary electrons. Most of the secondary electrons are produced within the first few nm of the surface and thus contain information of only that region. So the production of secondary electrons is highly topography related [13]. In field emission SEM (FESEM), the cathode is a field emission gun. The narrower probing beams provide better spatial resolution and less sample charging and damage [14].

The surface micrographs of the samples are taken using *Carl Zeiss Sigma* operating at 30 kV with a resolution of 1.8 nm. A double sided conducting tape is lightly covered with the powder sample and is mounted on a pin disc made of aluminium. The disc is then fixed on a large round mounting platform and is placed in the holder for imaging.

2.4.3 Energy-Dispersive X-ray spectroscopy (EDX)

The chemical composition of the prepared sample plays an important role in deciding its properties. Energy dispersive analysis of X-ray technique is a powerful technique used for the elemental analysis of a sample. In EDX, high energy (>200 kV) electrons interacting with the sample allow X-ray generation that are characteristic of the elements emitting them. EDX analysis is usually performed using a SEM system equipped with EDX attachment. The *OXFORD XMX N EDS* attachment is used for the present study.

2.4.4 Transmission Electron Microscopy (TEM)

TEM is one of the most efficient and versatile tools used to characterize the microstructure of materials with very high spatial resolution. TEM can be used to characterize nanomaterials to obtain information about particle shape, size distribution, crystallinity and interparticle interaction. It can also reveal the nature of crystallographic defects. In TEM, a beam of high energy electrons (typically 100 –400 keV) emitted from an electron gun travels through the specimen under study. The magnetic coils placed at specific intervals act as an electromagnetic condenser lens system to focus the electron beam. The whole system is kept under very high vacuum to avoid scattering of electrons. An image formed from the interaction of the electrons transmitted through the specimen is magnified and focused by an objective lens onto an imaging device [15].

Two methods of specimen observation - image mode and diffraction mode are possible in TEM. A real space image of the illuminated sample area is produced in the image mode. Three primary

image modes are used in TEM, bright field, dark field and high resolution. In bright-field mode, a small aperture is placed at the back focal plane to block all diffracted beams and to pass only the transmitted electron beam. In dark field images, the direct beam is blocked, while diffracted beams are allowed to pass the objective. High resolution TEM (HRTEM) uses a large-diameter objective that admits the transmitted as well as diffracted beams. These beams are then made to recombine, in such a way that their amplitudes and phases are conserved. When viewed at high-magnification, it is possible to see the contrast in the image in the form of periodic fringes [14].

In diffraction mode, the electron diffraction pattern is obtained on the fluorescent screen, originating from the sample area illuminated by the electron beam. The selected area electron diffraction (SAED) pattern is the superposition of diffraction patterns from crystallites in the illuminated area with distinct orientations. A single crystal will produce a spot pattern on the screen, a powder or ring pattern will be obtained for polycrystals and a diffused pattern for amorphous materials. Different crystal planes in the sample can be identified from the SAED image [13].

For TEM analysis, the powder sample is dispersed in isopropyl alcohol and dropped on a carbon coated copper grid. After drying, the copper grid containing the sample is placed in the holder for imaging. TEM images of the samples are recorded using *JEOL JEM 2100* transmission electron microscope with a resolution of 0.23 nm and accelerated by 200 kV. Figure 2.1 shows the photograph of the JEOL model JEM-2100 transmission electron microscope.

Figure 2.1 : JEOL model JEM-2100 transmission electron microscope

2.4.5 Fourier Transform Infrared Spectroscopy (FTIR)

FTIR spectroscopy is a technique that can provide information about chemical bonding in a material. The functional groups present in a molecule can be easily identified by analyzing the peaks in IR spectrum. The absorption bands help us to confirm the identity of a pure compound and also to detect the presence of specific impurities. The principle underlying this technique is based on the fact that chemical bonds in a molecule vibrate at characteristic frequencies. When exposed to IR radiation, these molecules absorb energy that is characteristic of their structure. The absorbed energy will be utilised for excitation to higher vibrational levels. Only molecules with a net dipole moment are IR active [16].

The schematic diagram of the FTIR spectrophotometer is shown in Figure 2.2, which employs a Michelson's interferometer [17]. The radiation from an IR source is split into two beams using a beam splitter. An optical path difference is introduced between the beams by changing the position of the movable mirror. The resulting beams are then superposed, passed through the sample and finally focused on the detector. In the FTIR spectra, transmittance percentage (*%T*) is recorded against wave number ($1/\lambda$) cm^{-1}.

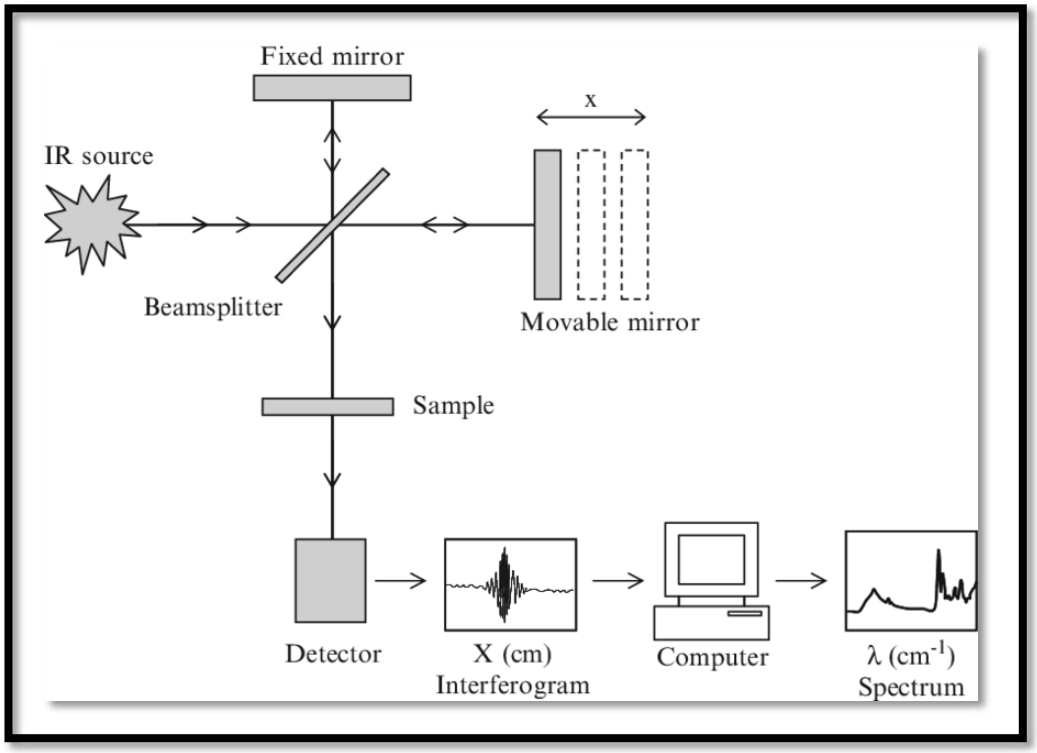

Figure 2.2 : Schematic diagram of FTIR spectrometer

.

In the present work, FTIR spectrum is recorded between 4000-400 cm^{-1} using *Thermo Nicolet, Avathar 370 spectrometer* having a resolution of 4 cm^{-1}.

2.4.6 X-ray Photoelectron Spectroscopy (XPS)

X-ray photoelectron spectroscopy also referred to as electron spectroscopy for chemical analysis (ESCA) is a quantitative surface analysis technique used for investigating the elemental composition of the material, chemical state and empirical formula of the elements present in the material. This technique involves bombarding the material with X-rays and analyzing the electrons emitted from the surface of the material. When the surface of the material is irradiated with X-ray photons of sufficient energy, hυ, electrons are ejected from the inner shells with a kinetic energy (KE) given by

$$KE = h\upsilon - E_B \qquad (2.7)$$

E_B is the binding energy of the atomic orbital or core level from where the electron is ejected. As each element has a unique set of binding energies, XPS can be used to identify and determine the concentration of the elements in the surface. Depending on the chemical nature of the surroundings, variations in the elemental binding energies can arise. These chemical shifts can be used to identify the chemical state of the materials being analyzed [18, 19].

Three main components of an XPS are X-ray source, energy analyzer for the photoelectrons and electron detector. The powder sample

is dusted lightly on a polymer based adhesive tape and attached to the specimen mount. The sample should be placed in an ultra-high vacuum chamber so as to enable the electrons to reach the analyser without any scattering. Once these photo-ejected electrons are in the vacuum, they are collected by the electron analyzer that measures their kinetic energy. In XPS spectra, the intensity of photoelectrons is plotted against binding energies.

In the present work, XPS analyses of the samples have been carried out using *AXIS ultra photoelectron spectrometer of Kratos analytical* using AlKα (1468 eV) as the radiation source.

2.5 Optical Characterization

Ultraviolet-Visible absorption spectroscopy and photolu minescence spectroscopy are the techniques employed for the optical characterization of the samples.

2.5.1 Ultraviolet-Visible Absorption Spectroscopy

Ultraviolet-visible (UV-Vis) spectroscopy is a reliable tool to characterize the absorption, transmission and reflection of the given material. It is an ideal technique for determining the electronic properties of nanomaterials. The absorption of electromagnetic radiation in the UV and visible regions that are characteristic of the material stimulates the excitation of an electron from a lower to higher molecular orbital. Since the electronic transitions are quantized, the spectrum is expected to exhibit a single, discrete line corresponding to each electronic transition. But in practice, the absorption bands are usually broad. This is due to the

superposition of vibrational and rotational energy levels on the electronic energy levels. Size dependent properties can also be observed in a UV-visible spectrum, particularly in nanomaterials, which include peak broadening and shifts in the absorption wavelength [20, 21].

The basic components of a spectrophotometer are the light source, sample holder, monochromator, detector and recorder. UV and visible light from the source is first collimated and then split into its component wavelengths using a monochromator. The light is divided into two beams by the beam splitter and one half of the beam passes through the sample and other through the reference. The transmitted beams are detected, amplified and processed by the computer to obtain the spectrum.

Diffuse reflectance spectroscopy is used to measure the reflectance data of the powder samples. When the light beam traverses a sample it may get reflected, transmitted or absorbed. The diffuse reflection reveals the part of the incident light beam scattered within the sample and comes back to the surface. The reflected component of the sample beam is collected by the integrating sphere and detected by the detector. Kubelka Munk transformation is employed to determine the absorption coefficients of the powder samples from the reflectance measurements [22]. The bandgap of the material is estimated by putting absorption coefficient α in the Tauc relation [23],

$$\boldsymbol{\alpha h\nu = A(h\nu - E_g)^n,} \qquad \textbf{(2.8)}$$

where A is a constant, $h\nu$ the photon energy and E_g the band gap. The value of n = 1/2 for the direct allowed, n = 3/2 for the direct forbidden, n = 2 for the indirect allowed and n = 3 for the indirect forbidden transitions. The bandgap of the samples can be estimated by plotting $(\alpha h\nu)^{1/n}$ as a function of $h\nu$ and extrapolating linear region of the curve to absorption equal to zero.

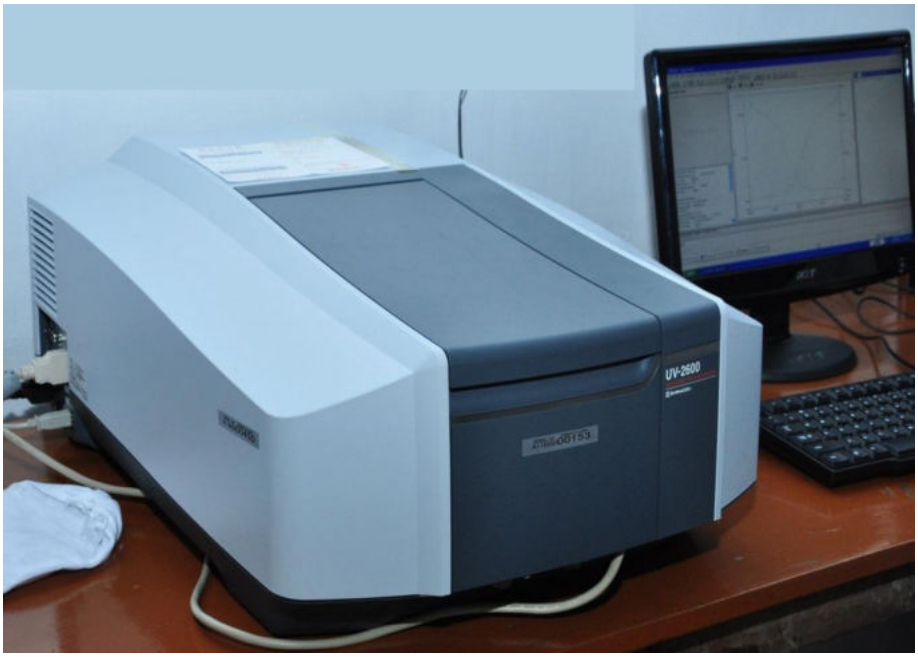

Figure 2.3 Shimadzu UV-2600 model UV-visible spectrophotometer

Diffuse reflectance data are collected over the spectral range 200-800 nm using Shimadzu *UV 2600 UV–Visible spectrophotometer* shown in Figure 2.3. For the measurement, nanoparticles are pressed into a thick pellet in a sample holder and placed at the entrance port of the integrating sphere. Barium sulphate is used as the reference material for the calibration of reflectance scale.

2.5.2 Photoluminescence spectroscopy (PL)

Photoluminescence refers to the emission of light that results from optical stimulation. The material under study absorbs electromagnetic radiation and makes a transition from the ground state to an excited state of an atom or molecule, or from the valence band to the conduction band of a semiconductor crystal which results in the creation of electron-hole pairs. The system then undergoes a non-radiative internal relaxation and the excited electron moves to a more stable state, such as the bottom of the conduction band, the lowest vibrational molecular state or a localized impurity level in the forbidden energy gap. After the lifetime in the excited state, the electronic system will return to the ground state releasing energy in the form of light. The spectral dependence of the intensity of the emitted light is analyzed to provide information about the properties of the material. The most common configuration for PL studies is the spectral emission analysis where the material is excited with a light of fixed wavelength and the intensity of the PL emission is measured over a range of wavelengths. The spectral dependence of the intensity of the emitted light is analyzed to provide information about the impurities, surface defects and trap levels in the sample [13].

Light from the source, a high pressure Xenon arc lamp falls on the excitation monochromator, which transmits a narrow range centred about the selected excitation wavelength. The transmitted light passes through the sample cell causing fluorescent emission. The emission monochromator transmits light in a narrow range centred about the specified emission wavelength. The light finally falls on the detector

which amplifies and creates a voltage that is proportional to the emitted intensity.

Figure 2.4 : Horiba Scientific-Fluoromax4 spectrophotometer

Horiba Scientific-Fluoromax4 spectrophotometer shown in Figure 2.4 is used to record the PL spectra of the samples at room temperature with a spectral accuracy of 0.5 nm in the present study.

2.6 Electrical Studies

For the electrical characterization, the samples are consolidated in the form of cylindrical pellets of diameter 13 mm and appropriate thickness using a hydraulic press by applying a pressure of 6 – 8 tons. Both faces of the pellets are coated with a silver paste to form parallel plate capacitor geometry with the material as the dielectric medium.

2.6.1 DC Conductivity

For measuring the DC conductivity, the nanoparticles are pressed into pellet form as described earlier. For samples of uniform cross-section, resistivity is calculated using the formula

$$\boldsymbol{\rho = RA/d}, \qquad \textbf{(2.9)}$$

where R is the resistance of the sample at a particular applied voltage, and A and d are the face area and thickness of the pellet respectively.

The reciprocal of resistivity gives the DC conductivity (σ_{DC}),

$$\boldsymbol{\sigma_{DC} = {}^{1}/_{\rho}} \qquad \textbf{(2.10)}$$

The Arrhenius equation is adopted to analyze the measured conductivity data given by,

$$\boldsymbol{\sigma_{DC} = A\,exp(-E_a\ /k_BT\ )}, \qquad \textbf{(2.11)}$$

where σ_{DC} is the conductivity, A the pre-exponential factor, k_B the Boltzmann's constant and T the temperature in K. The slope of the Arrhenius plot, $ln\ (\sigma_{DC})$ versus 1/T gives the activation energy E_a.

The DC resistance of the samples is recorded from room temperature to 423 K using *KEITHLEY 2450 Source Meter* in two probe mode.

2.6.2 Dielectric and AC Conductivity Studies

Every material has a unique set of electrical characteristics that are dependent on its dielectric properties. Any material having the ability

to store energy when an external electric field is applied is classified as the dielectric. The capacitance of a parallel plate capacitor with a dielectric medium introduced between the plates is given by,

$$\boldsymbol{C = \frac{\varepsilon_0 \varepsilon_r A}{d}}, \qquad \textbf{(2.12)}$$

where *A* and *d* are respectively the area of the capacitor plates and the distance between them, ε_0 the permittivity of free space and ε_r the relative permittivity or dielectric constant of the given sample. ε_r is a complex quantity which describes the interaction of materials with an electric field and can be expressed as

$$\boldsymbol{\varepsilon_r = \varepsilon_r' - j\varepsilon_r''}. \qquad \textbf{(2.13)}$$

The real part of permittivity (ε_r') is a measure of energy stored in a material from an external electric field and the imaginary part (ε_r'') represents energy loss [24]. The dielectric permittivity of the material can be calculated from Eq.2.12 using the relation,

$$\boldsymbol{\varepsilon_r = Cd/\varepsilon_0 A} \qquad \textbf{(2.14)}$$

When complex permittivity ε_r is drawn as a simple vector diagram (Figure 2.5), the real and imaginary components are 90° out of phase. ε_r makes an angle δ with the real axis [25]. The dissipation factor, D or loss tangent is defined as the ratio of the imaginary part of the dielectric constant to the real part.

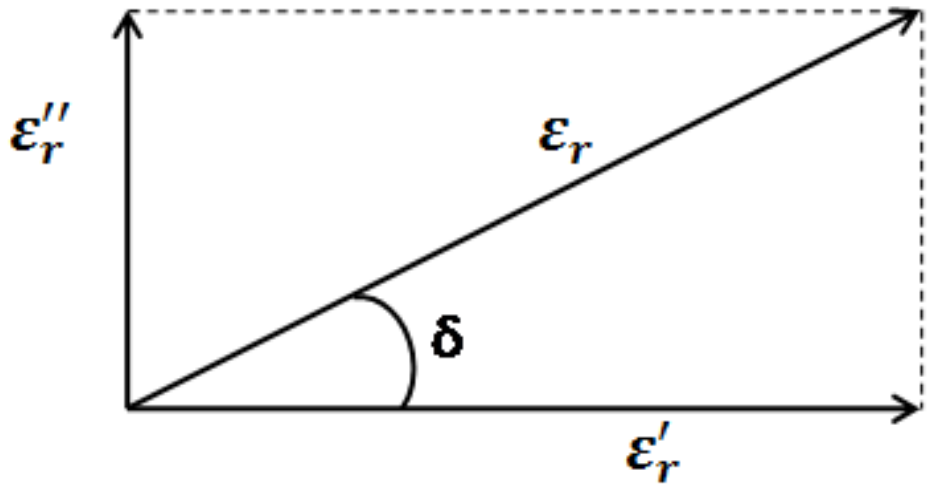

Figure 2.5 : Dielectric constant vector diagram

The loss tangent,

$$D = tan\delta = \frac{\varepsilon_r''}{\varepsilon_r'}. \qquad (2.15)$$

For a better understanding of the dielectric behaviour of the samples, the complex impedance spectroscopic technique is employed. In complex impedance diagrams (Nyquist plot), the imaginary part of the impedance $Z''(\omega)$ is plotted against the real part of impedance $Z'(\omega)$. The grain and grain boundary contributions to the overall impedance can be resolved by fitting the experimental response to that of an equivalent circuit. In the present study, the fitting is done using EIS spectrum analyser.

AC conductivity of the dielectric material can be evaluated using the relation [26]

$$\sigma_{ac} = \omega\varepsilon_r'' = 2\pi f\varepsilon_r' \tan\delta, \quad (2.16)$$

where $\omega = 2\pi f$ is the angular frequency of the applied field.

Generally, the electrical conductivity depends on the amount of free charge carriers available and their mobility. The real part of AC conductivity σ consists of two parts,

$$\sigma = \sigma(T) + \sigma(\omega, T). \quad (2.17)$$

The first term is the frequency independent DC conductivity which is due to band conduction while the second term is the AC conductivity due to hopping, which is frequency dependent [27, 28]. The variation of AC conductivity can be described by the universal Jonscher's power law [29, 30],

$$\sigma(\omega, T) = \sigma_{AC} = A\omega^s, \quad (2.15)$$

where ω is the angular frequency of the applied field, and A and n are constants which depend on both the temperature and composition. The constant s is the frequency exponent which varies between zero and unity.

Wayne Kerr H-6500B model impedance analyzer is used for the dielectric and AC conductivity measurements in the present study. The capacitance (C) and loss tangent (D) are recorded in the frequency range of 100 Hz – 5 MHz at selected temperatures. The dielectric constant, dielectric loss and AC conductivity of the samples are calculated using Eqs 2.14, 2.15 and 2.16, respectively. The experimental set-up for the dielectric measurements is shown in Figure 2.6.

Figure 2.6 : Experimental set up for dielectric measurements

2.7 Vibrating Sample Magnetometry (VSM)

Vibrating sample magnetometer is used for the measurement of magnetic parameters of the sample. It is based upon Faraday's law according to which an *emf* is induced in a conductor by a time varying magnetic flux. By measuring the electric field, the changing magnetic field can be determined [31].

Figure 2.7 shows the schematic arrangement of VSM. The steady magnetic field is produced by a pair of electromagnets. The magnetic sample placed in the steady magnetic field vibrates with respect to the stationary pick-up coils. This induces a voltage in the pick-up coils, which is proportional to the magnetic moment of the sample. The induced voltage is measured using a lock-in amplifier. The magnetic moment of the sample can be estimated by feeding the signals from the pick-up coils and the reference signal from the sample holder.

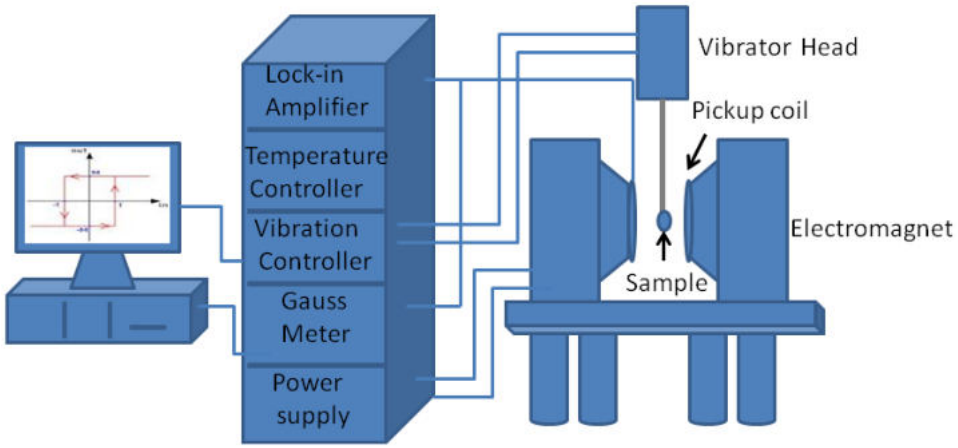

Figure 2.7 : Schematic arrangement of VSM

In the present work, magnetic measurement has been performed using *Lakeshore VSM 7410* with a maximum magnetic field of 15 kOe for all the samples at room temperature (300 K).

References

1) C. N. R. Rao, S. R. C. Vivekchand, K Biswas, A. Govindaraj, Dalton Trans. 2007, 3728–374

2) W. M. Breck, Nanotechnology Vol. I, CBS (2016)

3) R. Chen, Y. Kirsh, The Analysis of Thermally Stimulated Processes, Pergamon, Amsterdam, (1981),

4) S. Zhang, L. Li, A. Kumar, Material Characterization Techniques, CRC Press (2008).

5) D. Liu, Q. Wang, H.L.M. Chang, H. Chen, J. Mater. Res. 10 70 (1995) 1516

6) C. Kittel, Introduction to Solid State Physics, John Wiley and Sons, New York (1997)

7) H.S. Nalwa, Encyclopaedia for Nanoscience and Nanotechnology, Vol.1, American Scientific Publishers(2004)

8) B.D. Cullity, Elements of X-ray diffraction, Addison-Wesley, MA (1967)

9) J. Markmann, V. Yamakov, J. Weissemüller, Scr. Mater., 59 (2008) 15

10) G. K. Williamson, W. H. Hall, Acta Metall., 1 (1953) 22-31.

11) A.W. Burton, K. Ong, T. Rea, I.Y. Chan, Microporous Mesoporous Mater.,117 (2009) 75–90

12) J. I. Goldstein, D. E. Newbury, P. Echlin, D. C. Joy, A. D. Romig Jr., C. E. Lyman, C. Fiori, E. Lifshin, Scanning Electron Microscopy and X-Ray Microanalysis**,** Plenum Press, New York (1981).

13) C. R. Brundle, C.A. Evans Jr., S. Wilson, Encyclopedia of Materials Characterization, Butterworth-Heinemann, USA (1992)

14) K. K. Chattopadhyay, A. N. Banerjee, Introduction to Nanoscience and Nanotechnology, PHI, New Delhi (2009)

15) D. B. Williams, C. B. Carter, Transmission Electron Microscopy, 2 ed. Springer US, (2009).

16) B. C. Smith, Fundamentals of Fourier Transform Infrared Spectroscopy, 2nd ed. (CRC Press, Taylor & Francis Group, London, 2011)

17) J. J. Ojeda, M. Dittrich, Methods in molecular biology (Clifton, N.J.) 881(2012)187-211

18) T. A. Carlson, Photoelectron and Auger Electron Spectroscopy, Plenum Press, New York) (1978)

19) J. F. Moulder, W. F. Stickle, P. E.'Sobol, K. D. Bomben, Handbook of X-ray Photoelectron Spectroscopy, Perkin-Elmer Corporation,U.S.A. 1992

20) T. Owen, Fundamentals of UV-visible Spectroscopy: Primer Agilent Technologies,(2000)

21) L. D. S. Yadav, Organic Spectroscopy Springer, Dordrecht (2005)

22) P. Kubelka, J. Opt. Soc. Am. 44 (1954) 330 - 335

23) J. Tauc, Amorphous and Liquid Semiconductors, 1 ed. Plenum Press, New York (1974)

24) A. Dias, R. Luiz Moreive, J. Mater. Res. 12 (1998) 2190

25) http://academy.cba.mit.edu/classes/input_devices/meas.pdf.

26) S. Bhat, S.K. Khosa, P.N. Kotru, R.P. Tandon, Mater. Sci. Eng. B., 309 (1995) 7–11

27) M. A. El Hiti, J. Phys. D: Appl. Phys., 29 (1996) 501-505.

28) A. M. Abo El Ata, M. K. El Nimra, S. M. Attia, D. El Kony, A. H. Al-Hammadi, J. Magn. Mater., 297 (2006) 33-43.

29) A. K. Jonscher, Nature, 267 (1977) 673.

30) A.K. Jonscher, Dielectric Relaxation in Solids, Chelsea Dielectric Press, London (1983)

31) B.D. Cullity , C. D. Graham, Introduction to magnetic materials 2nd ed. John Wiley and sons (2009)

32) M. McElfresh, Fundamentals of Magnetism and Magnetic Measurements, Quantum Design, San Diego, Purdue University, USA (1994)

…..ꕥ❋ꕥ…..

Chapter 3

EFFECT OF CALCINATION TEMPERATURE ON THE PROPERTIES OF SYNTHESIZED NICKEL OXIDE NANOPARTICLES

The synthesis of nanocrystalline nickel oxide by chemical precipitation method and its structural, optical, electrical and magnetic characterization are described in this chapter. The effect of calcination temperature on the properties of nickel oxide nanoparticles is also discussed.

3.1 Introduction

Nanocrystalline nickel oxide (NiO) has attracted a great deal of scientific attention because of its novel physical and chemical properties, and potential applications. To explore the potential of NiO, a deeper insight into its structure and properties are needed. A systematic and detailed analysis of the structural, optical, electrical and magnetic properties of nanocrystalline NiO synthesized by chemical precipitation method is discussed in this chapter. The effect of calcination temperature on the structure and properties of NiO nanoparticles is also elucidated in this chapter.

The thermal stability of synthesized material is studied using thermogravimetric and differential thermal analysis. The structural characterization of the NiO nanoparticles is done using X-ray diffraction and Fourier transform infrared spectroscopy. The morphology of nanoparticles is studied using scanning electron microscopy and transmission electron microscopy. The quantitative compositional information of the synthesized material is provided using energy dispersive X-ray analysis and X-ray photoelectron spectroscopy. The optical properties of the samples are investigated using UV-visible and photoluminescence spectroscopic methods. The dielectric and AC and DC conductivity measurements are conducted to examine the electrical properties. The magnetic behaviour of the samples is studied using vibrating sample magnetometer.

3.2 Synthesis of NiO Nanoparticles

Nickel nitrate hexahydrate (Ni $(NO_3)_2 6H_2O$) (99.8%, Merck) and ammonium carbonate ($(NH_4)_2CO_3$) (99.9%, Merck) are used for the synthesis of pristine NiO nanoparticles. Nanocrystalline NiO samples are prepared by reacting aqueous solutions of nickel nitrate hexahydrate and ammonium carbonate (0.1M each). The reactants are slowly mixed at room temperature under magnetic stirring. The precipitate is allowed to settle down overnight and is collected by the decantation of the supernatant liquid. It is then washed with distilled water several times to remove the unreacted salts and impurities. Finally, the precipitate is filtered and dried in a hot air oven at 70°C for 18 h [1]. As the complete decomposition of nickel carbonate into nickel oxide occurs around 400°C, the precursor is calcined in a muffle furnace for 3 h at 400°C to synthesize NiO nanoparticles. To study the effect of calcination, the precursor is calcined at 500 and 600°C for 3 h. The colour of the sample changes from black to dark green as the calcination temperature increases from 400 to 600°C. NiO that is closely stoichiometric appears green, while the material with an excess of oxygen will have a black appearance [2]. Synthesized NiO samples calcined at 400, 500 and 600°C are designated as N0, N1 and N2 respectively. The scheme of preparation of nanocrystalline NiO is shown in Figure 3.1. The chemical reaction for the formation of NiO is as follows:

$$Ni\,(NO_3)_2\,(aq) + (NH_4)_2CO_3\,(aq) \longrightarrow NiCO_3\,(\downarrow) + 2NH_4NO_3\,(aq)$$

$$NiCO_3 \longrightarrow NiO + CO_2$$

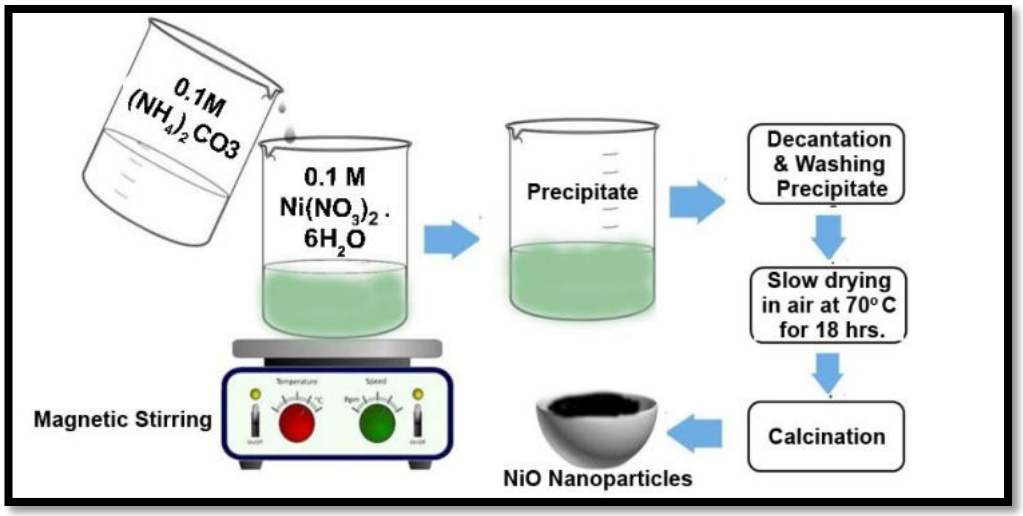

Figure 3.1 : Scheme of preparation of NiO nanoparticles

3.3 Results and Discussion

3.3.1 Thermal Analysis

The thermal stability of the precursor from the ambient temperature to 870°C is studied using thermogravimetric and differential thermal analysis techniques. The TGA/DTA and DTG curves of the precursor are shown in Figure 3.2. The TGA curve indicates an appreciable weight loss of the precursor from 50 to 350°C. This suggests a complete decomposition of the precursor at 350°C to become NiO [3]. Therefore the choice of suitable calcination temperature is highly dependent on the results of TG analysis.

Two distinct intervals of weight loss are observed in the TGA curve, accompanied by two peaks of weight loss rate in the DTG curve. The first peak located around 100°C (weight loss 0.779 mg/min) might be attributed to the thermal dehydration of the precursor and the

evaporation of physically adsorbed impurities. The second peak and the endothermic peak indicated by DTA near 300°C may be related to the decomposition of nickel carbonate into nickel oxide and carbon dioxide [4, 5]. The TGA curve indicates a weight loss of 0.805 mg/min in this region. No change in the weight of the precursor is observed above 400°C. Based on the results of TGA, a temperature of 400°C was chosen to ensure the complete decomposition of the precursor to form nickel oxide.

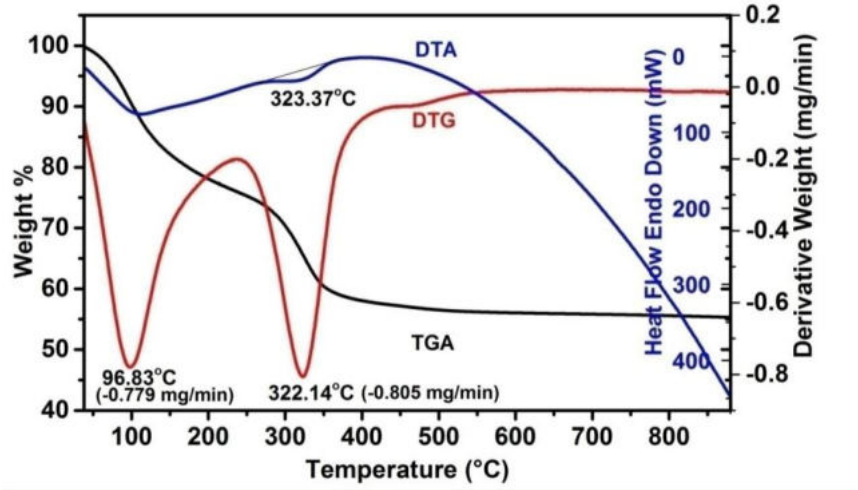

Figure 3.2 : TGA/DTA/DTG curves of NiO precursor

3.3.2 Structural Characterization

The microstructural characterization of the synthesized NiO nanoparticles is done by following the procedures described in *Section 2.4.*

3.3.2.1 Powder XRD Analysis

The structure in terms of size and strain and the phase purity of the synthesized samples are examined using XRD technique. XRD

pattern of the precursor before heat treatment is shown in Figure 3.3. No well-defined diffraction peaks corresponding to NiO are detected, which indicates that the precursor has not changed to nanocrystalline NiO.

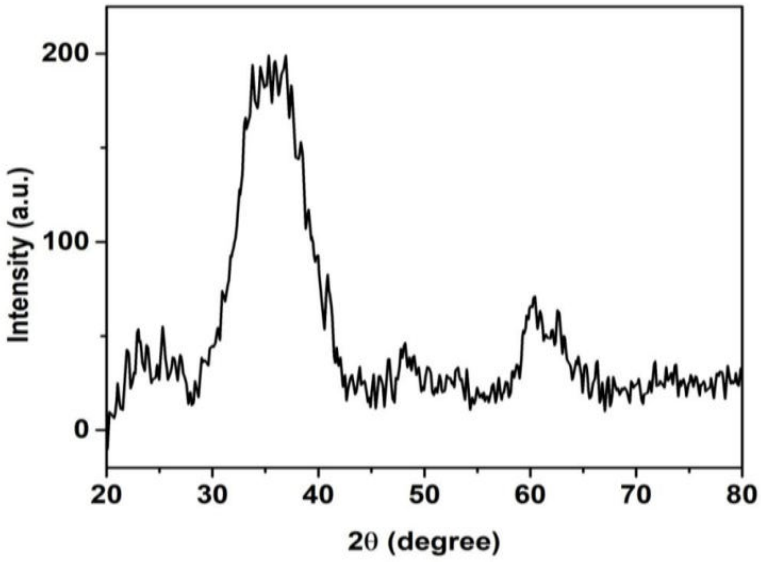

Figure 3.3 : XRD pattern of NiO precursor

Figure 3.4 shows the XRD patterns of NiO nanoparticles calcined at different temperatures collected using Bruker D8 Advance X-ray diffractometer (step size = 0.020^o, step time = 59.7 s) with Cu-Kα radiation (λ = 1.5406 Å) in the 2θ range from 30 to 90^o. Well defined diffraction peaks with preferential orientation along the (200) planes are observed for all the samples, which confirm their crystalline nature. The peaks corresponding to (111), (200), (220), (311) and (222) planes can be indexed to face centred cubic bunsenite structure (space group: *Fm3m*) of NiO [3], which is in agreement with the standard spectrum (JCPDS No.73-1519). A high degree of phase purity for the samples is evident from the absence of additional peaks. The peaks get sharper and more intense with an increase in calcination temperature.

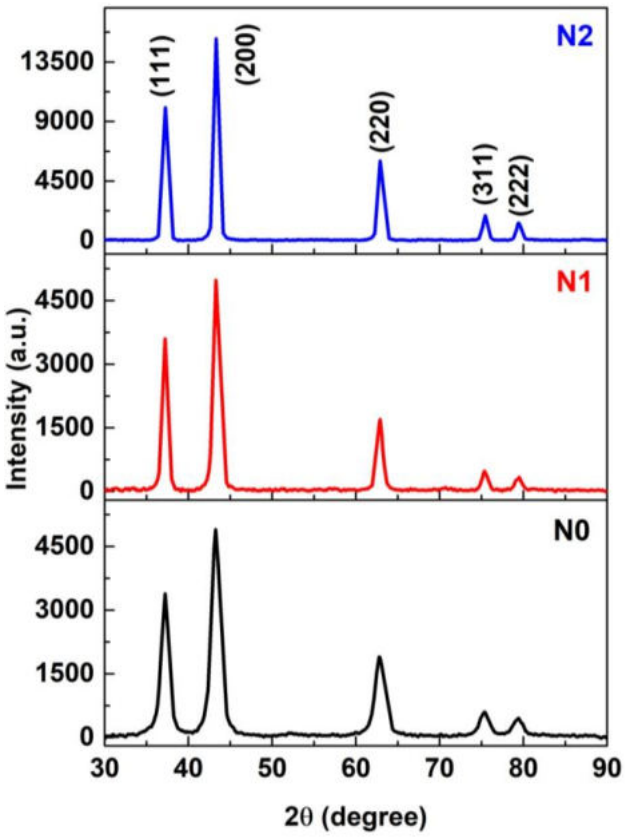

Figure 3.4 : XRD patterns of NiO samples calcined at 400 (N0), 500 (N1) and 600°C (N2)

The average crystallite sizes calculated using Scherrer equation [6] are 8.2, 12.4 and 18.5 nm respectively for N0, N1 and N2 samples. These sizes can be smaller than the actual value, as the lattice defects and strain can have an effect on the XRD peaks [7]. Hence the effect of crystallite size and lattice strain on the broadening of XRD peaks has been studied using the W – H method [8] as described in *Section 2.4.1*. W-H plots for the nickel oxide samples are shown in Figure 3.5. The points are getting closer towards its linear fit with the increase in calcination temperature, which confirms the increase in crystallinity of NiO nanoparticles.

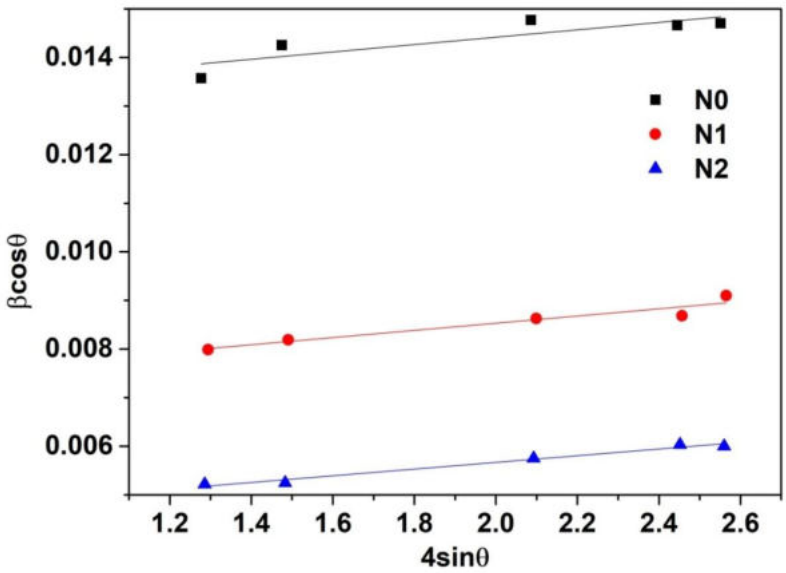

Figure 3.5 : W-H plots of NiO samples N0, N1 and N2

The structural parameters of the samples calculated from XRD data are tabulated in Table 3.1. The decrease in full width at half maximum (FWHM) with increase in calcination temperature is an indication of increased crystallite size. Due to the decrease in interplanar spacing, XRD peaks shift to higher 2θ values upon calcination. The lattice constant (*a*) of the samples estimated from the spacing of the *(200)* lattice planes and the unit cell volume ($V = a^3$) is presented in the table. These results match with the values given in the XRD pattern of JCPDS Card No. 73-1519 for NiO. It can be seen from Table 3.1 that calcination leads to a decrease in lattice constant and hence to lattice contraction. The decrease in micro-strain with increase in calcination temperature indicates that defects like dislocations, edges or cuts are removed during calcination [9].

Table 3.1: Structural parameters of NiO samples N0, N1 and N2 from XRD data

Sample	Average crystallite size (nm)		FWHM (200) plane	2θ ((200) plane)	Lattice spacing d_{200} (Å)	Lattice constant a (Å)	Unit cell volume ($Å^3$)	Micro-strain (x 10^{-4})
	Scherrer method	W-H method						
JCPDS Card No.73-1519	--	--	--	43.253^o	2.090	4.168	72.43	--
N0	8.2 ± 0.16	9.3 ± 0.19	0.968^o	43.259^o	2.090	4.179	73.003	13.110
N1	12.4 ± 0.25	14.7 ± 0.30	0.673^o	43.276^o	2.089	4.178	72.930	9.718
N2	17.8 ± 0.35	21.9 ± 0.44	0.445^o	43.301^o	2.088	4.175	72.773	6.397

In brief, XRD results reveal an increase in crystallite size and lattice contraction with increase in calcination temperature. Calcination can reduce the grain boundary discontinuities, which in turn enhance the crystallinity of the sample [10]. All these structural modifications alter the physical properties of NiO nanoparticles.

3.3.2.2 FESEM and EDX Analyses

The surface morphology of the samples is analysed using FESEM technique**.** FESEM images of the samples N0, N1 and N2 are shown in Figure 3.6. The particles are non-spherical with nearly uniform size and are well dispersed in the bulk lattice. The images clearly show the aggregation of nanoparticles. The increase in particle size upon calcination is also evident from the images.

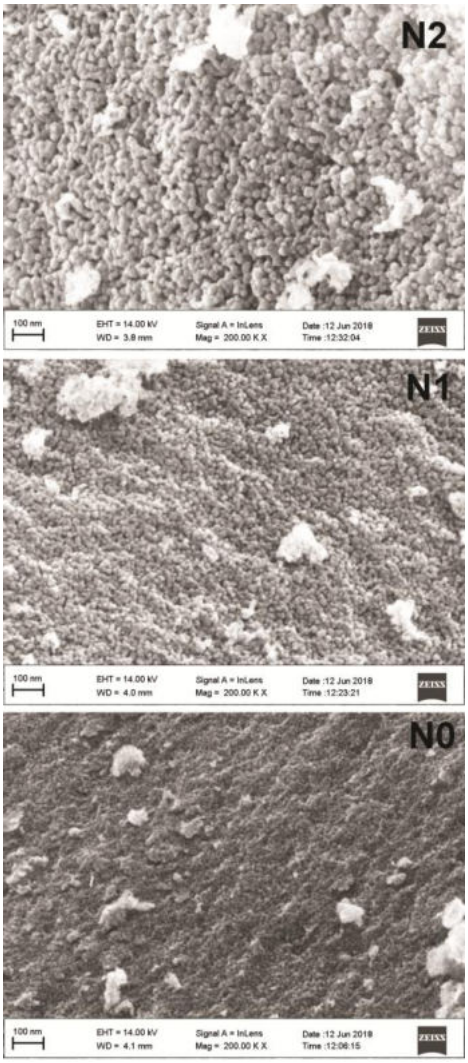

Figure 3.6 : FESEM images of NiO samples N0, N1 and N2

EDX analysis is done to confirm the chemical composition and stoichiometry of the samples. The representative EDX patterns of the samples are shown in Figure 3.7, which indicates the presence of only Ni and O. The average mass and atomic percentages of the samples taken from three different regions are presented in Table 3.2, which confirms the formation of pure NiO nanoparticles.

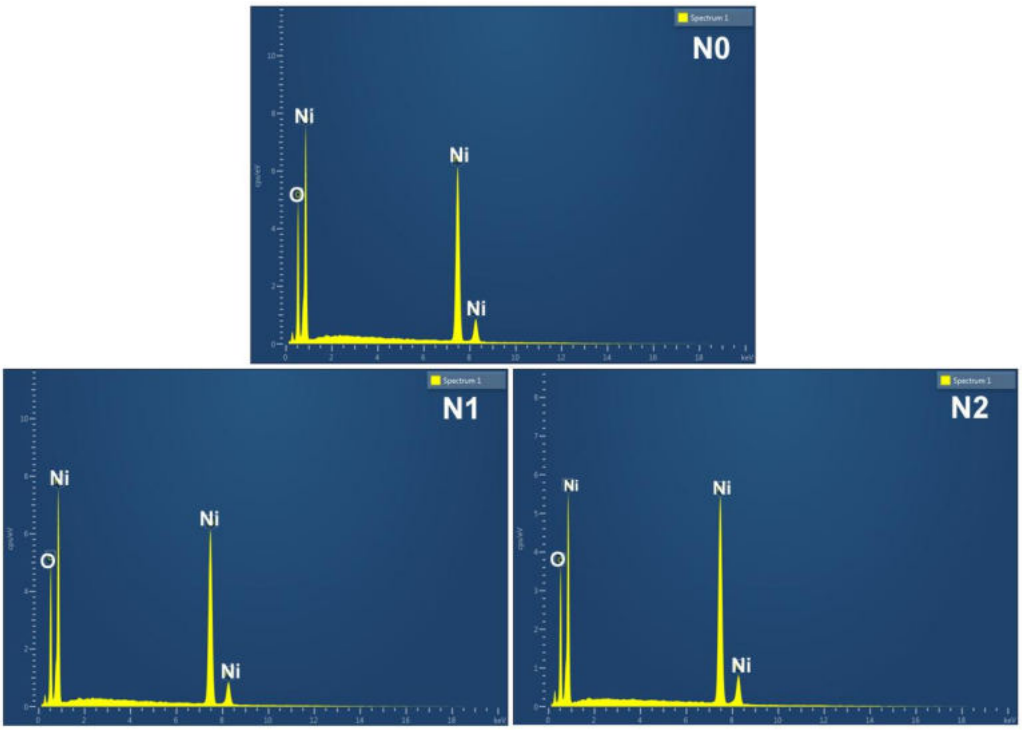

Figure 3.7 : EDX patterns of NiO samples N0, N1 and N2

From the results of EDX analysis, the sample N0 is found to deviate from stoichiometry with excess oxygen, N1 possesses oxygen vacancies and N2 is stoichiometric with $N_{50}O_{50}$ elemental ratio.

Table 3.2 : Chemical composition of NiO samples N0, N1 and N2

Sample	Element	Series	Mass %	Atom %
N0	**Ni**	K	72.79	42.27
	O	K	27.21	57.73
Total			100	100
N1	**Ni**	K	81.96	55.34
	O	K	18.04	44.66
Total			100	100
N2	**Ni**	K	78.34	50.33
	O	K	21.66	49.67
Total			100	100

3.3.2.3 TEM Analysis

Microstructural analysis of the samples is done using TEM. The bright field (BF) image, HRTEM image, SAED pattern and the histogram illustrating the size distribution of all the samples are displayed in Figure. 3.8- 3.10.

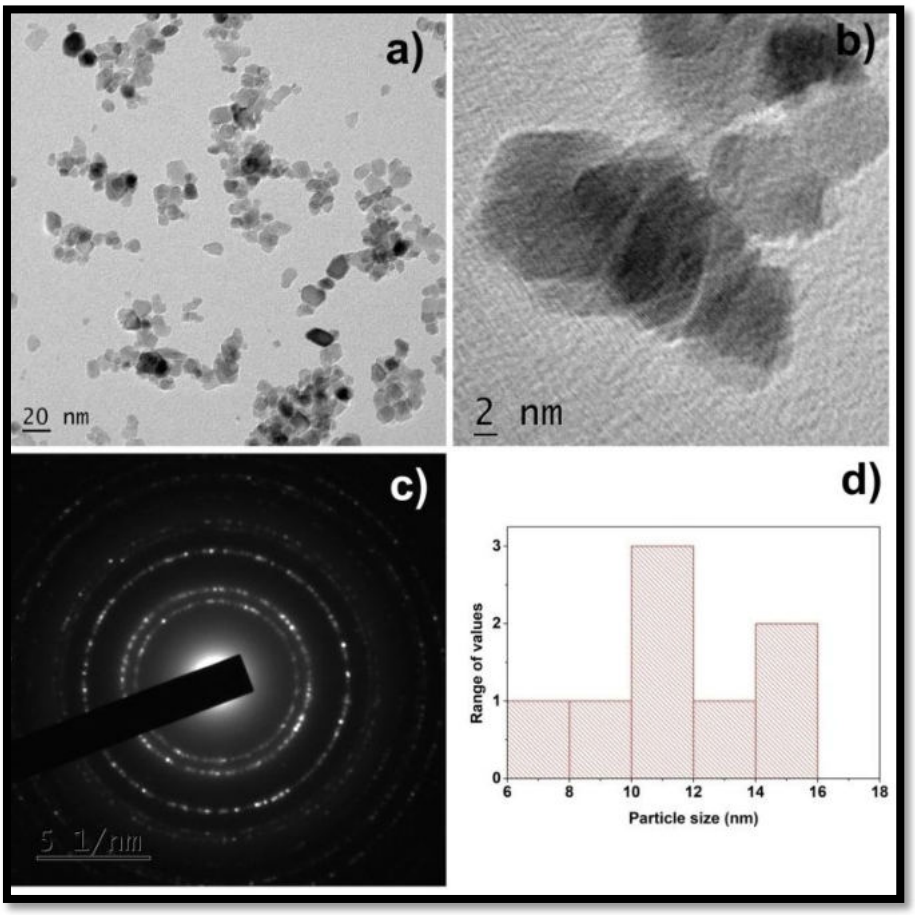

Figure 3.8 : **(a)** TEM bright field image,
(b) HRTEM image,
(c) SAED pattern and
(d) Particle size distribution of sample N0

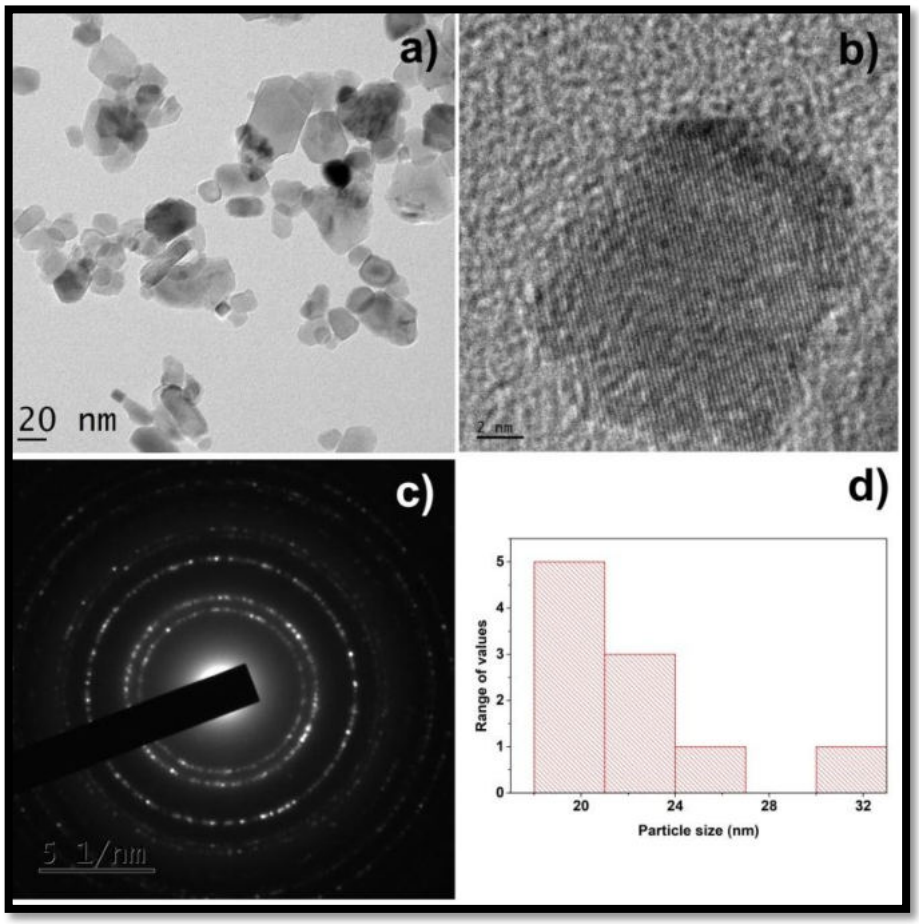

Figure 3.9 : **(a)** TEM bright field image,
(b) HRTEM image,
(c) SAED pattern and
(d) Particle size distribution of sample N1

The bright field images of the samples show large number of particles with almost hexagonal shape. The particle growth upon calcination is evident from the BF images. The unidirectional fringe patterns are clearly observed for all the samples from HRTEM images. The bright spots in the SAED patterns confirm the crystalline nature of all the samples. The average particle size obtained from TEM images is

shown in Table 3.3. The spacing between the successive planes for the three prominent peaks is calculated from the SAED patterns and is tabulated. The large size for N2 indicates aggregation of grains upon calcination.

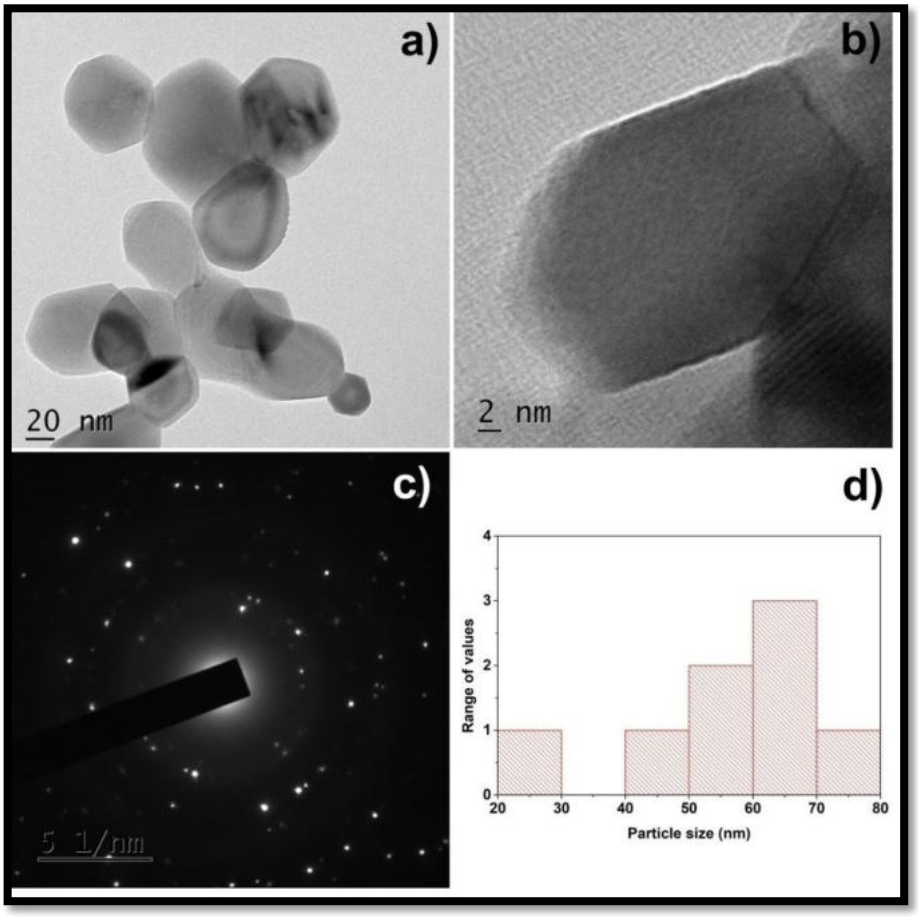

Figure 3.10: **(a)** TEM bright field image,
(b) HRTEM image,
(c) SAED pattern and
(d) Particle size distribution of sample N2

Table 3.3 : Structural parameters of NiO samples N0, N1 and N2 from TEM images

Sample	Average particle size from TEM images (nm)	d spacing from SAED patterns (Å)		
		(111)	(200)	(220)
N0	11.4± 0.23	2.856	2.463	1.745
N1	21.8±0.44	2.786	2.472	1.718
N2	57±1.14	2.656	2.406	1.609

3.3.2.4 FTIR Spectroscopy

FTIR spectra of the samples are recorded in the range 400 – 4000 cm^{-1}. The spectrum of the precursor powder before heat treatment is shown in Figure 3.11. The peaks at 1378, 835 and 686 cm^{-1} are the characteristic frequencies of carbonate species (CO_3^{2-}) in the precursor [11, 12]. Also the Ni – O bond at 413 cm^{-1} is not prominent in the spectrum. Thus from the IR data, it is clear that the precursor sample is a nickel carbonate species.

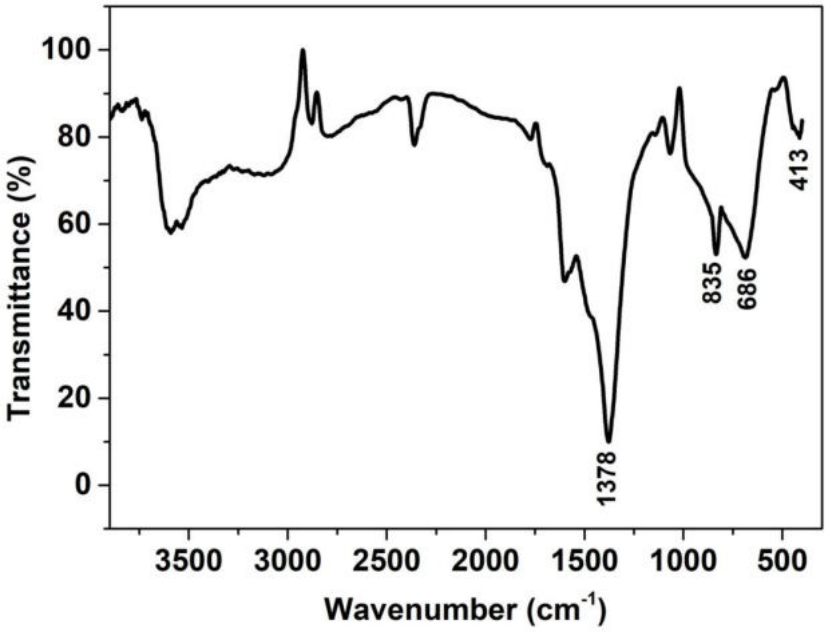

Figure 3.11 : FTIR spectrum of NiO precursor

Figure 3.12 shows the FTIR spectra of the NiO samples after calcination. The prominent absorption peak near 410 cm^{-1} is assigned to Ni - O stretching vibration mode [13, 14]. The broad absorption band centred at 3440 cm^{-1} is assigned to O - H stretching vibration and that at 1630 cm^{-1} is attributable to H-O-H bending vibration of the adsorbed water molecules [3, 15]. The small peak located at 1378 cm^{-1} indicates the trace of CO_3^{2-} ions in the sample [13]. With the increase of calcination temperature, it can be observed that the intensity of the peaks of hydroxyl groups deteriorated and the peak of CO_3^{2-} ions at 1378 cm^{-1} almost disappeared. The broadening and shift of the IR peak to lower wavenumber on calcination may be due to particle size variation caused by the heat treatment.

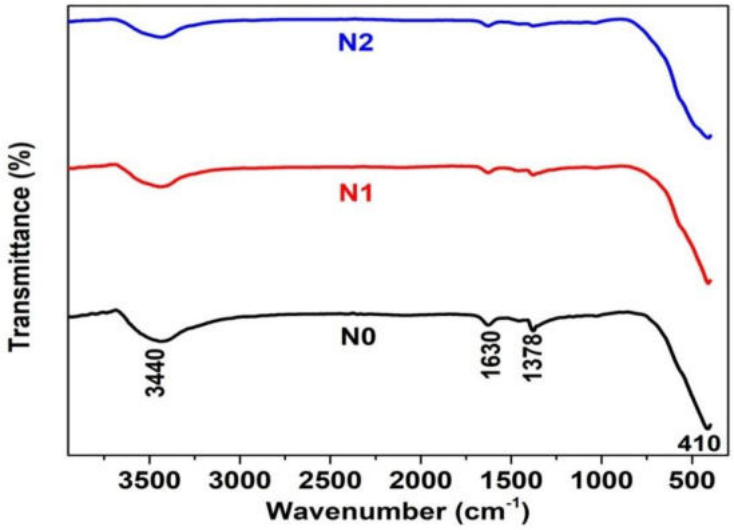

Figure 3.12 : FTIR spectra of NiO samples N0, N1 and N2

3.3.2.5 XPS Analysis

The XPS spectra of the sample N0 has been analysed to investigate the binding energy and oxidation state of the constituent elements. The full scan spectrum of NiO shown in Figure 3.13 a) indicates the characteristic peaks corresponding to nickel (Ni) and oxygen (O) in the sample. The high resolution spectra of nickel (Ni) and oxygen (O) are shown in Figure 3.13b) and c), respectively.

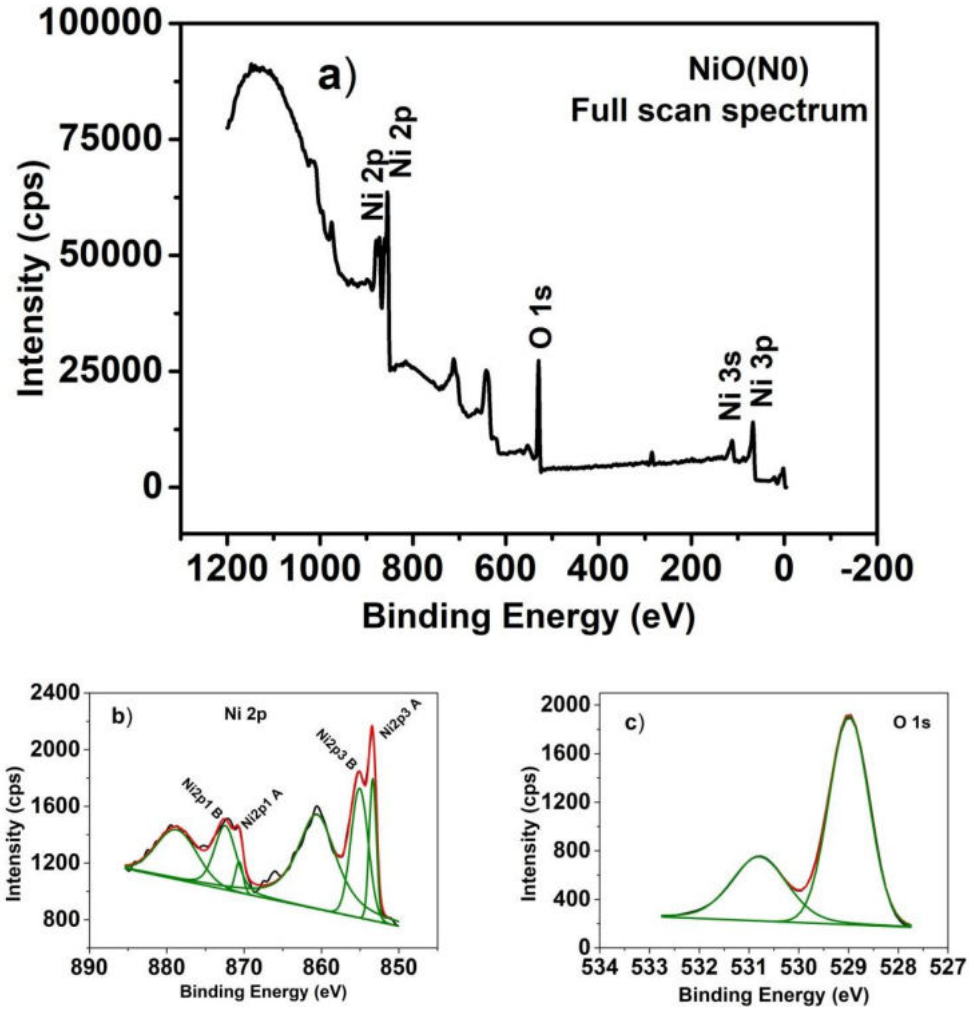

Figure 3.13 : XPS spectra of **(a)** NiO (wide scan), **(b)** Ni *2p* and **(c)** O *1s*

The Ni*2p* spectra are often complex and contain multiple peaks. The characteristic double peaks for $2p_{3/2}$ and $2p_{1/2}$ main lines are observed in the spectrum, which indicate the presence of traces of Ni^{3+} along with Ni^{2+} states [16, 17]. Non-stoichiometric NiO contains many Ni^{2+} vacancies, some of which are oxidised to Ni^{3+} in order to maintain charge neutrality near the Ni^{2+} vacancies. Hence, the Ni^{3+} state refer to a structure containing Ni^{2+} with a hole [18]. The peaks at binding energies

853.5 and 855.2 eV correspond to Ni$2p_{3/2}$A and Ni$2p_{3/2}$B and those at 870.8 and 872.1 eV to Ni$2p_{1/2}$A and Ni$2p_{1/2}$B respectively. Due to shake up process, the satellite peaks corresponding to Ni$2p_{3/2}$ and Ni$2p_{1/2}$ appear at 860.7and 878.8 eV respectively [19]. The high resolution O*1s* spectra can be resolved into two components at 528.9 and 530.8 eV. The high intense peak at 528.9 eV corresponds to O*1s* core level of the O^{2-} anions in the sample and the other represents oxygen ions in the oxygen deficient regions [20, 21]. The Ni*2p* and O*1s* spectra match well with the reported XPS peak positions and shapes. The elemental peak positions are compared with the standard peaks and are depicted in Table 3.4.

Table 3.4 : Binding energy positions for major peaks in the XPS spectra of sample N0

	Ni $2p_{3/2}$ (eV)	**Ni $2p_{1/2}$ (eV)**	**O *1s* (eV)**
Observed peak position	853.5	870.8	528.9
Standard elemental values [22]	852.6	869.9	529.4

3.3.3 Optical Properties

UV-Vis absorption spectroscopy and photoluminescence spectroscopy are the techniques employed to study the optical absorption and emission properties of the synthesized NiO nanoparticles. The analyses are carried out by following the procedure as given in *Section 2.5*.

3.3.3.1 UV-Visible Spectroscopy

UV-visible absorption spectra of NiO nanoparticles calcined at different temperatures are recorded in the wavelength range 200 – 800 nm. The absorbance is calculated from the transformation of reflectance data by the Kubelka–Munk function for diffused reflectance. Figure 3.14 shows the optical absorption spectra of the samples N0, N1 and N2. A strong absorption peak in the UV region at a wavelength of ~230 nm is observed for all samples which can be attributed to the bandgap absorption of NiO [23, 24]. The strong optical absorption between 4 and 6 eV correspond to the electronic transition from the valence band to the conduction band [24].

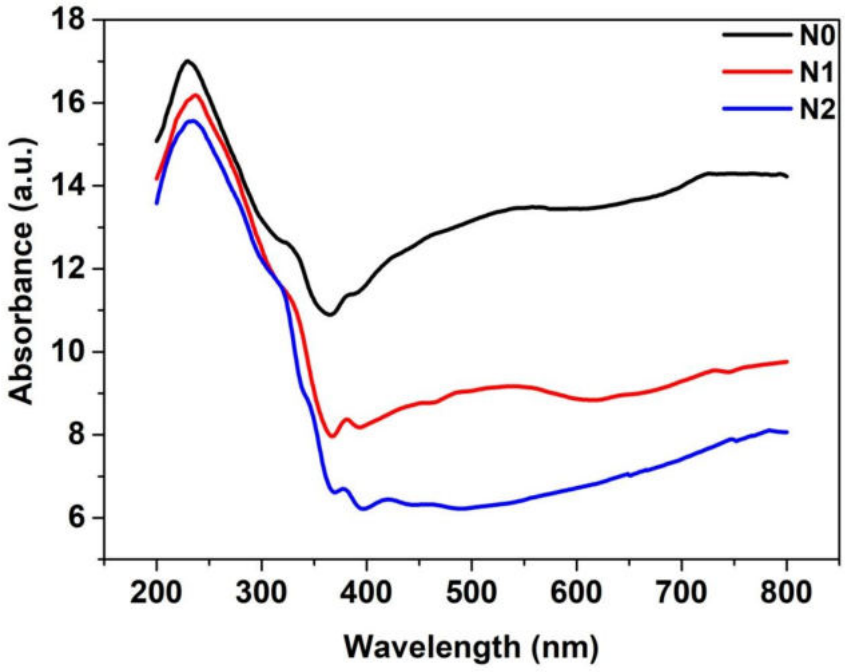

Figure 3.14 : Optical absorption spectra of NiO samples N0, N1 and N2

The absorption spectrum of sample N0 extends into the visible region which is due to the presence of excess oxygen in the lattice. This leads to the creation of Ni^{2+} vacancies and in order to acquire local charge neutrality, two Ni^{3+} ions are produced. This change in the oxidation state of Ni, which is consistent with the XPS measurement, is the reason for the featureless absorption in the visible region [25]. With an increase in calcination temperature, broad absorption in the visible region decreases which may be due to the change in stoichiometry as evident from the EDX data. The optical transitions in the lower energy range are related to the localized states in the forbidden energy gap. The small peak seen in the spectrum at 333 nm (3.73 eV) is purely intraionic $3d^8$ - $3d^8$ transition corresponding to the Ni^{2+} vacancies. The peak gets less pronounced in N1 and N2 due to the lower concentration of uncompensated Ni^{2+} vacancies [26].

The fundamental bandgap of the samples can be determined from the Tauc relation as discussed in Section 2.5. Figure 3.15 shows the $(\alpha h\nu)^2$ vs $h\nu$ graphs (Tauc plots) of N0, N1 and N2. The optical bandgap values obtained for samples N0, N1 and N2 are 3.72, 3.58 and 3.52 eV respectively. This decrease in bandgap energy with increase in particle size confirms the quantum size effect. The optical bandgap of NiO nanoparticles obtained in the present study is less than that of single crystalline NiO (~ 4eV) [27, 28]. This may be due to the chemical defects or vacancies present in the crystal generating new energy levels which reduce the bandgap energy [28]. This wide bandgap of NiO makes it serve as an electron blocking layer in polymer bulk heterojunction solar cells [29].

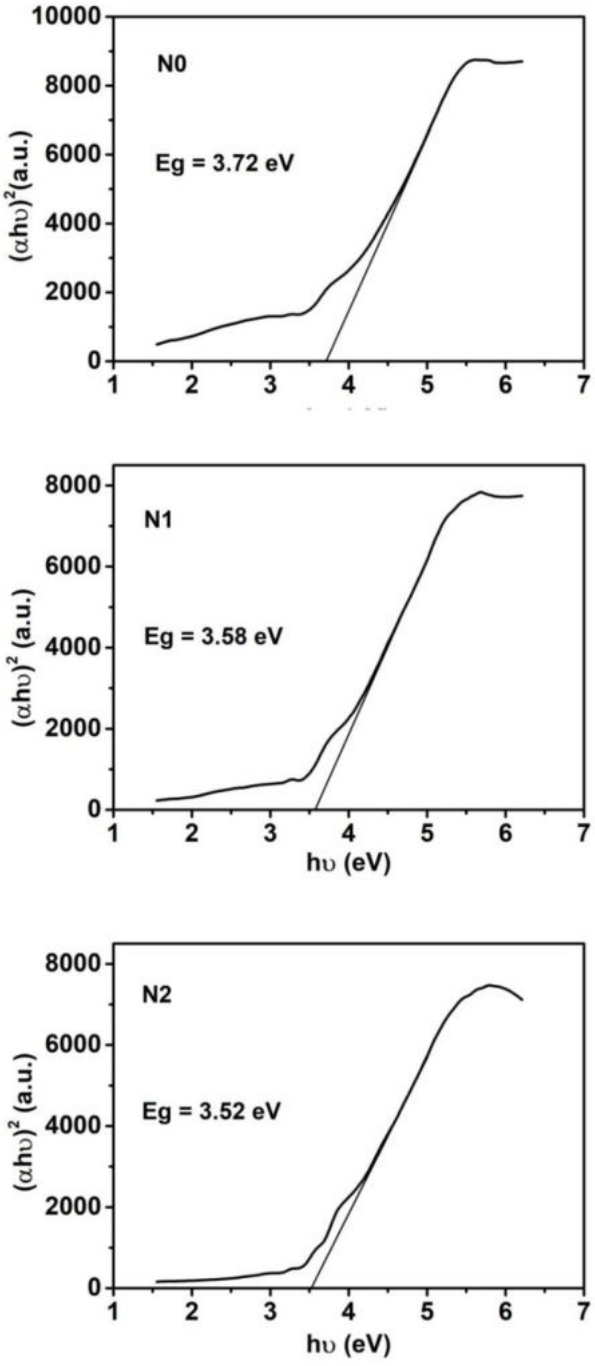

Figure 3.15 : Tauc plots of NiO samples N0, N1 and N2

3.3.3.2 PL Spectroscopy

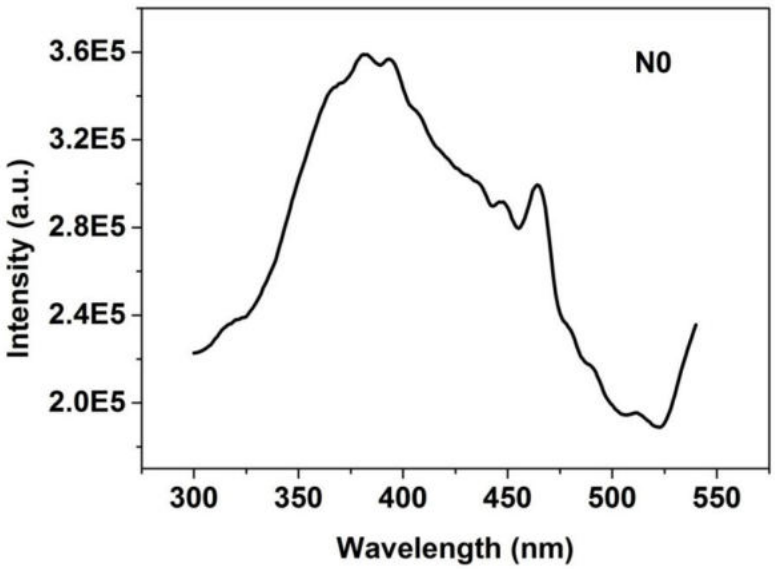

Figure 3.16 : PL emission spectrum of sample N0

The room temperature PL spectra of nanocrystalline NiO samples are measured using an excitation wavelength of 280 nm. Figure 3.16 shows the PL spectrum of sample N0. The wide range of emission extending from UV to visible region confirmed the highly defective nature of NiO nanoparticles [30]. Two peaks at 365 (3.4 eV) and 393 nm (3.16 eV) in the UV region with accompanying shoulder peaks at 448 nm (2.77 eV) and 465 nm (2.67 eV) in the visible region can be clearly seen. The emission in the UV region originated from excitonic recombination corresponding to the near band edge (NBE) transition of NiO, while the shoulder peaks in the visible region are attributed to defect related deep level emissions [31]. The first peak located at 3.4 eV is due to NBE emission and the peak at 3.16 eV is attributed to the electronic transitions of the Ni^{2+} ions from $^3A_{2g}$ to $^3T_{1g}(G)$ state [32]. The blue emissions

appearing at 448 nm (2.77 eV) and 465 nm (2.67 eV) result from the doubly ionized Ni vacancy (V_{Ni}^{2-}) of NiO nanoparticles [33].

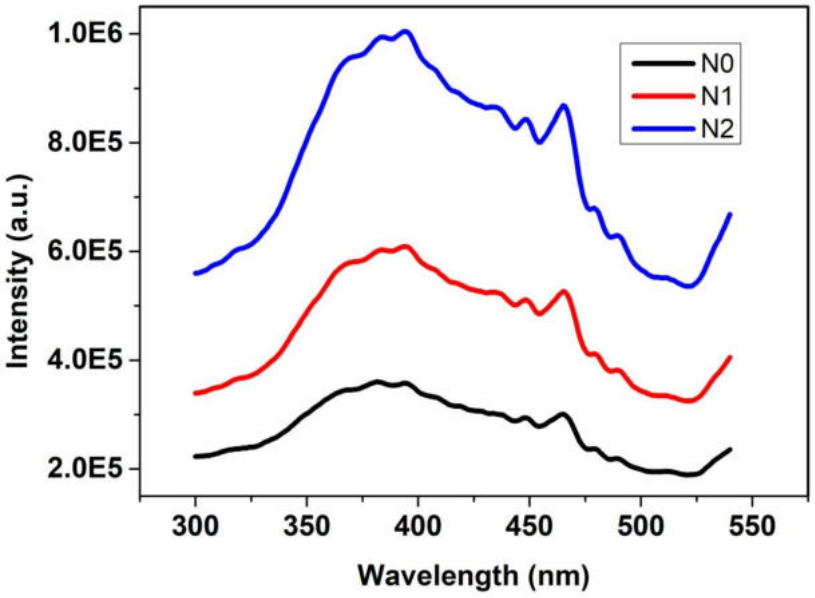

Figure 3.17 : PL emission spectra of NiO samples N0, N1 and N2

Figure 3.17 illustrates the PL emission spectra for N0, N1 and N2 samples at room temperature. All the samples exhibit similar type of PL spectra with no significant change in the curve shape. No shift in the peak positions is observed, indicating the relatively stable energy levels of excitons and surface states [34]. However, it can be seen that the emission intensity increases with calcination which indicates a reduction of non – radiative recombination effects. The increase in crystallite size with calcination results in a decrease of the surface-to-volume ratio, which in turn eliminates the luminescence quenching defects [35]. Also, the agglomeration of nanoparticles upon calcination leads to the passivation of surface states which act as non – radiative centres [36].

3.3.4 Electrical Properties

The electrical studies of the samples have been done by following the procedure given in *Section 2.6*. For this, the samples are consolidated in the form of cylindrical pellets of diameter 13 mm and thickness 1.5 mm by applying a pressure of 7 tons using a hydraulic press. Dielectric and AC conductivity measurements are carried out in the frequency range 50 Hz – 5 MHz using an impedance analyzer (*Wayne Kerr H-6500B model*). DC conductivity of the samples is recorded using *KEITHLEY 2450 Source Meter* in two probe method.

3.3.4.1D C Conductivity

The variation in DC conductivity (σ_{DC}) over the temperature range of 313-423 K for the samples N0, N1 and N2 is shown in Figure 3.18. The increase in electrical conductivity with temperature shows the semiconducting behaviour of all the samples. At 313 K, the values of σ_{DC} obtained for N0, N1 and N2 are 3.69×10^{-7}, 7.78×10^{-7} and 1.37×10^{-7} $ohm^{-1}m^{-1}$ respectively. At 423 K, the corresponding values are 3.05×10^{-5}, 6.35×10^{-5} and 2.08×10^{-5} $ohm^{-1}m^{-1}$ respectively. The charge carriers are thermally activated with increase in temperature, which increases their drift mobility and hence the conductivity. The DC conductivity values of all samples are much higher than that of NiO single crystals having apparent room temperature conductivity of 10^{-9}–$10^{-11}$$ohm^{-1}m^{-1}$[37]. The enhanced conductivity in NiO nanoparticles is due to the presence of a large number of Ni^{2+} vacancies on the surface [38]. The band structure of NiO consists of multiple valence band made up of 3d band of Ni^{2+} and 2p band of O^{2-}, and conduction band with a 4s band of Ni^{2+} and the 3s

band of O^{2-}. The Ni^{2+} vacancies in the sample correspond to an acceptor like level in the energy gap close to the Fermi level just above the localized 3d band of Ni^{2+} and the wide 2p band of O^{2-}. These vacancies in the lattice lead to the transformation of two adjacent Ni^{2+} ions into Ni^{3+} ions to acquire charge neutrality and induce distortion in the lattice. The created Ni^{3+} ions serve as acceptors that donate a hole into the lattice. If a 3d electron from an adjacent Ni^{2+} ion is transferred to a Ni^{3+} ion, a hole is created in the 3d band. This hole along with the associated lattice distortion constitutes a small polaron in the localized 3d band of Ni^{2+}. Also, a hole is created in the 2p band of O^{2-} ion when a 2p electron is transferred from a nearby O^{2-} ion to the Ni^{3+} ion. This hole along with the associated lattice distortion constitutes a large polaron in the 2p band of O^{2-}. As the number of Ni^{2+} vacancies in the sample increases, the number of small polarons in the localized 3d band of Ni^{2+} and the large polarons in the 2p band of O^{2-} increase, enhancing the conductivity [39, 40]. The dominant conduction mechanism in NiO in the temperature range of 200 – 1000 K is the band like conduction due to large polarons [40].

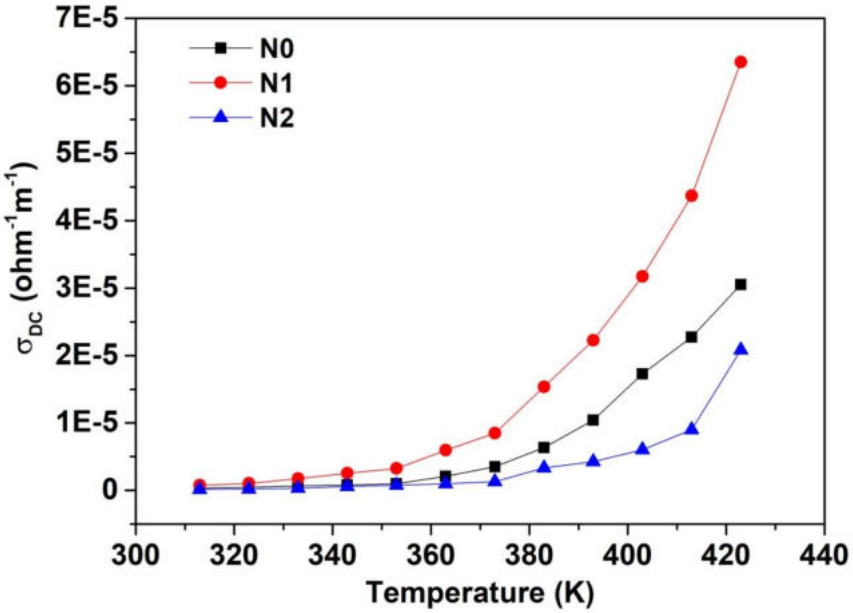

Figure 3.18 : Variation of DC conductivity with temperature of NiO samples N0, N1 and N2

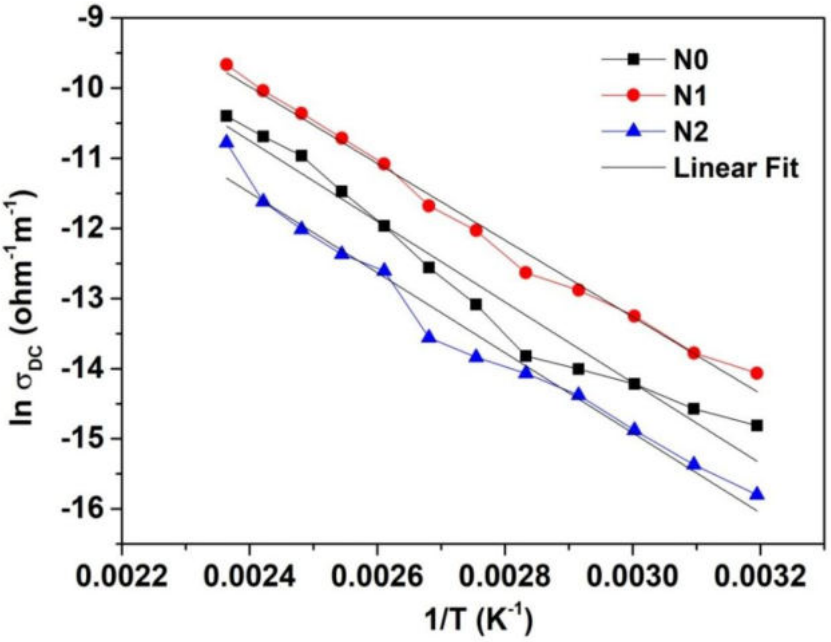

Figure 3.19: Arrhenius plots of NiO samples N0, N1 and N2

The conductivity first increases with an increase in calcination temperature from 400 (N0) to 500^{o}C (N1), thereafter it decreases. The result indicates the finite-size effect on the variation in DC conductivity of nanocrystalline NiO. In nanocrystalline materials with crystallite size less than 10 nm, the interfacial region composed of grain boundaries and triple junctions has an important role in deciding its transport properties [41, 42]. Triple junctions which are intersection lines of three or more adjoining crystallites can be viewed as line defects. Unlike grain boundaries, triple junctions act as a potential barrier, causing scattering of charge carriers and hence the decrease in conductivity [43]. The grain boundaries enhance conductivity in polycrystalline NiO as they contain a large number of Ni^{2+}vacancies [44]. The volume fraction associated with triple junction falls off sharply for crystallite size greater than 10 nm. This causes an enhanced conductivity for the sample N1. With further increase in size, the grain boundary per unit volume decreases which in turn decreases the number of Ni^{2+} vacancies, and hence the conductivity.

The activation energy is obtained by fitting the DC conductivity data with the Arrhenius equation:

$$\sigma_{dc} = \sigma_0 \exp(-Ea/k_B T) \qquad \textbf{(3.1)}$$

where σ_0 is the pre-exponential term, E_a is the activation energy, T is the absolute temperature of the sample and k_B is the Boltzmann's constant. The E_a values obtained from *ln* σ_{dc} vs (*1/T*) graphs (Figure 3.19) are 0.484, 0.472 and 0.493 eV for samples N0, N1 and N2, respectively. The values are much larger than the activation energy associated with

small polaron hopping which is of the order of 0.01 eV [45]. Hence the mechanism of conduction in NiO nanoparticles is Arrhenius type due to large polarons. But the observed activation energy is less than that of large polaron conduction in NiO single crystals (0.6 eV) due to the presence of a large number of Ni^{2+} vacancies [45]. With the increased number of Ni^{2+} vacancies, the acceptor like levels will move closer to the valence band, thus enhancing the probability of formation of polarons. Due to the increase in the number of polarons, the Fermi level falls below the normal value resulting in a decrease in activation energy [40]. Thus the defect chemistry plays a significant role in controlling the electrical properties of the material.

3.3.4.2 Dielectric Studies

Dielectric response of the samples is examined in the frequency range of 100 Hz–5 MHz at selected temperatures.

Dielectric Constant

The frequency dependence of dielectric constant ε′ of the samples at selected temperatures is discussed here. The numerical value of ε′ is of the order of $10^4 – 10^3$ in the low frequency regime. The high density of Ni^{2+} vacancies makes nanocrystalline NiO a dielectric material with a high concentration of hopping charge carriers. Such carrier dominated dielectrics are reported to have a very high value of dielectric constant [46, 47].

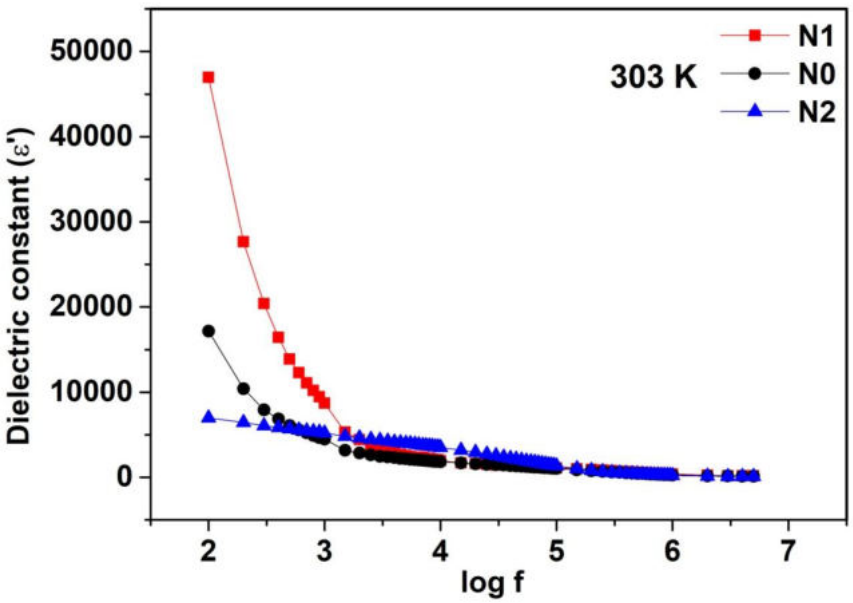

Figure 3.20 : Variation of dielectric constant (ε′) with frequency of NiO samples N0, N1 and N2 at 303 K

The variation of dielectric constant with frequency at room temperature for the samples N0, N1 and N2 is portrayed in Figure 3.20. The value of ε′ for N0, N1 and N2 are 8727, 4493 and 5219 respectively, at 1 kHz. The corresponding values at 1 MHz are 381, 224 and 281 respectively. The value of ε′ is very high in the low frequency region for all the samples, which decreases rapidly with increase in frequency and becomes almost constant at higher frequencies. The dielectric behaviour of nanostructured materials at low frequencies depends on the excitation of bound electrons, lattice vibrations, dipole orientation and space-charge polarization [48]. The dielectric dispersion curve can be described using Koop's theory [49], which is based on the Maxwell–Wagner model [50]. According to this model, the dielectric structure can be imagined as a

system consisting of grains which are highly conducting, separated by relatively resistive regions called grain boundaries. Under the influence of the electric field, localized accumulation of charges occurs at the grain boundaries which results in interfacial/space charge polarization. The conduction process in NiO is described by the correlated barrier hopping model (CBH) [51]. The CBH model suggests two types of carrier hopping in NiO, (i) Inter-well hopping: the hopping of a hole from a Ni^{3+} ion located in one defect potential well to a Ni^{2+} or O^{2-} ion in an adjacent defect potential well and (ii) Intra-well hopping: the hopping of holes between ions within one defect potential well. These holes on reaching the grain boundary get piled up due to its high resistivity, thereby producing space charge polarization. The sharp increase of ε' at low frequency is due to the space-charge polarization caused by impurities and crystal defects [52]. With an increase in frequency, the charge carriers contributing to polarization lag behind the applied field and hence results in a decrease in dielectric constant. Beyond a certain frequency, dipoles are unable to follow the alternating field and hence a frequency independent dielectric behaviour is noticed. The value of ε' of N1 is higher than that of N0, but falls rapidly for N2. The enhanced volume fraction of triple junctions in the interfacial region of N0 affects the polarization mechanism causing a decrease in its dielectric constant. Several factors like the disordered structure of the surface, surface energy and Ni^{2+} vacancy distribution can affect the dielectric constant [46].

The variation of dielectric constant with frequency for the sample N2 at different temperatures is depicted in Figure 3.21. It is observed that at any particular frequency the dielectric constant increases with increase in temperature. At 1 kHz of applied frequency, the dielectric constant of N2 is 5219, 5599 and 5889 for the temperatures 303, 333 and 363 K, respectively. The corresponding values at 1 MHz decrease to 221, 321 and 443 respectively. The variation of ε′ with temperature is more pronounced in the low frequency region, where the temperature dependent dipolar and space charge polarizations predominate. The other two samples also show the same behaviour.

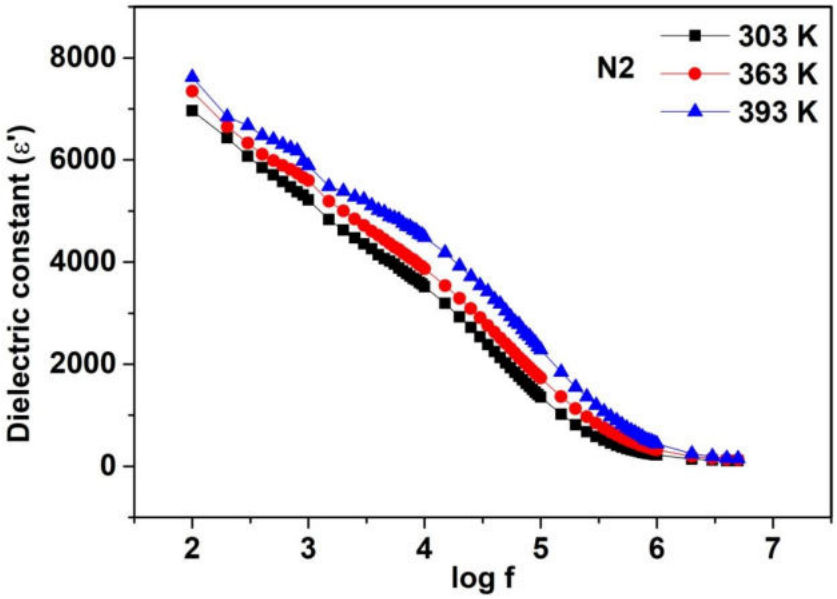

Figure 3.21 : Variation of dielectric constant (ε') with frequency of sample N2 at selected temperatures

High dielectric constant of NiO makes them suitable for the gate dielectric in metal oxide semiconductor field effect transistors. Transition metal oxides like NiO are high dielectric constant materials with the best resistive switching property which can be utilized for improving the performance of resistive random access memory [53].

Loss Tangent

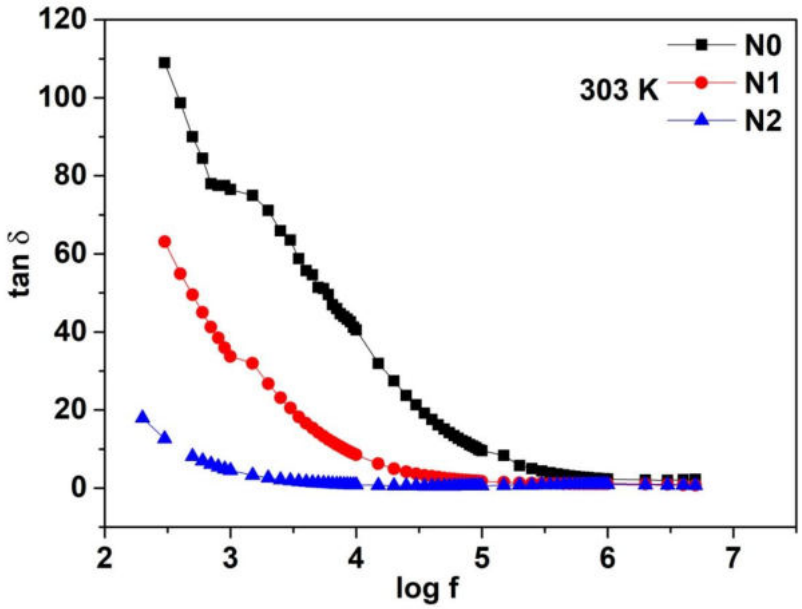

Figure 3.22 : Variation of tan δ with frequency of NiO samples N0, N1 and N2 at 303 K

Loss tangent (*tan δ*) represents the energy dissipation in the dielectric system. The variation of *tan δ* with frequency for the NiO samples N0, N1 and N2 at room temperature is shown in Figure 3.22. It decreases with increase in frequency and attains a constant value in the high frequency region for all samples. In nanomaterials, the absorption current produced due to impurities, defects and space charge formation in the interphase layers results in a dielectric loss [54]. The absorption current and hence the dielectric loss gets reduced as the applied frequency increases. With the increase in frequency, the response of dipoles to the changing field decreases and hence the loss tangent approaches a low value. The loss tangent is found to decrease with an increase in calcination temperature. The maximum value of loss tangent is observed for sample with the smallest crystallite size. With decrease in

crystallite size, the volume fraction of interfacial regions and grain boundaries, and the number of defects that contribute to dielectric loss might increase.

The variation of loss tangent of sample N2 as a function of frequency at selected temperatures is shown in Figure 3.23. The loss is found to get elevated with an increase in temperature. With an increase in temperature the hopping probability per unit time increases, which in turn increases the loss tangent. The surface electrons are captured by the impurity ions in the bulk crystal matrix leading to surface space charge polarization. The electron capture process increases with the increase in temperature which in turn enhances the loss tangent [55]. Similar behaviour is exhibited by the samples N0 and N1.

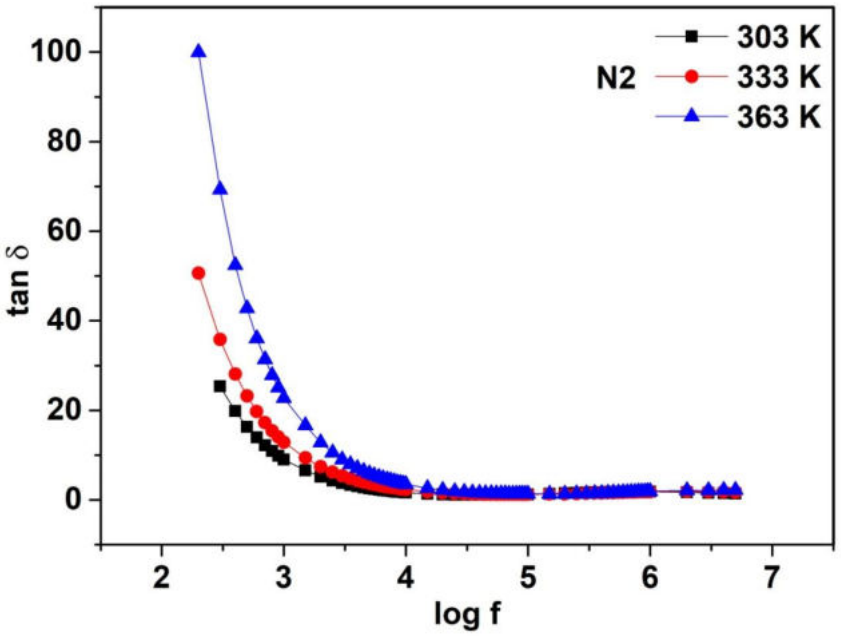

Figure 3.23 : Variation of tan δ with frequency of sample N2 at selected temperatures

It is observed that the loss tangent has a high value for all the samples. The dielectric loss is related to the conductivity of materials.

The material with lower resistivity would exhibit higher loss and vice versa.

3.3.4.3 Impedance Analysis

The complex impedance spectroscopy is a powerful tool for characterizing the electrical/dielectric properties of polycrystalline materials. The grain and grain boundary contributions to the overall impedance can be resolved using this technique. This is done by fitting the experimental response to that of an equivalent circuit using the software EIS Spectrum Analyser.

The Nyquist plots of the samples N0, N1 and N2 at room temperature and the corresponding equivalent circuit are shown in Figure 3.24. Two partially overlapping semicircular arcs are observed at all temperatures which represent two different relaxation mechanisms [56]. The arc at higher frequency represents the contribution of grains and the other in lower frequency is attributed to the grain boundary effects [57]. From the Nyquist plot, it is clear that both grain and grain boundaries are contributing to the electrical properties of NiO as presented by Maxwell Wagner model.

The data can be modelled with a circuit consisting of two parallel *R-CPE* (Constant Phase Element) circuits connected in series. CPE takes into account the frequency dispersion of the capacitance values and the spatial inhomogeneity of the system [58]. The impedance of CPE is of the form $Z_Q = 1/(j\omega)^{\beta}$CPE, where $0 < \beta < 1$. β is a measure of the capacitive nature of the component [56, 59]. Typical values of the parameters R, C and β, both for grain (R_g, CPE_g, β_g) and grain boundaries (R_{gb}, C_{gb}, β_{gb}) obtained from the fits are given in Table 3.5.

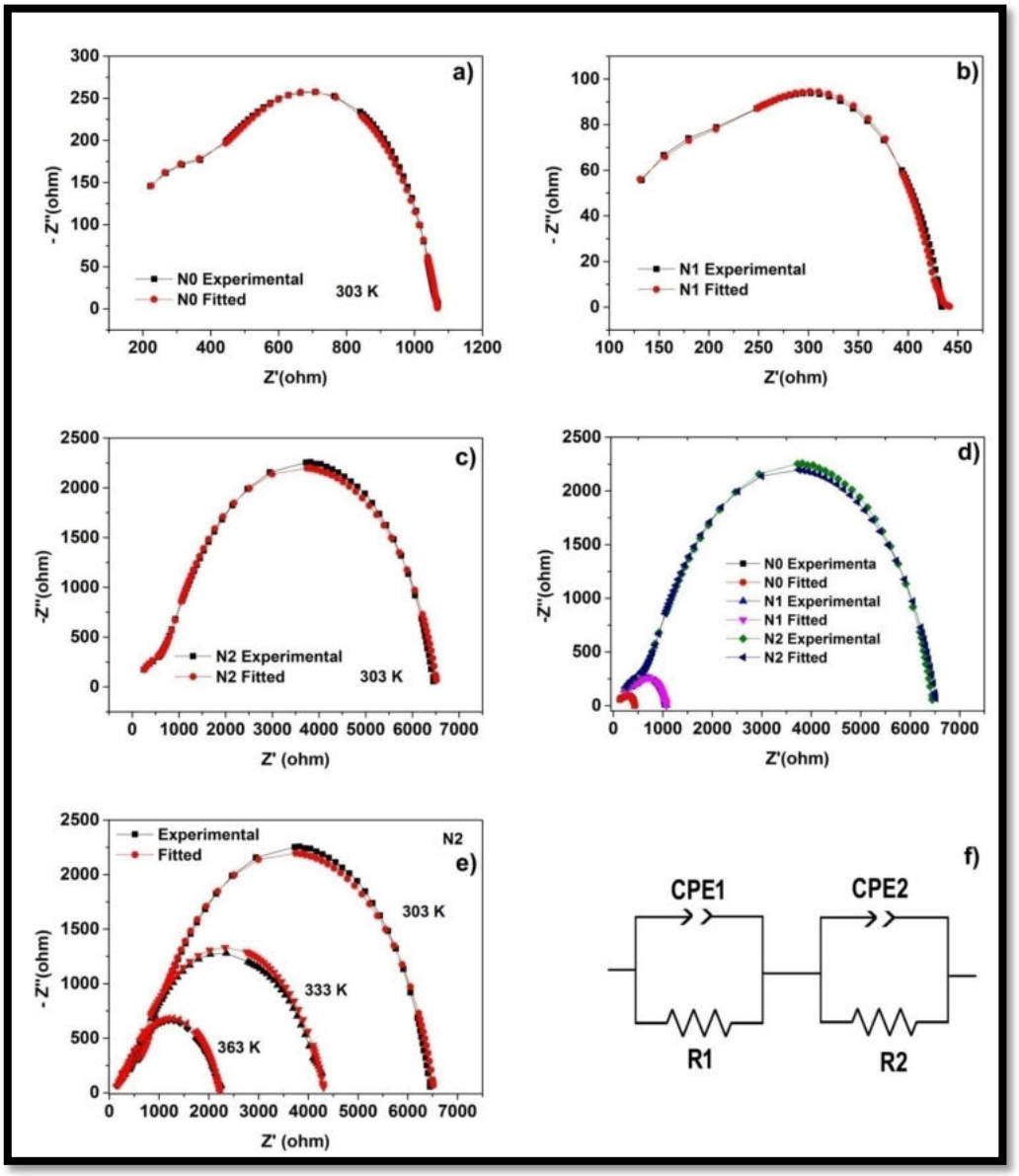

Figure 3.24: **(a – c)** Nyquist plots of NiO samples N0, N1 and N2 at 303 K, **(d)** combined plots of N0, N1 and N2 at 303 K, **(e)** Nyquist plot of N2 at selected temperatures and **(f)** equivalent circuit

Table 3.5 : Impedance parameters of NiO samples N0, N1 and N2 at 303 K

Sample	CPE_g (nF)	R_g (Ω)	β_g	CPE_{gb} (nF)	R_{gb} (Ω)	β_{gb}
N0	0.142	359	0.965	27.02	709	0.774
N1	0.129	195	0.991	34.01	238	0.797
N2	13.19	723	0.696	18.75	5813	0.821

The grain boundaries are found to be more capacitive and resistive than the grains for all the samples. The value of β (<1) confirms the non-Debye type of relaxation for all the samples. Figure 3.24(e) shows the Nyquist plot of the sample N2 at selected temperatures whose impedance parameters are presented in Table 3.6.

Table 3.6 : Impedance parameters of sample N2 at selected temperatures

Temperature	CPE_g (nF)	R_g (Ω)	β_g	CPE_{gb} (nF)	R_{gb} (Ω)	β_{gb}
303 K	13.190	724	0.696	18.750	5813	0.821
333 K	2.591	381	0.806	45.849	3948	0.754
363 K	1.548	247	0.848	51.596	1990	0.763

A decrease in the grain and grain boundary resistances with increase in temperature is observed in Table 3.6, which is due to the enhanced thermal movement of defects and charge carriers present in the grain interior and the boundary. This suggests an increase in conductivity with temperature which is a typical behaviour of semiconductors.

3.3.4.4 A C Conductivity

The variation of AC conductivity (σ_{AC}) with frequency of the applied field for the samples N0, N1 and N2 at 303 K is illustrated in Figure 3.25. The measured AC conductivity for all the samples is found to be much higher than that of single crystalline NiO which is of the order of 10^{-11} S/m at room temperature. At 10 KHz of applied frequency, the value of σ_{AC} at room temperature for the samples N0, N1 and N2 are 1.74×10^{-2}, 3.94×10^{-2} and 3.23×10^{-3} S/m respectively. The reason for this enhanced conductivity is the high density of Ni^{2+} vacancies present in the nanostructured NiO samples [60]. For all samples, σ_{AC} is found to be independent of the applied signal frequency up to about 50 kHz, while at higher frequencies, it shows an increasing trend. This frequency independent behaviour at lower frequencies indicates the dominance of DC conductivity in this region [61]. In the presence of an AC signal, both inter-well and intra-well charge transfer mechanisms suggested by CBH model have a finite probability of occurrence. Several factors like energy of the charge carriers, frequency of the applied signal, mean site separation, depth and extent of percolation of the potential wells associated with Ni^{2+} vacancies influence the relative probabilities of these hopping mechanisms. In the low frequency region, inter-well hopping which is responsible for DC conduction dominates intra-well hopping [62, 63]. However, as the signal frequency is increased intra-well hopping probability which contributes to AC conductivity increases. The pumping force that helps in transferring the charge carriers between the different localized states as well as liberating the trapped charges from the different trapping centres increases with frequency [52].

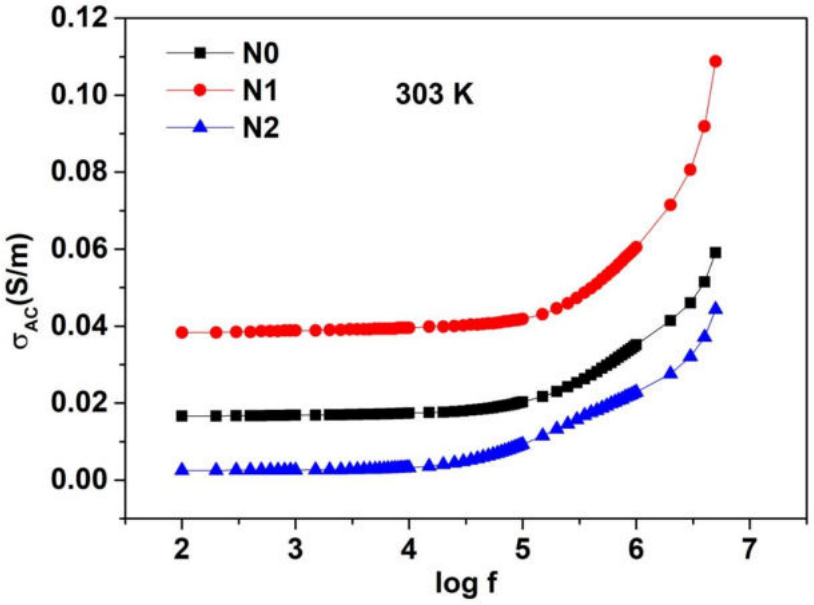

Figure 3.25 : Variation of σ_{AC} with frequency of NiO samples N0, N1 and N2 at 303 K

A convenient formalism to investigate the frequency dependence of conductivity is based on the power-law relation proposed by Jonscher [64, 65]. The measured AC conductivity (σ_{AC}) consists of two parts: a frequency independent DC component σ_{DC} (due to inter-well hopping) and a frequency dependent AC component $\sigma_{AC}(\omega)$ (due to intra-well hopping).

AC Conductivity, $\sigma_{AC} = \sigma_{DC} + \sigma_{AC}(\omega)$ **(3.2)**

The frequency dependence of AC conductivity can be described by Jonscher's power law,

$\sigma_{AC}(\omega) = A\omega^{s}$, **(3.3)**

where ω is the angular frequency of the applied AC field, and A and s are composition and temperature dependent parameters. The values of s determined for the samples N0, N1 and N2 at room temperature from the slope of log ω versus log σ_{AC} plots in Figure 3.26 are 0.27, 0.16 and 0.43 respectively. The results show that the value of s lies between 0 and 1 for all the samples and confirm the barrier hopping conduction mechanism in NiO [66].

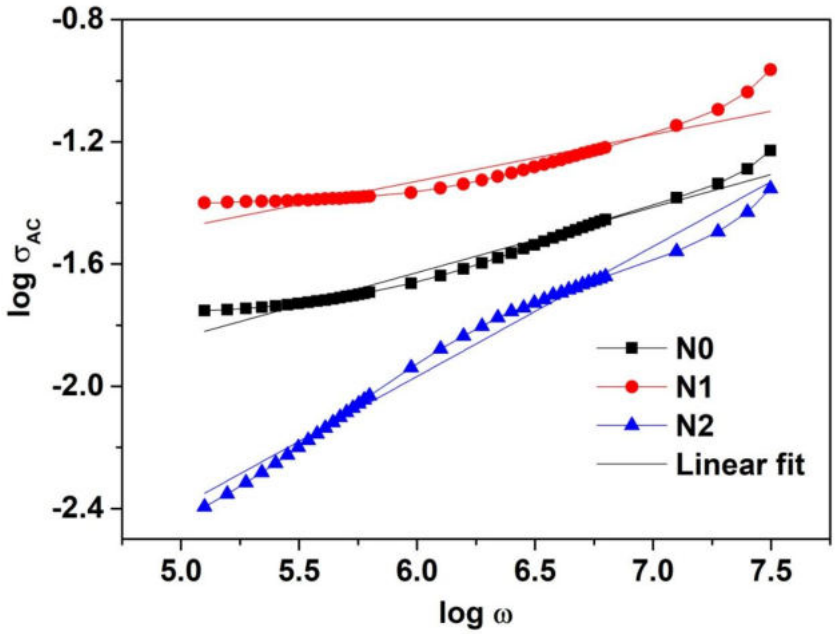

Figure 3.26 : Jonscher's power law plots of NiO samples N0, N1 and N2 at 303 K

It is found from Figure 3.25 that the AC conductivity first increases and then decreases with the increase in calcination temperature. As explained earlier, the variation in the structure of the interfacial region is the reason for the low value of AC conductivity for N0. As the grain boundaries and triple junctions have contrasting effects on conductivity, the value of σ_{AC} of NiO nanoparticles with size <10 nm

will be determined by the relative volume fractions of the grain boundaries and triple junctions constituting the interfacial region [60]. The decrease in σ_{AC} for N2 is due to the decrease in grain boundary density. According to the correlated barrier-hopping model, the AC conductivity,

$$\sigma_{AC} = \frac{\pi^3}{24} N^2 \varepsilon R_\omega^6 \omega, \qquad \textbf{(3.4)}$$

where N is the concentration of defect sites contributing to hopping mechanism, ε the dielectric permittivity and R_ω the hopping distance [67, 68]. Calcination increases the grain size and hence decreases the grain boundary density. This, in turn, decreases the value of N which contributes to the AC conductivity of the sample.

The variation of AC conductivity of sample N2 with frequency at three different temperatures is shown in Figure 3.27. The AC conductivity is found to increase with the increase in temperature. A similar variation is observed for other samples also. This increase in the conductivity with temperature is due to the increase in drift mobility of the charge carriers [69].

Figure 3.28 illustrates the Jonscher's power law plots of the sample N2 at different temperatures. The value of the frequency exponent*s* determined for the sample N2 from the slope of *log* ω versus *log* σ_{ac} plots are 0.42, 0.44 and 0.43 at temperatures 303, 333 and 363 K respectively. The values of *s* lie between zero and unity implying hopping to be the main conduction mechanism in the sample.

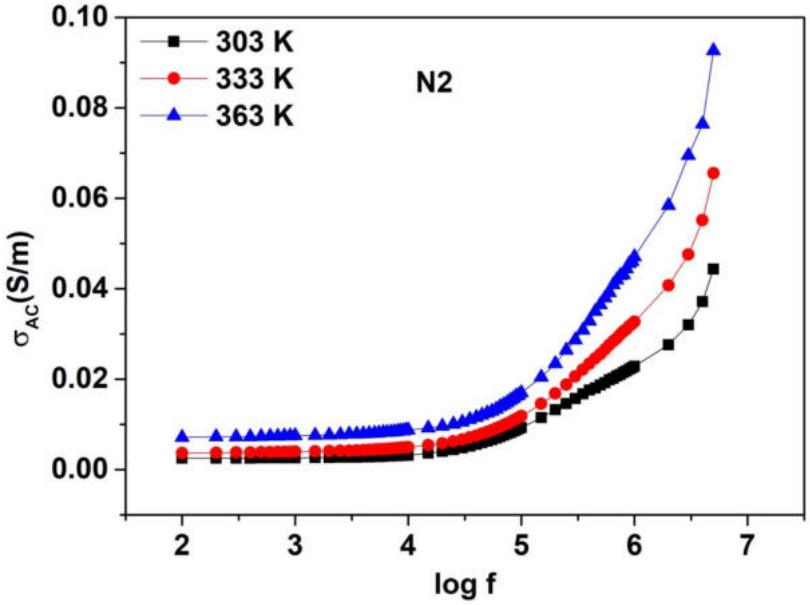

Figure 3.27: Variation of σ_{AC} with frequency of sample N2 at selected temperatures

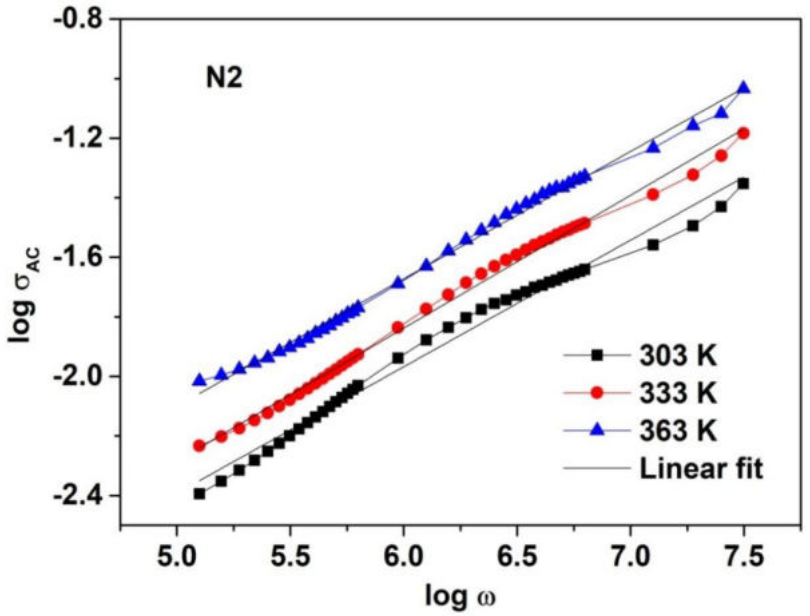

Figure 3.28: Jonscher's power law plots of sample N2 at selected temperatures

To summarise, the dielectric properties of NiO comply with Koop's theory of space charge polarization in accordance with the Maxwell–Wagner's two layer model. Two semicircles in the Nyquist plots confirm the grain and grain boundary contributions to the overall impedance. The transport properties of nanostructured NiO are strongly affected by the structure of the interfacial region.

3.3.5 Magnetic Properties

Magnetic studies of the samples have been carried out using Vibrating Sample Magnetometer (*Lakeshore VSM 7410*) as discussed in *Section 2.7*. To determine the field dependence of magnetization, M−H hysteresis curves are plotted at room temperature with a maximum applied field of ±1.5 T for NiO nanoparticles with different sizes as shown in Figure 3.29.

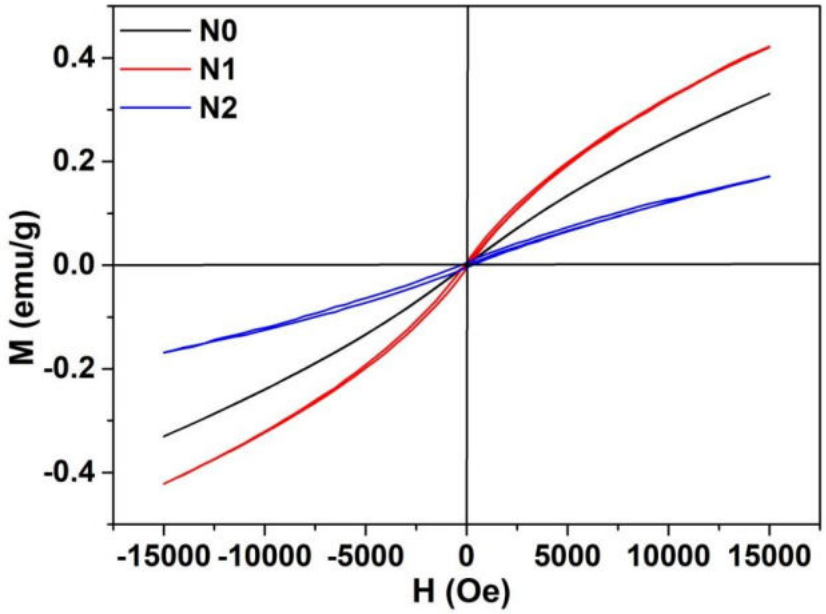

Figure 3.29: M – H curves of NiO samples N0, N1 and N2 at room temperature

The M-H curve for sample N0, with the smallest average crystallite size of 8.2 nm does not have any hysteresis and thus show the property of superparamagnetism with very low retentivity and coercivity. However, the samples N1 and N2 with an average size of 12.4 and 18.5 nm exhibit weak ferromagnetic behaviour with a small hysteresis loop and a low coercive field. The magnetization does not saturate at the highest field of 15 kOe for the samples, indicating the presence of superparamagnetic phase. Néel suggested that nanoparticles of an antiferromagnetic material will exhibit magnetic properties such as superparamagnetism and weak ferromagnetism [70]. Single crystalline NiO has a rhombohedral structure and is antiferromagnetic below the Neel temperature (573K) [71]. However, as the grain size is reduced, the surface to volume ratio becomes sufficiently large and the surface effects start to govern the magnetic properties. Because of the structural disorder, the surface spin can be more easily deviated from the antiferromagnetic alignment by a magnetic field. Then the uncompensated spins at the surface can create a non-zero net magnetic moment for the particles. As the particles can have varying size and shape, the magnetic moments will be of different size, and they get randomly oriented and interact with each other magnetically [72]. If the size of the grains is further reduced thermal fluctuations will also become an important factor which gives rise to superparamagnetism [73].

The variation in retentivity and coercivity as a function of grain size is depicted in Figure 3.30. The superparamagnetic behaviour is reflected in the very low values of coercivity and retentivity for the sample N0. When the particles reach the superparamagnetic size, the energy barrier separating the two energetically degenerate magnetic

orientations is small. The thermal activation is then sufficient to switch the magnetic orientation at any temperature. Hence, the coercivity is very small for superparamagnets [74]. With an increase in grain size, the coercivity starts rising as they exhibit ferromagnetic behaviour. This variation of coercivity with grain size can be explained on the basis of domain structure, critical diameter and the anisotropy of the crystal [75, 76]. For small values of grain size, the crystallites prefer to remain as a single domain. Coercivity is found to increase with increasing grain size until a maximum value is reached at the critical diameter corresponding to the transition stage from the single domain to the multi domain state [77]. The magnetic moment of the individual particle and the magnetic anisotropy energy increases with increase in size and therefore stronger field is required for demagnetization. The retentivity is also affected by the grain size. The value increases from a very low value (4.38×10^{-4} emu/g) for N0, which is superparamagnetic, to a maximum value of 6.17×10^{-3} emu/g for N1 and then decreases to 4.70×10^{-3} emu/g for N2. With an increase in grain size the number of grain boundaries decreases, thereby decreasing the structural defects and subsequently the value of retentivity [78]. Thus the magnetic response of nanostructured nickel oxide undergoes significant changes when the average grain size is reduced from 18.5 to 8.2 nm.

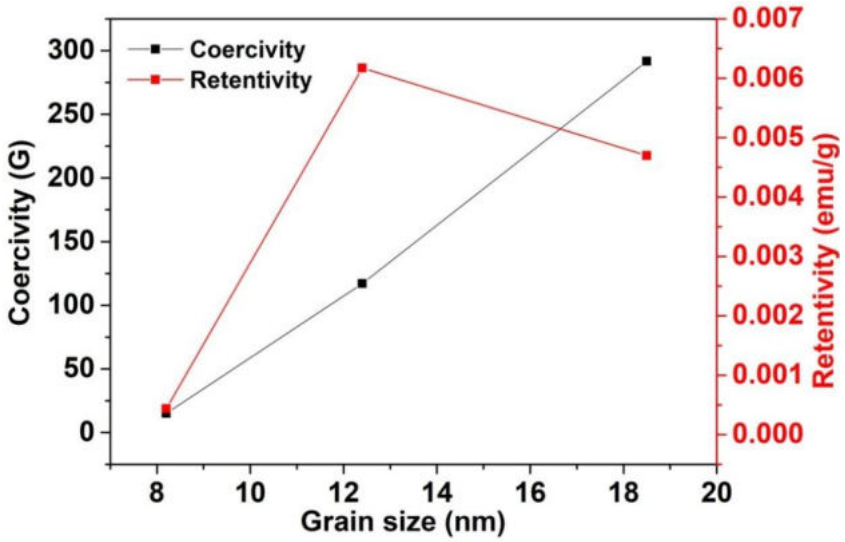

Figure 3.30 : Variation of magnetic parameters with grain size of NiO samples

3.4 Conclusion

- Nanocrystalline NiO in powder form has been successfully synthesized by chemical precipitation technique using nickel nitrate and ammonium carbonate.

- Thermal analysis shows that the complete decomposition of the precursor occurs around 400^{o}C to form nickel oxide.

- Structural characterization confirms the nanocrystalline nature and cubic bunsenite structure of the synthesized NiO.

- Effect of calcination on the structural, optical, electrical and magnetic properties of the synthesized samples is studied.

- The crystallite size of the sample is found to increase with an increase in calcination temperature, which results in slight lattice contraction.

- The UV-Visible absorption maximum for NiO is found in the ultraviolet region and a bandgap of 3.72 eV is obtained for the sample calcined at 400°C. The optical bandgap is found to decrease with an increase in calcination temperature due to the elevation in crystallite size caused by calcination.

- The PL emission in the UV region corresponds to the near band edge transition of NiO, while the shoulder peaks in the visible region are attributed to defect related deep level emissions.

- Grain size variation caused by the calcination exhibits a significant effect on the electrical properties of nanocrystalline NiO. The interfacial region consisting of grain boundaries and triple junctions has an important role in deciding the dielectric properties and conductivity of the samples.

- DC conductivity values of all samples are much higher than that of NiO single crystals due to the presence of a large number of Ni^{2+} vacancies on the surface. The dominant conduction mechanism in NiO is Arrhenius type due to large polarons.

- All the samples exhibit dielectric dispersion showing a decrease in dielectric constant with increase in frequency.

- The dielectric loss tangent is found to be decreasing with frequency and the sample with minimum particle size showed a large value of the dielectric loss at a specific frequency.

- Two semicircles in the Nyquist plots confirm the grain and grain boundary contributions to the overall impedance.

- AC conductivity first increases and then decreases with an increase in calcination temperature. The variation in the structure of the interfacial region is the reason for the low value of AC conductivity for the sample calcined at 400 °C.

- The magnetic response of nanostructured nickel oxide undergoes significant change upon calcination. With an increase in calcination temperature, the magnetic property of the sample undergoes a transition from superparamagnetic to a weak ferromagnetic state.

References

1) P. A. Sheena, K. P. Priyanka, N. A. Sabu, B. Sabu, T. Varghese, Nanosystems: Phys. Chem. Math., 5(2014) 441- 449
2) R. Newman, R.M. Chrenko, Phys. Rev., 114 (1959) 1507 - 1513
3) M. Alagiri, S. Ponnusamy, C.J. Muthamizhchelvam, J. Mater. Sci. - Mater. Electron., 23 (2012) 728 - 732
4) D.Y. Han, H.Y. Yang, C.B. Shen, X. Zhou, F.H. Wang, Powder Technol., 147 (2004) 113 - 116
5) T. Nathan, A. Aziz, A. F. Noor, S. R. S. Prabaharan, J. Solid State Electrochem., 12 (2008) 1003 - 1009
6) B.D. Cullity, S. R. Stock, Elements of X-ray Diffraction, 3rd Edn., Prentice Hall, New Jersey (2001)
7) I. Navas, R. Vinodkumar, K. J. Lethy, M. Satyanarayana, V. Ganeshan, V. P. Mahadevan Pillai, J. Nanosci. Nanotechnol., 9 (2009) 5254 - 5261
8) G. K Williamson, W. H Hall, Acta. Metall. 1(1953) 22 - 31
9) K. P. Priyanka, P. A. Sheena, N. A. Sabu, T. George, K. M. Balakrishna, T. Varghese, Ind. J. Phys., 88 (2014), 657- 663
10) I. Navas, R. Vinodkumar, K. J. Lethy, A. P. Detty, V. Ganesan, V. Sathe, V. P. Mahadevan Pillai, J. Phys. D: Appl. Phys.42 (2009) 175305
11) N. Mikova, I. Krusteva, G. Nikolov, J. Mol. Struct., 115 (1984) 23 - 26

12) A. S. Bhatt, D. K. Bhat, M. S. Santosh, C. Tai, J. Mater. Chem., 21 (2011) 13490 - 13497

13) L. Wu, Y. Wu, H. Wei, Y. Shi, C. Hu, Mater. Lett. 58 (2004) 2700 – 2703

14) D. N. Srivastava, V. G. Pol, O. Palchik, L. Zhang, J. C. Yu J, A. Gedanken, Ultrason. Sonochem. 12 (2005) 205 - 212

15) J. Li, R. Yan, B. Xiao, D.T. Liang, D.H. Lee, Energy & Fuels. 22 (2008) 16 - 23

16) K. S. Usha, R. Sivakumar, C. Sanjeeviraja, V. Sathe, V. Ganesan, T. Y. Wang, RSC Adv., 6 (2016) 79668 – 79680

17) M.A. van Veenendaal, G.A. Sawatzky, Phys. Rev. Lett. 70 (1993) 2459 - 2462

18) L. Cao, D. Wang, R. Wang, Mater. Lett. 132 (2014) 357 – 360

19) K. S. Kim, N. Winograd, Surf. Sci. 43 (1974) 625 - 643

20) B. Sasi, K.G. Gopchandran, Nanotechnology 18 (2007) 115613

21) T. V. Thi, A. K. Rai, J. Gim, J. Kim, J. Power Sources 292 (2015) 23 – 30

22) B. Vincent Crist, Handbook of Monochromatic XPS Spectra: The Elements of Native Oxides, XPS International, Inc. (1999)

23) X. Li, X. Zhang, Z. Li, Y. Qian, Solid State Commun.,137 (2006) 581 - 584

24) D. Adler, J. Feinleib, Phys. Rev. B., 2 (1970) 3112–3134.

25) A. Mendoza-Galvan, M. A. Vidales-Hurtado, A. M. Lopez Beltran, Thin Solid Films, 517 (2009) 3115–3120

26) G. Madhu, V. Biju, Physica E, 60 (2014) 200–205

27) P. Puspharajah, S. Radhakrishna, J. Mater. Sci., 32 (1997) 3001-3006

28) A. J. Varkey, A. F. Fort, Thin Solid Films, 235 (1993) 47-50

29) M. D. Irwin, D. B. Buchholz, A. W. Hains, R. P. H. Chang, T. J. Marks, PNAS, 105 (2008) 2783–2787, doi10.1073 pnas. 0711990105

30) S. M. Meybodi, S.A. Hosseini, M. Rezaee, S.K. Sadrnezhaad, D. Mohammadyani, Ultrason. Sonochem., 19 (2012) 841–845

31) B. Kisan, P.C. Shyni, S. Layek, H.C. Verma, D. Hesp, V. Dhanak, S. Krishnamurthy, A. Perumal, IEEE Trans. Magn., 50 (2014) 1–4.

32) V. V. Volkov, Z. L. Wang, B. S. Zou, Chem. Phys. Lett., 337 (2001)117–124

33) A. C. Gandhi, S. Y. Wu, Nanomaterials, 7 (2017) 231

34) J. Liqiang, Q. Yichun, W. Baiqi, L. Shudan, J. Baojiang, Y. Libin, F. Wei, F Honggang, S. Jiazhong, Sol. Energy Mater. Sol. Cells 90 (2006) 1773– 1787

35) R. Hari Krishna, B. M. Nagabhushana, H. Nagabhushana, N. Suriya Murthy, S. C. Sharma, C. Shivakumara, R. P. S. Chakradhar, J. Phys. Chem. C, 117 (2013) 1915−1924

36) S. Seto, S. Yamada, K. Suzuki, AIP Conference Proceedings 1583 (2014) 337 - 340

37) M. A. Wittenauer, L. L.Van Zandt, Philos. Mag. B, 46 (1982) 659 -667

38) M. Nachman, L. N. Cojocaru, L. V. Ribco, phys. stat. sol. 8 (1965) 773 - 783

39) D. Adler, J. Feinleib, Phys. Rev. B 2 (8) (1970) 3112–3134.

40) V. Biju, M. A. Khadar, Mater. Res. Bull., 36 (2001) 21 - 23

41) C. Suryanarayana, Bull. Mater. Sci., 17 (1994) 307 - 346

42) G. Palumbo, S. J. Thorpe, K. T. Aust, Scr. Metal. Mater., 22 (1990) 1347 - 1350

43) S. A. Makhlouf, M. A. Kassem, M. A. Abdel-Rahim, J. Mater. Sci., 44 (2009) 3438 - 3444

44) F.J. Morin, Phys. Rev. B, 93 (1954) 1199 - 1204

45) S.A. Makhlouf, Thin Solid Films 516 (2008) 3112–3116

46) V. Biju, M. A. Khadar, J. Mater. Sci., 38 (2003) 4055 – 4063

47) A. K. Jonscher, J. Mater. Sci. 13 (1978) 553 - 562

48) K. V. Rao, A. Smakula, J. Appl. Phys. 36 (1965) 2031-2038

49) C.G. Koops, Phys. Rev., 83, (1951)121

50) K.W. Wagner, Am. Phys., 40, (1973) 317

51) P. Lunkenheimer, A. Loidl, C.R. Ottermann, K. Bange, Phys. Rev., B 44, (1991) 5927 - 5930

52) A.M.M. Farea, S. Kumar, K. M. Batoo, A. Yousef, C. G. Lee, Alimuddin, J. Alloys Compd., 464 (2008) 361–369

53) P Mario Lanza, Materials**7** (2014) 2155

54) K.P. Priyanka, J. Sunny, T. Smitha, E.M. Mohammed, T. Varghese, J. Basic Appl. Phys. 2 (2010) 105

55) S. A. Ansari, A. Nisar, B. Fatma, W. Khan, M. Chaman, A. Azam, A.H. Naqvi, Mater. Res. Bull., 47 (2012) 4161 - 4168

56) A. Singh, R.Chatterjee, S. K. Mishra, P. S. R. Krishna,S. L. Chaplot, J. Appl. Phys. 111 (2012) 014113

57) B. Gokul, P. Matheswaran, K. M. Abhirami, R. Sathyamoorthy, Journal of Non-Crystalline Solids 363 (2013) 161–166

58) L. D. Sappia, M. R.Trujillo, I. Lorite, R. E. Madrid, M. Tirado, D. Comedi, P. Esquinazi, Mater. Sci. Eng. B. 200 (2015)124

59) V. Varade, G.V. Honnavar, P Anjaneyulu, K P Ramesh, R. Menon, J. Phys. D: Appl. Phys., 46 (2013) 365306

60) V. Biju, M. Abdul Khadar, J. Mater. Sci. 36 (2001) 5779 – 5787

61) M. Sayer, A. Mansingh, J. B. Webb, J. Noad, J. Phys. C. Solid. State. Phys. 11 (1978) 315

62) A. J .Bosman, H. J.Van Daal, Adv. Phys.19(77) (1970) 1

63) S. A. Gad, M. Boshta , A. M. Abo El-Soud, M. Z. Mostafa, Fizika A 18 (2009) 173–184

64) A.K. Jonscher, Dielectric Relaxation in Solids (Chelsea Dielectric Press, London, 1983)

65) A.K. Jonscher, Universal Relaxation Law (Chelsea Dielectrics Press, London, 1996)

66) A. R. Long, Adv. Phys., 31 (1982) 553

67) B. Viswanathan, V.R.K. Murthy, Ferrite Materials, Science and Technology (New Delhi : Narosa Publishing House,1990)

68) M. George, S. S. Nair, K. A.Malini, P. A. Joy, M. R.Anantharaman, J. Phys. D: Appl. Phys. 40(2007) 1593

69) R. Nongjai, S. Khan, K. Asokan, H. Ahmed, I. Khan, J. Appl. Phys. 112(2012) 084321

70) L. Néel, Low Temp. Phys., edited by C. Dewitt et al. (Gordon and Beach, New York, 1962) p.413

71) J. S. Smart, S. Greenwald, Phys. Rev. 82 (1951) 113

72) S. D. Tiwari, K. P. Rajeev, Phys. Rev. B 72, 104433

73) A.G. Kolhatkar, A. C. Jamison, D. Litvinov, R. C. Willson, T. R. Lee, Int. J. Mol. Sci. 14(2013) 15977-16009; doi:10.3390/ ijms140815977

74) S. Roy, I. Dubenko, D.D. Edorh, N. Ali, J. Appl. Phys.96 (2004) 1202

75) M. George, A. M. John, S. S. Nair, P.A. Joy, M.R. Anantharaman, J. Magn. Magn. Mater. 302 (2006) 190–195

76) B.D. Cullity, Introduction to Magnetic Materials, Addison-Wesely Publishing Company Inc, Reading, MA, 1972

77) M. Sajjia, A. Baroutaji, A.G. Olabi, Reference Module in Materials Science and Materials Engineering 2017, doi.org/10.1016/B978-0-12-803581-8.09264-X

78) S. B.Waje, M.Hashim, W. D. W.Yusoff, Z. Abbas, J. Magn. Magn. Mater. 322 (2010) 686–691

…..ꕥ…..

Chapter 4

EFFECT OF COBALT DOPING ON THE PROPERTIES OF NICKEL OXIDE NANOPARTICLES

This chapter focuses on the modification in the structural, optical, electrical and magnetic properties of nickel oxide nanoparticles due to cobalt (Co) doping. NiO nanoparticles doped with 1, 3, 5 and 10 mol % of cobalt are prepared by chemical co-precipitation method and characterized using various characterization techniques.

4.1 Introduction

Doping is the primary technique used to modify the properties of nanostructured semiconductors and to obtain new materials of technological importance. The high solubility and abundant electron states make cobalt (Co^{2+}) a promising dopant in NiO systems [1]. As cobalt is a good luminescence activator, it can also modify the emission properties of NiO [2]. Both, nickel oxide and cobalt oxide have rock salt structure with lattice parameters 4.195 and 4.261 Å, respectively. Also, the crystal ionic radius of Ni (0.69 Å) closely matches with that of Co (0.74 Å) [3]. Hence NiO can be doped with a relatively high amount of cobalt without causing much lattice strain. A systematic and detailed study of the structural, optical, electrical and magnetic properties of Co^{2+} doped NiO nanoparticles synthesized by chemical precipitation method is presented here. The tuning of bandgap and PL intensity has been achieved by cobalt doping of suitable concentrations, which makes NiO nanoparticles competent for various optoelectronic applications.

4.2 Synthesis of Cobalt Doped NiO Nanoparticles

The reagents used for the synthesis of cobalt doped nickel oxide nanoparticles are nickel nitrate hexahydrate (Ni $(NO_3)_2 \cdot 6H_2O$, 99.8%, Sigma Aldrich), ammonium carbonate ($(NH_4)_2CO_3$, 99.9%, Merck) and cobalt nitrate hexahydrate (Co $(NO_3)_2.6H_2O$, 99.8%, Sigma Aldrich).

NiO nanoparticles doped with 1, 3, 5 and 10 mol % of cobalt are prepared by chemical co-precipitation method. The required weighed mol % of Co $(NO_3)_2.6H_2O$ and Ni $(NO_3)_2 \cdot 6H_2O$ are dissolved in distilled

water using magnetic stirring to make 0.1 M solution. The carbonate precursor is chemically precipitated by slowly adding 0.1 M aqueous solution of ammonium carbonate [$(NH_4)_2CO_3$] at room temperature under magnetic stirring for 30 min. The precipitate is allowed to settle down overnight and then washed with distilled water several times to remove the unreacted salts and impurities. Finally, the precipitate is filtered and dried in a hot air oven at 70^oC for 18 h. The dried product obtained is powdered and calcined at 400^oC for 3 h in a muffle furnace to obtain Co^{2+} doped NiO nanoparticles. NiO nanoparticles doped with 1, 3, 5 and 10 mol % of cobalt are denoted as Co1, Co3, Co5 and Co10 respectively. N0 represents the pristine NiO sample.

4.3 Results and Discussion

The structural, optical, electrical and magnetic characterizations of the samples are done using various techniques as described in *Chapter 2*.

4.3.1 Structural Characterization

The structural analyses of the synthesized samples have been carried out using powder X-ray diffraction, Fourier transform infrared spectroscopy, Field enhanced scanning electron microscopy, Transmission electron microscopy and Energy dispersive X-ray analysis , by following the procedure described in *Section 2.4.*

4.3.1.1 Powder XRD Analysis

The powder X-ray diffraction patterns of pure and Co doped NiO nanoparticles are shown in Figure 4.1. All the diffraction peaks of both pristine and doped samples are well indexed and exactly matched with the standard JCPDS Card no. (73-1519). All patterns exhibit a cubic structure with a preferential orientation along (200) plane without any additional impurity phase, indicating that the structure is not affected by Co substitution. The peaks corresponding to (111), (200), (220), (311), and (222) planes confirmed the formation of face-centred cubic (fcc) structure with space group *Fm3m*. For all dopant concentrations, no evidence of secondary phases or phases other than that of NiO is found which indicates that the Co gets substituted at the Ni site without changing the cubic structure. Only a slight shift in the diffraction peaks is observed in the doped samples which confirm substitutional doping. In addition, a decrease in the intensity of diffraction peaks is observed with an increase in doping concentration, indicating degradation of crystallinity and a decrease in crystal symmetry due to lattice distortion. This suggests an increase in micro-strain due to disorder in the crystalline structure with cobalt doping [4]. The broadening of peaks indicates a reduction in grain size on doping with cobalt.

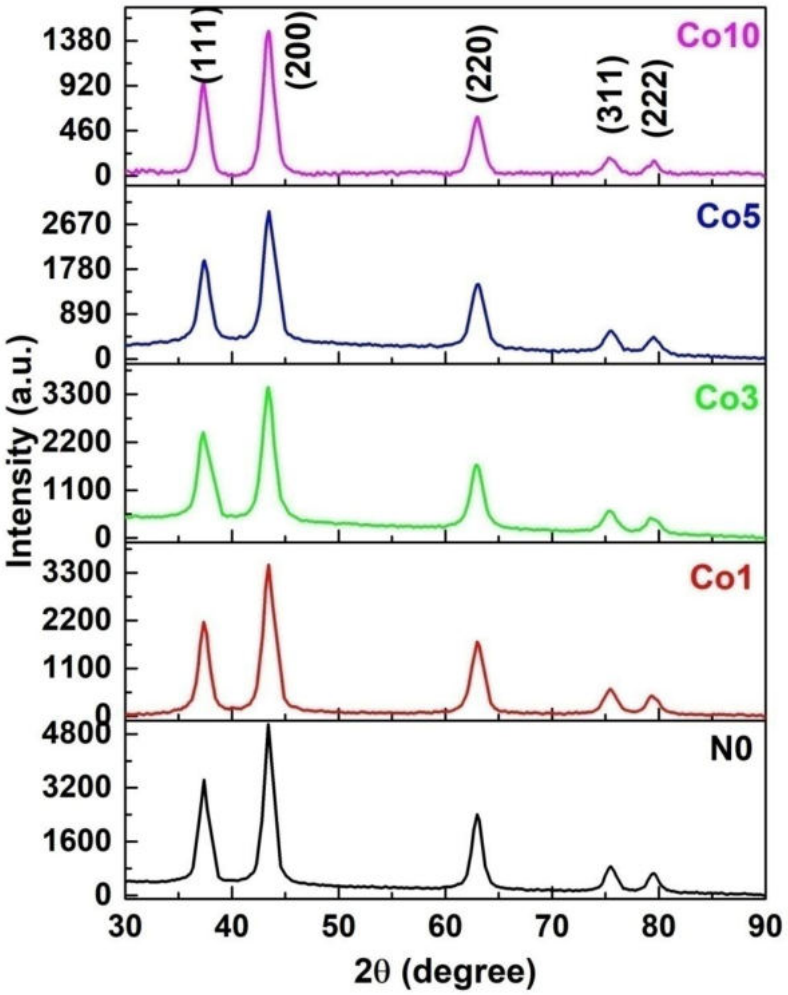

Figure 4.1 : XRD patterns of pristine and Co doped NiO samples

The structural parameters of the samples calculated from XRD data are presented in Table 4.1. The average crystallite sizes of the samples calculated using Scherrer equation *(Section 2.4.1)* are found to be 9.7, 7.7, 7, 7.5 and 8.2 nm respectively for N0, Co1, Co3, Co5 and Co10 samples. The crystallite size is found to decrease with increase in doping concentration up to 3 mol %, but shows an increasing trend thereafter. This indicates that for lower doping concentrations, filling up

of Ni^{2+} vacancies with the dopant ions and substitutional replacement of Ni^{2+} ions with Co^{2+} may occur. However at higher doping levels, the dopant ions enter into the interstitial sites of NiO lattice [5]. Furthermore, the lattice parameters and cell volume slightly decrease with the increase in Co content. This suggests complete incorporation of Co ions into the NiO lattice.

Table 4.1: Structural parameters of pristine and Co doped NiO nanoparticles from XRD data

Sample	Average crystallite size (nm)	Lattice spacing d_{200} (Å)	Lattice constant a (Å)	Unit cell volume ($Å^3$)
N0	9.7 ± 0.19	2.0897	4.1794	73.003
Co1	7.7 ± 0.15	2.0895	4.1790	72.982
Co3	7 ± 0.14	2.0894	4.1788	72.972
Co5	7.5 ± 0.15	2.0890	4.1780	72.930
Co10	8.2 ± 0.16	2.0866	4.1732	72.679

The contributions of size (D) and micro-strain (ε) to XRD line broadening are calculated using the procedures described by Williamson and Hall [6]. W-H plots for the pristine and doped samples are shown in Figure 4.2. The crystallite size and micro-strain obtained from the W-H analysis are presented in Table 4.2. The crystallite size estimated from Williamson-Hall plot matches with that calculated using the Scherrer equation. The micro-strain is less for Co1 and Co3 samples compared to

the pristine one, which is due to the proper substitution of Ni^{2+} with Co^{2+} ions. The comparatively large values of micro-strain for the Co5 and Co10 samples confirm the increase in imperfections due to the interstitial incorporation of cobalt ions into the NiO lattice.

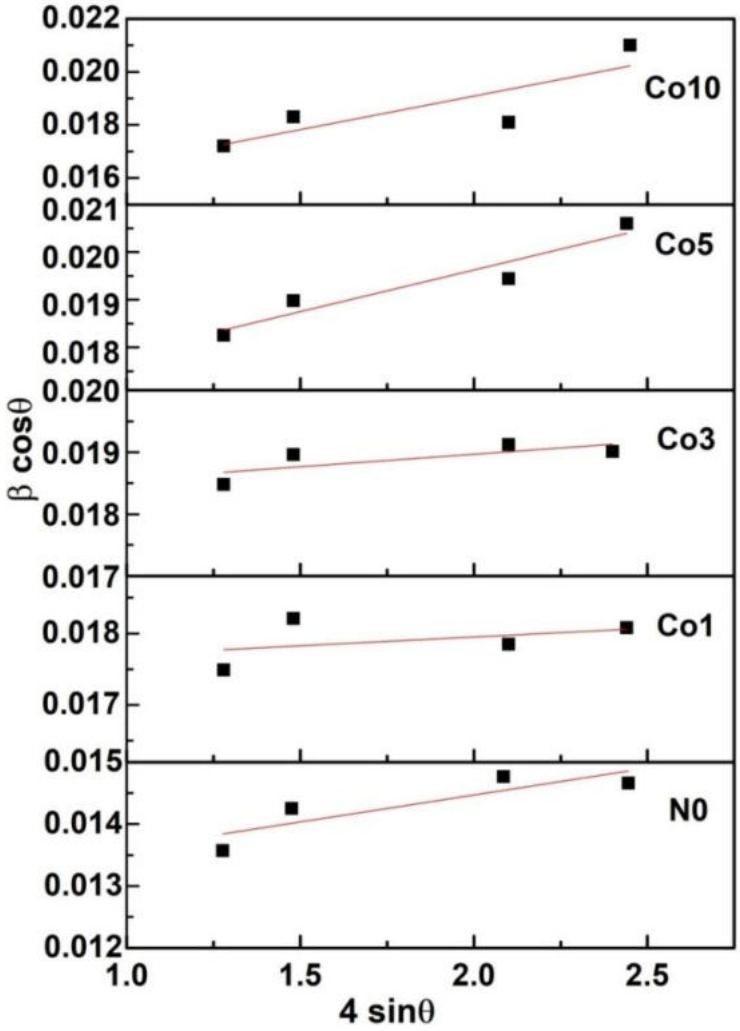

Figure 4.2 : W – H plots of pristine and Co doped NiO samples

Table 4.2 : Structural parameters of pristine and Co doped NiO samples from W-H plot

Sample	Crystallite size (nm)	Micro-strain
N0	10.6±0.212	8.690x 10^{-4}
Co1	7.90±0.158	2.454x 10^{-4}
Co3	7.55±0.151	4.035x 10^{-4}
Co5	8.50±0.170	17.51x 10^{-4}
Co10	9.80±0.196	25.30x 10^{-4}

In short, XRD studies reveal a reduction in crystallite size with Co doping, without affecting the structure of NiO. No dopant phase is introduced into the host structure up to 10% of doping.

4.3.1.2 FESEM and EDX Analyses

Figure 4.3 shows the FESEM images of pristine and cobalt doped NiO samples. No change in morphology is observed for the doped samples. The micrographs show aggregates of smaller individual nanoparticles of non-spherical shape. The chemical compositions of the synthesized NiO nanoparticles doped with different Co concentrations measured by EDX analysis are shown in Figure 4.4. The patterns confirm the presence of nickel, oxygen and cobalt as the only elementary species in the sample. Hence the synthesized materials are pure and without any contamination. The results of EDX analysis match with the doping percentage and is presented in Table 4.3.

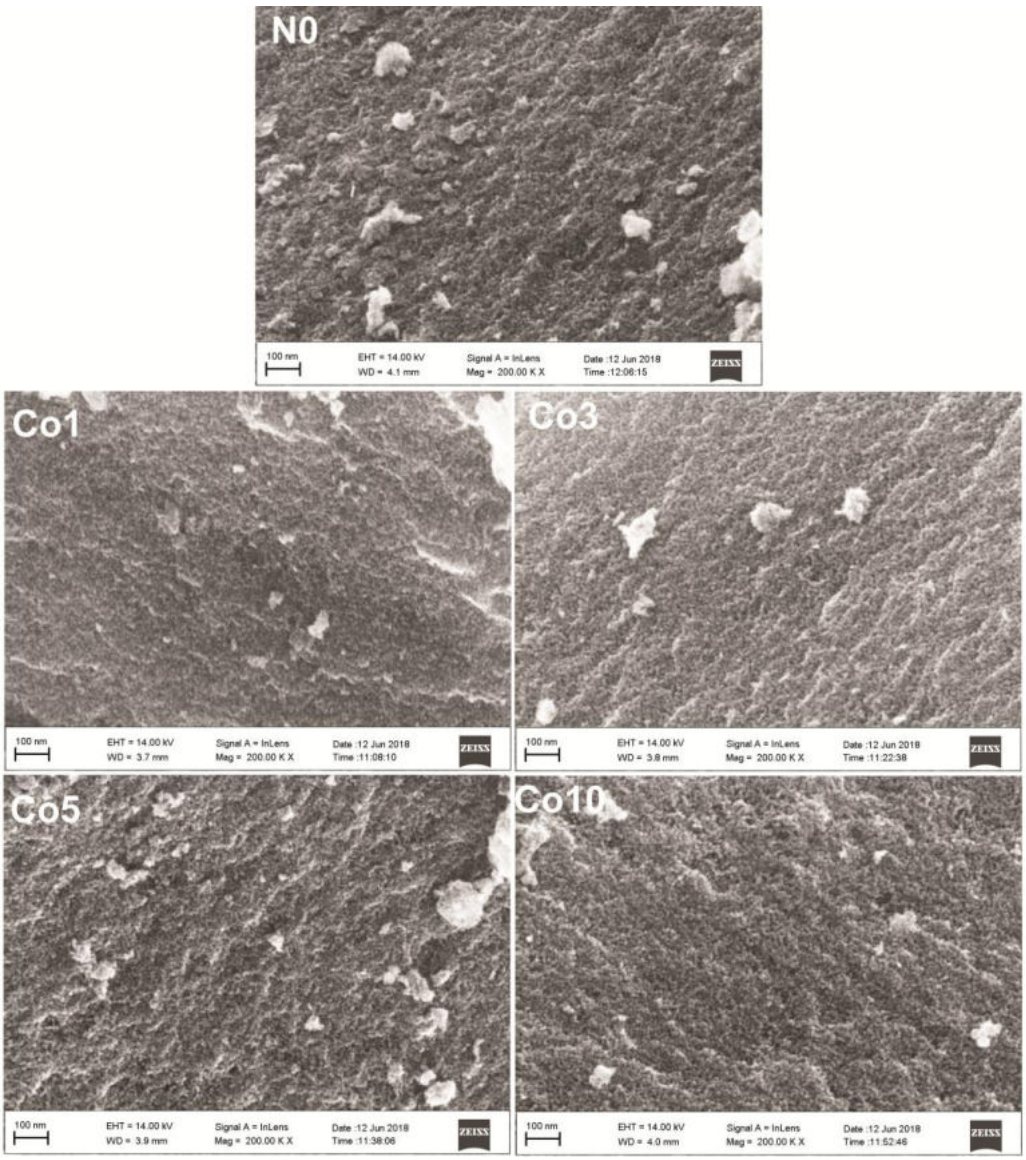

Figure 4.3 : FESEM images of pristine and Co doped NiO samples

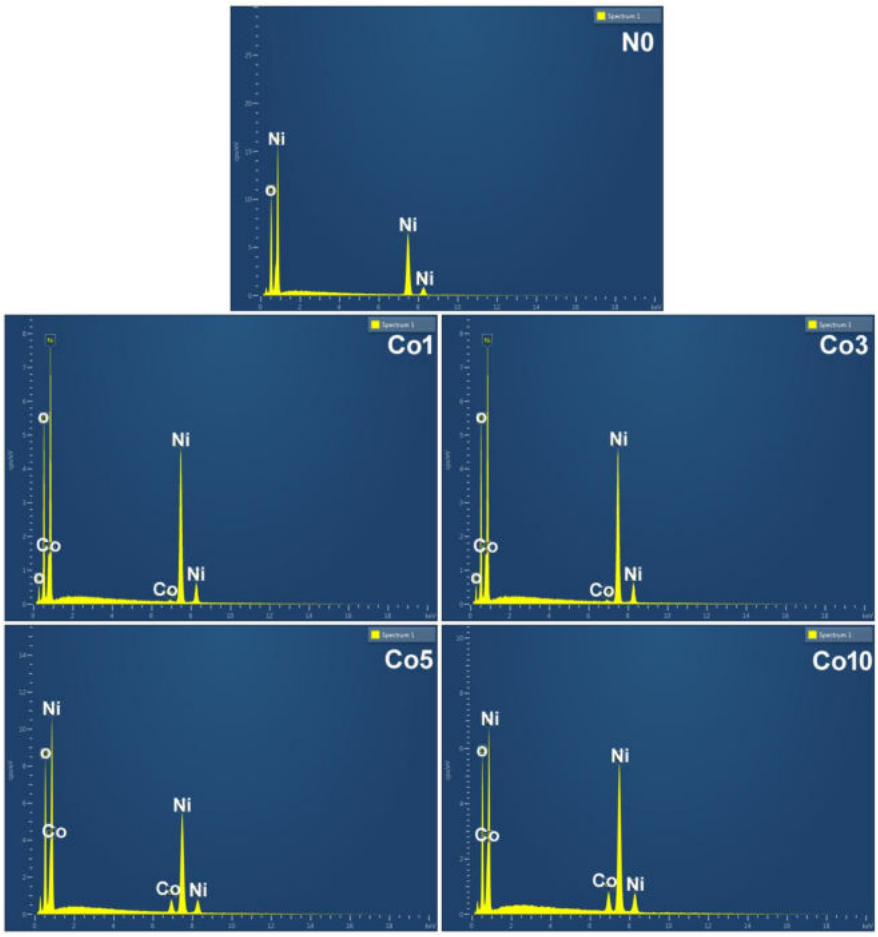

Figure 4.4 : EDX patterns of pristine and Co doped NiO samples

Table 4.3 : EDX data of pristine and Co doped NiO samples

Sample	Atomic percentage		
	Ni	O	Co
N0	39.25	60.75	0
Co1	40.97	58.43	0.6
Co3	61.52	36.26	2.22
Co5	52.01	44.20	3.79
Co10	48.57	43.89	7.54

4.3.1.3 TEM Analysis

TEM analysis is done to further elucidate morphological features, particle size, crystallinity and lattice spacing of pure and Co doped NiO nanoparticles samples. TEM bright field images, HRTEM images and SAED patterns of pristine and Co doped samples are portrayed in Figure 4.5. The decrease in size upon Co doping is evident from the bright field images. TEM images reveal the non spherical shape of the particles. The particle size for the pristine sample varies in the range 9 – 16 nm. This size decreases to 7 – 11 nm for Co1, 5 – 9 nm for Co3, 8 – 11 nm for Co5 and 6 – 11 nm for Co10. HRTEM images show fringe patterns for all the samples. SAED patterns of all samples show clear spots arranged in a ring shape corresponding to different planes of NiO. The patterns confirm the crystalline nature and phase purity of the samples. Table 4.4 gives the structural parameters obtained from TEM images. The decrease in d - spacing may be due to size reduction caused by doping.

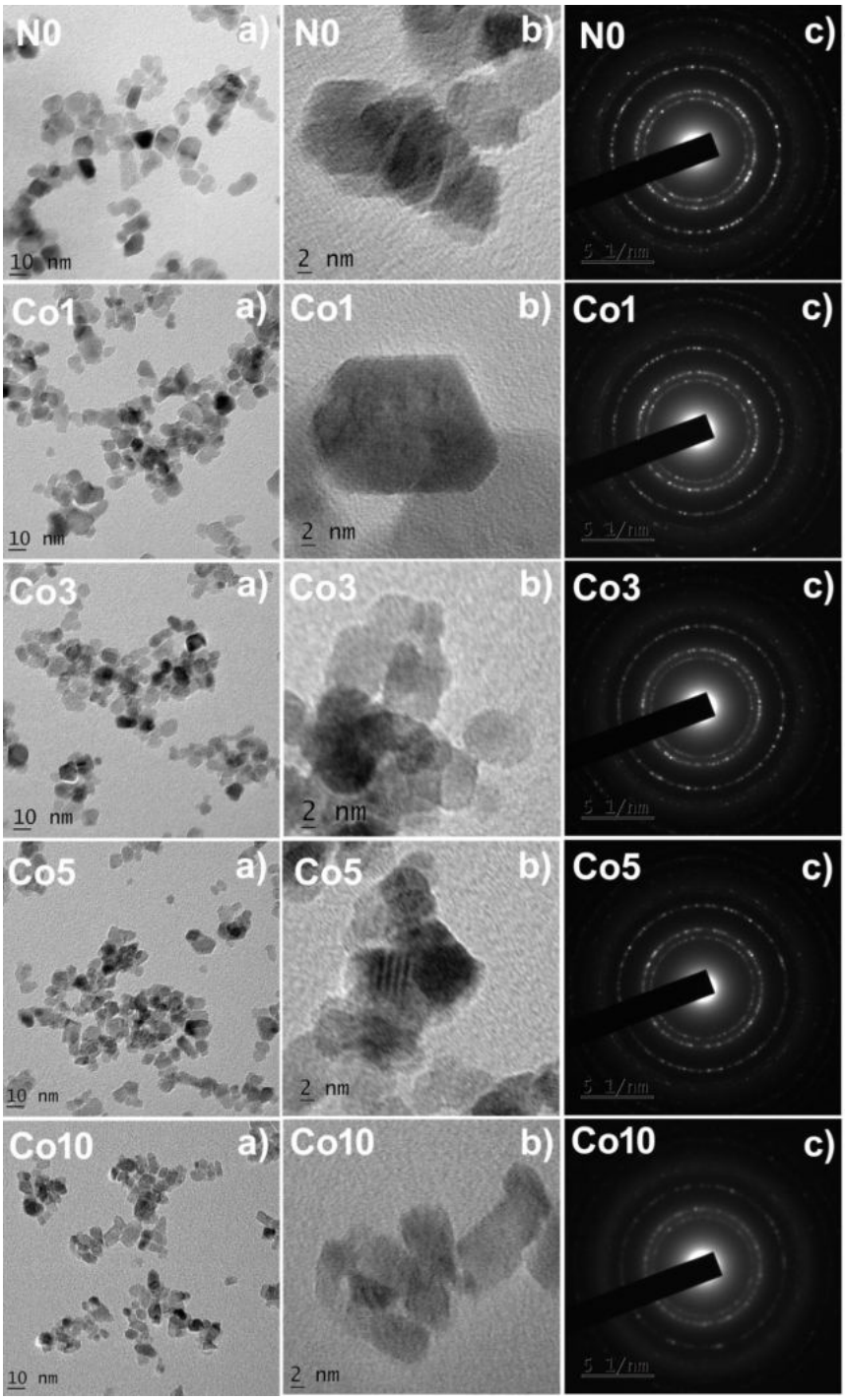

Figure 4.5 : **(a)** TEM bright field images, **(b)** HRTEM images and **(c)** SAED patterns of pristine and Co doped NiO samples

Table 4.4 : Structural parameters of pristine and Co doped NiO samples from TEM images

Sample	Average particle size from TEM images (nm)	d spacing from HRTEM images (nm)	d spacing from SAED patterns (Å)		
			(111)	(200)	(220)
N0	11.4±0.23	0.21 (200)	2.856	2.463	1.745
Co1	9.9±0.20	0.21(200)	2.841	2.462	1.742
Co3	8.1±0.16	0.17 (220)	2.857	2.435	1.740
Co5	9.5±0.19	0.16 (220)	2.834	2.418	1.730
Co10	9.0±0.18	0.21(200)	2.790	2.410	1.719

4.3.1.4 FTIR Spectroscopy

In order to understand the chemical bonds and molecular structure of the samples, FTIR spectra are recorded. Figure 4.6 shows the FTIR spectra of pure and Co doped NiO samples in the range 400 to 4000 cm^{-1}. An almost same spectrum is obtained for all the samples. The infrared absorption band centred at 415 cm^{-1} is assigned to Ni–O stretching vibration mode [7]. The broad absorption band centered at 3427 cm^{-1} is assigned to O-H stretching vibration and the band at 1630 cm^{-1} is attributed to H-O-H bending vibration mode [8, 9]. The sharp peak located at 1383 cm-1 indicates the trace of CO_3^{2-} ions in the sample [10]. No additional absorption peaks are observed in the spectrum with the addition of Co, which indicates the homogeneous dispersion of the dopant in the host material. This is in accordance with the XRD results.

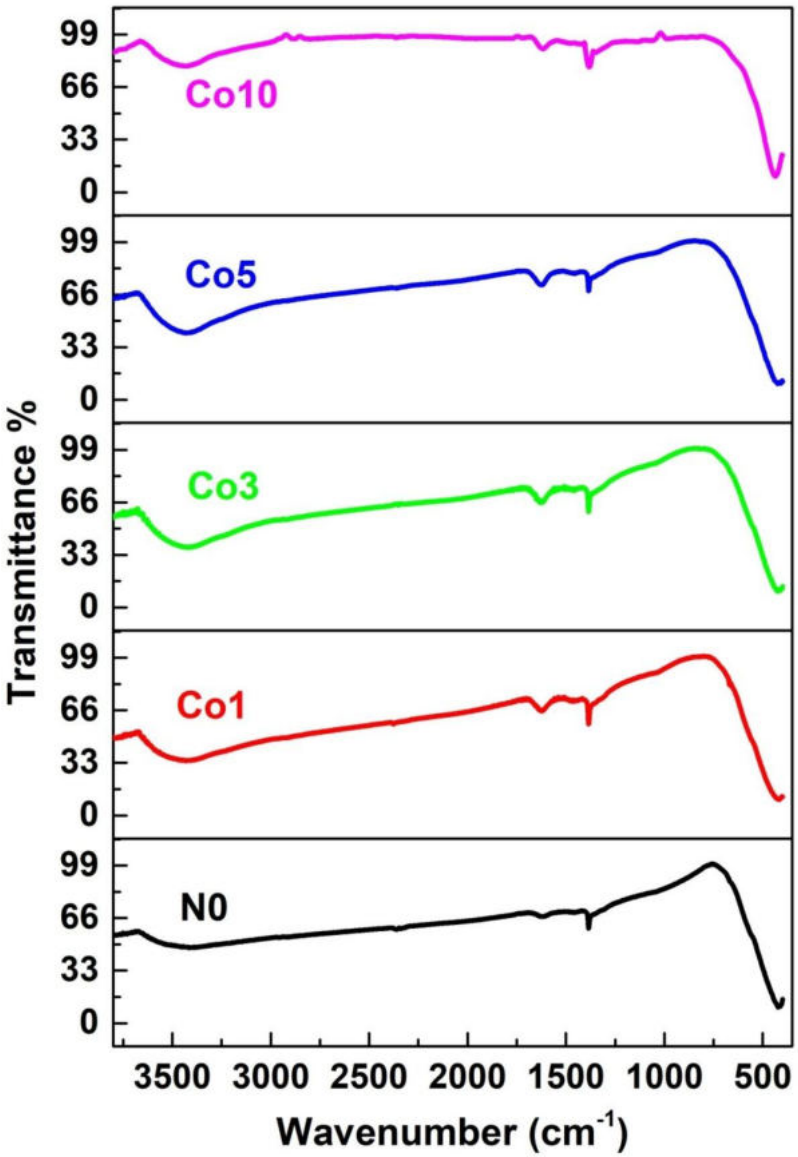

Figure 4.6: FTIR spectra of pristine and Co doped NiO samples

4.3.1.5 XPS Analysis

XPS analysis aims to examine the binding energy and oxidation states of the constituent ions present in the sample. The XPS wide spectrum of a typical sample of Co doped NiO is shown in Figure 4.7(a). The characteristic peaks corresponding to Ni, O and Co are observed in the spectrum. Figure 4.7 (b-d) shows the core level spectrum of Ni, O and Co respectively in the sample. Similar to the pristine NiO, the Ni *2p* spectrum of the doped sample also exhibits the characteristic double peaks for $2p_{3/2}$ and $2p_{1/2}$ main lines. The peaks at binding energies 853.4 and 855.2 eV correspond to Ni$2p_{3/2}$A and Ni$2p_{3/2}$B and those at 870.9 and 873.5 eV to Ni$2p_{1/2}$A and Ni$2p_{1/2}$B respectively. The double peak structure is ascribed to the presence of Ni^{2+} and Ni^{3+} states for the lower and higher binding energies respectively, as discussed in *Section 3.3.2.5* [11, 12]. The satellite peaks due to shake up process appear at 860.7 eV (Ni$2p_{3/2}$) and 878.8 eV (Ni$2p_{1/2}$) [13]. The high resolution O*1s* spectra can be resolved into two components at 529 and 530.9 eV, which corresponds to O*1s* core level of the O^{2-} anions in the sample and oxygen ions in the oxygen deficient regions respectively [12, 13]. In the spectrum of cobalt, two peaks at binding energies 777.8 and 792.95 eV corresponding to Co$2p_{3/2}$ and Co$2p_{1/2}$ respectively are seen, which match with the standard values [14]. These energy states with a difference of 15.2 eV confirm the presence of Co^{2+} ions in the sample [13, 15].

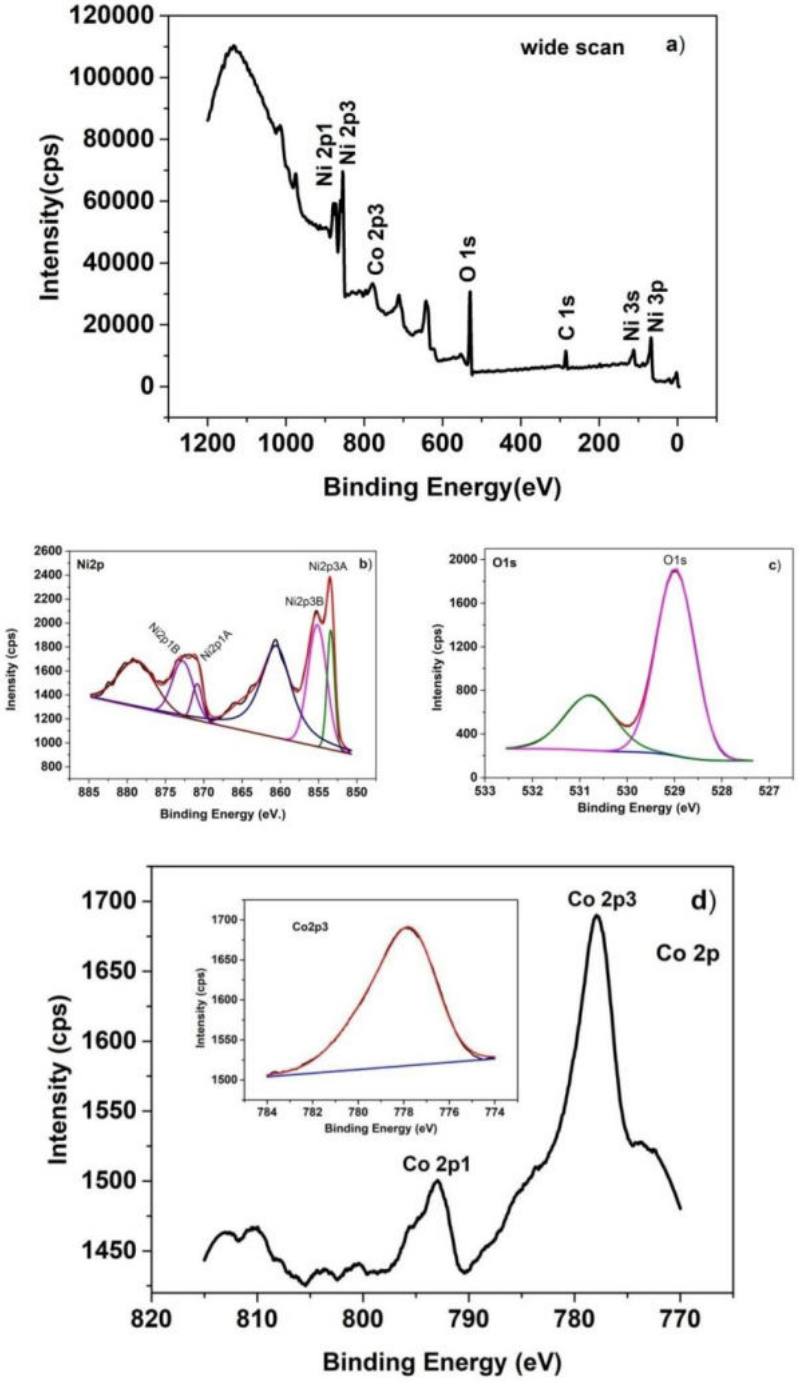

Figure 4.7 : XPS spectra of Co3 **(a)** wide scan, **(b)** Ni 2p, **(c)** O 1s and **(d)** Co 2p

4.3.2 Optical Properties

UV-Vis absorption and photoluminescence spectra studies of pristine and Co^{2+} doped NiO nanoparticles at room temperature are presented here. The analyses are carried out by following the procedure as given in *Section 2.5.*

4.3.2.1 UV- Visible Spectroscopy

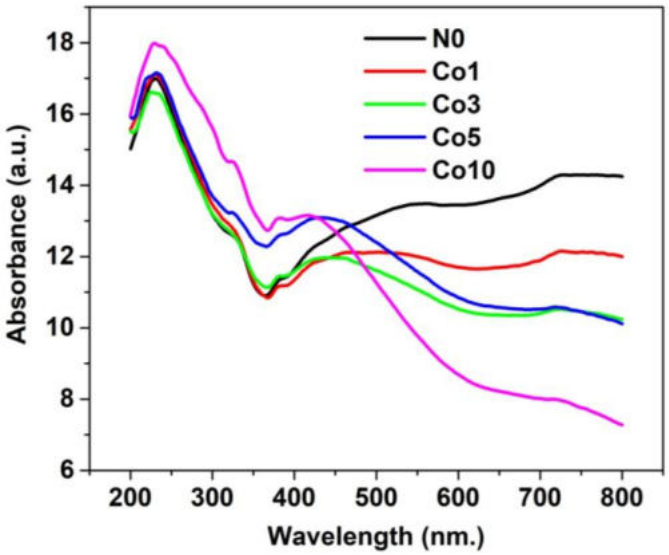

Figure 4.8 : UV – visible absorption spectra of pristine and Co doped NiO samples

UV-visible absorption spectra of pure and doped samples of NiO nanoparticles are shown in Figure 4.8. All samples exhibit strong UV absorption along with extended visible light absorption. The UV absorption corresponds to the bandgap absorption of NiO. Pristine NiO has absorption in the entire visible range which is due to the presence of excess oxygen in the lattice. This leads to the creation of Ni^{2+} vacancies. Presence of each Ni^{2+} vacancy results in the formation of two Ni^{3+} ions in order to acquire local charge compensation. This change in the

oxidation state of Ni is the reason for the featureless absorption in the visible region [16, 17]. This inference is consistent with the XPS measurement. As the doping concentration increases, broad absorption in the visible region decreases which may be due to the change in stoichiometry as evident from the EDX data. The absorption becomes more selective, with the samples Co5 and Co10 having a hump in the 350 – 500 nm range. This is due to the ligand to dopant ($O^{2-} \rightarrow Co^{2+}$) charge transfer [18]. The intensity of the Co related peak is found to increase with the increase in dopant concentration. The pristine NiO sample has the absorption edge at 360 nm which is found to get red shifted with the increase in doping concentration.

The optical bandgap values determined from the Tauc plots (Figure 4.9) for N0, Co1, Co3, Co5 and Co10 are 3.72, 3.65, 3.58, 3.56 and 3.25 eV respectively. The decrease in the optical bandgap on Co doping is due to the structural modifications of NiO. Since the XRD data show no obvious structural changes, local structural modifications surrounding the Co dopant atoms may play a key role in the mechanism underlying the observed bandgap narrowing. Doping introduces oxygen vacancies, which is clear from the EDX data. According to XPS results, cobalt exists in Co^{2+} oxidation state in the sites occupied by cations in the host lattice [19]. Such Co ions and oxygen vacancies introduce some additional energy levels in the NiO bandgap near the valence band edge [20]. Consequently, the absorption edge transition for the doped material can be from O *2p* to Co *3d* state which leads to the decreased optical bandgap. The increased sp-d exchange interactions between the band

electrons and the localized d electrons of Co^{2+} cations also contribute to bandgap narrowing [21]. Therefore, the sub-band states of Co^{2+} and the oxygen vacancy states are responsible for the reduction of the effective bandgap of NiO nanoparticles. As the doping concentration increases, the defect levels go deep into the bandgap which further reduces the bandgap energy. Thus the bandgap of NiO can be reduced considerably by Co doping without causing any significant structural modifications, which makes them useful for various optoelectronic applications.

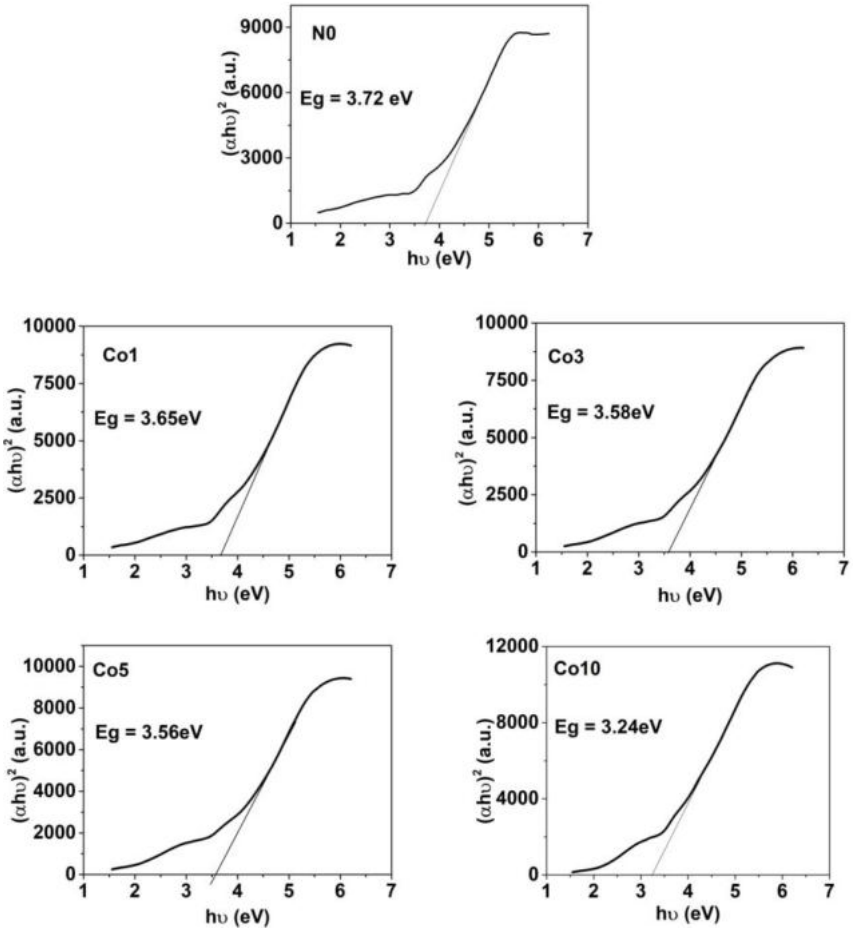

Figure 4.9: Tauc plots of pristine and Co doped NiO samples

4.3.2.2 PL Spectroscopy

The room temperature PL spectra of pure and Co doped NiO samples excited at a wavelength of 280 nm are shown in Figure 4.10. Strong UV emission with peaks at 365 nm (3.4 eV) and 393 nm (3.16 eV) is observed along with well-resolved shoulder peaks at 448 nm (2.77 eV) and 465 nm (2.67 eV). This broad emission extending from UV to the visible region originates from the defect levels of NiO nanoparticles. It is reported that the UV emission due to excitonic recombination corresponds to the near band edge emission of NiO [22]. The shoulder peaks in the visible region originate from the radiative recombination of photo-generated holes with electrons occupying the surface oxygen vacancies and defects [23].

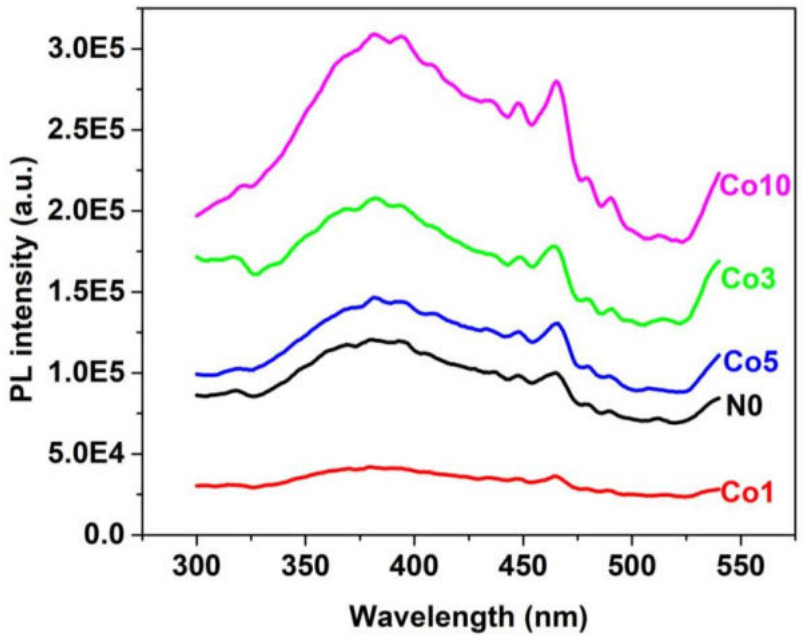

Figure 4.10 : PL emission spectra of NiO and Co doped NiO samples

Co doping does not give rise to new emission compared to that of undoped NiO; however, it has a great effect on the PL intensity. 1 mol % of Co doping led to a significant decrease in the emission intensity compared with that of pure NiO. The quenching of PL intensity confirms that an appropriate amount of Co doping inhibits the recombination rate of photogenerated electron–hole pairs. The PL intensity of C3, C5 and C10 samples are higher than that of pure NiO. The increase in the surface oxygen vacancies and defects, as evident from the EDX data, can enhance the PL intensity of the doped samples. The levels corresponding to oxygen vacancies and defects in the bandgap bind the photo-induced electrons easily to form excitons, so that the PL emission can occur easily [24]. As the doping concentration increases, the dopant levels introduced in the energy gap can also act as recombination centres of photo-generated electron–hole pairs and lead to an increase in PL intensity. PL intensity for sample C3 is higher than that of C5, which may be due to the smaller particle size. The decrease in particle size may also lead to an increase in oxygen vacancies which in turn enhances the PL intensity [25]. The PL emission results are in good agreement with EDX and UV-Visible studies. Thus the PL emission study of NiO with varying Co concentration is an efficient method for the exploration of point defects such as oxygen/nickel vacancies and interstitials in the host lattice. In short, results of the optical studies confirm that Co doping can be done to tune optical bandgap and PL emission of NiO nanoparticles.

4.3.3 Electrical Properties

Electrical studies have been carried out by following the procedure given in *Section 2.6*. The samples N0, Co1, Co3, Co5 and Co10 are consolidated in the form of cylindrical pellets of diameter 13

mm and thickness 1.5 mm by applying a pressure of 7 tons using a hydraulic press.

4.3.3.1 DC Conductivity

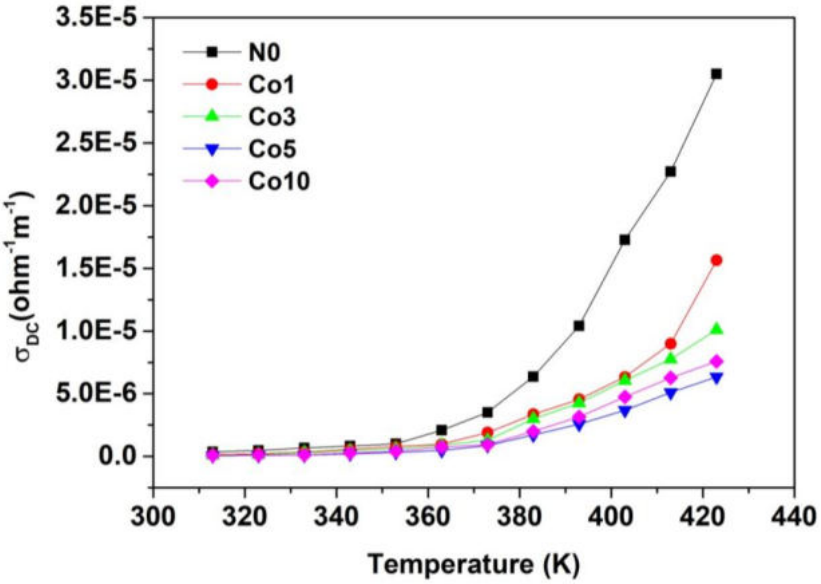

Figure 4.11 : Variation of DC conductivity with temperature of pristine and Co doped NiO samples

The variation of DC electrical conductivity (σ_{DC}) with temperature for pristine and cobalt doped NiO nanoparticles in the temperature range 313 - 423 K is depicted in Figure 4.11. The figure shows a positive temperature coefficient of conductance for all the samples, indicating their semiconducting behaviour. The increase in conductivity with temperature is due to the increase in drift mobility of the thermally activated charge carriers [26]. At 313 K, the values of DC conductivity for N0, Co1, Co3, Co5 and Co10 are found to be 3.69×10^{-7}, 1.37×10^{-7}, 8.76×10^{-8}, 5.37×10^{-8} and 7.19×10^{-8} $\Omega^{-1}m^{-1}$ respectively. The conductivity is found to decrease with an increase in Co concentration indicating a

decrease in the number of free charge carriers. The electrical conductivity of pristine NiO strongly depends on the concentration of microstructural defects, such as nickel vacancies and interstitial oxygen in NiO crystallites [27]. When Co^{2+} ions are introduced into the host lattice, they will fill up the cation vacancies. With an increase in dopant concentration, the replacement of Ni^{2+} ions with dopant ions also will occur. Such dopant ions and the oxygen vacancies in the doped samples enhance the defect scattering centres in the system which leads to a reduction in conductivity [28]. Also, the reduction in crystallite size with doping increases the grain boundary density that will hinder the motion of charge carriers.

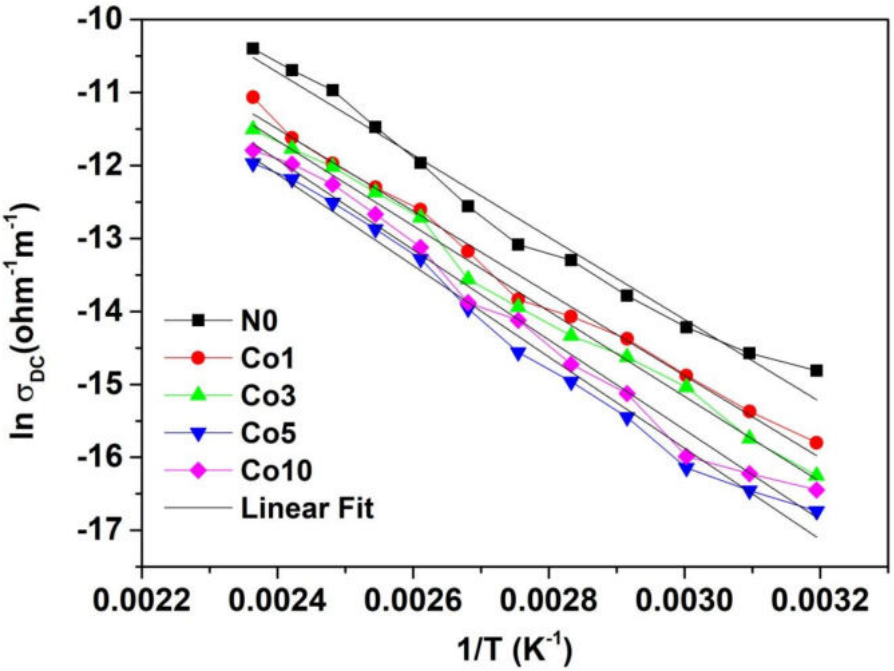

Figure 4.12 : Arrhenius plots of pristine and Co doped NiO samples

Figure 4.12 shows the Arrhenius plots for the pristine and doped samples. The activation energies (*Ea*) of DC conductivity for the samples are calculated using $ln\ \sigma_{DC}$ vs $1/T$ graphs (Figure 4.12). The calculated values are 0.484, 0.487, 0.504, 0.539 and 0.532 eV for N0, Co1, Co3, Co5 and Co10 samples, respectively in the temperature range of 313-423 K. The increasing values of activation energy in the doped samples confirm the enhanced defect scattering and the consequent requirement of higher energies for activation into conducting states [29].

4.3.3.2 Dielectric Studies

The frequency dependence of dielectric constant (ε') and loss tangent ($tan\delta$) of pristine and doped samples at selected temperatures are studied. Figure 4.13 illustrates the variation in dielectric constant with frequency at room temperature of the samples N0, Co1, Co3, Co5 and Co10 in a broad frequency spectrum (50 Hz-5 MHz). All the samples exhibit the same behaviour as seen from the figure. The dielectric constant has strong frequency dependence in the low frequency region, which decreases with increase in frequency and becomes almost constant at high frequencies for all samples. This variation of ε' with frequency reveals the dispersion due to Maxwell-Wagner type [30] interfacial polarization in agreement with Koops phenomenological theory [31]. The interfacial/space charge polarization due to inhomogeneity in the dielectric structure contributes to the high value of dielectric constant at very low frequency [32]. With the increase in frequency, the charge carrier hopping between various metal ions is unable to follow the applied field causing a reduction in dielectric constant.

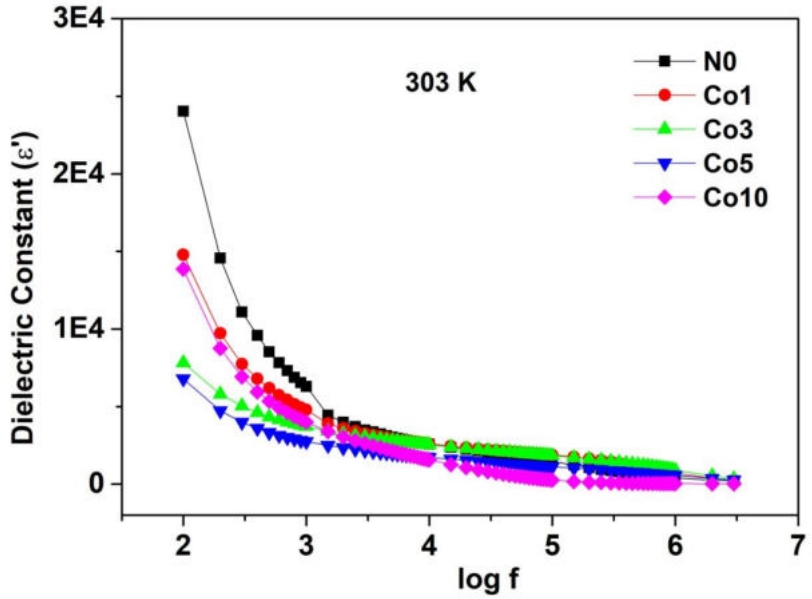

Figure 4.13 : Variation of dielectric constant with frequency of pristine and Co doped NiO samples at room temperature

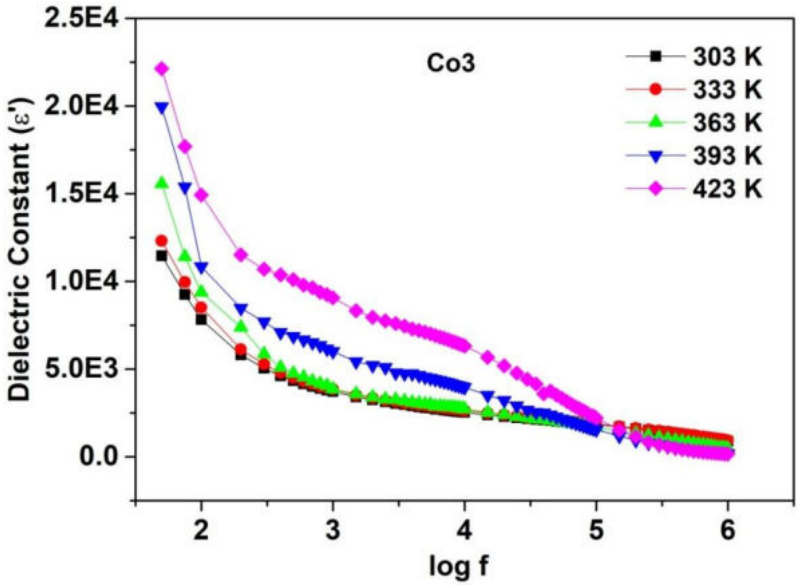

Figure 4.14 : Variation of dielectric constant with frequency of sample Co3 at selected temperatures

At 303 K and 1 kHz, the values of dielectric constant for N0, Co1, Co3, Co5 and Co10 are found to be 6290, 4787, 3722, 2748 and 4005 respectively. The compositional variation reveals the decrease of ε′ with an increase in Co^{2+} content up to 5 mol %. This decrease may be due to interfacial charge transfer [33]. At lower frequencies, the effect of grain boundaries is predominant, as suggested by Koops [31]. Doping can thicken the grain boundary and cause a decrease in interfacial and dipolar polarization, and hence a decrease in dielectric constant [34, 35]. The value of ε′ for the Co10 sample is found to be higher than that of pristine NiO. For high doping concentration, more Co^{2+} ions will be added into the NiO lattice in the form of Ni^{2+}substitution and interstitial incorporation, and the dielectric polarizability of cobalt ions is large compared to that of nickel ions [36]. With the increase in Co content, oxygen vacancies will be increased, which increases the dipole moment and in turn the orientational polarization [37].

Figure 4.14 depicts a representative graph of variation of dielectric constant as a function of frequency at different temperatures (303 K – 423 K) for Co3. It is observed that the dielectric constant increases with an increase in temperature at any particular frequency. All the other samples show the same behaviour. At 10 kHz, the value of ε′ for Co3 is 2535, 2647, 2732, 3966 and 6319 for 303, 333, 363, 393 and 423 K, respectively. As the conduction mechanism is thermally activated, the probability of charge carriers reaching the grain boundary increases with increase in temperature. As a result, the orientational polarization of the specimen increases, resulting in the increase of ε′ [38]. With the increase in temperature, a step like variation in ε′ is observed,

which indicates the speeding up of dipolar reorientation driven by thermal activation [39].

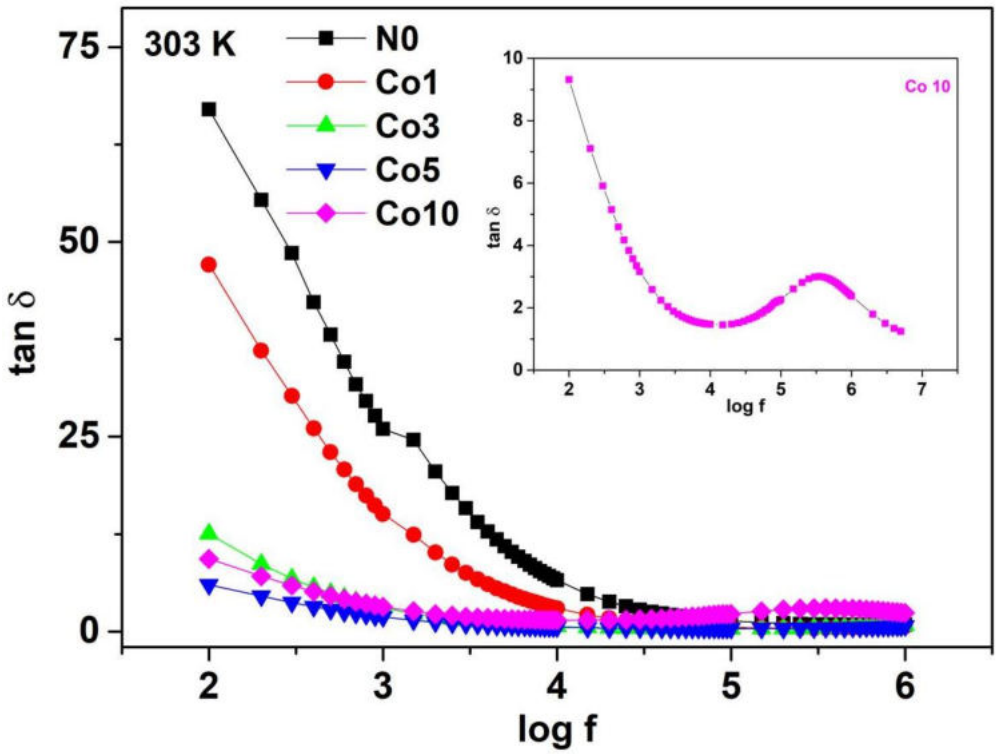

Figure 4.15 : Variation of loss tangent with frequency of pristine and Co doped NiO samples at room temperature

The variation of loss tangent (*tan δ*) of pristine and cobalt doped NiO as a function of frequency at room temperature is shown in Figure 4.15. A significant reduction in dielectric loss is observed on Co doping which improves the dielectric properties of NiO nanoparticles with Co doping. At 303 K and 10 kHz, *tan δ* values are 6.56, 2.97, 0.34, 0.28 and 0.74 respectively for N0, Co1, Co3, Co5 and Co10 samples. The low values of loss tangent for the doped samples indicate that Co doped NiO nanoparticles are low-loss materials which are suitable for high frequency applications. Thus energy dissipation, unwanted noises and signal losses can be considerably reduced by cobalt doping. *Tan δ* is

observed to decrease rapidly in the low frequency region; the rate of decrease slows down as the frequency rises and finally becomes almost constant at high frequencies. A relaxation peak is observed in the measured frequency range for the Co10 sample (inset of Figure 4.15). The peak occurs when the hopping frequency of the localized charge carriers becomes equal to the frequency of the applied AC field [40].

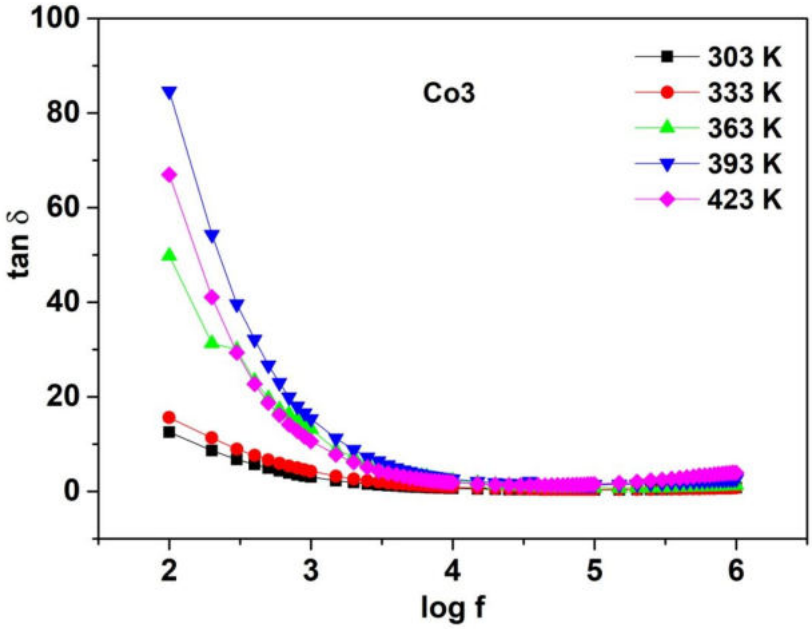

Figure 4.16: Variation of loss tangent with frequency of sample Co3 at selected temperatures

Figure 4.16 portrays the variation of *tan δ* with the frequency of the sample Co3 at selected temperatures in the range 303 - 423 K. The normal dielectric behaviour is exhibited by the sample where the loss tangent increases with increase in temperature. At 10 kHz, the value of *tan δ* for Co3 is 0.68, 0.96, 2.26, 2.59 and 1.87 at 303, 333, 363, 393 and 423 K, respectively. With the increase in temperature, the extra thermal energy boosts the mobility of charge carrier; hence their rate of hopping

is enhanced. This increases the dielectric polarization and hence the dielectric loss with temperature [41].

4.3.3.3 Impedance Analysis

Figure 4.17 shows the Nyquist plots of pristine and Co doped NiO nanoparticles. Inset shows the high frequency region of the plot for N0 and Co1 samples. The solid lines represent experimental data and the symbols represent fitted data. It is evident that all the samples show double semicircular behaviour suggesting the grain and grain boundary contribution to the impedance of the samples [42]. These two semicircles can be modelled by two parallel R-CPE (Constant Phase Element) equivalent circuits in series configuration. CPE represents the deviation from an ideal capacitor, whose impedance is given by $[(j\omega)^{\beta}CPE]^{-1}$ [43].

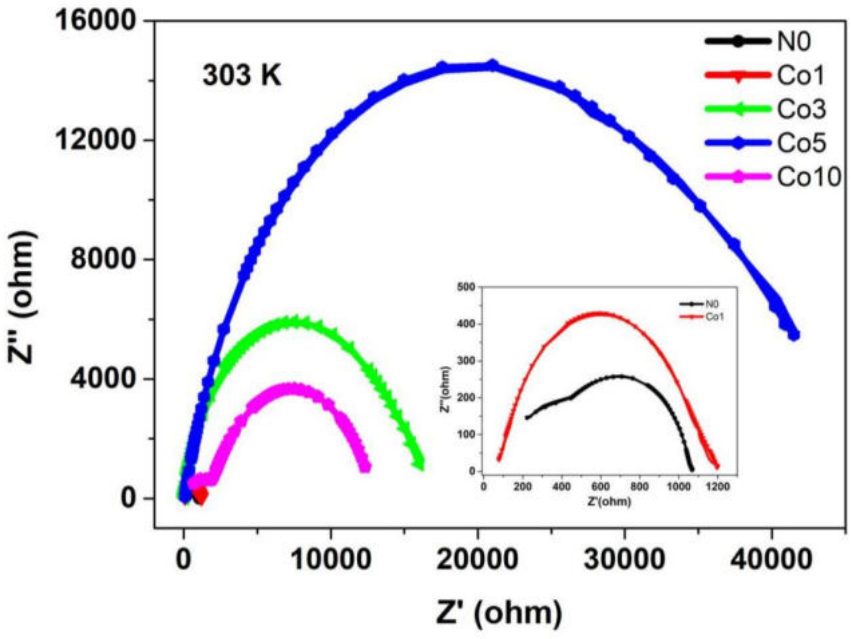

Figure 4.17 : Nyquist plots of pristine and Co doped NiO samples

Typical values of the parameters R, C and β, both for grain (R_g, CPE_g, β_g) and grain boundaries (R_{gb}, C_{gb}, β_{gb}) obtained from the fits are summarized in Table 5.5. The obtained values of grain boundary resistances are higher than that of grain – core resistance. Both the grain and grain boundary resistances are found to increase with dopant concentration up to 5 mol% of Co doping. The increase in the dopant amount and decrease in grain size increases the concentration of defect ions which segregate at the grain boundary. This aids the formation of defect barriers at the grain boundary leading to an increase in resistivity [44, 45]. The impedance parameters of Co10 indicate a slight increase in conductivity.

Table 4.5 : Impedance parameters of pristine and Co doped NiO samples

Sample	CPE_g (F)	R_g(Ω)	β_g	CPE_{gb} (F)	R_{gb} (Ω)	β_{gb}
N0	1.42E-10	359	0.965	2.702E-08	678	0.774
Co1	1.64E-07	480	0.522	4.25E-09	709	0.983
Co3	3.21E-07	5587	0.729	9.85E-09	10951	0.897
Co5	5.71E-07	15005	0.675	1.09E-08	31466	0.843
Co10	1.22E-07	1468	0.745	4.90E-09	9216	0.767

4.3.3.4 AC Conductivity

The variation of AC conductivity (σ_{AC}) with frequency for the pristine and Co doped NiO at room temperature is illustrated in Figure 4.18(a). At low frequencies up to about 50 kHz, a plateau which characterizes the DC conductivity is present, while at high frequencies, the conductivity increases with increasing frequency for all samples. At

303 K and 1 kHz, the value of σ_{AC} for N0 is 1.69×10^{-2} S/m while the corresponding values for samples Co1, Co3, Co5 and Co10 are 4×10^{-3}, 6.31×10^{-4}, 2.86×10^{-4} and 7.04×10^{-4} S/m, respectively. The conductivity is found to be less for the doped samples compared to pristine NiO, and is found to decrease with increase in dopant concentration up to 5 mol%. The dopant ions introduce defects such as nickel interstitials and oxygen vacancies which segregate at the grain boundaries. This aids the formation of a defect barrier at the grain boundary that blocks the flow of charge carriers, which in turn decreases the conductivity of the sample [40]. Also, the enhanced surface to volume ratio with decrease in size on doping can cause surface scattering, leading to a reduction in conductivity [46].

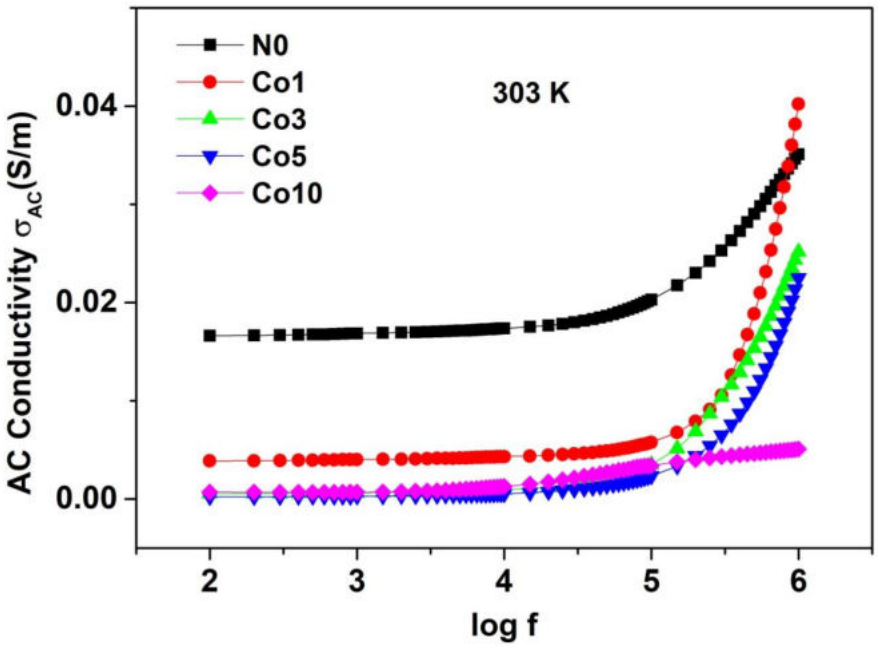

Figure 4.18 : Variation of AC conductivity with frequency of pristine and Co doped NiO samples at room temperature

A slight increase in σ_{AC} is observed for the Co10 sample, which is a consequence of the increase in dielectric permittivity of the sample [47]. The plot of AC conductivity for sample Co3 with frequency and temperature is shown in Figure 4.19. The increase in AC conductivity with temperature is evident from the Figure. A detailed explanation for such a variation of AC conductivity with frequency and temperature is presented in *Section 3.3.4.4.*

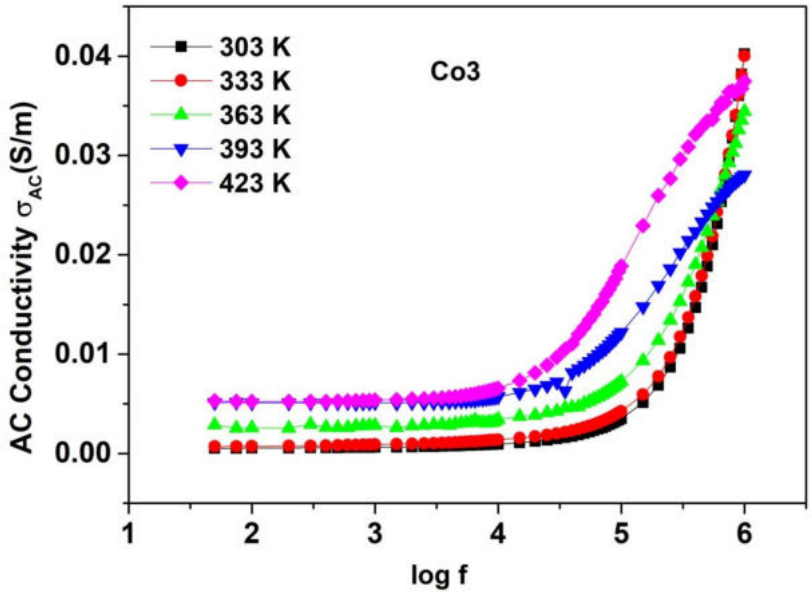

Figure 4.19 : Variation of AC Conductivity with frequency of sample Co3 at selected temperatures

Figure 4.20 illustrates the Jonscher's power law plots of the samples N0, Co1, Co3, Co5 and Co10 [48]. The '*s*' values for conduction are calculated from the slopes of *log* (ω-σ_{AC}) plots and the obtained values are 0.27, 0.62, 0.84 , 0.9 and 0.3 for the samples N0, Co1, Co3, Co5 and Co10, respectively. The values of 's' evidently lie between zero and unity exhibiting frequency dependent hopping as the main conduction mechanism for the investigated samples [49].

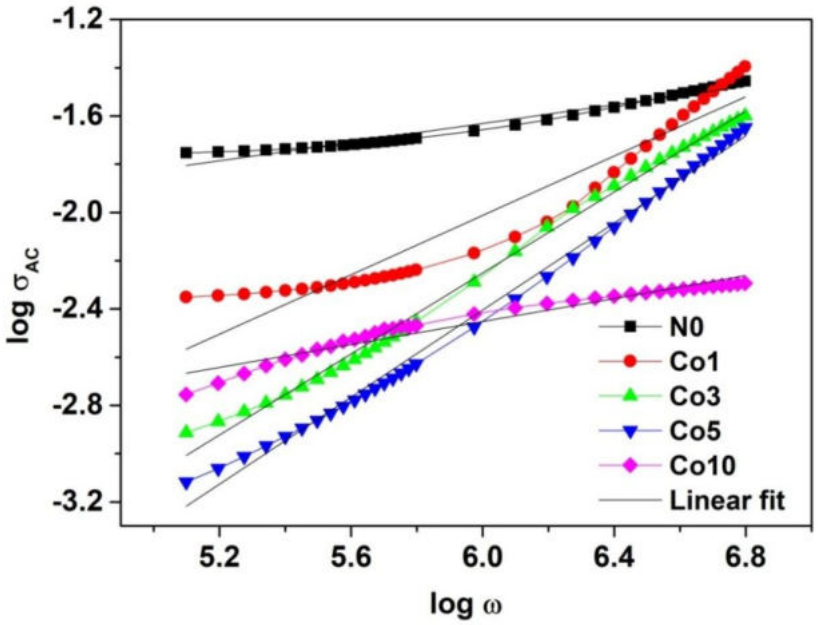

Figure 4.20 : Jonscher's power law plots of pristine and Co doped NiO samples

4.3.4 Magnetic Properties

Magnetization versus magnetic field (M−H) curves of pristine and Co doped NiO nanoparticles measured at 300 K with a maximum applied field of ±1.5 T, are used to identify the effect of Co doping on magnetic properties of NiO nanoparticles. Figure 4.21 shows the M-H curves of all the samples with that of Co10 as inset. All the samples exhibit superparamagnetic behaviour, which is evident from their low values of coercivity lying within the range of 15 – 41 Oe. However, a linearization of the M-H curve is observed for Co10 sample indicating an antiferromagnetic character. With the increase in doping concentration the *sp – d* exchange interaction between Co *d* orbitals and the conduction band of NiO becomes stronger leading to this behaviour [50, 51]. The superparamagnetic property of the samples proposes them as a promising material for imaging and drug delivery [52].

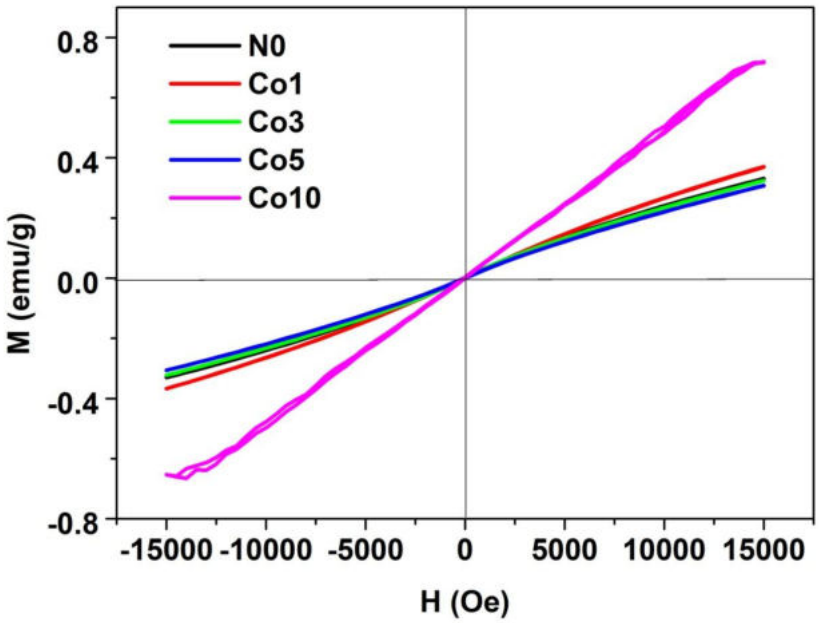

Figure 4.21 : M – H curves of pristine and Co doped NiO samples at room temperature

4.4 Conclusion

- Chemical co-precipitation method has been successfully employed for the doping of cobalt ions into pristine NiO nanoparticles.

- A systematic study has been conducted on the effect of cobalt doping on the structural, optical, electrical and magnetic properties of pristine nanocrystalline NiO.

- XRD studies reveal a reduction in particle size with Co doping, without affecting the structure of NiO.

- XPS studies reveal the presence of Co^{2+} ions in the samples.

- The bandgap of NiO can be reduced considerably by Co doping without causing any significant structural modifications, which makes them useful for various optoelectronic applications.

- PL emission studies of NiO with varying Co concentration give an account of the point defects and interstitials in the host lattice.

- A decrease in dielectric permittivity, loss tangent and conductivity is observed for the Co doped samples, which is attributed to the incorporation of Co^{2+} ions.

- The sequence of two semicircles in the Nyquist plots reveals the grain and grain contributions to the transport properties of pristine and doped samples.

- Jonscher's power law plots confirm frequency dependent hopping as the main conduction mechanism for pristine and Co^{2+} doped NiO.

- Superparamagnetic property is exhibited by all the samples except Co10, which shows an antiferromagnetic behaviour.

References

1) A. Chanda, S. Gupta, M. Vasundhara, S. R. Joshi, G. R. Mutta, J. Singh, RSC Adv.,7 (2017) 50527 - 50536

2) M. J. Chithra, K. Pushpanathan, M. Loganathan, Mater. Manuf. Processes, 29 (2014) 771 - 779

3) R.D. Shannon, Acta Cryst. A 32 (1976) 751- 767

4) P.M. Ponnusamy, S. Agilan, N. Muthukumarasamy, M. Raja, D. Velauthapillai, J. Mater. Sci: Mater. Electron.**27** (2016) 399 - 406

5) R. Sharma, A.D. Acharya, S. Moghe, S.B. Shrivastava, M. Gangrade, T. Shripathi, V. Ganesan, Mater. Sci. Semicond. Process. 23 (2014) 42 - 49

6) G. K. Williamson, W. H. Hall, Acta Metall., 1 (1953) 22-31.

7) D.N. Srivastava, V.G. Pol, O. Palchik, L. Zhang, J.C. Yu, A. Gedanken, Ultrason. Sonochem. 12 (2005) 205 - 212

8) M. Alagiri, S. Ponnusamy, C. Muthamizhchelvan, J Mater Sci: Mater Electron 23 (2012) 728 - 732

9) L. Wu, Y. Wu, H. Wei, Y. Shi, C. Hu, Mater. Lett. 58 (2004) 2700 - 2703

10) A.C. Tas, P.J. Majewski, F. Aldinger, J. Am. Ceram. Soc., 85(2002)1421- 1429

11) M.A. van Veenendaal, G.A. Sawatzky, Phys. Rev. Lett. 70 (1993) 2459 – 2462

12) L. Cao, D. Wang, R. Wang, Mater. Lett. 132 (2014) 357 – 360

13) T. V. Thi, A. K. Rai, J. Gim, J. Kim, J. Power Sources, 292 (2015) 23 – 30

14) B. Vincent Crist, Handbooks of Monochromatic XPS Spectra,Vol.1, 1999 XPS International, Inc, USA

15) A. A. Jacob, L. Balakrishnan, K. Shambavi, Z. C. Alex, RSC Adv., 7 (2017) 39657 - 39665

16) A. Mendoza-Galvan, M. A. Vidales-Hurtado, A. M. Lopez-Beltran, Thin Solid Films, 517(2009) 3115 - 3120

17) R. Newman, R.M. Chrenko, Phys. Rev. 114 (1959) 1507 - 1513

18) M. Salavati-Niasari, A. Khansari, F. Davar, Inorg. Chim. Acta, 362 (2009) 4937 - 4942

19) T. Taşköprü, F. Bayansal, B. Şahin, M. Zor, Philos. Mag., 95 (2014) 32 - 40

20) B. Sahin, F. Bayansal, M. Yüksel, H.A. Çetinkara, Mater. Sci. Semicon. Proc. 18 (2014) 135 – 140

21) R. He, R.K. Hocking, T. Tsuzuki, Mater. Chem. Phys.,132 (2012) 1035 - 1040

22) L. Kumari, W.Z. Li, C.H. Vannoy, R.M. Leblanc, D.Z. Wang, Cryst. Res. Technol., 44 (2009) 495 - 499

23) S.A. Makhlouf, M.A. Kassem, M.A. Abdel-Rahim, Optoelectron. Adv. Mater. 4 (2010) 1562.

24) M. M. Khan, S. A. Ansari, D. Pradhan, M. O. Ansari, D. H. Han, J. Lee, M. H. Cho, J. Mater. Chem. A, 2 (2014) 637 - 644

25) J. Liqiang, S. Xiaojun, X. Baifu, W. Baiqi, C. Weimin, F. Honggang, J. Solid State Chem. 177 (2004) 3375 - 3382

26) L. G. V. Uitert, J. Chem. Phys., 23 (1995)1883 - 1887. http://dx.doi.org/10.1063/1.1740598

27) E. Antolini, J. Mater Sci., 27 (1992) 3335-3340

28) U. Godavarti, V.D. Mote, M. Dasari, J. Asian Ceramic Societies 5 (2017) 391 - 396

29) M. Naeem, S. K. Hasanain, A. Mumtaz, J. Phys.: Condens. Matter 20 (2008) 025210

30) J. C. Maxwell, Electricity and Magnetism (Oxford University Press, New York, 1973), Vol. 1, p. 828.

31) C. G. Koops, Phys. Rev., 83 (1951) 121-124

32) S. Sagadevan, I. Das, J. Poddar, J Mater Sci: Mater Electron 27 (2016) 13016–13021

33) A.K. Abdul Gafoor, M.M. Musthafa, K. Pradeep Kumar, P.P. Pradyumnan, J. Mater. Sci.: Mater. Electron. 23 (2012) 2011

34) K. V. Arun Kumar, T. Sunil, G. Manju, P. R. Biju, N. V. Unnikrishnan, J Mater Sci: Mater Electron. 24 (2013) 1727–1733

35) A.K. Abdul Gafoor, J. Thomas, M.M. Musthafa, P.P. Pradyumnan, J. Electron. Mater. 40 (2011)2152

36) R. D. Shannon, J. Appl. Phys. ,73 (1993) 348 – 366

37) C. Jayachandraiah, G. Krishnaiah, Adv. Mater. Lett., 6 (2015)743-748

38) A.K. Thomas, K. Abraham, J. Thomas, K.V. Saban, J. Asian Ceramic Societies 5 (2017) 56 - 61

39) P. Lunkenheimer, A. Loidl, The Scaling of Relaxation Process, Springer, 2018. 23 – 60

40) S. A. Ansari, A. Nisar, B. Fatma, W. Khan, A.H. Naqvi, Mater. Sci. Eng., B 177 (2012) 428– 435

41) J. Hasson, F.M. Yen, M.H. Ashim, Ionics, 13 (2007) 219-222

42) D. O. Neill, R. M Bowman, J. M. Gregg, Appl. Phys. Lett. 77 (2000) 1520-1522

43) K. Omri, I. Najeh, L. El Mir, Ceram. Int., 42 (2016) 8940 – 8948

44) C. Li, J. Wang, W. Su, H. Chen, W. Zhong, P. Zhang, Ceram. Int. 27 (2001) 55

45) R. N. Aljawfi, F. Rahman, K. M. Batoo, J. Mol. Struct., 1065 (2014) 199–204

46) K. Karthik, S. K. Pandian, N. V. Jaya, Appl. Surf. Sci., 256 (2010) 6829–6833

47) B. Rajesh Kumar, B. Hymavathi, T. SubbaRao, J. Science: Advanced Materials and Devices (2018) 1 - 7

48) A.K. Jonscher, Dielectric Relaxation in Solids (Chelsea Dielectric Press, London, 1983)

49) A. R. Long, Adv. Phys., 31 (1982) 553

50) J. Singh, N. K. Verma, Bull. Mater. Sci., 37 (2014) 541–547

51) M. J. Benitez, O. Petracic, H. Tüysüz, F. Schüth, H. Zabel, Phys. Rev. B, 83 (2011) 134424

52) U. Jeong, X. Teng, Y. Wang, Y. Xia, Adv. Mater., 19 (2007) 33 - 60

…..❀…..

Chapter 5

EFFECT OF CERIUM DOPING ON THE PROPERTIES OF NICKEL OXIDE NANOPARTICLES

The effect of cerium (Ce) doping on the structural, optical, electrical and magnetic properties of nickel oxide nanoparticles is dealt with in this chapter. NiO nanoparticles doped with 0.5 and 1 mol % of Ce are prepared by chemical co-precipitation method and characterized using various characterization techniques.

5.1 Introduction

Doping can modify the electronic structure of nanoparticles to achieve improved catalytic, electro-optical, magnetic, chemical and physical properties [1, 2]. The dopant ions can be incorporated into the host lattice by means of substitutional or interstitial incorporation, or they can segregate on the lattice surface. Generally, metal oxide semiconductors doped with rare earth ions exhibit modified catalytic properties, high surface activity and fast oxygen ion mobility [3]. Doping of a rare earth metal into metal oxide semiconductors temporarily generates charge carriers [4]. Among different rare earth metals, cerium has received much attention due to its unique properties such as the shift of cerium oxide between CeO_2 and Ce_2O_3 due to the formation of redox couple Ce^{3+}/Ce^{4+} under oxidizing and reducing conditions, and easy formation of oxygen vacancies with relatively high mobility of bulk oxygen species [3, 5, 6]. The creation of active sites and enhanced surface area improved the NO_2 gas sensing property of porous Ce doped NiO, as reported by Gawali *et al.* [6]. The minimal internal resistance and high surface area of the Ce doped NiO nanoparticles enhance its specific capacitance and thereby widely preferred for energy storage applications [5]. Gawali *et al.* reported the enhanced electrochemical performance of NiO electrodes with Ce doping [7]. Herein, a systematic and detailed study of the structural, optical, electrical and magnetic properties of Ce doped NiO nanoparticles synthesized by co - precipitation method is presented.

5.2 Synthesis of Cerium Doped NiO nanoparticles

Nickel nitrate hexahydrate (Ni $(NO_3)_2 \cdot 6H_2O$, 99.8%, Sigma Aldrich), ammonium carbonate ($(NH_4)_2CO_3$, 99.9%, Merck) and cerium nitrate hexahydrate (Ce $(NO_3)_2.6H_2O$, 99.8%, Sigma Aldrich) are the chemicals used for the synthesis of cerium doped nickel oxide nanoparticles.

NiO nanoparticles doped with 0.5 and 1 mol % of Ce are prepared by chemical co-precipitation method. The required mol % of Ce $(NO_3)_2.6H_2O$ and Ni $(NO_3)_2 \cdot 6H_2O$ are dissolved under magnetic stirring in distilled water to make 0.1 M solution. The carbonate precursor is chemically precipitated by slowly adding 0.1 M aqueous solution of ammonium carbonate [$(NH_4)_2CO_3$] at room temperature under magnetic stirring for 30 minutes. The precipitate is allowed to settle down overnight and then washed with distilled water several times to remove the unreacted salts and impurities. Finally, the precipitate is filtered and dried in a hot air oven at 70^oC for 18 h. The dried product obtained is powdered and calcined at 600^oC for 3 h in a muffle furnace to obtain Ce doped NiO nanoparticles. NiO nanoparticles doped with 0.5 and 1 mol % of Ce are denoted as Ce0.5 and Ce1 respectively. N2 represents the pristine NiO which is calcined at 600^oC.

5.3 Results and Discussion

The thermal stability of the synthesized precursor is studied using the procedure described in *Section 2.3*. The structural, optical, electrical and magnetic characterizations of the samples are carried out using various techniques described in *Chapter 2*.

5.3.1 Thermal Analysis

The thermal stability of the precursor from the ambient temperature to 700°C is studied using thermogravimetric analysis techniques. The TGA and DTG curves of the precursor are shown in Figure 5.1.

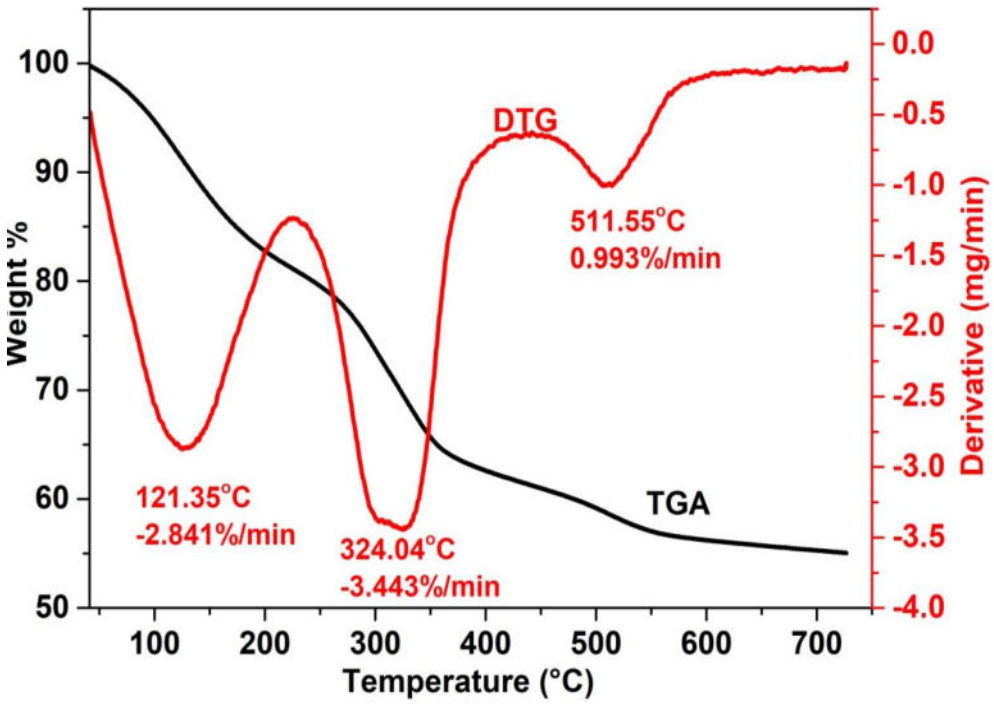

Figure 5.1 : TGA/DTG curves of Ce doped precursor

An appreciable weight loss of the precursor up to 550°C is evident from the TGA curve. The DTG curve reveals three prominent weight loss peaks centred at 121.35, 324.04 and 511.55°C with an overall weight loss of ~ 7.3 % in the temperature range from 40 to 700 °C. The first weight loss (2.84%/min) is related to the loss of adsorbed water and

trapped solvents. The second peak (3.44%/min) can be attributed to the decomposition of nickel carbonate into nickel oxide and carbon dioxide. The decomposition of anhydrous salts results in the third minor weight loss (0.99%/min) [8]. The amount of defects and their microstructure also play an important role in the thermal stability of the materials [9]. Based on the above observations, the calcination temperature of Ce doped NiO is chosen as 600^{o}C.

5.3.2 Structural Characterization

The structural analyses of the synthesized samples have been carried out using powder X-ray diffraction , Fourier transform infrared spectroscopy, Field enhanced scanning electron microscopy, Transmission electron microscopy, Energy dispersive X-ray analysis and X-ray Photoelectron Spectroscopy, by following the procedure described in *Section 2.4*.

5.3.2.1 Powder XRD Analysis

X-ray diffraction patterns of pristine and Ce doped NiO nanoparticles are shown in Figure 5.2.

The peaks observed in the XRD patterns of doped samples are well indexed to face centred cubic NiO (JCPDS Card, No. 73 - 1519) with space group *Fm3m*. The XRD profiles of Ce0.5 and Ce1 samples retain the structure of pure NiO, which indicates that Ce doping has not changed the crystal structure of the host material. The presence of a small and broad peak at $2\theta = 28.747^{o}$ in the diffraction pattern of Ce1

corresponds to (111) plane of cubic phase of CeO_2 [10]. The structural parameters of the samples are tabulated in Table 5.1. The diffraction angles corresponding to the (200) plane are 43.29, 43.34 and 43.37^o for N2, Ce0.5 and Ce 1 samples respectively. This gradual shift to higher diffraction angles as well as narrowing of peaks with the increase in doping concentration implies the formation of larger crystallites with doping. This might occur due to the lattice strain and local distortion induced by the size mismatch between Ni^{2+} and Ce^{3+} ions [6, 11]. The difference in ionic radii between Ni^{2+} (0.69 Å) and Ce^{3+} ions (1.01 Å) will be a constraint for Ce to occupy the Ni sites in the lattice [12]. Hence, relatively large number of dopant ions will stay on the particle surface causing a compression of the crystal lattice, and hence a decrease in lattice constant and unit cell volume [13].

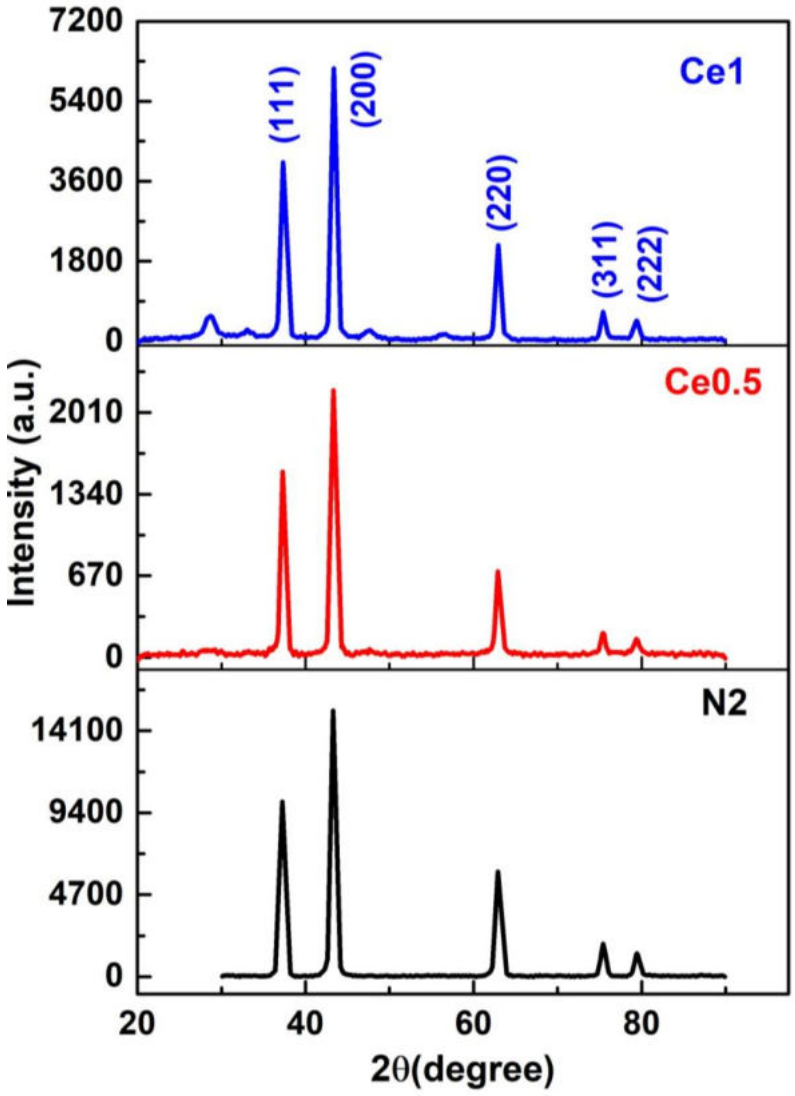

Figure 5.2 : XRD patterns of pristine and Ce doped NiO samples

The average crystallite sizes calculated using Scherrer equation (*Chapter 2, Eq: 2.2*) are 17.8, 18.4 and 18.9 nm, respectively for N2, Ce0.5 and Ce1 samples. This increase in size can be attributed to the replacement of Ni^{2+} ions with Ce^{3+} ions for low doping concentration.

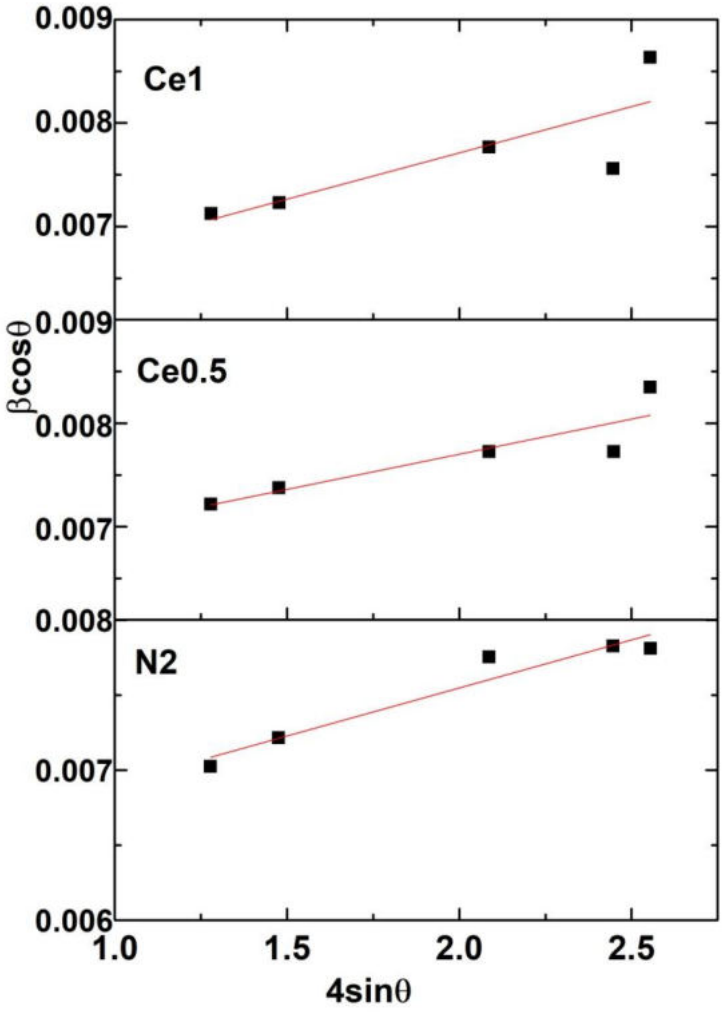

Figure 5.3 : W-H plots of pristine and Ce doped NiO samples

The crystallite size and microstrain calculated using W-H method (*Section 2.4.1*) are given in Table 5.1. These values are almost analogous to the size calculated from their XRD patterns. Micro-strain is found to increase with doping concentration, which indicates the increase in defects and lattice imperfections caused by doping.

Table 5.1 : Structural parameters of pristine and Ce doped NiO samples

Sample	FWHM (200) plane	Lattice spacing d_{200} (Å)	Lattice constant a (Å)	Unit cell volume (Å^3)	Average crystallite size (nm)		Microstrain (x 10^{-4})
					Scherrer method	W-H method	
N2	0.485^o	2.088	4.176	72.83	17.8±0.35	21.8±0.44	6.39
Ce0.5	0.455^o	2.086	4.172	72.62	18.4±0.37	21.6±0.43	6.79
Ce1	0.446^o	2.085	4.17	72.50	18.9±0.38	23.1±0.46	8.94

5.3.2.2 FESEM and EDX Analyses

FESEM analysis was performed to observe the morphological features and changes of Ce doped samples from that of pristine NiO nanoparticles. The resulting images are depicted in Figure 5.4. The samples contain polygonal faceted nanoparticles which are well dispersed in the bulk lattice. The voids observed in the pristine sample are covered with clusters of nanoparticles as evident from Ce0.5 and Ce1 micrographs, caused by doping. A careful inspection of SEM images under higher magnification further revealed the haziness on the surface of Ce doped NiO nanoparticles. This may be due to the accumulation of Ce ions over NiO crystals and is in good agreement with the results of XRD analysis.

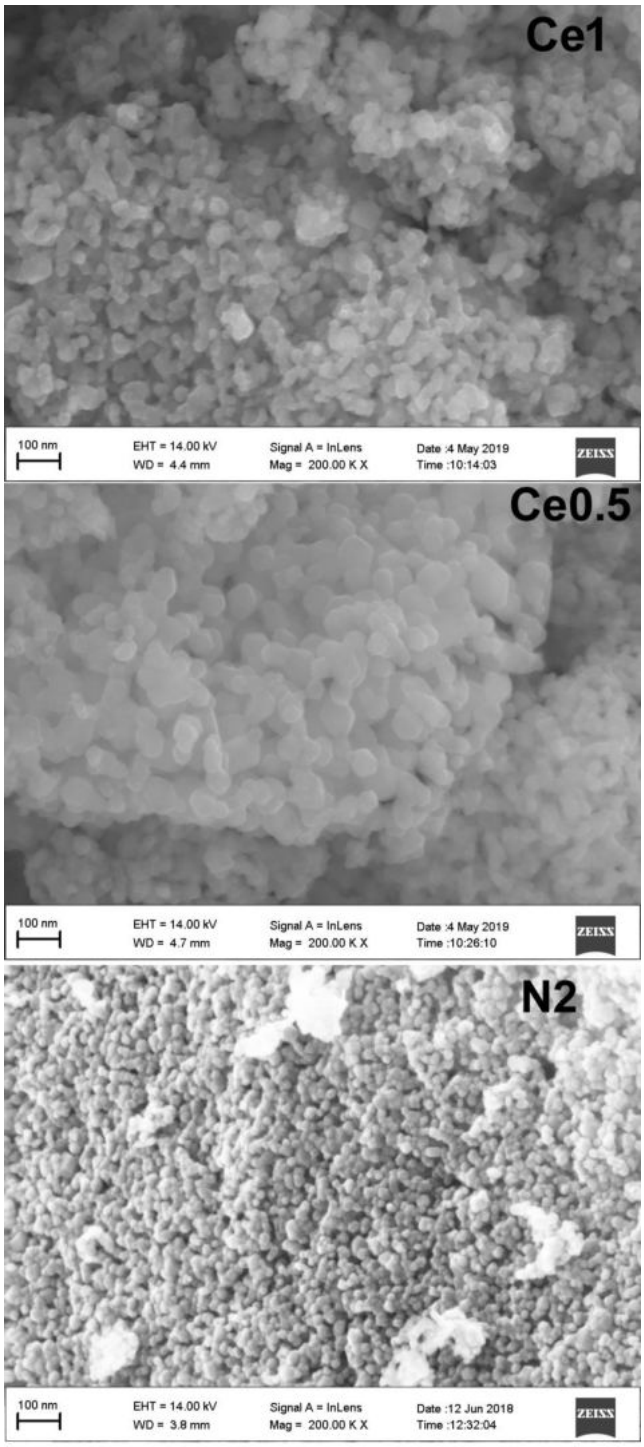

Figure 5.4 : FESEM images of pristine and Ce doped NiO samples

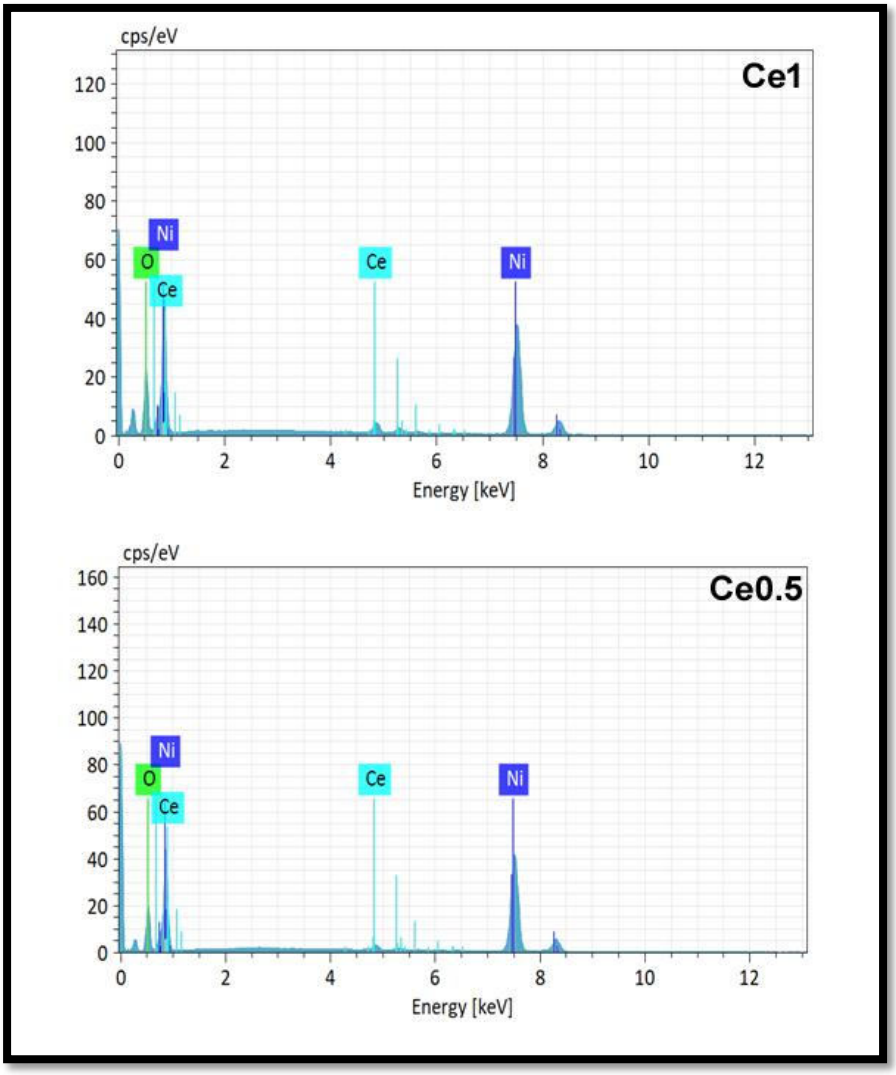

Figure 5.5 : EDX patterns of Ce0.5 and Ce1 samples

Figure 5.5 illustrates the EDX patterns of Ce0.5 and Ce1samples, which confirm the presence of nickel, oxygen and cerium as the only elementary species in the sample. The presence of Ce in the EDX spectrum shows the successful formation of Ce doped NiO. The absence of the other element peaks in the spectrum reveals the purity of the prepared nanoparticles. The chemical composition of the doped samples is presented in Table 5.2.

Table 5.2 : Chemical composition of Ce0.5 and Ce1 samples

Sample	Atomic percentage		
	Ni	**O**	**Ce**
Ce0.5	53.05	45.88	1.08
Ce1	48.73	49.53	1.74

5.3.2.3 TEM Analysis

The size and morphology of Ce-doped NiO samples are further investigated by TEM analysis. The TEM bright field images, HRTEM images and SAED patterns of the samples N2, Ce0.5 and Ce1 are shown in Figure 5.6. The bright field images of the samples (Figure 5.6 (a)) show a uniform distribution of nanoparticles with polygonal morphology. The crystallinity of the samples is confirmed by the unidirectional fringe pattern in the HRTEM images. The structural parameters obtained from TEM images are shown in Table 5.3. The HRTEM image (Figure 5.6 (b)) of Ce0.5 sample shows fringe patterns with different orientations, one with a d - spacing of 0.24 nm corresponding to (200) plane and the other with a d - spacing of 0.28 nm representing (111) plane of NiO, while Ce1 sample has fringe patterns with a d – spacing of 0.18 nm and 0.28 nm corresponding to the (220) and (111) planes respectively. The SAED pattern shows diffraction rings corresponding to (111), (200), (220), (311) and (222) planes of NiO revealing the highly crystalline nature of these nanoparticles. The innermost faint ring corresponds to the (111) plane of CeO_2. The TEM images show the presence of CeO_2 in the doped sample, which is in

agreement with the XRD result. Histograms showing the particle size distribution of the samples are shown in Figure 5.7. The large size of N2 indicates aggregation of the particles. The particle size of the doped samples reduced considerably. Thus the addition of Ce ions prevents aggregation of NiO nanoparticles.

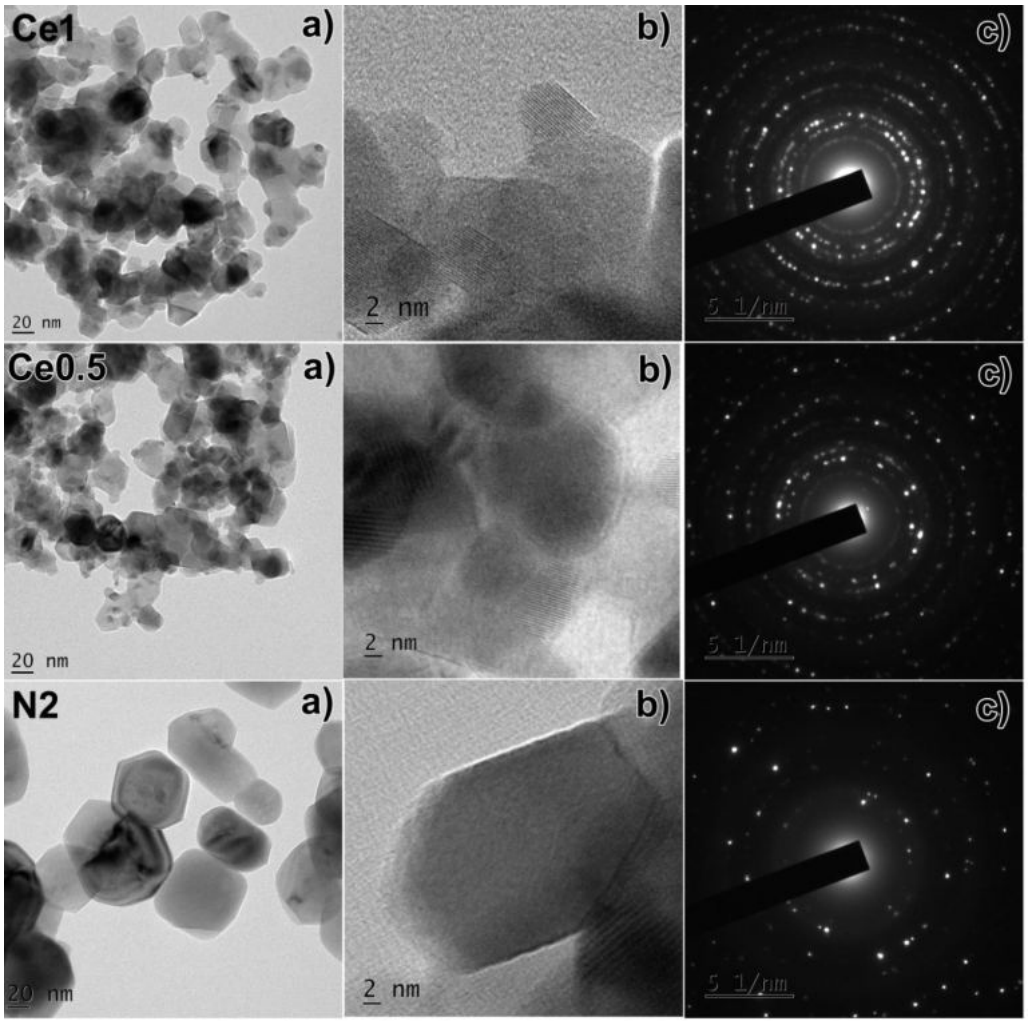

Figure 5.6 : **(a)** Bright field images,
(b) HRTEM images and
(c) SAED patterns of pristine and Ce doped NiO samples

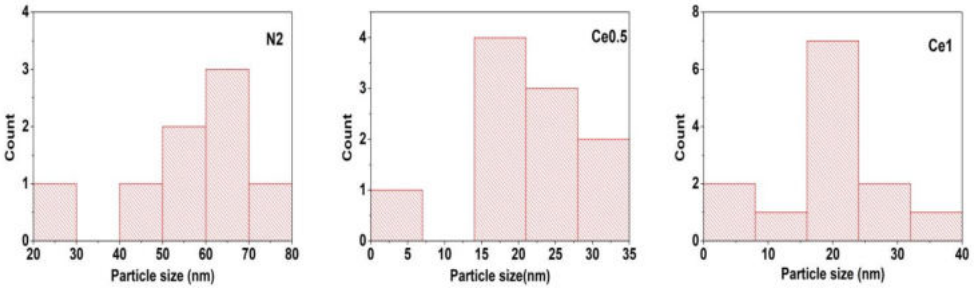

Figure 5.7 : Particle size distributions of pristine and Ce doped NiO samples

Table 5.3 : Lattice parameters of pristine and Ce doped NiO samples from TEM images

Sample	Particle size from TEM images (nm)	d spacing from SAED patterns (Å)		
		(111)	(200)	(220)
N2	57±1.14	2.786	2.472	1.718
Ce0.5	21.9±0.44	2.800	2.413	1.696
Ce1	21.5±0.43	2.856	2.432	1.720

5.3.2.4 FTIR Spectroscopy

Figure.5.8 shows the FTIR spectra of pure and Ce doped NiO samples in the range 400 to 4000 cm^{-1}. All the samples exhibited a strong absorption peak at around 410 cm^{-1} which corresponds to Ni-O stretching vibration of face-centred cubic crystal structure [14]. A wide absorption band between 3300 and 3600 cm^{-1} and a narrow band at 1625 cm^{-1} are seen, their intensities increase with increase in doping concentration of Ce in NiO. These bands are attributed to the stretching vibrations of the

O– H groups and the bending vibrations of the adsorbed water molecules, respectively [15, 16]. No additional absorption peaks are observed in the spectrum of doped samples. The peak corresponding to Ni-O bond shifts to lower wavelength indicating the incorporation of Ce ions.

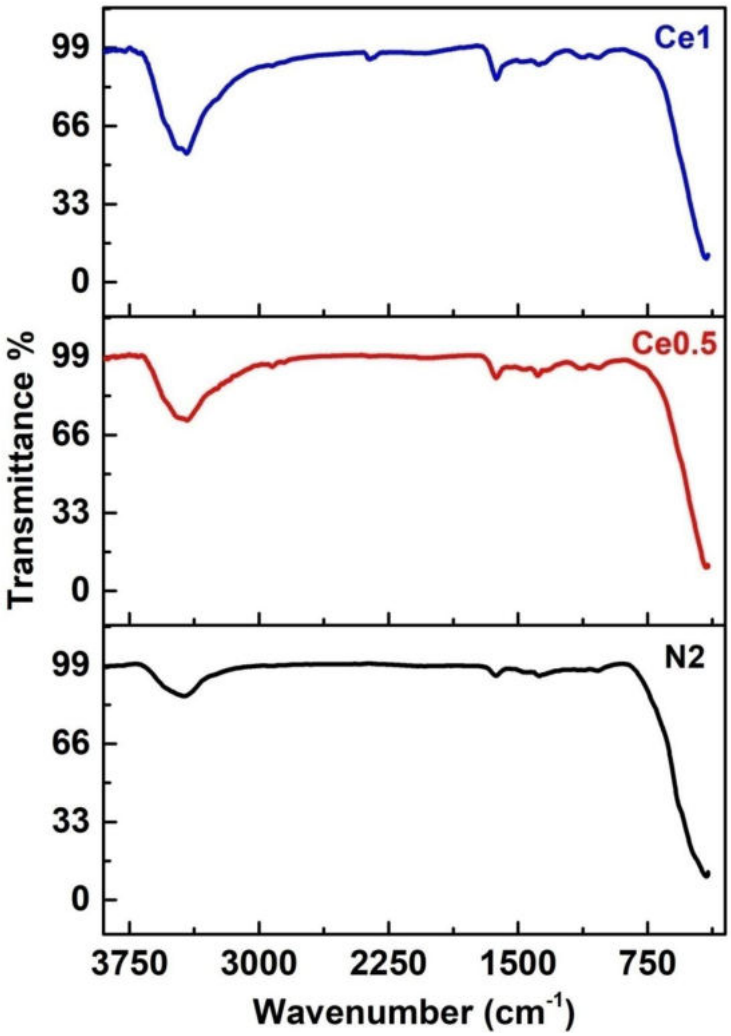

Figure 5.8 : FTIR spectra of pristine and Ce doped NiO samples

5.3.2.5 XPS Analysis

The binding energy and oxidation states of the constituent ions present in the samples are examined using XPS technique. The XPS wide spectrum of a typical sample (Ce1) of Ce doped NiO is shown in Figure 5.9(a). The characteristic peaks corresponding to Ni, O and Ce are observed in the spectrum. The high-resolution scans of Ni 2p, O1s and Ce 3d are shown in Figure 5.9(b) – (d), respectively. The Ni *2p* spectrum of the doped sample exhibits the characteristic double peaks for $2p_{3/2}$ and $2p_{1/2}$ main lines. The peaks appearing at binding energies 853.8 and 855.1 eV correspond to Ni$2p_{3/2}$A and Ni$2p_{3/2}$B and those at 871.5 and 872.6 eV to Ni$2p_{1/2}$A and Ni$2p_{1/2}$B respectively [17]. The high resolution O*1s* spectra can be resolved into three peaks centred at 529.2, 531 and 533.3 eV, which corresponds to O*1s* core level of the O^{2-} anions in the sample, oxygen ions in the oxygen deficient regions and OH related species or the loosely bound oxygen on the surface from H_2O, respectively [18]. In the XPS spectrum of Ce element shown in Figure 5.9 (d), the peaks at binding energies of 898.6 and 916.5 eV can be attributed to Ce^{4+} *3d3/2* and Ce^{4+} *3d5/2*, respectively. The peaks at binding energies of 881.2 and 907.5 eV can be attributed to Ce^{3+} *3d3/2* and Ce^{3+} *3d5/2*, respectively [19, 20]. Thus, mixed valences of Ce^{3+} and Ce^{4+} coexisted in Ce doped NiO samples.

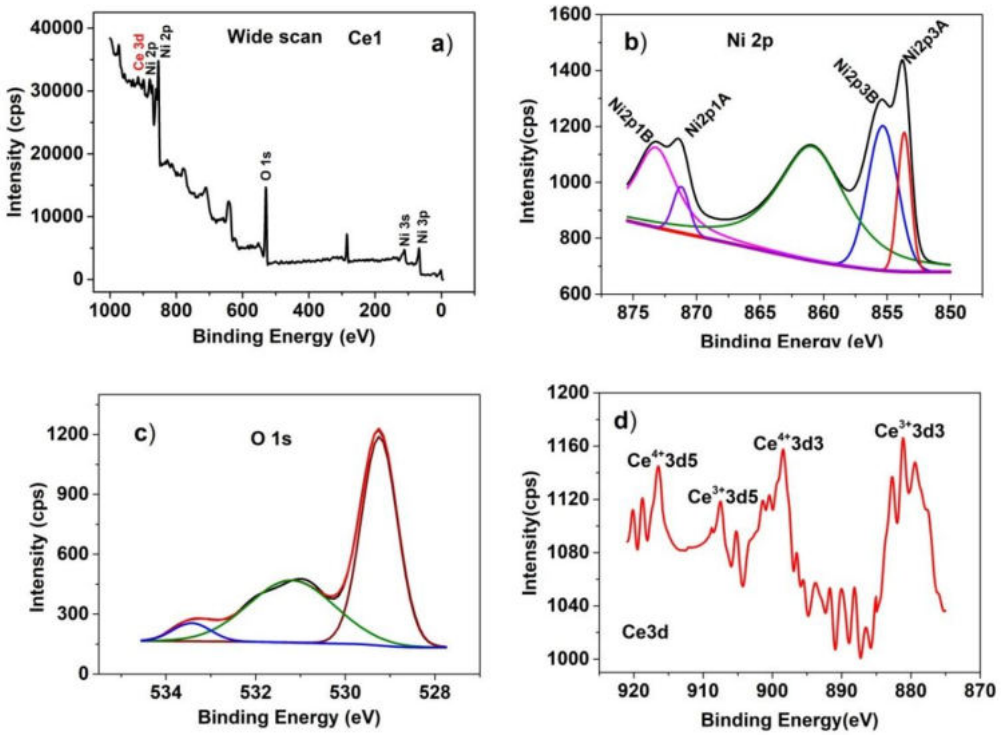

Figure 5.9 : XPS spectra of sample Ce1 **(a)** wide scan, **(b)** Ni 2p, **(c)** O 1s and **(d)** Ce 3d

5.3.3 Optical Properties

UV-Vis absorption and photoluminescence studies of pristine and Ce doped nanocrystalline NiO are presented here. The analyses were carried out by following the procedure as given in *Section 2.5.*

5.3.3.1 UV-Visible Spectroscopy

Optical properties of pristine and Ce doped NiO nanoparticles are measured in the wavelength range 200 – 800 nm by diffuse reflectance spectroscopy at room temperature. The absorbance of the samples obtained by Kubelka–Munk transformation is shown in Figure.5.10. The doped samples exhibit a single and well defined absorption peak in the UV region similar to the pristine NiO. An enhanced UV absorption has been observed for the doped samples.

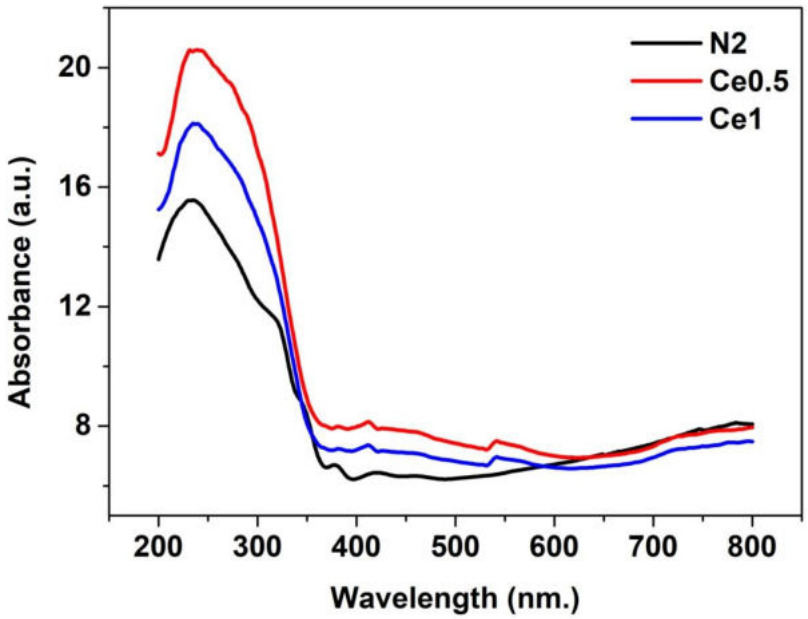

Figure 5.10 : UV visible absorption spectra of pristine and Ce doped NiO samples

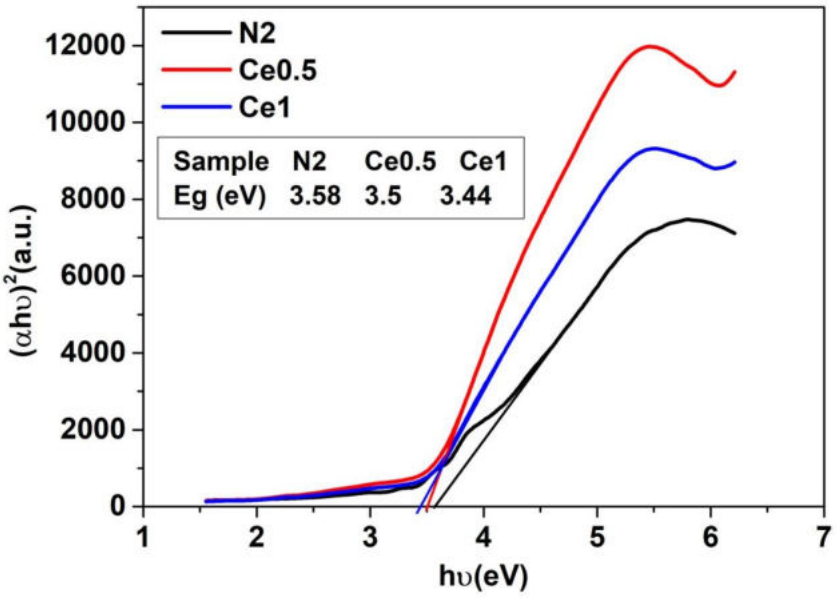

Figure 5.11 : Tauc plots of pristine and Ce doped NiO samples

The optical bandgap values obtained from the Tauc plots shown in Figure 5.11 for N2, Ce0.5 and Ce1 are 3.58, 3.5 and 3.44 eV, respectively. The reduction in bandgap energy may be due to the formation of Ce related defect levels in the forbidden energy gap close to the conduction band minima of NiO [21]. The Ce *4f* and oxygen defect levels formed beneath the conduction band minimum allow a maximum of the electronic transitions to occur to these levels only [22, 23].

5.3.3.2 PL spectroscopy

The room temperature emission spectra of N2, Ce0.5 and Ce1 samples at an excitation wavelength of 280 nm are shown in Figure 5.12. Broad emission in the spectral range from 300 to 500 nm, along with well resolved shoulder peaks are observed in the PL spectrum of pristine NiO. As discussed in *Section 3.3.3.2,* these are attributed to the near band edge (NBE) transition of NiO and defect related deep level emissions [24]. Ce dopant does not give rise to new PL emission, but shows a decrease in intensity with increase in doping concentration. It is obvious that the near bandgap emission suffers suppression on doping with Ce. The impurity band formed below the minimum of the conduction band on Ce doping traps the excited electrons and inhibits the recombination of the photo-generated electron–hole pairs [22]. The shoulder peaks experience intensity reduction as the surface bound states formed by doping act as defect states causing non – radiative relaxation [25]. Thus, enhanced photocatalytic activity is expected for the Ce doped NiO samples.

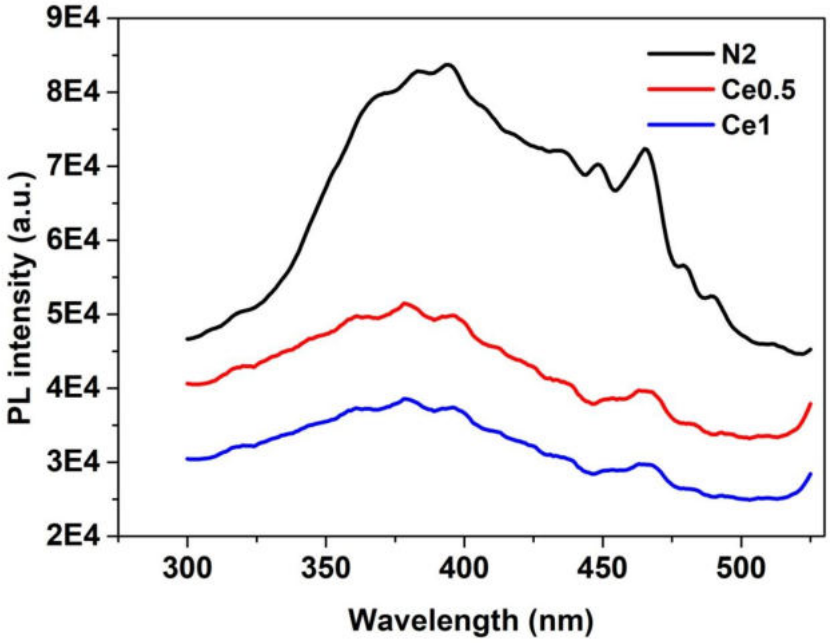

Figure 5.12 : PL emission spectra of pristine and Ce doped NiO samples

5.3.4 Electrical Properties

The electrical studies are carried out by following the procedure discussed in *Section 2.6*. The pristine and Ce doped NiO nanoparticles are consolidated in the form of cylindrical pellets of diameter 13 mm and thickness 1.2 mm by applying a pressure of ~ 7 tons using a hydraulic press.

5.3.4.1 Dielectric Properties

The dielectric constant (ε') and loss tangent ($tan\ \delta$) of Ce doped NiO nanoparticles are studied as a function of frequency in the range 100 Hz – 5 MHz at different temperatures.

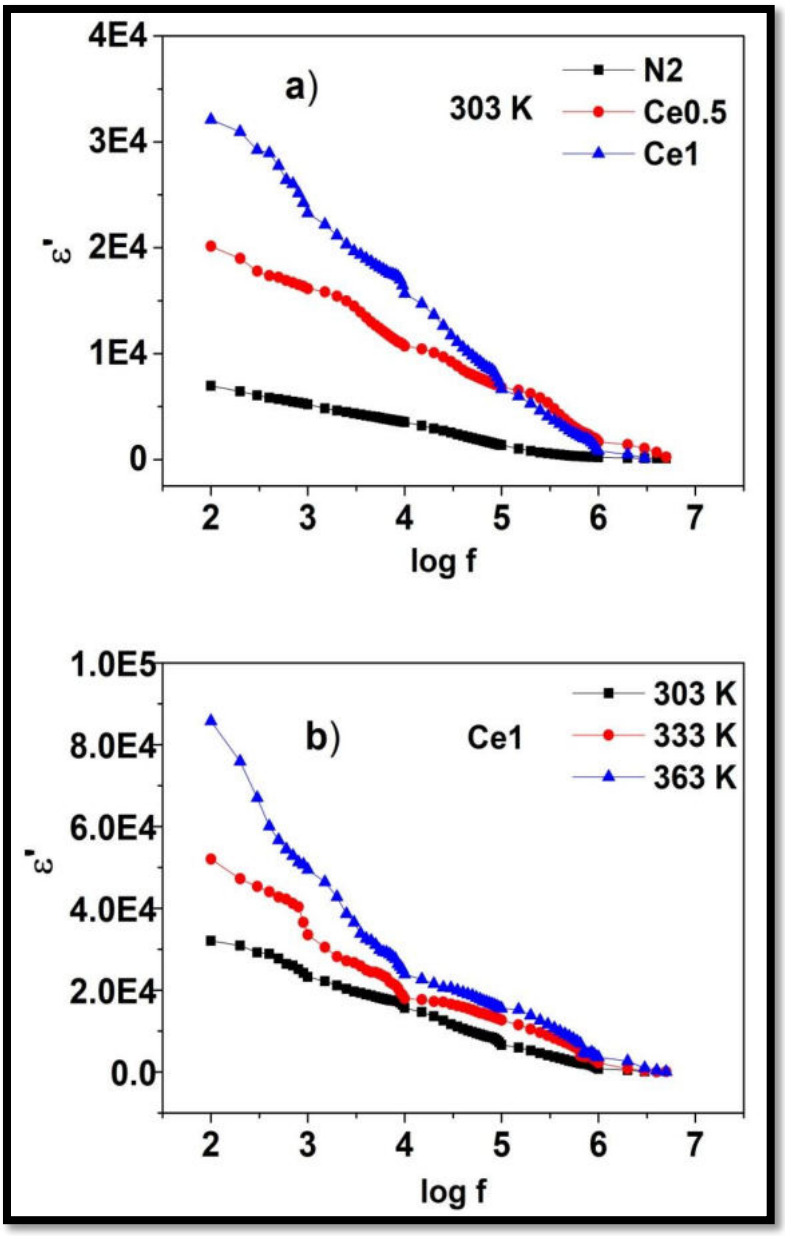

Figure 5.13 : Variation of dielectric constant with frequency and temperature;
(a) pristine and Ce doped NiO samples at 303 K, and
(b) Ce1 at selected temperatures

The variation of dielectric constant with frequency at room temperature of the samples N2, Ce0.5 and Ce1 is shown in Figure 5.13(a). All the samples exhibit the same behaviour. The value of ε' is high in the low frequency region and exhibits a gradual decrease with increase in frequency and remains almost constant in the high frequency area. The dielectric behaviour of the samples can be explained by Maxwell–Wagner type interfacial polarization using Koop's phenomenological theory [26, 27] as discussed in *Section 3.3.4.2.* The dielectric constant is also found to increase with the increase in dopant concentration. It may be due to the very high dielectric polarizability of Ce^{3+} ions (6.01) compared to Ni^{2+} ions (1.23) [28]. Hence with an increase in dopant concentration, more Ni ions will be replaced by Ce ions, thereby increasing the dielectric polarization and hence the dielectric constant [29].

The representative graph showing the variation of dielectric constant as a function of frequency at different temperatures for the sample Ce1 is shown in Figure 5.13 (b). The dielectric constant is found to increase with the increase in temperature of the sample (from 303-363 K) due to the increase in number of thermally promoted carriers. As a result, the accumulation of charge carriers at the grain boundaries increases causing an increase in interfacial polarization and hence the dielectric constant [30].

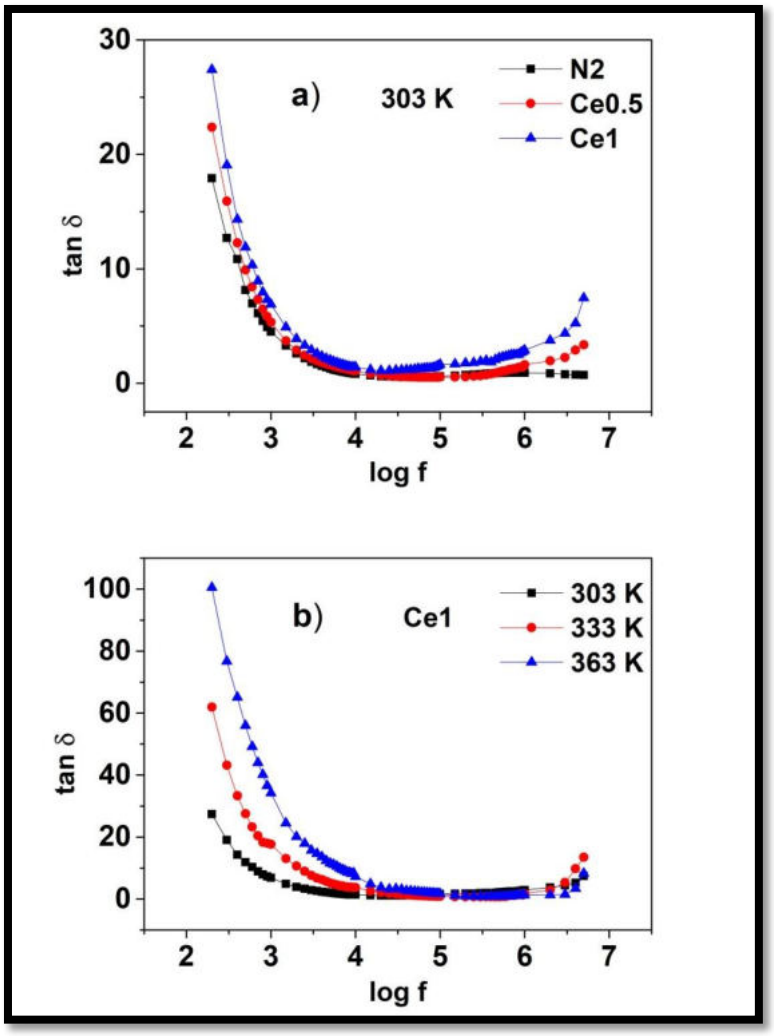

Figure 5.14 : Variation of dielectric loss with frequency and temperature;
(a) pristine and Ce doped NiO samples at 303 K, and
(b) Ce1 at selected temperatures

The dielectric loss as a function of frequency at room temperature is shown in Figure 5.14 (a). Due to space charge polarization, *tan δ* is high in the frequency region and it decreases with increase in frequency for all the samples [31]. The loss tangent is found to increase with dopant concentration. The absorption current produced due to impurities, defects

and space charge formation in the interphase layers results in a dielectric loss [32]. The presence of doping species further enhances the defects and interstitial ions, which leads to an increase in *tan δ.*

The representative graph showing the variation of *tan δ* of sample Ce1 with frequency, at different temperatures is shown in Figure 5.14 (b). The value of *tan δ* is found to increase with the increase in temperature. The impurity ions in the bulk crystal matrix capture the surface electrons, leading to the surface charge polarization. The increase in temperature increases the electron capture process, which in turn enhances the dielectric loss [33].

5.3.4.2 Impedance Analysis

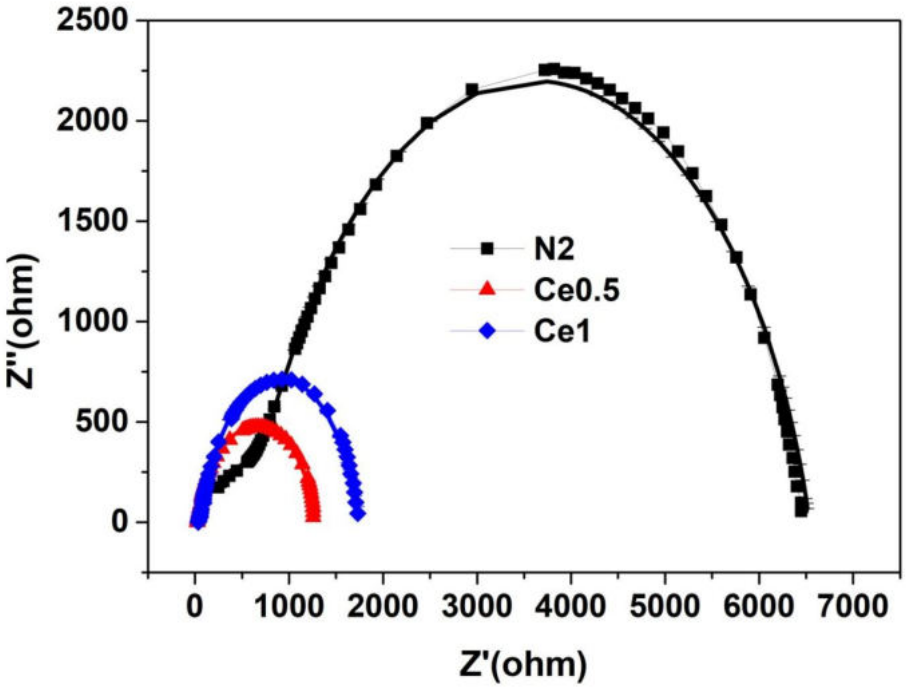

Figure 5.15 : Nyquist plots of pristine and Ce doped NiO samples

Figure 5.15 shows the Nyquist plots of pristine and Ce doped NiO nanoparticles. The experimental data are fitted using EIS Spectrum Analyser software. The solid lines represent experimental data and the symbols represent fitted data. The plot of imaginary impedance versus the real impedance shows two semicircles for undoped NiO, the first one is assigned to the charge transfer in the grains and the second semicircle is attributed to grain boundaries. The semicircle corresponding to grain contribution is not resolved in Ce0.5 and Ce1 indicating the predominance of grain boundary resistance over grain resistance.

Table 5.4 : Impedance parameters of pristine and Ce doped NiO samples

Sample	**CPE_g (F)**	**R_g (Ω)**	**β_g**	**CPE_{gb} (F)**	**R_{gb} (Ω)**	**β_{gb}**
N2	1.32E-08	723	0.696	1.88E-08	5813	0.821
Ce0.5	-	-	-	7.86E-08	1675	0.890
Ce1	-	-	-	9.86E-08	1270	0.844

Typical values of the parameters R, C and β for grain (R_g, CPE_g, β_g) and grain boundaries (R_{gb}, C_{gb}, β_{gb}) obtained from the fits are summarized in Table 5.4. The grain resistance is very small for the doped samples.

5.3.4.3 AC Conductivity

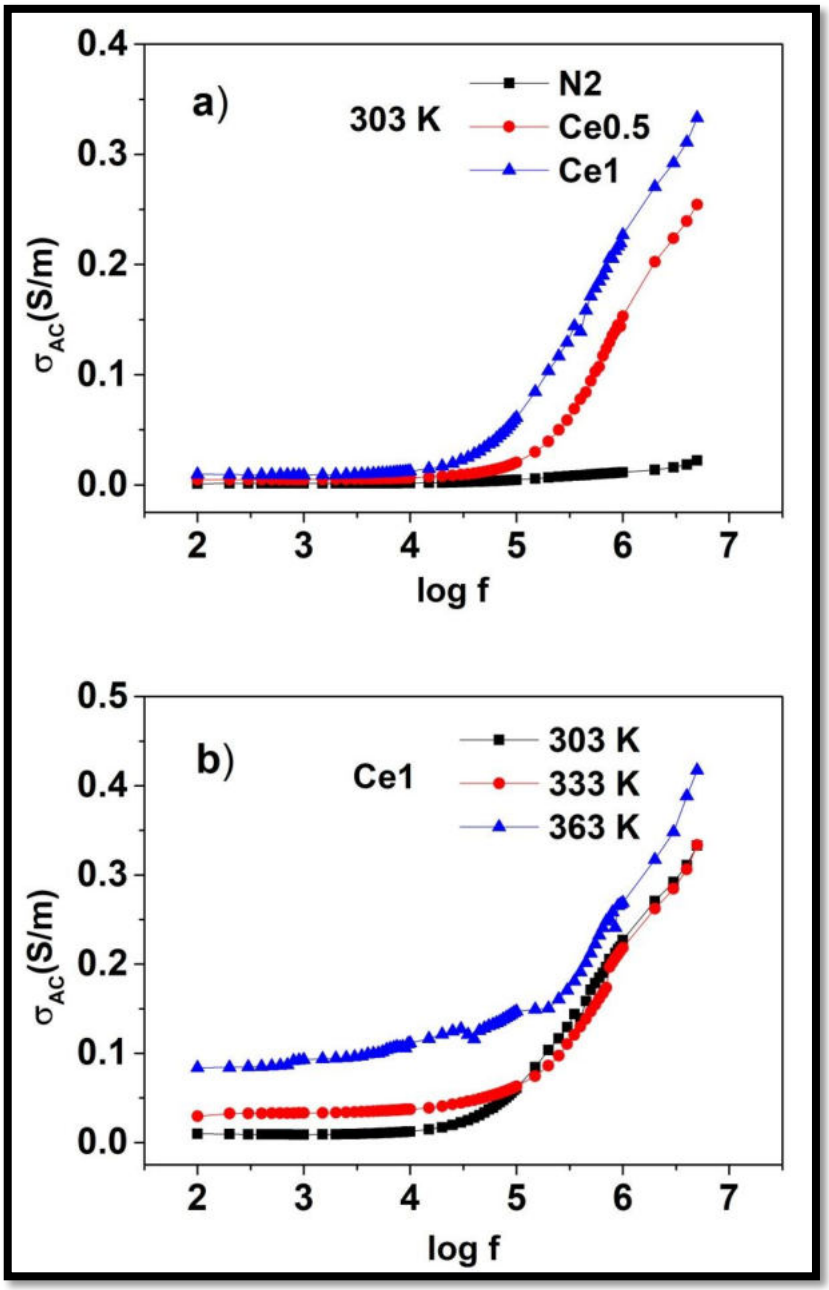

Figure 5.16 : Variation of AC conductivity with frequency and temperature;
(a) pristine and Ce doped NiO samples at 303 K, and
(b) Ce1 at selected temperatures

The variation of AC conductivity (σ_{AC}) with frequency of the applied field for the pristine and Ce doped NiO nanoparticles at 303 K is illustrated in Figure 5.16 (a). For all the samples σ_{AC} is found to be frequency independent up to about 10 kHz, thereafter increases rapidly with increase in frequency. The conductivity in the low frequency region represents DC conductivity due to band conduction. The increase in σ_{AC} with frequency is related to the increase in the drift mobility of the electrons and holes by the hopping conduction [34]. The value of σ_{AC} is found to increase with the increase in dopant concentration. The incorporation of Ce ions into the NiO lattice increases the number of charge carriers, which leads to the enhanced conductivity of doped samples [35].

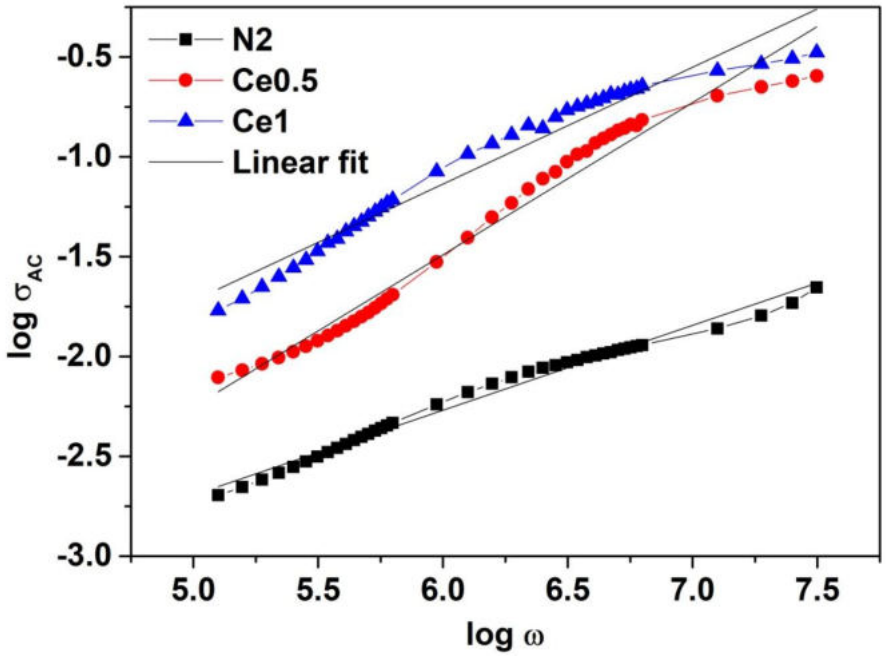

Figure 5.17 : Jonscher's power law plots of pristine and Ce doped NiO samples at 303 K

Figure 5.17 shows the Jonscher's power law plot of N2, Ce0.5 and Ce1 samples [36]. The values of the exponent ***s*** calculated from the slope of the logarithmic plots of AC conductivity versus angular frequency are 0.43, 0.76 and 0.58 respectively for N2, Ce0.5 and Ce1 samples. The values of ***s*** lie between 0 and 1 characterizing hopping conduction [37].

The variation of σ_{AC} with the frequency of Ce1 sample at selected temperatures is shown in Figure 5.16 (b). The increase in conductivity with temperature is due to the increase in drift mobility of the charge carriers, which enhances the carrier hopping probability [38].

5.3.5 Magnetic Properties

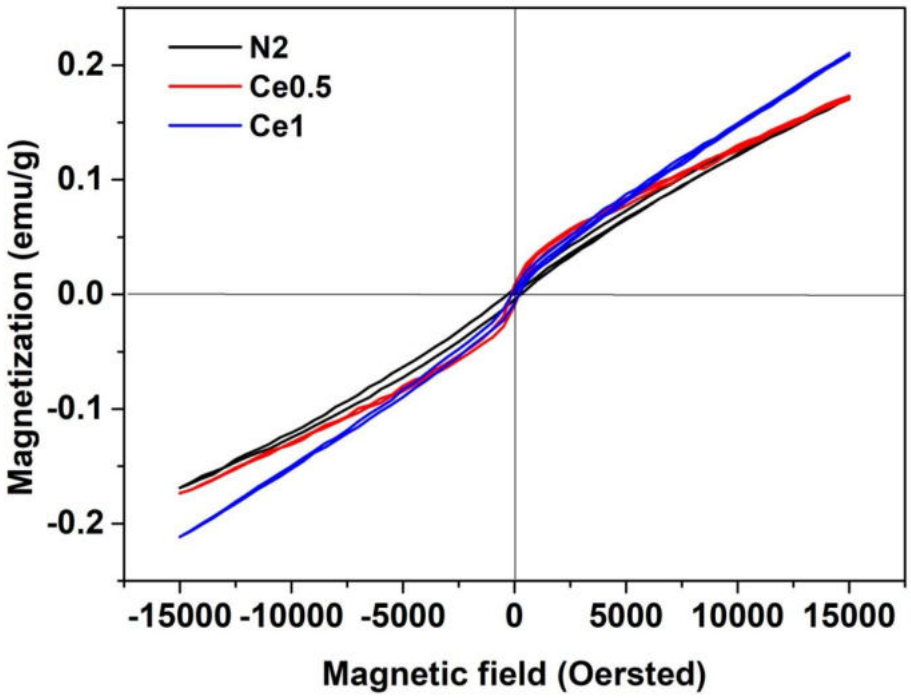

Figure 5.18 : M – H curves of pristine and Ce doped NiO samples

The room temperature magnetic behaviour of pristine and Ce doped NiO nanoparticles are presented in Figure 5.18. The curves of all the samples show hysteresis loops representing weak ferromagnetic behaviour. However, saturation is not attained even for a maximum applied field of 15 kOe, which is a characteristic of the superparamagnetic ordering of the spins in the samples [4]. The magnetization is found to increase with the increase in Ce doping concentration. Measured values of maximum magnetization are 0.17 0.173 and 0.211 emu/g for N2, Ce0.5 and Ce1 samples respectively. The change in the oxidation state of Ce from +4 to +3 generates unpaired spin in the Ce *f* orbital, which is responsible for the increased magnetization of the doped sample [39]. Also, the coercivity values of the samples are 291.7, 170.8 and 163.3 respectively, for N2, Ce0.5 and Ce1. The decrease in the value of coercivity reflects the superparamagnetic nature of the samples. With an increase in dopant concentration, the overlap of the Ce *4f* and Ni *3d* orbitals could enhance the superparamagnetic ordering in the samples [4].

5.4 Conclusion

- Cerium doped NiO nanoparticles have been synthesized by chemical co - precipitation method.

- Thermal analysis shows that the samples become thermally stable at 600^{o}C.

- A systematic study has been conducted on the effect of cerium doping on the structural, optical, electrical and magnetic properties of pristine nanocrystalline NiO.

- Crystallite size is found to increase with the increase in Ce doping concentration. XRD studies reveal the presence of CeO_2 phase in the sample doped with 1 mol% of Ce.

- XPS results show the coexistence of Ce^{3+} and Ce^{4+} states in the doped NiO samples.

- Enhanced UV absorption and reduction in bandgap occurred on Ce doping.

- Ce doped NiO nanoparticles show a decrease in PL intensity than that of pristine NiO due to the lower rate of electron–hole recombination. Thus, an enhanced photocatalytic property is expected for Ce doped NiO samples.

- Electrical properties of Ce doped NiO exhibit the same behaviour as that of the pristine sample, but an increase in dielectric permittivity, tangent loss and AC conductivity values are observed, which is attributed to the incorporation of dopant ions.

- The superparamagnetic ordering in the samples is found to increase with the dopant concentration.

References

1) L. Liao, H. X. Mai, Q. Yuan, H. B. Lu, J.C. Li, C. Liu, C.H. Yan, Z.X. Shen, T. Yu, J. Phys. Chem. C, 112 (2008) 9061 - 9065

2) L.F. Koao, H.C. Swart, F.B. Dejene, J. Rare Earths 2010, 28(2010) 206 - 210.

3) M. Yousefi, M. Amiri, R. Azimirad, A.Z. Moshfegh, J. Electroanal. Chem. 661 (2011) 106 - 112.

4) G. Anandha Babu, G. Ravi, T. Mahalingam, M. Navaneethan, M. Arivanandhan, Y. Hayakawa, J. Phys. Chem. C, 118 (2014) 23335 - 23348

5) P. Anjali, R. Wani, T.S. Sonia, A. S. Nair, S. Ramakrishna, R. Ranjusha, K.R.V. Subramanian, N. Sivakumar, C. Gopi Mohan, V. S. Nair, A. Balakrishana, Sci. Adv. Mater. 6 (2014) 1 - 8

6) S. R. Gawali, V. L. Patil, V. G. Deonikar, S. S. Patil, D. R. Patil, P. S. Patil, J. Pant, Journal of Physics and Chemistry of Solids 114 (2018) 28 - 35

7) S. R. Gawali, D. P. Dubal, V.G. Deonikar, S. S. Patil, S. D. Patil, P. Gomez-Romero, D. R. Patil, J. Pant, Chemistry Select, 1(2016) 3471 – 3478, doi.org/10.1002/slct.201600566

8) N. Krishna Chandar, R. Jayavel, J. Phys. Chem. Solids 73 (2012) 1164–1169

9) S. Jain, P. Swarup, IOSR-JAP e-ISSN: 2278-4861, 11(2)(2019) 75-85

10) K.K. Babitha, A. Sreedevi, K.P. Priyanka, B. Sabu, T. Varghese, Indian J. Pure Appl. Phys. 53 (2015) 596 – 603

11) P.E. Saranya, S. Selladurai, New J. Chem., 43 (2019) 7441-7456

12) R.D. Shannon, Acta Cryst. A 32 (1976) 751- 767

13) C. Mrabetn, M. Ben Amor, A. Boukhachem, M. Amlouk, T. Manoubi, Ceramics International 42 (5) (2016) 5963-5978

14) D.N. Srivastava, V.G. Pol, O. Palchik, L. Zhang, J.C. Yu, A. Gedanken, Ultrason. Sonochem. 12 (2005) 205 – 212

15) M. Alagiri, S. Ponnusamy, C. Muthamizhchelvan, J Mater Sci: Mater Electron 23 (2012) 728–732

16) L. Wu, Y. Wu, H. Wei, Y. Shi, C. Hu, Mater. Lett. 58 (2004) 2700 – 2703

17) M.A. van Veenendaal, G.A. Sawatzky, Phys. Rev. Lett. 70 (1993) 2459 – 2462

18) L. Cao, L.P. Zhu, Z.Z. Ye, .J. Phys. Chem. Solids, 74 (2013) 668–72

19) Y. N. Ou, G. R. Li, J. H. Liang, Z. P. Feng, Y. X. Tong, J. Phys. Chem. C, 114(2010) 13509 – 13514

20) Z. Wang, Z. Quan, J. Lin, Inorg. Chem., 46 (2007) 5237 – 5242

21) P. Pandey, R. Kurchania, F.Z. Haque, Optik (2015), http://dx.doi.org/10.1016/j.ijleo.2015.06.026

22) S.W. Chen, J. M. Lee, K. T. Lu, C. W. Pao, J. F. Lee, T. S. Chan, J. M. Chen, Appl. Phys. Lett. 97 (2010) 012104 - 012106.

23) B. Choudhury, B. Borah, A. Choudhury, Photochem. Photobiol., 88 (2012) 257 - 264

24) A. George, S. K. Sharma, S. Chawla, M.M. Malik, M.S. Qureshi, J. Alloys Compd., 509 (2011) 5942–5946

25) S. Muthu Kumaran, R. Gopalakrishnan, J. Sol-Gel Sci. Technol., 62 (2012) 193 – 200

26) K. W. Wagner, Am. Phys., 40 (1973) 317

27) C. G. Koops, Phys. Rev., 83 (1951) 121-124

28) R. D. Shannon, J. Appl. Phys., 73 (1993) 348 - 366

29) J. Kaur, V. Gupta, R. K. Kotnala, K.C. Verma, Indian J. Pure Ap. Phy., 50 (2012) 57 – 63

30) M. Ishaque, M.U. Islam, I. Ali, M.A. Khan, I.Z. Rahman, Ceramic Inter. 38 (2012) 3337

31) S. Kamba, V. Bovtun, J. Petzelt, I. Rychetsky, R. Mizaras, A. Brilingas, J. Banys, J.Grigas, M. Kosec, J. Phys.: Condens. Matter 12 (2000) 497

32) K.P. Priyanka, J. Sunny, T. Smitha, E.M. Mohammed, T. Varghese, J. Basic Appl. Phys. 2(2010)105

33) I. Khan, S. Khan, W. Khan, Mater. Sci.Semicond. Process., 26 (2014) 516 – 526

34) F.S.H. Abu-Samaha, M.I.M. Ismail, Mater. Sci. Semicond. Process., 19 (2014) 50 - 56.

35) N. Sharma, R. Kant, V. Sharma, S. Kumar, J. Electron. Mater., (2018) doi.org/10.1007/s11664-018-6305-7

36) A.K. Jonscher, Nature, 267 (1977) 673

37) A. R. Long, Adv. Phys., 31 (1982) 553

38) R. Nongjai, S. Khan, K. Asokan, H. Ahmed, I. Khan, J. Appl. Phys. 112 (2012)084321

39) S. Kumar, M. Srivastava, J. Singh, S. Layek, M. Yashpal, A. Materny, A. K. Ojha, AIP Adv., 5 (2015) 027109

…..ଘ❋ଌ…..

Chapter 6

SYNTHESIS AND CHARACTERIZATION OF NiO/M-Pc (M = Co, Sn) NANOPARTICLES

The synthesis of nickel oxide/metal phthalocyanine (NiO/M-Pc) nanocomposites and the studies on their structural, optical, electrical and magnetic properties are discussed in this chapter. NiO/M-Pc (M=Co, Sn) nanocomposites are prepared by solvent evaporation method and characterized using various characterization techniques.

6.1 Introduction

Organic/inorganic nanocomposite materials have attracted much attention because of the blending of their distinct physical and chemical properties. Organic materials offer interesting optical properties, structural flexibility, tunable electronic properties and the potential for semiconducting behaviour [1]. Phthalocyanines are p-type organic semiconductors with high stability, having a wide range of applications from medicine to microelectronics. Out of them, metal phthalocyanines (M-Pc) have invited attention due to their good thermal and chemical stability, photoconductivity and semiconducting nature [2]. Inorganic metal oxide nanoparticles provide the potential for high carrier mobility, bandgap tunability and a range of magnetic and dielectric properties [1]. This chapter focuses on the synthesis and characterization of nickel oxide/metal phthalocyanine (NiO/M-Pc; M=Co, Sn) nanocomposites. To date, no reports are available on the studies of the properties of NiO/M-Pc nanocomposite. The objective of this work is to study the effect of cobalt and tin phthalocyanines on the structural, optical, electrical and magnetic properties of NiO in detail.

6.2 Synthesis of NiO/M-Pc (M = Co, Sn) Nanocomposites

The solvent evaporation method is employed for the synthesis of NiO/M-Pc (M = Co, Sn) nanocomposites. NiO nanoparticles calcined at 500^{o}C, cobalt phthalocyanine (CoPc) and tin phthalocyanine (SnPc) (Sigma-Aldrich), dimethyl formamide, dimethyl sulphoxide and ethanol (Merck) are used for the synthesis of the nanocomposites.

A solvent mixture containing 50% dimethyl sulphoxide, 30% dimethyl formamide and 20% ethanol is prepared. 1 wt % cobalt/tin phthalocyanine is dissolved in the mixture under constant magnetic stirring and simultaneous heating at 60^{o}C. NiO nanoparticles prepared by chemical precipitation method and calcined at 500^{o}C [3] are gradually added to this solution under stirring and heating, resulting in a homogeneous suspension. After complete evaporation of the solvent mixture, the obtained material is dried at 100^{o}C in a hot air oven to get the sample in powder form. The scheme for the synthesis is shown in Figure 6.1. The synthesized NiO nanoparticles, NiO/CoPc nanocomposite and NiO/SnPc nanocomposites are denoted as N1, NCo and NSn respectively.

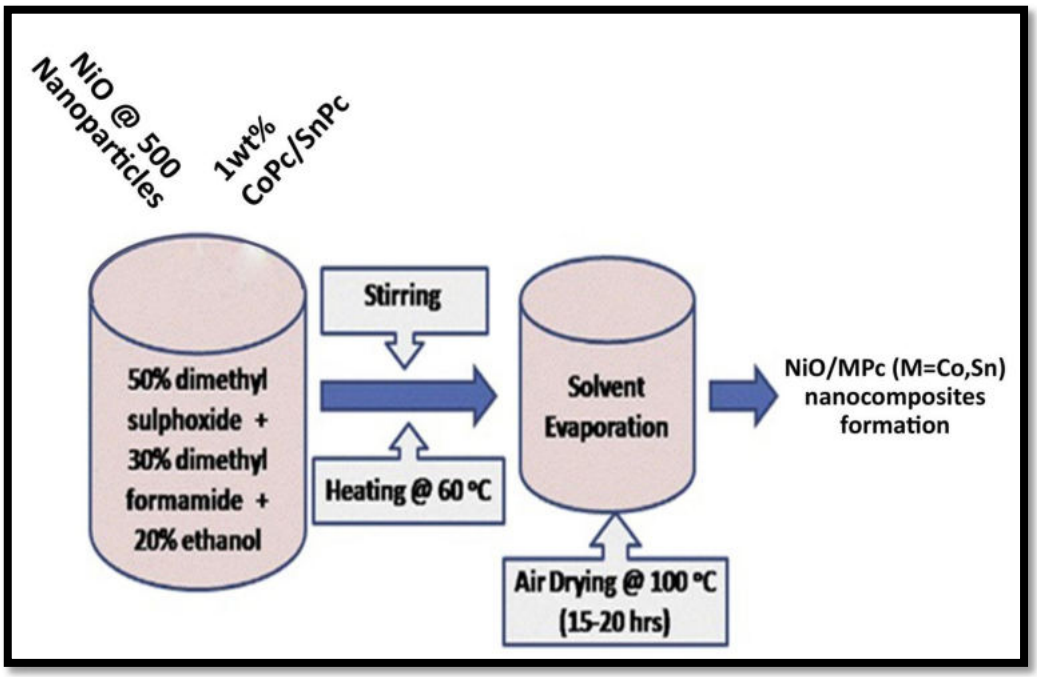

Figure 6.1 : Scheme of preparation of NiO/M-Pc (M = Co, Sn) nanocomposites

6.3 Results and Discussion

The thermal stability of the synthesized precursor is studied using the procedure described in *Section 2.3*. The structural, optical, electrical and magnetic characterizations of the samples are carried out using various techniques described in *Chapter 2*.

6.3.1 Thermal Analysis

The thermal analysis of the synthesized nanocomposites is carried out using the procedure described in *Section 2.3*. The TGA/DTA/DTG curves of NCo and NSn nanocomposites are shown in Figure 6.2 (a) and (b). The TGA curves for both the samples show a small weight loss from room temperature to 700^{o}C. The total weight loss is around 5% for both the samples which confirms the thermal stability of the nanocomposites. The weight loss up to 400^{o}C is related to the evaporation of trapped solvents such as water and ethanol. A comparatively sharp weight loss (1%) around 400^{o}C occurred due to the partial decomposition of macrocyclic structure, which results in the loss of low weight atoms from the composite structure [4].

The DTG curve of NCo shows two endothermic peaks positioned around 60 and 428°C, while three endothermic peaks are observed in the DTG curve of NSn at around 60, 369 and 475°C. These peaks correspond to the combustion of organic residues, oxidative degradation and fragmentation of one unit of the peripheral environment of the phthalocyanine molecule [5]. Thermal analysis confirms the thermal stability of the nanocomposite in the temperature range.

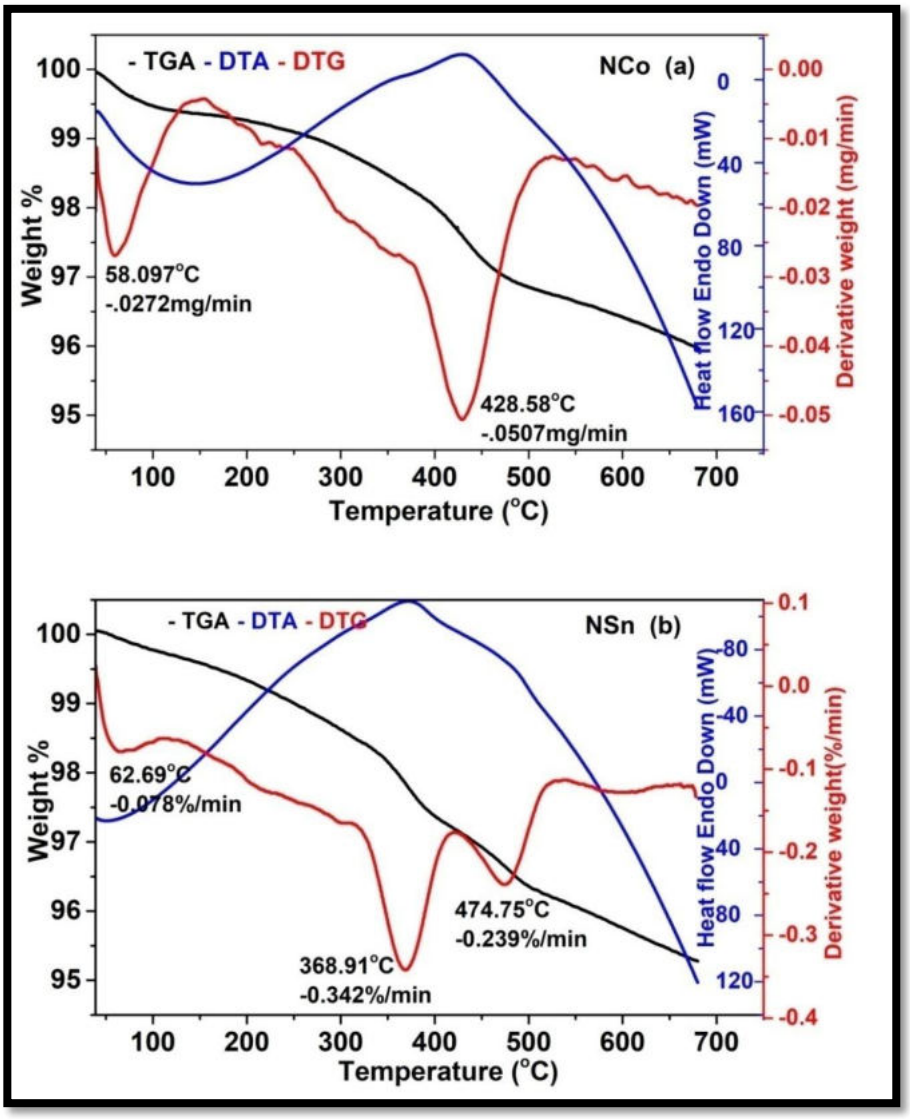

Figure 6.2 : TG/DTA curves of samples **(a)** NCo **(b)** NSn

6.3.2 Structural characterization

The structural analyses of the nanocomposites are done by following the procedure described in *Section 2.4*.

6.3.2.1 Powder XRD Analysis

Figure 6.3 represents the XRD patterns of synthesized nanocomposites and pristine NiO samples.The nanocomposite samples are scanned in the 2θ range from 0 to 90° at increments of 0.02° with a step time of 59.7s.

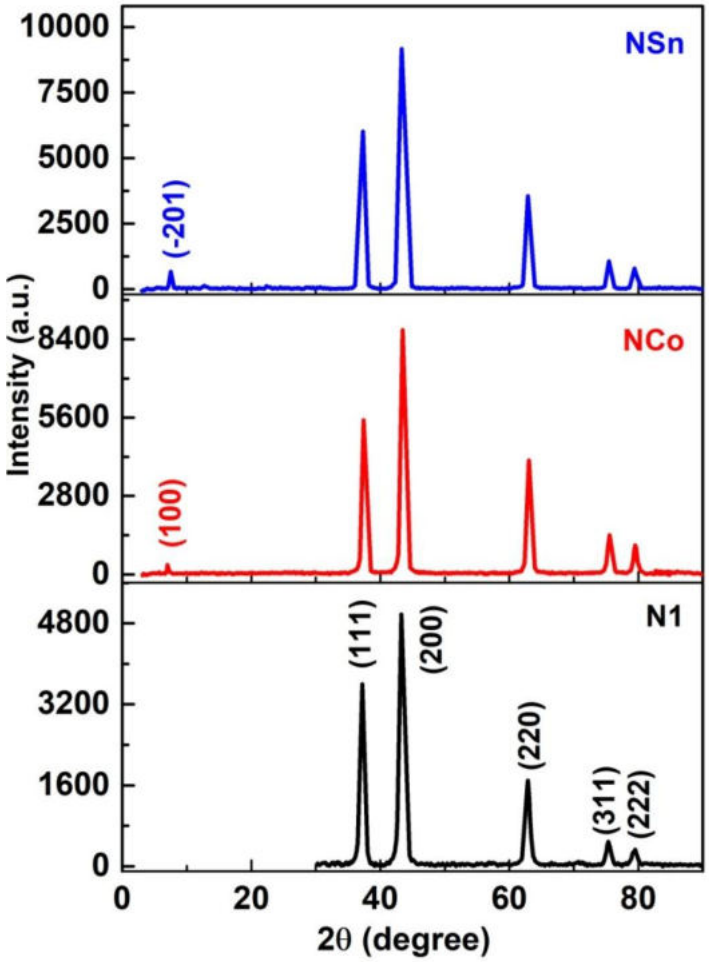

Figure 6.3 : XRD patterns of samples N1, NCo and NSn

The crystalline nature of the synthesized nanocomposites is evident from the sharp diffraction peaks in the XRD patterns of NCo and NSn. The intensity of the peaks is relatively higher in the nanocomposite

samples. The 2θ values revealed the formation of face centred cubic phase of NiO (JCPDS Card 73-1519) which can be indexed as (111), (200), (220), (311) and (222) planes. The diffraction pattern of NCo contains a weak additional peak at 7.085° which confirms the formation of NiO/CoPcnanocomposite. This peak corresponds to (100) plane of β CoPc [6]. The peak at 7.522° in the diffraction pattern of NSn corresponds to the (-201) plane of SnPc [7].

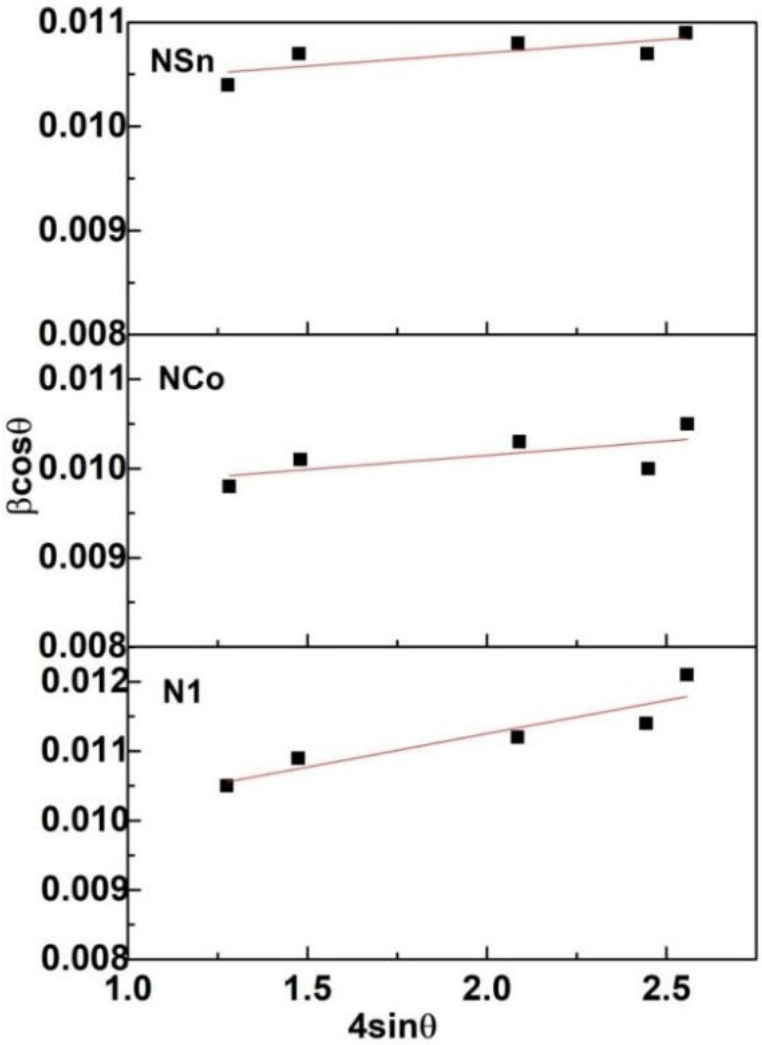

Figure 6.4 : W-H plots of samples N1, NCo and NSn

The structural parameters of samples calculated from XRD patterns are given in Table 6.1. The shifts of the (200) peaks to higher angles indicate a reduction in the lattice constant for the nanocomposite samples. The average crystallite sizes estimated using Scherrer's equation (*Eq: 2.3*) are 12.4, 13.3 and 13.8 nm for samples N1, NCo and NSn respectively. W-H plots of NiO and the nanocomposite samples are shown in Figure 6.4. The crystallite size calculated from W–H analysis for samples N1, NCo and NSn are 13.5, 14.7 and 14.4 nm respectively. The micro-strain is slightly reduced in the nanocomposite samples which indicate the successful incorporation of phthalocyanine into the NiO lattice.

Table 6.1 : Structural parameters of samples N1, NCo and NSn from XRD data

Sample	Average crystallite size (nm)		Lattice spacing d_{200} (Å)	Lattice constant a (Å)	Micro-strain (x 10^{-4})
	Scherrer method	W-H analysis			
N1	12.4±0.25	14.7±0.30	2.089	4.178	9.718
NCo	13.3±0.27	15.7±0.31	2.082	4.164	3.203
NSn	13.8±0.28	15.4±0.31	2.087	4.174	2.578

6.3.2.2 FESEM and EDX Analyses

FESEM images of N1, NCo and NSn samples are shown in Figure 6.5. The micrographs of both nanocomposites show more clusters of

particles indicating particle growth. Compared to the pristine sample, the particles are aggregated leaving no space in between them.

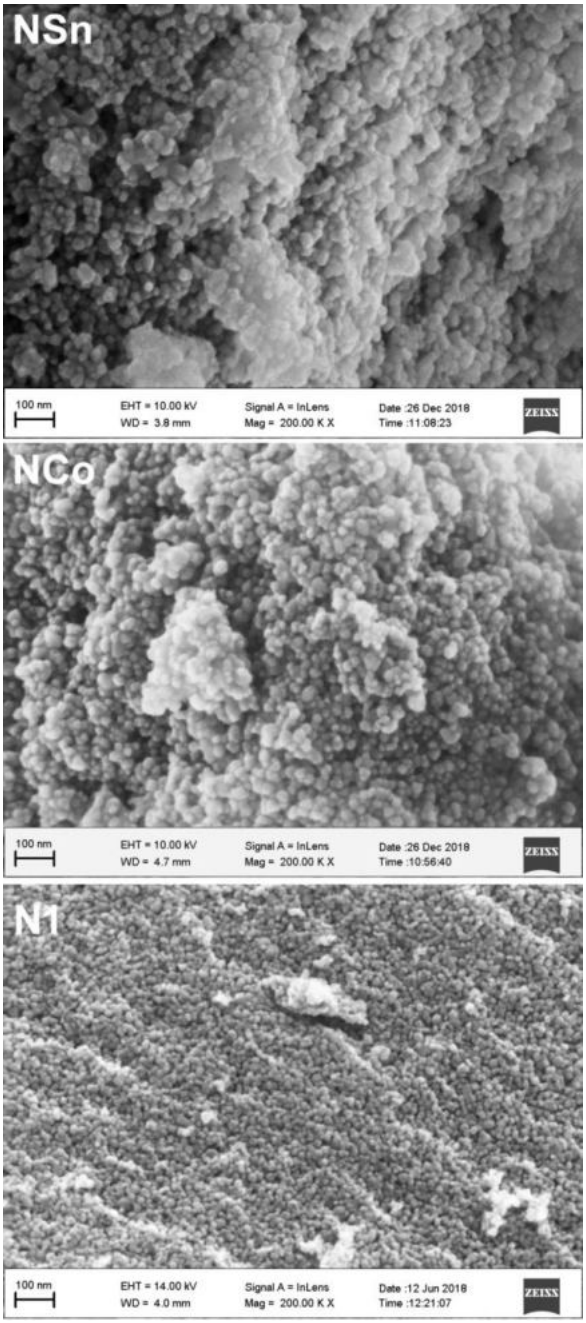

Figure 6.5 : FESEM images of samples N1, NCo and NSn

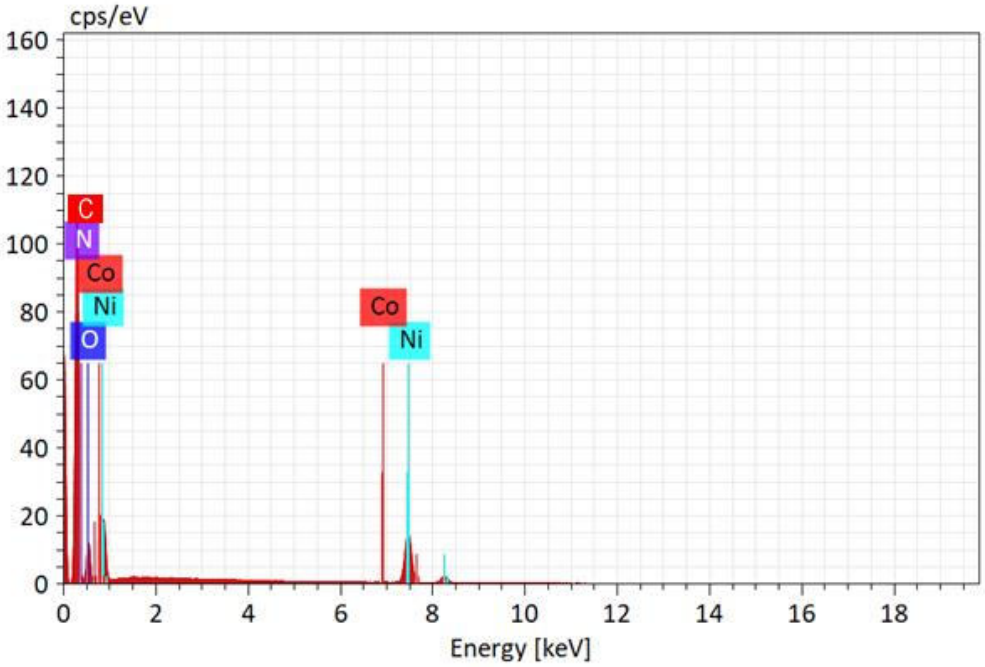

Figure 6.6 : EDX pattern of NCo nanocomposite

Table 6.2 : EDX data of NCo nanocomposite

Elements	Weight %	Atom %
Nickel	51.72	29.11
Oxygen	22.53	34.19
Carbon	16.63	24.1
Nitrogen	8.98	12.54
Cobalt	0.14	0.06
Total	100.00	100.00

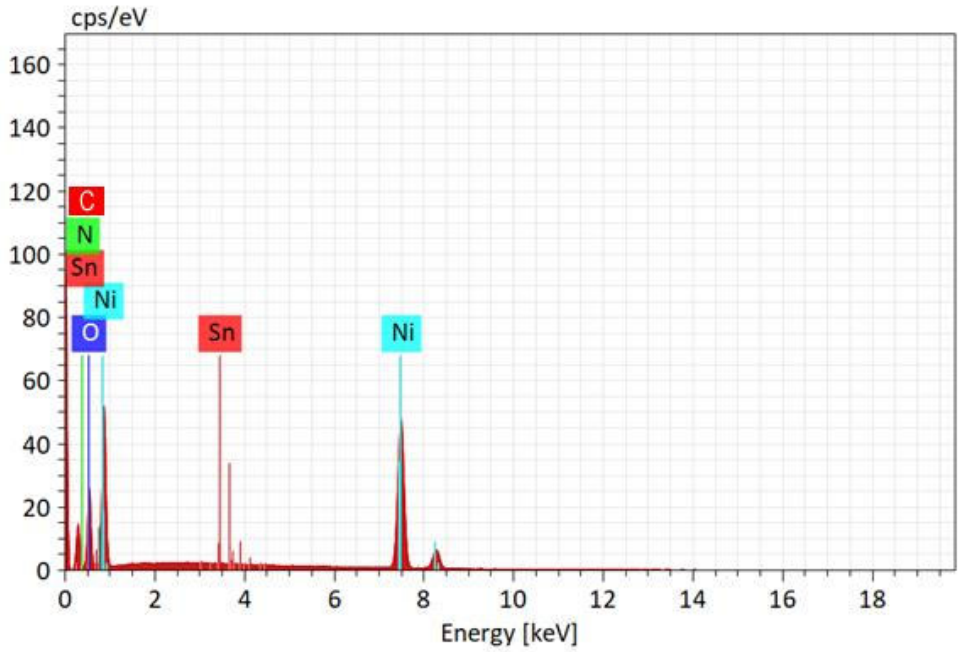

Figure 6.7: EDX pattern of NSn nanocomposite

Table 6.3 : EDX data of NSn nanocomposite

Elements	Weight %	Atom %
Nickel	61.13	39.97
Oxygen	20.84	36.59
Carbon	10.98	18.17
Nitrogen	6.81	8.22
Tin	0.24	0.08
Total	100.00	100.00

EDX is used to determine the chemical composition of the nanocomposites. Figures 6.6 and 6.7 shows the EDX analysis results of NCo and NSn samples. The signals corresponding to nickel, oxygen, carbon, nitrogen and cobalt in NCo and tin instead of cobalt in NSn confirms the formation of NiO/CoPc and NiO/SnPc nanocomposites. The absence of peaks corresponding to other elements shows the purity of the prepared nanocomposites. The weight and atom percentages of NCo and NSn samples are presented in Tables 6.2 and 6.3 respectively.

6.3.2.3 TEM Analysis

The TEM images of pristine and nanocomposite samples are shown in Figure 6.8. The bright field images (Figure 6.8(a)) reveals the hexagonal shape of majority of the particles. The increased particle size for the nanocomposites is evident from the images. The unidirectional fringe pattern in the HRTEM images (Figure 6.8 (b)) of all samples confirms their crystalline nature. The extra diffraction spots in the SAED patterns (Figure 6.8 (c)) of nanocomposite samples confirm the presence of phthalocyanine in the samples**.** The particle size distribution graphs of N1, NCo and NSn samples are plotted in the histogram in Figure 6.9. The average particle sizes obtained from TEM images are 21.8, 23.7 and 22.9 nm for N1, NCo and NSn respectively. Table 6.4 gives the structural parameters obtained from TEM images.

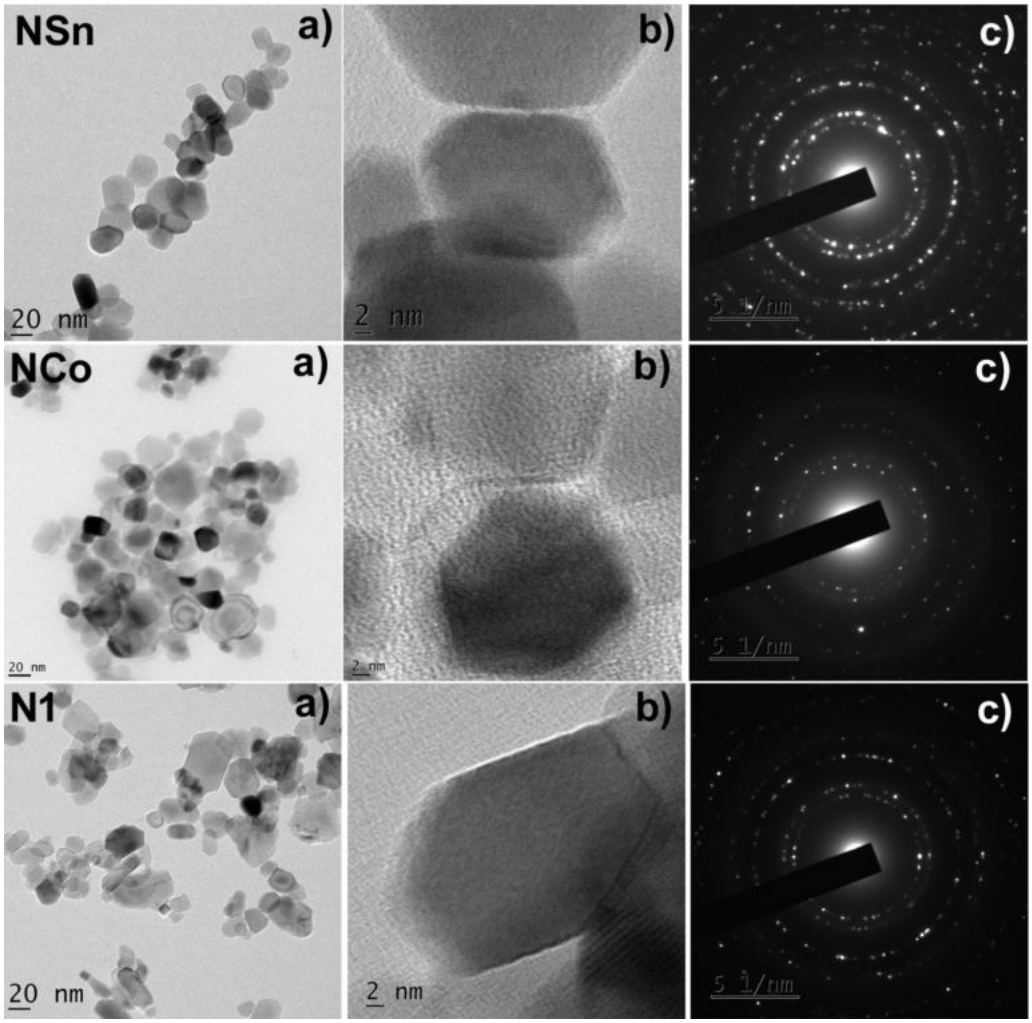

Figure 6.8 : **(a)** Bright field images, **(b)** HRTEM images and **(c)** SAED patterns of samples N1, NCo and NSn

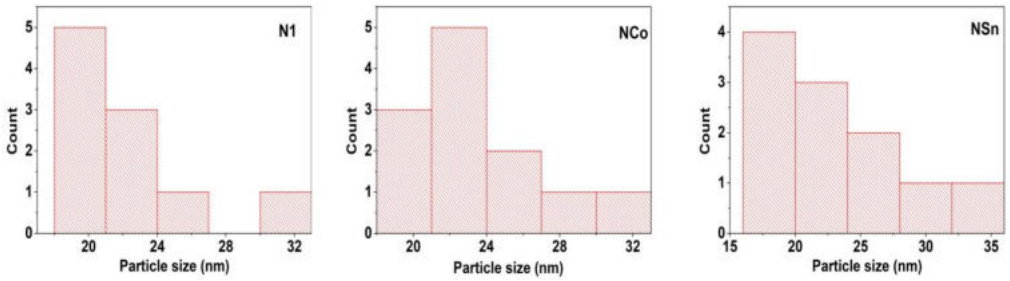

Figure 6.9 : Particle size distributions of samples N1, NCo and NSn

Table 6.4 : Lattice parameters of samples N1, NCo and NSn from TEM images

Sample	Particle size from TEM images (nm)	d spacing from SAED patterns (Å)		
		(111)	(200)	(220)
N1	21.8±0.43	2.786	2.472	1.718
NCo	23.7±0.47	2.789	2.398	1.682
NSn	22.9±0.45	2.840	2.450	1.727

6.3.2.4 FTIR Spectroscopy

The bonds between the atoms in the synthesized organic-inorganic nanocomposite are analysed using FTIR spectroscopy. The FTIR spectra of the pristine NiO and M-Pc (M=Co, Sn) nanocomposites are shown in Figure 6.10. In addition to the characteristic peak of NiO, the spectra of nanocomposite samples show some prominent peaks which confirm the presence of cobalt/tin phthalocyanine. Figure 6.11 shows the FTIR spectra of NCo and NSn in the range 1500 – 700 cm^{-1}, where the prominent peaks of phthalocyanine are present. Table 6.5 presents the observed modes in N1, NCo and NSn along with the reported values for CoPc and SnPc.

The intense peak observed in all the samples around 410 cm^{-1} is due to Ni – O stretching vibration [8]. The broad band centred at 3450 cm^{-1} is assigned to O-H stretching vibrations and the band at 1630 cm^{-1} is attributed to H-O-H bending vibration mode [9].

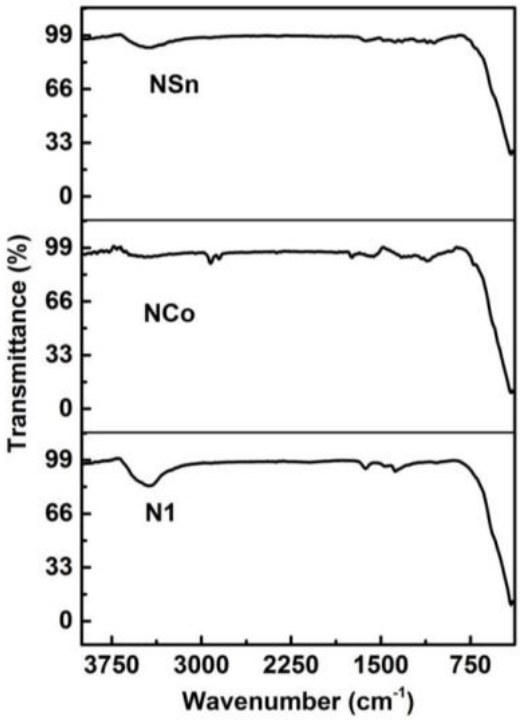

Figure 6.10 : FTIR spectra of samples N1, NCo and NSn

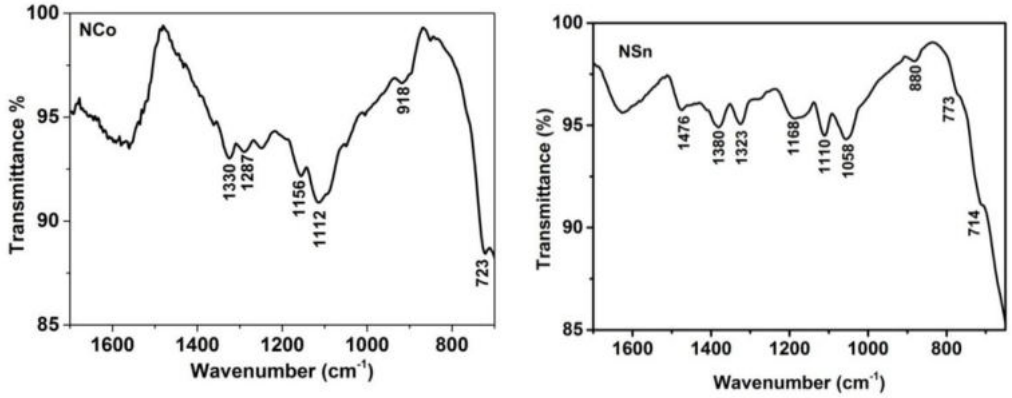

Figure 6.11 : FTIR spectra of NCo and NSn nanocomposites in the range 1600 – 700 cm^{-1}

Table 6.5 : Comparison of observed IR modes of samples N1, NCo & NSn

Samples (cm^{-1})			Literature values (cm^{-1})	
N1	**NCo**	**NSn**	**CoPc[10]**	**SnPc[11]**
410	414	408	..	..
	723	714	721	724
	..	773	771	770
	..	880	878	887
	918	..	911	952
	..	1058	..	1062
	1112	1110	1117	1119
	1156	1168	1162	1160
	1287	..	1287	1285
	1330	1323	1329	1333
	..	1380	..	1383
	..	1476	..	1493

In the spectrum of NCo, the bands at 723 cm^{-1} (C-H out of plane deformation), 918 cm^{-1} (metal ligand vibration), 1112 cm^{-1} (C-H in plane bending), 1156 cm^{-1} (C-N in plane bending), 1287 cm^{-1} (C-N stretching) and 1330 cm^{-1} (C-C stretching) confirm the existence of CoPc in the composite [10,12]. The band located at 723 cm^{-1} represents the characteristic α-phase of CoPc [13]. Thus, the FTIR study confirms the successful formation of NiO/CoPc nanocomposite.

In the spectrum of NSn, the peaks at 714 and 773 cm^{-1} are due to the phthalocyanine ring vibrations [14]. The bands at 880, 1058, 1110 and 1168 cm^{-1} correspond to the in plane vibration and C-H in-plane deformation respectively. Stretching of C–C and C–N bonds associated with the corresponding double bonds and in-plane C–H bending deformation produces the IR peaks at 1110, 1168 and 1323 cm^{-1} respectively. The peak at 1476 cm^{-1} is due to stretching of C=N and C=C bonds [15]. These peaks confirm the successful attachment of SnPc into the NiO structure.

6.3.3 Optical Properties

UV-Visible absorption and photoluminescence spectra of the synthesized nanocomposites are carried out by following the procedure as given in *Section 2.5.*

6.3.3.1 UV-Visible Spectroscopy

The UV-Visible absorption spectra of N1, NCo and NSn in the wavelength range 200 – 800 nm are shown in Figure 6.12. All samples show strong absorption band centred around 235 nm in the UV range, originating from the bandgap absorption of NiO. The enhancement of optical absorption in the visible region is clearly observed in NiO/M-Pc nanocomposite samples.

An obvious red shift in the absorption edge into the visible region is observed for the nanocomposite samples revealing the perturbance in the electronic states of NiO/M-Pc nanostructures [16]. The absorption edge observed for N1 at 365 nm is shifted to 400 and 474 nm for the

synthesized nanocomposites NSn and NCo, respectively. Compared to NiO, NiO/CoPc shows very good absorption in the range 300–800 nm (shown as inset of Figure 6.12). This corresponds to the B band (Sorret band) and Q band which are characteristic of metal phthalocyanines. This indicates the successful incorporation of M-Pc in NiO. Both these bands arise from π–π* transitions, from the highest occupied molecular orbital (HOMO) to the lowest unoccupied molecular orbital (LUMO) [17]. For NCo, the two absorption peaks in the Q band are at 2.02 and 1.83 eV. The higher-energy peak (Q1) has a slightly larger intensity compared to the second peak (Q2), which is a typical feature of CoPc α-phase [18]. Instead of a broad Q band of SnPc, a relatively sharp band with a main peak at 1.7 eV is observed for the nanocomposite due to the formation of the monomeric form of SnPc [14, 19].

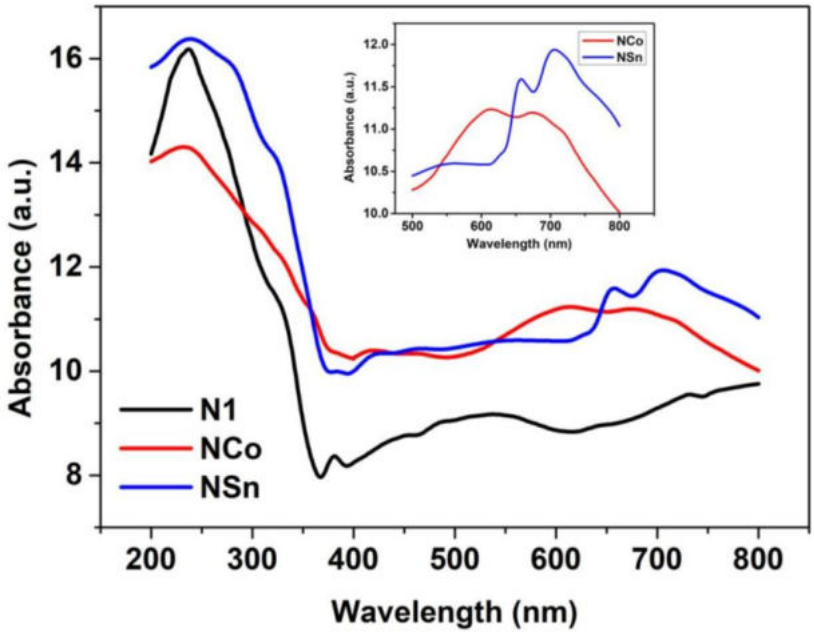

Figure 6.12 : UV – Visible absorption spectra of samples N1, NCo and NSn

Bandgap values of NiO and the nanocomposite samples are measured from Tauc plot [20], as discussed in *Section 2.5.1.* Figure 6.13 depicts the $h\upsilon$ *vs* $(\alpha h\upsilon)^2$ graphs of the samples.

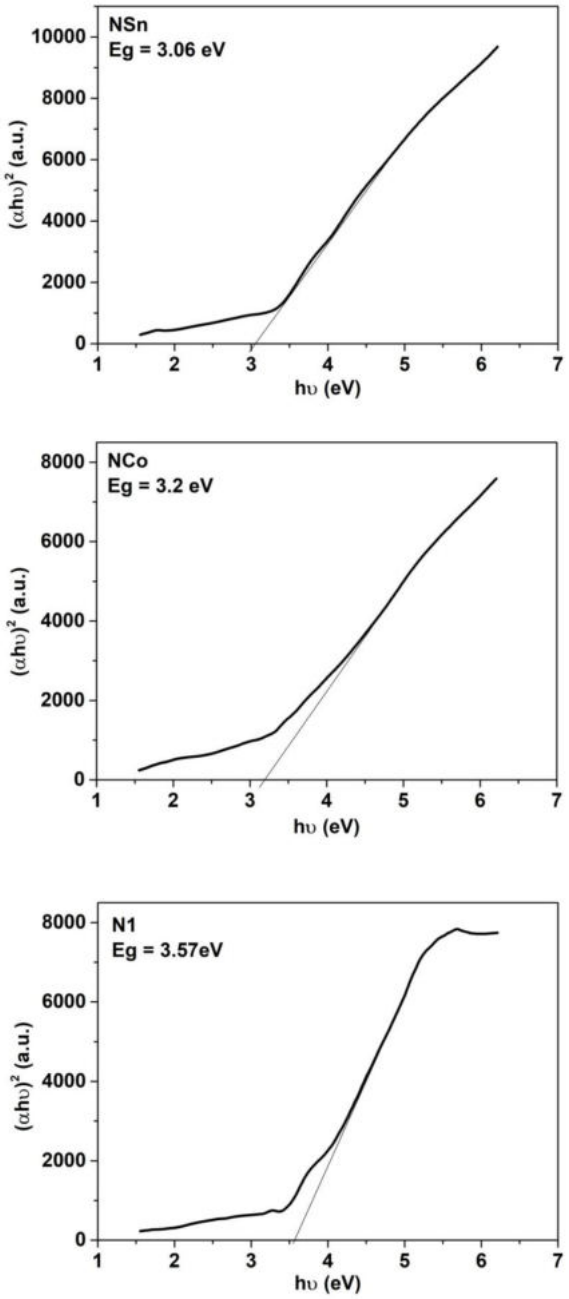

Figure 6.13 : Tauc plots of samples N1, NCo and NSn

The optical bandgaps of the samples are found to be 3.57, 3.2 and 3.06 eV for N1, NCo and NSn, respectively. Lowering of bandgap values for the composite samples indicate an electronic interaction between NiO and M-Pcs. The addition of CoPc and SnPc helps to extend the optical absorption spectrum of NiO into the entire span of the visible region, in addition to the enhanced absorption intensity. Thus, the modifications in the optical absorption properties suggest visible light-driven photocatalytic applications for the nanocomposite.

6.3.3.2 PL Spectroscopy

The emission spectra of NiO, NiO/CoPc and NiO/SnPc samples are recorded in the range 300–550 nm using an excitation wavelength of 280 nm and are presented in Figure 6.14. The shapes of the PL spectra of the composite samples are similar to that of NiO indicating that the inclusion of CoPc does not cause new fluorescent phenomena because of strong spin–orbit interaction [21]. The emission in the UV region originated from excitonic recombination corresponding to the near band edge (NBE) transition of NiO, while the shoulder peaks in the visible region are attributed to defect related deep level emissions [22].

The efficiency of electron trapping and recombination of electrons and holes determines the emission peak intensity. Compared to pure NiO, PL spectra of the composite samples suffer a reduction in intensity. The emission intensity of NSn is less than that of NCo, as the intensity and width of the PL spectrum are dependent on the metal ion incorporated into the lattice [23]. This emission quenching represents the

interaction and electron transfer process between MPc and NiO. The result indicates that the composite can effectively block the electron–hole recombination in NiO, and improve the efficiency of separation of electrons and holes [24]. This will, in turn, enhance the photocatalytic activity of the composite. Hence, the photo-efficiency and photo-activity of NiO nanoparticles can be improved with the addition of metal phthalocyanine of appropriate concentration which makes them suitable for potential applications in solar cells and photocatalysis.

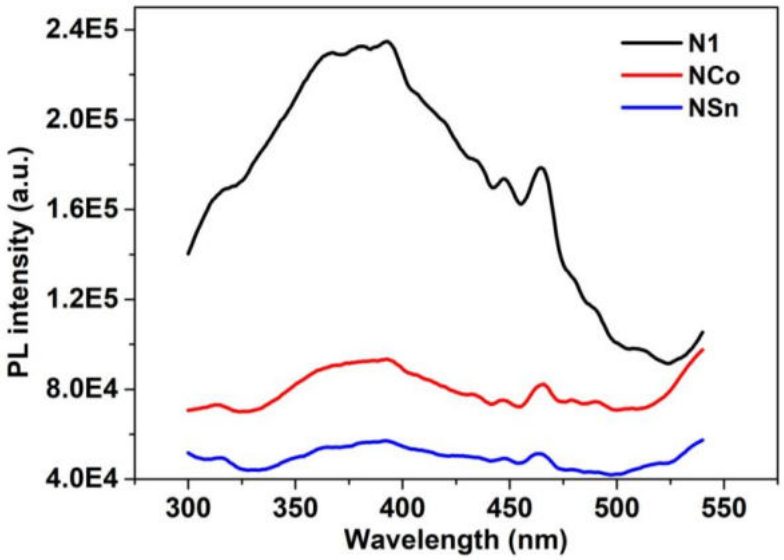

Figure 6.14 : PL spectra of samples N1, NCo and NSn

6.3.4 Electrical Properties

The electrical studies are carried out by following the procedure given in *Section 2.6*. The samples N1, NCo and NSn are consolidated in the form of cylindrical pellets of diameter 13 mm and thickness 1.5 mm by applying a pressure of 7 tons using a hydraulic press. DC conductivity

of the samples has been recorded using *KEITHLEY 2450 Source Meter* in two probe method and the dielectric and AC conductivity measurements are performed using an impedance analyzer (*Wayne Kerr H-6500B model*).

6.3.4.1 DC Conductivity

The DC conductivity (σ_{DC}) of all samples in the temperature range of 313-423 K is shown in Figure 6.15. The conductivity of all the samples increases with the increase in temperature confirming the semiconducting nature of the synthesized nanocomposites. At 313 K, the values of σ_{DC} obtained for N1, NCo and NSn are 7.78×10^{-7}, 1.65×10^{-6} and 4.22×10^{-6} $ohm^{-1}m^{-1}$ respectively. The corresponding values at 423 K are 6.354×10^{-6}, 7.944×10^{-6} and 8.912×10^{-6} $ohm^{-1}m^{-1}$. This increasing trend is due to the increase in the drift mobility of thermally activated charge carriers [25]. From the figure it is clear that the conductivity of the nanocomposites is higher than that of NiO. The higher resistivity of NiO compared to NCo and NSn can be due to its smaller size. The smaller bandgap of the nanocomposites compared to pristine NiO will also contribute to their conductivity.

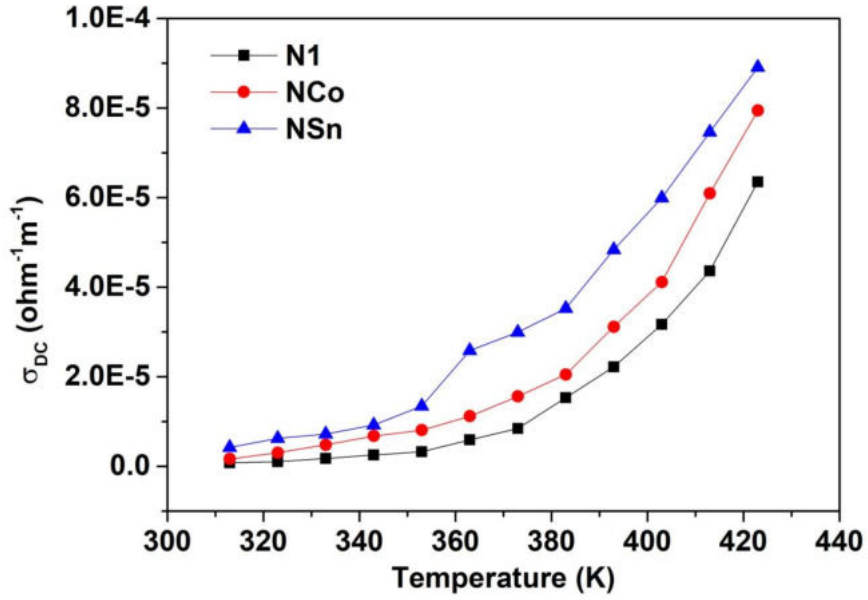

Figure 6.15 : Variation of DC conductivity with temperature of samples N1, NCo and NSn

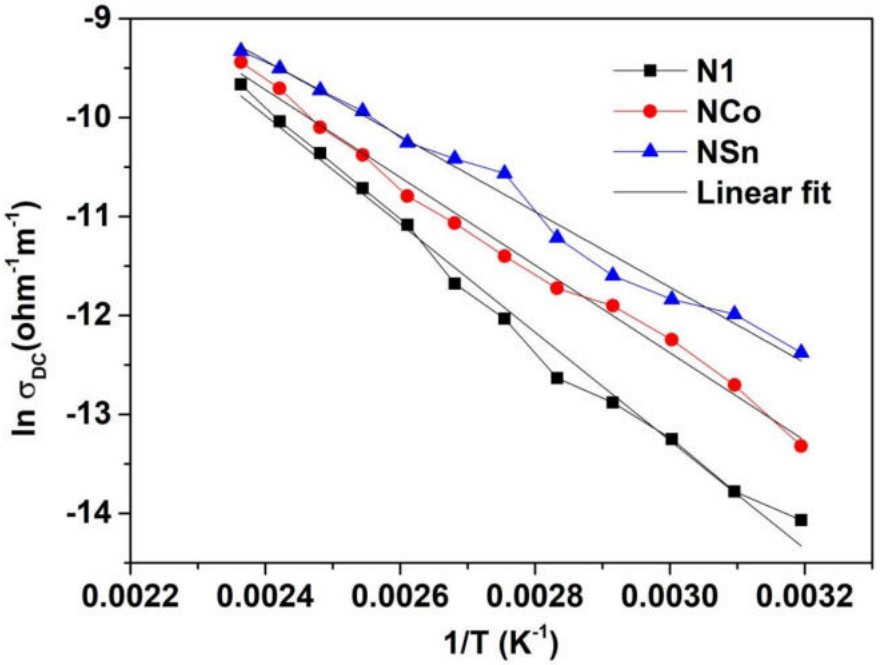

Figure 6.16 : Arrhenius plots of samples N1, NCo and NSn

The Arrhenius plots of the samples are shown in Figure 6.16. The activation energies (*Ea*) of DC conductivity for the samples are calculated from the slopes of ($ln\sigma_{DC}$) vs ($1/T$) graphs (Figure 6.16). The obtained values are 0.47, 0.38 and 0.33 eV for N1, NCo and NSn respectively, in the temperature range 313 to 423 K. The decreased activation energy is an indication of increased conductivity of the nanocomposites.

6.3.4.2 Dielectric Studies

The variation of dielectric constant (ε′) and loss tangent ($tan\ \delta$) with frequency for different temperatures are studied for the nanocomposite samples. Figure 6.17 illustrates the variation of the dielectric constant of the nanocomposite samples in a broad spectrum (100 Hz-5 MHz) at selected temperatures. ε' has very high value in the low-frequency region, which decreases rapidly with increase in frequency and becomes almost constant at higher frequencies for all the samples. The dielectric dispersion curve can be described using Koop's theory [26], which is based on the Maxwell Wagner model [27]. As explained in *Section 3.3.4.2*, the enhanced dielectric constant at low frequency is due to the space-charge polarization caused by impurities or crystal defects. The decrease of dielectric constant at higher frequencies is due to the lagging of charge carriers contributing to polarization behind the applied field [28, 29].

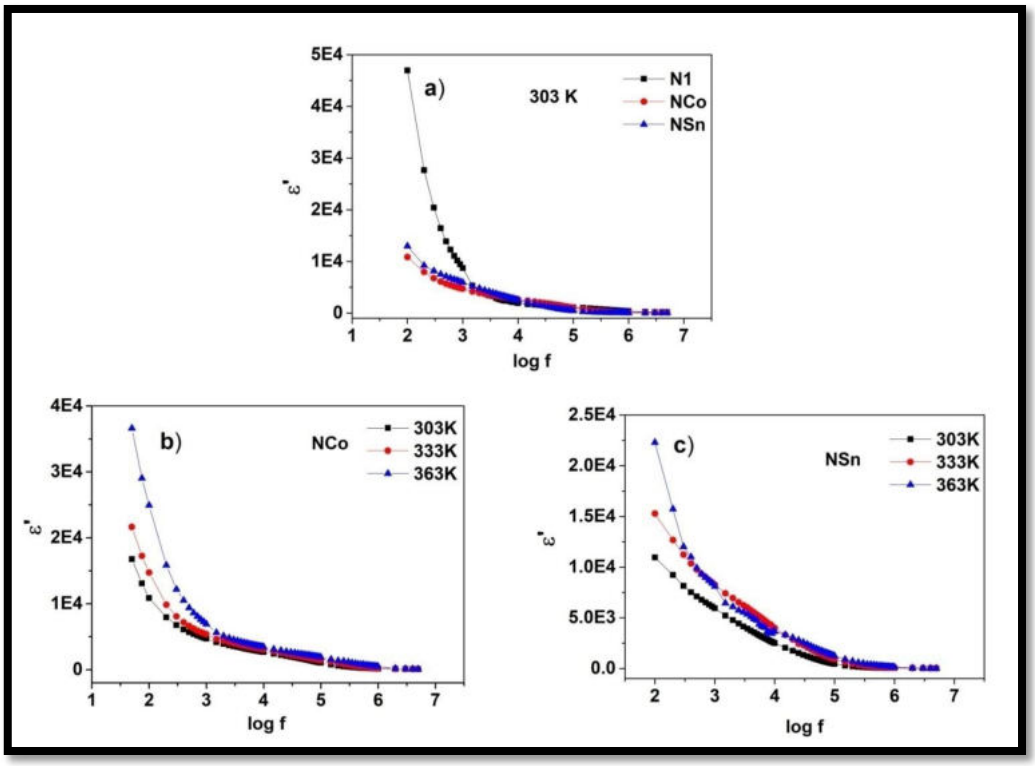

Figure 6.17 : Variation of dielectric constant with frequency and temperature;

(a) Samples N1, NCo and NSn at 303 K,
(b) NCo and
(c) NSn at selected temperatures

Figure 6.17(a) compares the dielectric behaviour of NiO/CoPc and NiO/SnPc with NiO nanoparticles at 303K. It is observed that dielectric constant is low for both the nanocomposite samples as compared to pristine NiO. At 303 K and 1 kHz, ε′ for N1is found to be 8727 while for NCo and NSn, the corresponding values are 4709 and 5945, respectively. The addition of CoPc can cause alterations in the space charge distribution, which in turn decreases the dielectric constant, thus showing the stronger influence of metal phthalocyanines in NiO nanostructures [30]. The delocalized π electrons associated with metallophthalocyanines play a major role in their transport property [31].

Figures 6.17(b) and (c) show dielectric permittivity as a function of frequency at different temperatures for NCo and NSn samples. An increase in dielectric permittivity with an increase in temperature is observed for both samples. With the increase in temperature, the orientation of interfacial dipoles are facilitated causing an increase in dipolar polarizability, and hence the permittivity of the material. At 393 K and 1 kHz, the value of ε′ for NCo is 6915 and that for NSn is 8101. This difference in values of ε' may be due to the presence of different central metal ions [32].

The variation of the loss tangent of pristine and composite NiO samples as a function of frequency at 303 K is shown in Figure 6.18(a). The absorption current produced due to impurities, defects and space charge formation in the interphase layers results in a large dielectric loss in the low frequency region [33]. *Tan* δ is found to get reduced with increase in frequency for all samples. NiO exhibits a larger dielectric loss than the other two composite samples in the low frequency regime. At 303 K and 1 kHz, *tan* δ values are 33.8, 8.18 and 11.6, respectively for N1, NCo and NSn samples. These values decrease to 1.76 (N1), 1.26 (NCo) and 5.12 (NSn) at 100 kHz. The existence of a single relaxation peak in the high-frequency region for NSn (Figure 6.18(c)) leads to a slight increase in *tan* δ value. This may be attributed to the dipole moment of the defect pair formed from the oxygen vacancy and the central metal ion of phthalocyanine [34].

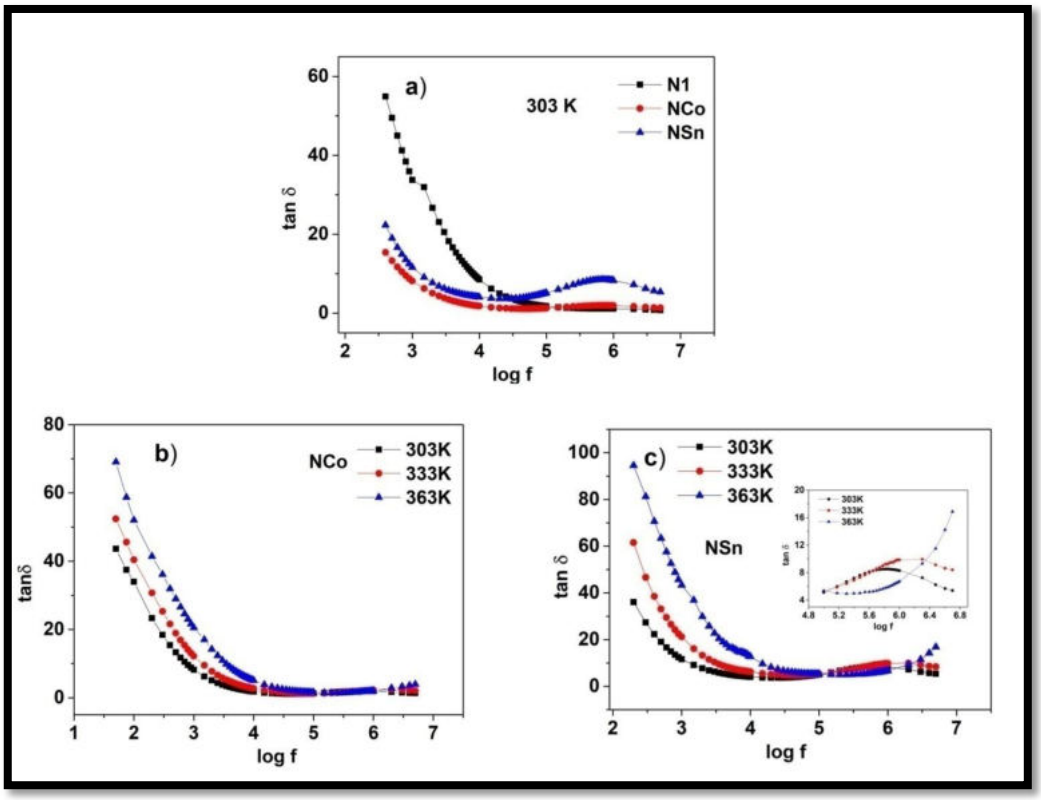

Figure 6.18 : Variation of loss tangent with frequency and temperature;
(a) samples N1, NCo and NSn at 303 K,
(b) NCo and **(c)** NSn at selected temperatures

The variation of loss tangent with frequency at selected temperatures for NCo and NSn samples are shown in figures 6.18 (b) and (c). Normal dielectric behaviour is observed for both samples, with an increase in loss tangent with temperature. At 363 K and 1 kHz, *tan δ* of NCo and NSn are found to be 20.5 and 43.4 respectively. The hopping probability of electrons increases with temperature, causing an increase in loss tangent [35]. The intensity of relaxation peak observed in figure 6.18 (c) of NSn increases and shifts to high frequency side with an increase in temperature. The oxygen vacancies released from the defect centres leads to an increase in peak intensity with temperature [34]. The

dielectric loss of NiO can be considerably reduced by forming nanocomposite with M-Pc, particularly CoPc. High dielectric constant and reasonably low dielectric loss are the basic features of dielectric materials to be used in embedded capacitors for decoupling applications [36].

6.3.4.3 Impedance Analysis

For a better understanding of the dielectric behaviour of the pristine and nanocomposite samples, the Nyquist plots at room temperature are drawn, as shown in Figure 6.19. The solid lines represent experimental data and the symbols represent fitted data. It is evident that all the samples show two semicircles, the higher frequency dispersion corresponds to the grain conduction and the lower frequency dispersion represents the grain boundary effects [37]. The results in the figure can be modelled by an equivalent circuit with two parallel R – CPE (Constant Phase Element) circuits in series as shown in the inset of Figure 6.19. The features of CPE have been already discussed in *Section 3.3.4.3.* The impedance of CPE is of the form $Z_Q = 1/(j\omega)^{\beta}$CPE, where $0 < \beta < 1$. β is a measure of the capacitive nature of the component [38]. Typical values of the parameters R, C and β, both for grain (R_g, CPE_g, β_g) and grain boundaries (R_{gb}, C_{gb}, β_{gb}) obtained from the fits are given in Table 6.6.

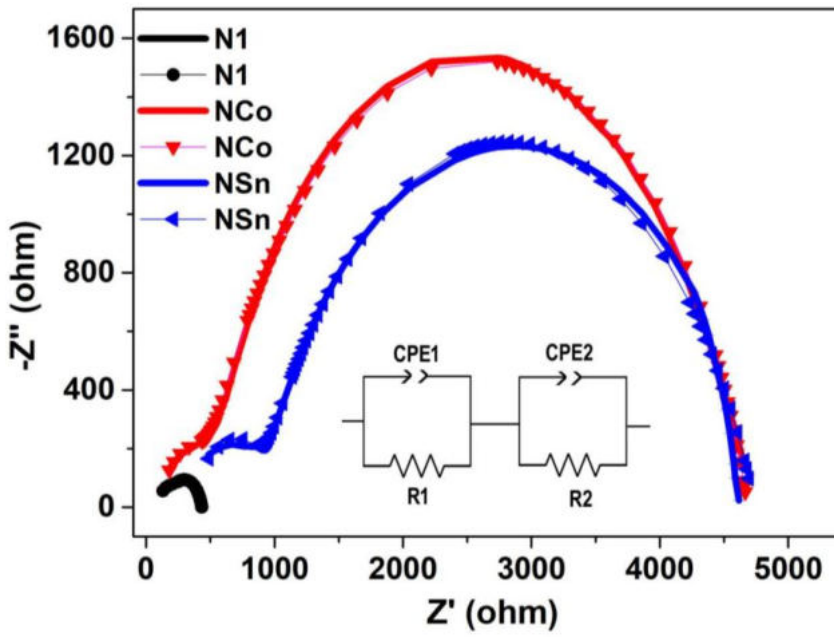

Figure 6.19 : Nyquist plots of samples N1, NCo and NSn

Table 6.6 : Equivalent circuit parameters of N1, NCo and NSn samples

Sample	CPE_g(nF)	R_g(Ω)	β_g	CPE_{gb}(nF)	R_{gb} (Ω)	β_{gb}
N1	0.129	195	0.991	34.01	238	0.797
NCo	1.803	484	0.830	31.9	4198	0.799
NSn	0.221	885	0.890	111	3855	0.730

It is clear that the grain boundaries are more capacitive and resistive than the grains for all the samples. The value of β (<1) confirms the non Debye type of relaxation for all the samples [39].

6.3.4.4 AC Conductivity

The variation of AC conductivity (σ_{AC}) with frequency at room temperature for pristine and NiO nanocomposite samples is presented in figure 6.20. All the samples exhibit a plateau or frequency independent AC conductivity region at lower frequencies where long range motion of charge carriers responsible for DC conduction dominates. With an increase in frequency, short range (intra well) hopping contributing to AC conductivity increases [40].

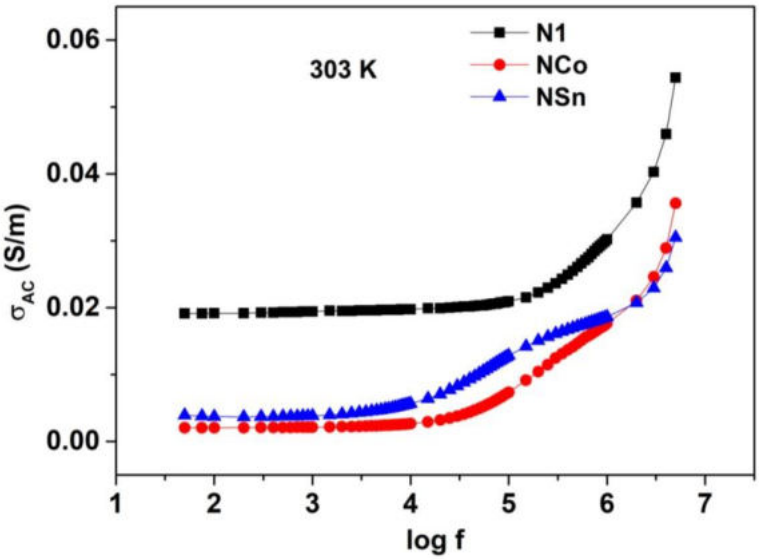

Figure 6.20 : Variation of AC conductivity with frequency of samples N1, NCo and NSn at 303 K

A decrease in AC conductivity is observed for the nanocomposite samples compared to pristine NiO, which may be due to the trapping of charge carriers between the localized states [30]. At 303 K and 1 kHz, the values of σ_{AC} for N1, NCo and NSn are 1.95×10^{-2}, 2.14×10^{-3} and 3.85×10^{-3} S/m, respectively. At 1 MHz, these values increase to 3.02×10^{-2}, 1.76×10^{-2} and 1.87×10^{-2} S/m, respectively for N1, NCo and NSn samples.

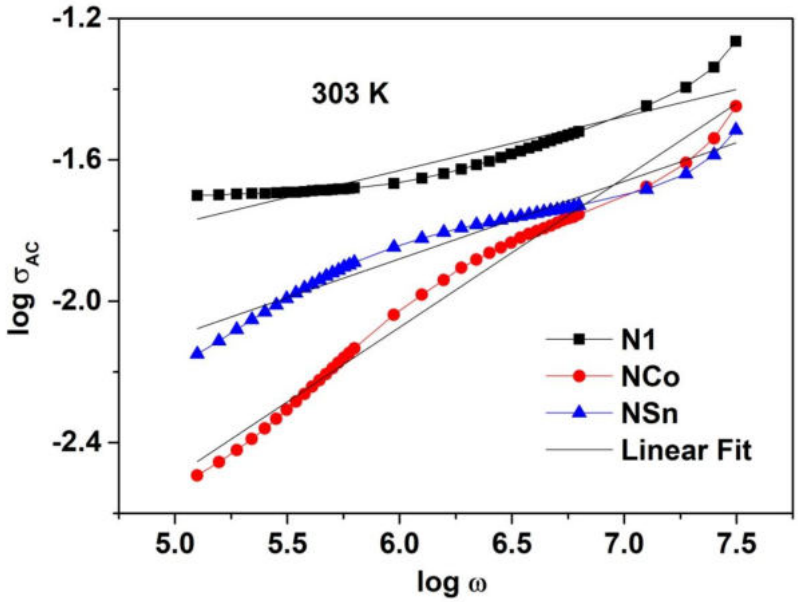

Figure 6.21 : Jonscher's power law plots of samples N1, NCo and NSn at 303 K

The frequency dependence of AC conductivity can be described by Jonscher's power law [41]. Figure 6.21 illustrates the Jonscher's power law plots of the synthesized nanocomposites. The values of *s* determined for samples N1, NCo and NSn samples at room temperature, from the slope of log ω versus log σ_{AC} plots are 0.16, 0.42 and 0.22 respectively. The values of *s* lie between zero and one, confirming the barrier hopping conduction mechanism in all samples [42].

Figures 6.22 (a) and (b) illustrate the variation of AC conductivity as a function of frequency at selected temperatures for NCo and NSn samples. An increase in conductivity with temperature is observed for both samples, due to the increase in mobility of charge carriers [42]. At 1 kHz, the value of σ_{AC} for NCo increased from 2.14×10^{-3} to 7.89×10^{-3} S/m when the temperature is increased from 303 to 363 K. The corresponding increase for NSn is from 3.85×10^{-3} to 19.55×10^{-3} S/m. The difference in

σ_{AC} for the two composite samples may be due to the presence of different central atoms (Co, Sn) in their structure.

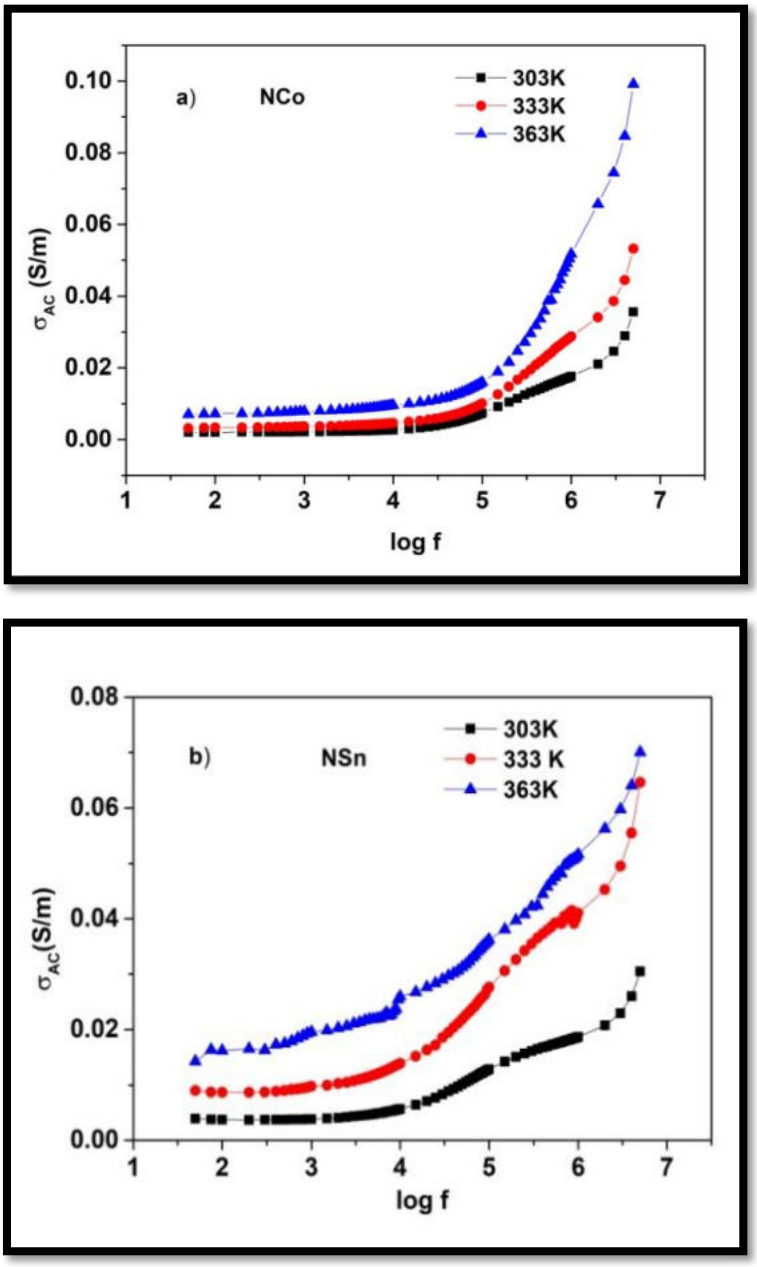

Figure 6.22 : Variation of σ_{AC} with frequency at selected temperatures of **(a)** NCo and **(b)** NSn nanocomposites

6.3.5 Magnetic Studies

Magnetic studies of the samples have been carried out using Vibrating Sample Magnetometer (*Lakeshore VSM 7410*) by following the procedure discussed in *Section 2.7*.

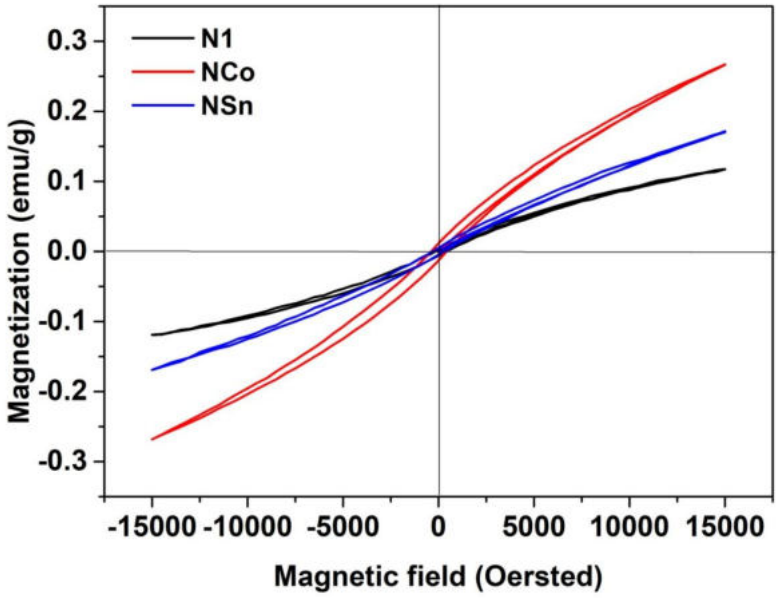

Figure 6.23 : M – H curves of samples N1, NCo and NSn at room temperature

Figure 6.23 shows the magnetization versus magnetic field (M−H) curves of N1, NCo and NSn samples measured at 300 K with a maximum applied field of ±1.5 T. A weak ferromagnetic behaviour is observed for all the samples. As discussed in *Section 3.3.5,* the uncompensated surface spins of NiO nanoparticles can give rise to a net magnetic moment favouring their ferromagnetic nature [43]. An increase in coercivity from 287 G to 398.5 G and retentivity from 0.0043 to 0.012 emu/g is observed for the NCo nanocomposite, from that of pristine NiO. The magnetic properties of CoPc arise from unpaired spins in the 3*d* orbitals of the central Co atom [44]. No significant change is observed in the magnetic parameters of NSn nanocomposite.

6.4 Conclusion

- NiO/M-Pc (M=Co, Sn) nanocomposites have been successfully synthesized by solvent-evaporation method.
- The structural characterization of the synthesized nanocomposites confirms the successful formation of NiO/M-Pc (M=Co, Sn) nanocomposites.
- UV–Visible absorption studies indicate good light absorption in the UV and visible region for the synthesized nanocomposites. A decrease in bandgap energy, together with improved absorption intensity has been observed for the nanocomposites.
- The emission quenching observed in the PL spectrum of the nanocomposites may enhance their photocatalytic activity.
- The semiconducting nature of the nanocomposites is confirmed by the DC conductivity studies.
- The dielectric loss of NiO can be considerably reduced by forming the nanocomposites.
- The presence of two semicircular arcs in the Nyquist plot points out the existence of grain and grain boundary conduction in the nanocomposite samples.
- The AC conductivity of the synthesized samples demonstrates polaron hopping transport mechanism in the materials and it is confirmed from Jonscher's universal power law. A decrease in AC conductivity is observed for the nanocomposites compared to pristine NiO.
- VSM studies reveal a weak ferromagnetic behaviour for the nanocomposite samples

References

1) A.A. Anees, M.A.M. Khan, K.M. Naziruddin, A.A. Salman, M. Alhoshan, M.S. Alsalhi, J. Semiconductors., 32 (2011) 043001–043006
2) C. C. Leznoff, A. B. P. Lever, Phthalocyanines: Properties and Applications. Wiley, New York (1989)
3) P.A. Sheena, K.P. Priyanka, N. A. Sabu, B. Sabu, T. Varghese, Nanosystems: Phys. Chem. Math., 5(2014) 441 - 449
4) F.V. Burgos, S. Utsumi, Y. Hattori, Fuel, 99 (2012) 106 - 117
5) S. F. Pop, R. M. Ion, J. Optoelectron. Adv. Mater., 12 (2010) 1976 -1980
6) H.S. Soliman, A.M.A. El-Barry, N.M. Khosifan, M.M. El Nahass, Eur. Phys. J. Appl. Phys., 37(2007) 1 - 9
7) M.M. El-Nahass, A.A. Atta, E.A.A. El-Shazly, A.S. Faidah, A.A. Hendi, Mater. Chem. Phys., 117 (2009) 390–394
8) J. Li, R. Yan, B. Xiao, D.T. Liang, D.H. Lee, Energy Fuels., 22 (2008) 16 - 23
9) K. Anandan, V. Rajendran, Mater. Sci. Semicond. Process., 14 (2011) 43 - 47
10) D. Verma, R. Dash, K.S. Katti, D.L. Schulz, A.N. Caruso, Spectrochim. Acta Part A 70 (2008) 1180 - 1186
11) W. J. Kroenke, M. E. Kenney, Inorg. Chem., 3 (1964) 696 - 698
12) Z. Zhao, J. Fan, S. Liu, Z. Wang, Chem. Eng. J., 151 (2009) 134 - 140

13) K. K. Babitha, K. P. Priyanka, A. Sreedevi, Int. J. Appl. Ceram. Technol., 13 (2016) 670 - 677

14) P. Kumar, A. Kumar, C. Joshi, R. Singh, S. Saran, S. L. Jain, RSC Adv. 5 (2015) 42414 - 42421

15) E. Salomon, T. Angot, N. Papageorgiou, J.-M. Layet, Surf. Sci., 596 (2005) 74 - 81

16) V. Mani, R. Devasenathipathy, Shen-Ming Chen, Jiun-An Gu, Sheng-Tung Huang, Renewable Energy, 74 (2015) 867 – 874

17) K. Sakamoto, E. Ohno-Okumura, Materials, 2 (2009) 1127-1179

18) K. P. Priyanka, S. Sankararaman, K. M. Balakrishna, T. Varghese, J. Alloys Compd., 720 (2017) 541-549

19) Y. Kashimoto, K. Yonezawa, M. Meissner, M. Gruenewald, T. Ueba, S. Kera, R. Forker, T. Fritz, H. Yoshida, J. Phys. Chem. C, 122 (2018) 12090 - 12097

20) J. Tauc, Amorphous and Liquid Semiconductors, 1 ed. Plenum Press, New York (1974).

21) W. Bała, M. Wojdyła, M. Rębarz, M. Szybowic, M. Drozdowski, A. Grodzicki, P. Piszczek, J. Optoelectron. Adv. Mater., 11 (2009) 264 - 269

22) B. Kisan, P.C. Shyni, S. Layek, H.C. Verma, D. Hesp, V. Dhanak, S. Krishnamurthy, A. Perumal, IEEE Trans. Magn., 50 (2014) 1 - 4

23) G. A. Kumar, J. Thomas, N. George, B. A. Kumhakrishnan, V. P. N. Nampoori, C. P. G. Vallabhan, Phys. Chem. Glasses, 41 (2000) 89-93

24) L. Gu, J. Wang, H. Cheng, Y. Zhao, L. Liu, X. Han, X., ACS Appl. Mater. Interfaces., 5 (2013) 3085 - 3083

25) D. R. Patil, B. K. Chougule, Materials Chem. Phys., 117 (2009) 35-40.

26) C.G. Koops, Phys. Rev. 83 (1951) 121

27) K.W. Wagner, Am. Phys. 40 (1973) 317

28) K. V. Rao, A. Smakula J. Appl. Phys. 36 (1965) 2031-2038

29) D. P Snowden, H Saltzburg, Phys. Rev. Lett. 14 (1965) 497 - 499

30) K. K. Babitha, K. P. Priyanka, H. Hitha, S. Rintu Mary, E. M. Mohammed, S. Sankararaman, T. Varghese, J. Electron. Mater. 46 (2017) 6234 - 6240

31) S. Saravanan, C. J.Mathai, M. R. Anantharaman, S. Venkatachalam, P. V. Prabhakaran, J. Appl. Polymer Sci., 91 (2004) 2529-2535

32) A. M. Saleh, S. M. Hraibat, R. M. L. Kitaneh, M. M. Abu-Samreh, S. M. Musameh, J. Semicond., 33(8) (2012) 082002

33) K.P. Priyanka, J. Sunny, T. Smitha, E. M. Mohammed, T. Varghese, J. Basic Appl. Phys., 2 (2010)105 - 108

34) S. K. Aniban, A. Dutta, RSC Adv. 5 (2015) 95736

35) J. Hasson, F. M. Yen, M. H. Ashim; Ionics, 13 (2007) 219 - 222

36) J. Xu, C. P. Wong, Compos. Part A Appl. Sci. Manuf., 38 (2007) 13

37) M.R. Biswal, J. Nanda, N.C. Mishra, S. Anwar, A. Mishra, Adv. Mater. Lett., 5 (2014) 531 - 537

38) L.D. Sappia, M.R. Trujillo, I. Lorite, R.E. Madrid, M. Tirado, D. Comedi, P. Esquinazi, Mater. Sci. Eng. B., 200 (2015)124 - 131

39) R. Tripathi, A. Dutta, S. Das, A. Kumar, T. P. Sinha, Appl. Nanosci., 6 (2016) 175 - 181

40) A. Singh, R. Chatterjee, S. K. Mishra, P. S. R. Krishna, S. L. Chaplot, J. Appl. Phys. 111 (2012) 014113

41) A.K. Jonscher, Dielectric Relaxation in Solids, Chelsea Dielectric Press, London (1983)

42) A. R. Long, Adv. Phys., 31 (1982) 553

43) S.A. Makhlouf, F.T. Parker, F.E. Spada, A.E. Berkowitz, J. Appl. Phys. 81(1997) 5561 - 5563

44) E. Annese, J. Fujii, I. Vobornik, G. Panaccione, G. Rossi, Phys. Rev. B, 84 (2011) 174443

…..ꕥ…..

Chapter 7

SUMMARY AND SCOPE FOR FUTURE WORK

In this chapter, the results of the present study along with the work to be carried out in future are summarized.

The present study describes the synthesis and characterization of NiO nanoparticles. The effect of various dopants on the properties of pristine NiO is also studied. Further, the nanocomposite structures of nickel oxide and metal phthalocyanines and their significant physico-chemical properties have been focused upon. The research work has been systematically presented in 7 chapters. The structure and fundamental properties of NiO nanoparticles and a brief review of the studies on the synthesis and properties of pristine and doped nickel oxide and its phthalocyanine composites are presented in Chapter 1. Nanocrystalline NiO is synthesized using simple chemical precipitation method and characterized using various tools as mentioned in Chapter 2. Chapter 3 depicts the structural, optical, electrical and magnetic characterization of the synthesized NiO nanoparticles. The effect of calcination on the properties of NiO nanoparticles is also discussed. The modification in the structural, optical, electrical and magnetic properties of NiO nanoparticles due to cobalt and cerium doping are described in Chapters 4 and 5 respectively. The synthesis and characterization results of NiO/CoPc and NiO/SnPc nanocomposites are presented in Chapter 6. A summary of all the work is presented in the current chapter. The important outcomes, promising applications of the materials synthesized and an outline of prospective research are mentioned as concluding remarks of the chapter.

7.1 Summary of the Present Work

NiO nanoparticles have been successfully synthesized using chemical precipitation method. The small crystallite size of the

synthesized material without the addition of any surfactant shows the versatility of this simple synthesis technique. Thermal analysis shows that complete decomposition of the precursor occurred around 400^{o}C to form nickel oxide. The effect of calcination temperature on the structural, optical, electrical and magnetic properties of the synthesized samples is studied. It is found that calcination process resulted in an increase in intensity of diffraction peaks, decrease in FWHM, increase in crystallite size, decrease in micro-strain, decrease in lattice constant and hence lattice contraction. An average crystallite size of 8.2 nm is estimated for the as-prepared NiO nanoparticles. The size is found to increase with the increase in calcination temperature due to the thermally promoted crystallite growth. FESEM analysis shows that the samples contain polygonal faceted nanoparticles which are well dispersed in the bulk lattice. EDX analysis confirms the presence of only the elements expected for NiO. The unidirectional fringe patterns in the HRTEM images and bright spots in the SAED patterns confirm the crystalline nature of the synthesized samples. FTIR results confirm the successful formation of NiO. The characteristic double peaks for $2p_{3/2}$ and $2p_{1/2}$ main lines are observed in the XPS spectrum of Ni 2p, which indicate the presence of traces of Ni^{3+} along with Ni^{2+} states in the as-synthesized NiO sample.

Optical absorption spectra show very good UV absorption for the samples. The bandgap obtained for pristine NiO is 3.72 eV and is found to decrease with the increase in calcination temperature. The PL emission in the UV region corresponds to the near band edge transition

of NiO, while the shoulder peaks in the visible region are attributed to defect related deep level emissions. Grain size variation caused by calcination exhibits a significant effect on the electrical properties of nanocrystalline NiO. The measured DC and AC conductivities of all the samples are found to be much higher than that of single crystalline NiO. The double semicircular behaviour of Nyquist plots confirms the grain and grain boundary contribution to the impedance of the samples. The magnetic property of the sample undergoes a transition from superparamagnetic to weak ferromagnetic state upon calcination.

The study of the effect of cobalt and cerium doping on the structural, optical, electrical and magnetic properties of nanocrystalline NiO proved that doping is a powerful method for modifying the properties of pristine NiO. The crystallite size of Co doped NiO is found to be less than that of the pristine sample. The bandgap of NiO can be reduced considerably by Co doping without causing any significant structural modification, which makes them useful for various optoelectronic applications. PL emission studies of NiO with varying Co concentration, is an efficient method for the exploration of point defects such as oxygen/nickel vacancies and interstitials in the host lattice. Electrical properties of Co doped NiO exhibit the same behaviour as that of pristine sample, but a decrease in the parameters is attributed to the incorporation of dopant ions. Energy dissipation, unwanted noise and signal loss can be considerably reduced by cobalt doping. Jonscher's power law plots for the samples confirmed frequency dependent hopping as the main conduction mechanism for pristine and Co doped NiO.

Thermal analysis shows that Ce doped NiO nanoparticles become thermally stable only at 600^{o}C. XRD studies reveal the presence of CeO_2 phase in the sample doped with 1 mol% of Ce. The coexistence of Ce^{3+} and Ce^{4+} states in the doped NiO samples is evident from the XPS studies. Optical studies show an enhancement in UV absorption and bandgap reduction upon Ce doping. Due to the reduction in PL intensity, an enhanced photocatalytic activity is expected for Ce doped NiO nanoparticles. The incorporation of Ce ions increased the dielectric permittivity, loss tangent and AC conductivity of the Ce doped samples. VSM studies reveal an increase in superparamagnetic ordering in the samples with the increase in dopant concentration.

A systematic study has been carried out to analyse the structural, optical, electrical and magnetic properties of NiO/M-Pc (M=Co, Sn) nanocomposites synthesized by solvent-evaporation method. The structure and morphology of the nanocomposite are characterized by XRD, TEM and FESEM. Compositional analysis using EDX confirms the presence of all the elements expected in the NiO/M-Pc (M=Co, Sn) nanocomposites. FTIR studies confirm the successful formation of the nanocomposites.

UV–Visible absorption studies indicate an extended light absorption into the visible region for the synthesized nanocomposites. A decrease in bandgap energy, together with improved absorption intensity has been observed for the nanocomposites. The emission quenching observed in the PL spectrum of the nanocomposites indicates enhanced

photocatalytic activity. The semiconducting nature of the synthesized materials is established from electrical characterization. The dielectric loss of NiO can be considerably reduced by forming the nanocomposites. The grain and grain boundary conduction in the nanocomposite samples are evident from the appearance of two semicircular arcs in the Nyquist plots. The AC conductivity of the synthesized samples demonstrates polaron hopping transport mechanism in the materials and it is confirmed by Jonscher's universal power law. A decrease in AC conductivity is observed for the nanocomposites compared to pristine NiO. VSM studies reveal a weak ferromagnetic behaviour for the nanocomposite samples. The study reveals that the presence of different central metal ions in the NiO/M-Pc (M=Co, Sn) nanocomposites substantially affects the properties of pristine NiO.

7.2 Important Outcomes

Major findings of the present investigation are listed below.

- Nickel oxide nanoparticles with an average crystallite size of 9 nm are successfully synthesized through chemical precipitation method without using any capping agent.

- The studies on the structural, optical, electrical and magnetic properties of NiO reveal that calcination has a profound effect on its properties.

- The interfacial region consisting of grain boundaries and triple junctions has an important role in deciding the transport properties of the samples.

- The magnetic property of the sample undergoes a transition from superparamagnetic to weak ferromagnetic state, with increase in crystallite size.

- The crystallite size of NiO is reduced with cobalt doping, without affecting its structure.

- Bandgap tuning of NiO is achieved by Co doping without causing any structural modifications.

- Significant reduction in the PL intensity of NiO is achieved with Ce doping.

- The addition of M-Pc (Co, Sn) in NiO nanoparticles can extend the optical absorption spectra from the UV region to the entire span of visible light.

7.3 Scope for Future Work

The work presented in this thesis can be extended in several directions and are briefly presented as follows:

- Nickel oxide nanoparticles are reported to have multiple applications. More extensive and systematic studies are required to explore their potential applications.

- The low temperature magnetic behaviour of pristine and doped samples needs to be explored.

- The study can be extended to analyze the applications of cobalt and cerium doped samples, NiO/CoPc and NiO/SnPc nanocomposites.

- The influence of surfactants on the properties of NiO can be studied.

- Investigation of the properties of NiO/CoPc and NiO/SnPc by varying the concentration of both CoPc and SnPc can be carried out.

…..❀…..